Abstract of “Measurement and Analysis of WIMP Detection Backgrounds, and Characterization and Performance of the Large Underground Xenon Dark Matter Search Experiment” by David Charles Malling, Ph.D., Brown University, May 2014.

The dominant component of matter in the universe, referred to as dark matter, cannot be explained by the standard model of particle physics. A leading candidate for dark matter is the weakly interacting massive particle (WIMP). The WIMP theory is well motivated by several extensions of the standard model, and has been tested directly in the laboratory over the last 30 years.

The Large Underground Xenon (LUX) experiment seeks to identify the signatures of WIMP interactions with baryonic matter. LUX measures particle interactions at the keV level by the detection of single-photon signals in a 250 kg Xe target mass. The LUX detector inner fiducial region is the lowest measured background particle detector in the world at keV energies, with background rates at the level of 10^{-3} counts keV^{-1} kg^{-1} day^{-1}. Low background rates are essential for identifying WIMP interactions in the detector, which occur with frequencies <1 kg^{-1} $(5 \text{ years})^{-1}$.

LUX completed its first low-background science run at the Sanford Underground Research Facility in August 2013. WIMP search results are reported from an 85 live day analysis. The experiment places the tightest constraint on WIMP spin-independent interaction cross-sections to date. Results from LUX also exclude several potential dark matter signal claims from other direct detection experiments, for WIMP masses in the range 6–15 GeV. The LUX result is the product of low detector background rates and high photon signal collection efficiency.

Analysis of the first WIMP search data has provided direct characterization of low-energy backgrounds in LUX. Measured background rates were found to be in agreement with expectations based on models of detector material radioactivity. The data also provides the first measurements of intrinsic radioactive contaminants in the detector, including short-lived cosmogenic Xe radioisotopes. I will describe the LUX background model, detailing work which was used in the design and early performance projections of the LUX detector, as well as background measurements which constrain and support the model.

Measurement and Analysis of WIMP Detection Backgrounds, and Characterization and Performance of the Large Underground Xenon Dark Matter Search Experiment

by

David Charles Malling

Submitted in partial fulfillment of the requirements
for the degree of Doctor of Philosophy
in the Program in Physics at Brown University

Providence, Rhode Island

May 2014

Copyright © 2013 David Charles Malling

This dissertation by David Charles Malling is accepted in its present form
by the Physics Department as satisfying the dissertation requirement
for the degree of Doctor of Philosophy.

Date: ______________ ________________________________

Richard Gaitskell, Advisor

Recommended to the Graduate Council

Date: ______________ ________________________________

David Cutts, Reader

Date: ______________ ________________________________

Savvas Koushiappas, Reader

Approved by the Graduate Council

Date: ______________ ________________________________

Peter Weber, Dean of the Graduate School

Curriculum Vitae

1984	Born in Syracuse, NY (USA)
2007	B.S. Engineering Physics. Syracuse University, Syracuse NY (USA)
2010	M.S. Physics. Brown University, Providence RI (USA)

Appointments and Teaching

2007-	Research Assistant. Brown University, Physics Department, Providence RI (USA)
2006-	Summer Undergraduate Research Fellowship. California Institute of Technology, Pasadena, CA (USA)
2006-2007	Undergraduate Teaching Assistant. Syracuse University, Physics Department, Syracuse NY (USA)
2005-2007	Research Assistant. Syracuse University, Physics Department, Syracuse NY (USA)

Refereed Publications

Corresponding author

- D.C. Malling et al., "Rare Event Search Backgrounds from Primordial Radionuclide Chain Disequilibrium." *Submitted to Astropart. Phys.* (2013). arXiv:1305.5183 [astro-ph.IM].

- D.S. Akerib et al., "An Ultra-Low Background PMT for Liquid Xenon Detectors." *Nucl. Instr. Meth.* **A703** (2013) 1–6. arXiv:1205.2272 [physics.ins-det].
- D.C. Malling et al., "After LUX: The LZ Program." *Proceedings of the 2011 Meeting of the Division of Particles and Fields of the American Physical Society*, eConf C110809 (2011). arXiv:1110.0103 [astro-ph.IM].

Contributing Author

- D.S. Akerib et al., "First results from the LUX dark matter experiment at the Sanford Underground Research Facility." *Submitted to Phys. Rev. Lett.* (2013). arXiv:1310.8214 [astro-ph.CO].
- D.S. Akerib et al., "The Large Underground Xenon (LUX) Experiment." *Nucl. Instr. Meth.* **A704** (2013) 111–126. arXiv:1211.3788 [physics.ins-det].
- D.S. Akerib et al., "The LUX Prototype Detector: Heat Exchanger Development." *Nucl. Instr. Meth.* **A709** (2013) 29–36. arXiv:1207.3665 [physics.ins-det].
- D.S. Akerib et al., "Technical Results from the Surface Run of the LUX Dark Matter Experiment." *Astropart. Phys.* **45** (2013) 34–43. arXiv:1210.4569 [astro-ph.IM].
- D.S. Akerib et al., "LUXSim: A Component-Centric Approach to Low-Background Simulations." *Nucl. Instr. Meth.* **A675** (2012) 63–77. arXiv:1111.2074 [physics.data-an].

Presentations

Talks

- American Physical Society April Meeting, February 2010, Washington D.C.
- American Physical Society Division of Particles and Fields, August 2011, Providence RI
- Brookhaven Forum, October 2011, Upton NY

- Identification of Dark Matter 2012, Kavli Institue for Cosmological Physics at the University of Chicago, July 2012, Chicago IL
- American Physical Society April Meeting, April 2013, Denver CO

Posters

- Topics in Astroparticle and Underground Physics 2013, September 2013, Asilomar CA

Honors and Awards

- 2007 - B.S. Engineering Physics. Magna Cum Laude.
- 2006 - Summer Undergraduate Research Fellowship, California Institute of Technology, Pasadena CA
- 2003 - Centennial Scholar, Syracuse University, Syracuse NY

ACKNOWLEDGMENTS

This dissertation represents a condensed version of only a few of the fascinating projects that I have had the opportunity to work on since my arrival at Brown in June 2007. I have worked hard, I have been fortunate, and I have been supported in all ways by a number of special people. Here I mention only a selection of those who have had the most direct impact on this dissertation. I have had the good fortune to know and work with many more people throughout my career at Brown, before this at Syracuse, and even earlier. I save their mention for what will undoubtedly be a best-selling autobiography.

I thank Rick Gaitskell for an immense number of things. I am deeply grateful for his guidance in matters both LUX and non-LUX, whether in the lab, in the office, or strolling around the east side attempting to find a patch of sunshine in the middle of New England "winter[1]." I have been truly inspired by Rick's ebullient approach to all things. I like to think that, in significant part from his mentoring, I have left Brown after six and a half years not only more knowledgeable, but actually *smarter*, and with a great deal more confidence.

I am thankful to Savvas Koushiappas and Dave Cutts for their extremely helpful guidance as my thesis committee, along with Rick. From their input, a great deal of refinement in both accuracy and precision have been made on the work captured in this dissertation. From their questions and comments, along with those from Bob Lanou and Ian Dell'Antonio, a very engaging and entertaining discussion has been had of this work, and of the bigger picture into which this work fits.

---

[1] I use quotations because I am from Syracuse; the gloomy, brisk, snowless tantrum thrown by the southern New England area from December through March hardly qualifies as the season that I came to know growing up as The Culling.

I gratefully acknowledge the immense amount of help I received from “Papa” Luiz de Viveiros and Peter “Den Mother” Sorensen during my first years in the group. It has been a pleasure continuing to work with them on LUX after their graduation from Brown, and our intellectual discourse and sessions at the bar were no less engaging or valuable after meeting again in South Dakota. I thank my fellow grads, Jeremy Chapman, Carlos Faham and James Verbus, as well as Simon Fiorucci, Monica Pangilinan, and our annexed Brownies, Alastair Currie and Attila Dobi, for their support in everything from our collaborative analysis efforts to begrudging me the walk to Mike’s for lunch two to three times per week. I also owe great thanks to Samuel Chan and Dongqing Huang for enthusiastically taking up the reins as I receded into a cocoon in the days of final analyses and writing. My thanks and appreciation extend out fondly to the entire LUX collaboration, past and present, for creating an incredible community based around an incredible experiment. It has been an honor to be a part of it.

I might have long ago drifted off of the planet if not for Alex “GS” Geringer-Sameth, Ryan Michney, Andy Blaeser, Indrit Alex Metaj and Mike Antosh. Thank you all for your camaraderie, and for prodding me to occasionally get physical exercise in these latter months. To GS, an additional great thanks for our late-night brainstorming sessions, which routinely sharpened my thoughts to the point at which solutions would seemingly drop out of thin air (and then would take until daybreak to get written up properly). I also gratefully thank Dina Lloyd for her love and support, and for allowing me to work as long and as hard as I was physically able, but no more than that.

I finally wish to thank my parents Glenn and Judith Malling for allowing me to ramble on in my excitement about every detail of these last months. Their love and encouragement has done much more than allow me to complete this dissertation. Their hard work and sacrifices afforded me an environment in which I was encouraged in my passion for science, and then given the opportunity to pursue that passion both in and out of school. The only thing they have asked for in return is the invention of a teleporter. I am working on it.

CONTENTS

1 DIRECT DETECTION OF DARK MATTER 1

1.1 The Concordance Model 2

1.2 A Multitude of Measurements 4

1.2.1 Dark Matter in Galaxies 5

1.2.2 The Bullet Cluster 7

1.3 WIMPs 8

1.3.1 Freeze-Out and Relic Abundance 9

1.3.2 WIMP Candidates 10

1.3.3 Detectability 11

1.3.3.1 Annihilation 12

1.3.3.2 Creation 13

1.3.3.3 Scattering 13

1.4 Direct Detection 13

1.4.1 WIMP / Nucleus Interactions 14

1.4.2 Recoil Spectra 15

1.4.3 Detection Parameter Space 18

1.4.4 Establishing a Quiet Detector 18

2 DIRECT DETECTION WITH THE LUX EXPERIMENT 23

2.1 Detection with Liquid Xenon 23

2.1.1 Xenon Properties 23
2.1.2 Energy Deposition Response 26
2.2 The LUX Detector 28
2.2.1 Observed Signals 30
2.2.2 PMTs and Light Collection 37
2.2.3 Electric Fields 37
2.2.4 Calibrations 38
2.2.5 Cryogenics 40
2.2.6 Circulation and Purification 41
2.2.7 Water Shield 41
2.2.8 Data Acquisition 42
2.2.9 Data Processing 45
2.3 LUX Timeline 46
2.3.1 LUX 0.1 46
2.3.2 LUX Surface Facility 46
2.3.3 Underground Deployment 50
2.4 Dark Matter Search 50

3 XENON TPC OPTICAL MODELING 54

3.1 Xenon TPC Light Collection Model 54
3.1.1 PTFE Reflectors 55
3.1.2 Electric Field Grids 56
3.1.3 Gas-Liquid Boundary Refraction and Reflection 57
3.1.4 Xenon Rayleigh Scattering Length 58
3.1.5 Xenon Scintillation Photon Absorption Length 59
3.1.6 PMT Windows 59
3.1.7 PMT Detective Efficiency 60
3.1.7.1 Definition of Quantum Efficiency 60
3.1.7.2 Variation of QE with Angle 61
3.2 Fitting XENON10 Data 65

3.2.1 Methodology 65
3.2.2 Scaling Factor Calculations 66
3.2.3 Results 68
3.3 Predicting LUX Light Collection 72
3.3.1 Geometric Collection Efficiency for Varying PTFE Reflectivities . 72
3.3.2 Measured Light Collection Efficiency for Varying PTFE Reflectivities 73
3.3.3 Specular vs. Diffuse Reflection and Impact on Geometric Collection Efficiency 74
3.3.4 Photon Angle-of-Incidence Distributions and Corrections to PMT QE Estimates 75
3.3.4.1 Photon Incidence Angles at the Photocathode 75
3.3.4.2 Measurements of $P_{loss,0}$ 76

4 Direct Measurement of Nuclear Recoil Scintillation Efficiency 78
4.1 Strategy 78
4.2 Materials 82
4.3 Calibration Simulations 83
4.3.1 Simulation Parameters 83
4.3.2 Neutron Energy Spectrum 85
4.3.3 Cut Definitions 87
4.3.3.1 Position Cut 87
4.3.3.2 EM Veto Cut 87
4.3.3.3 Energy Cut 88
4.3.4 Event Rates 88
4.4 Optimization of Conduit Placement 89
4.5 Data Analysis 94

5 The LUX Background Modeling Program 96
5.1 Analytic Model of Gamma Backgrounds 97

5.2 Monte Carlo Modeling of Gamma Backgrounds 101
  5.2.1 Analysis Cuts 102
  5.2.2 Fitting High-Energy Data 103
  5.2.3 Low-Energy Fiducial Background Rates 104
5.3 Intrinsic Background Modeling 106
  5.3.1 Activated Xenon Isotopes 107
  5.3.2 Radon 109
  5.3.3 ^{85}Kr 113
  5.3.4 ^{136}Xe 116
5.4 Gamma-X Background Modeling 117
  5.4.1 Model of Spectral Shape and Position Distribution 118
  5.4.2 Estimating Signal Size 120
  5.4.3 Simulation Results 121
5.5 Internal Neutrons 123
  5.5.1 Neutron Yield Rates 123
    5.5.1.1 PMTs 123
    5.5.1.2 ^{210}Pb Daughters 127
    5.5.1.3 Cryostats 128
  5.5.2 Neutron Backgrounds 128
5.6 External Gamma and Neutron Backgrounds 129
5.7 Neutrino Backgrounds 131
5.8 Fiducial Volume Optimization 132
5.9 Predicted Low-Energy ER Background Event Rates 133
5.10 S1 and S2 Distributions from Energy Depositions 135

6 DARK MATTER SEARCH BACKGROUNDS FROM PRIMORDIAL RADIONUCLIDE CHAIN DISEQUILIBRIUM 139
6.1 Abstract 139
6.2 Introduction 140

6.3 Screening Methodologies 141
6.4 Chain Disequilibrium for Primordial Radionuclides 144
6.4.1 ^{238}U Chain 144
6.4.2 ^{235}U Chain 145
6.4.3 ^{232}Th Chain 146
6.5 ^{238}U Alpha Emission Spectra and Neutron Yields 147
6.6 ^{238}U Disequilibrium Impact on Neutron Backgrounds for Dark Matter Experiments 149
6.7 ^{238}U Disequilibrium Impact on Gamma Backgrounds for Dark Matter Experiments 153
6.8 Conclusions 157
6.9 Acknowledgements 161

7 THE LUX MATERIALS SCREENING PROGRAM 162
7.1 Counting Goals 163
7.1.1 Goals for Major Internals 164
7.1.2 Goals for Small Internals 164
7.2 SOLO 165
7.2.1 The SOLO Facility and Diode-M Detector 165
7.2.2 Counting Methodology 171
7.3 Counting Results 173
7.3.1 Identified Radioisotopes and Predicted Cosmogenic Activation . . 173
7.3.2 PMTs 174
7.3.3 Major Internals 175
7.3.4 Small Internals 177
7.3.5 Steel Pyramid 180
7.3.6 Concrete and Rock 180
7.4 Comparison of Counting Goals with Results 183
7.5 LZ PMTs 184
7.5.1 Counting Results 185

7.5.2 Impact on Dark Matter Backgrounds 188

8 LUX Run 3 Results 190

8.1 S1-Only Data 191

8.2 Light Collection 195

8.3 Gamma Backgrounds 196

8.3.1 Data Quality Cuts 196

8.3.1.1 Gamma Selection Cuts 196

8.3.1.2 Single Scatter Cuts 198

8.3.2 Energy Reconstruction 199

8.3.2.1 Single-Scatter Calibration 199

8.3.2.2 Multiple-Scatter Calibration 201

8.3.2.3 Energy Nonlinearity 202

8.3.3 Comparison with Calibration 202

8.3.4 Peak Identification 202

8.3.5 Simulation Comparison 204

8.3.5.1 Simulation Datasets 204

8.3.5.2 Energy Resolution 205

8.3.5.3 Single-Scatter Cut Efficiencies 205

8.3.5.4 Comparison of Drift Region Spectra and Best-Fit Results 207

8.4 Activated Xenon Measurements 208

8.5 Radon 211

8.5.1 ^{214}Pb Activity Bounds from ^{222}Rn Daughters 211

8.5.2 Upper Bound from High-Energy Data 212

8.5.3 Geometric Series Activity Estimate 213

8.6 Xenon Flow Imaging with ^{222}Rn Decays 213

8.7 Neutron Multiple Scatter Analysis 215

8.7.1 Simulation Studies 217

8.7.1.1 Neutron Studies 217

8.7.1.2 NEST S1/S2 Studies 217

8.7.2 Event Reconstruction 219
8.7.2.1 S1 and S2 Reconstruction 219
8.7.2.2 Position 221
8.7.3 Cuts 221
8.7.3.1 MS Selection 221
8.7.3.2 S1 Range 222
8.7.3.3 Fiducial 222
8.7.3.4 S2/S1 Discrimination 222
8.7.3.5 Bad Area 223
8.7.4 Results 223
8.7.4.1 Multiple Scatters in LUX Data 223
8.7.4.2 Single Scatter UL for Run 3 and Run 4 225
8.8 Low-Energy ER Backgrounds 225
8.8.1 Observed Event Rates 225
8.8.2 Background Distributions 227
8.8.3 Time Variation of Low-Energy Backgrounds 228
8.8.4 Parameterization of Low-Energy Background Model 230
8.9 WIMP Search Results 231

BIBLIOGRAPHY 236

List of Tables

1.1 Component energy densities for the Λ-CDM model, as recently reported in [4]. Values are taken from Planck temperature power spectrum data. Uncertainties on Ω_b, Ω_{DM} and Ω_Λ are given at 68% CL (±34%). The constraint on Ω_K is taken from the combination of Planck, lensing, WMAP polarization, high-resolution CMB data, and BAO data constraints, with 95% (±47.5%) uncertainty. w_{DE} is constrained from Planck, WMAP polarization and BAO data, with 95% uncertainty. 4

3.1 Average values for the efficiency terms used in Eq. 3.1. 68

4.1 Event rates normalized per neutron emitted from the source. Rates are listed both for all incoming neutrons and for neutrons with energy >2.3 MeV when entering the active region. Cut definitions are listed in Sec. 4.3.3. 89

4.2 Event rates with N neutron scatters after application of various cuts, for all incoming neutron energies, assuming use of a 10^7 n s^{-1} D-D source outside of the water tank. Cut definitions are given in Sec. 4.3.3. 92

5.1 Results from fitting averaged radioisotope spectra to measured high-energy detector data. Screening values are taken from SOLO measurements of the PMTs (corresponding to top and bottom regions), and superinsulation and plastic thermal insulation (side region). Errors on the best fit decay rate values are estimated to be 25% based on variation of fitting parameters across expected ranges. Corresponding low-energy background rates are given for the 118 kg (Run 3) and 100 kg (Run 4) fiducial volumes in the range 0.9–5.3 $\mathrm{keV_{ee}}$. Errors on low-energy background rates are statistical from simulation results only, and do not propagate errors from decay rate estimates. Total background rate errors incorporate error from both rate estimates and simulation statistics. 105

5.2 Gamma backgrounds from PMTs, cosmogenic ^{60}Co, and other construction materials, for the Run 3 118 kg fiducial volume and a 100 kg fiducial volume. PMT contributions are estimated from screening results (Sec. 7.3.2). Cosmogenic contributions are estimated from assuming that the dominant ^{60}Co background, after subtraction of ^{60}Co backgrounds from PMTs, comes from activated Cu construction components. The background rate from other construction materials is calculated by subtraction of the PMT and cosmogenic background rates from the total observed background rate. 105

5.3 Activated Xe isotopes and their characteristic signatures. Only long-lived (>1 day) isotopes with significant abundances identified in LUX data are listed. Data is taken from [135, 136]. 109

5.4 (α,n) yields for each PMT construction component, sorted by total neutron contribution. Yields for ^{238}U and ^{232}Th are calculated using the USD Neutron Yield Tool [141, 142] Normalized yields integrate over all neutron energies above 100 keV. Values for several lighter elements are cross-checked with (α,n) yields from [143], and are found to agree within 10%. PMT construction components were obtained by confidential communication with Hamamatsu Photonics K.K. 127

5.5 Predicted low-energy NR rates in a 100 kg cylindrical fiducial volume, from neutrons generated in LUX internals. Fiducial and single-scatter cuts are applied as described in Sec. 5.2.1, as well as an EM veto cut described in Sec. 5.5. Rates are taken over the NR energy range 5–25 $\mathrm{keV_{nr}}$. 130

5.6 Projected low-energy event rates for LUX WIMP search runs. Rates are listed for Run 3, with 118 kg fiducial volume, and the projected Run 4, with a 100 kg fiducial volume. A 50 kg inner fiducial volume is also included, assuming no ^{127}Xe contamination. Fiducial volumes are cylindrical, and are unoptimized for background rejection. Fiducial volume physical definitions are listed in Sec. 5.2.1. 135

5.7 Parameters used in conversion of NEST (v0.99β) scintillation and ionization yields to S1 and S2 signals. All quantities are measured from LUX data during the 85 day WIMP search run. 138

6.1 ^{238}U sub-chain (α,n) neutron yields per parent decay, multiplied by 10^8, for common detector construction materials. Yields are calculated from α energies in Fig. 6.3 and (α,n) neutron yields in Fig. 6.4. Yields from the ^{238}U early sub-chain do not include contributions from ^{238}U spontaneous fission, the probability for which is 5.4×10^{-7}. 151

7.1 Detection efficiency ε for peaks used for identification of common radioisotopes, for a batch of five R11410-20 PMTs in the SOLO chamber. ε is calculated from Geant4 Monte Carlo, as described in Sec. 7.2.1, and folds in gamma branching ratio, sample geometry, material absorption, and finite detector size. 172

7.2 Commonly measured radioisotopes in detector materials, with their origins and characteristic attributes. Starred isotopes have associated decay chains which contribute to radiation emission. The relative γ contributions of the various decay chain isotopes are discussed further in Ch. 6. 175

7.3 LUX PMT batch counting results. All measurements were performed at SOLO. Five PMTs were counted in each batch. Actual ^{40}K concentrations in LUX PMTs are taken to be equal to those measured for the LUX R8778 #1 and #2 samples, as Hamamatsu took steps to control the ^{40}K levels in the tubes after initial measurements were performed. The Brown batch ^{40}K results are not applicable to current LUX tubes. 176

7.4 Counting description for major internal material samples. The Total Amount Used in LUX column lists the total mass or number of the component used in LUX, e.g. all PMTs in both top and bottom arrays. Counting results are listed in Table 7.5. 178

7.5 Counting data for major internal material samples. See Sec. 7.3.3 for a discussion of the column definitions and relative sensitivities. The measurement of ^{46}Sc for the first listed cryostat sample, highlighted in red, has a significantly higher ^{46}Sc decay rate than that predicted for LUX material (see Sec. 7.3.1). The elevated rate is caused by sample exposure in an airplane. Scandium-46 counting results for LUX are given by the second Ti material measurement. Descriptions of all counting results are listed in Table 7.4. 179

7.6 Counting data for small internal material samples. Columns are the same as in Table 7.5. 181

7.7 Counting results for several samples of steel for potential use in the construction of the external γ shield pyramid. All counting was performed at SOLO. 182

7.8 Counting results for Sanford underground concrete, counted at both SOLO and LBNL LBF. 182

7.9 Counting results for typical cavern materials in the LUX Underground Lab. Results are courtesy LBNL LBF [173]. 182

7.10 Estimated low-energy ER background contribution in an optimized 100 kg cylindrical fiducial volume from each major material, based on screening results only, using LUXSim background simulations described in Ch. 5. The goal for all materials combined was 1 $\mathrm{mDRU_{ee}}$. Titanium projections assume sufficient time underground for the ^{46}Sc background contribution to decay below upper limits from ^{238}U / ^{232}Th. Upper limits for individual materials are at 90% CL. The total upper limit is a naive addition of positive measurements and upper limits from screening, and has >90% CL. 184

7.11 R8778 and R11410-20 radioactivity screening results, obtained at SOLO. R8778 PMT average counting results are taken from Table 7.3. The R11410-20 sample was counted for 19 live days. Separate columns are provided for completeness for "early" and "late" ^{238}U chain measurements, allowing for potential equilibrium breakage primarily due to ^{226}Ra solubility in water; however, as discussed in Sec. 7.3.3 and Ch. 6, that there is no *a priori* reason to assume an equilibrium breakage. Errors are statistical and quoted at $\pm 1\sigma$. Upper limits are given at 90% confidence level. Results are normalized per PMT. 186

7.12 Counting results from Table 7.11, renormalized by PMT photocathode area. Based on this work, the R11410-20 offers the lowest radioactivity per PMT per unit photocathode area for all benchmark isotopes. In particular, ratios of R11410-20 upper limits to R8778 activities are $\times 1/45$ ^{238}U / $\times 1/19$ ^{232}Th / $\times 1/16$ ^{40}K. The ratio for ^{60}Co, detected in both PMTs, is $\times 1/3$. The very low normalized ratios make the R11410-20 the top candidate for use in the large-area tonne-scale LZ detectors. Included for comparison are counting results for the R8520 PMTs used in the XENON10 [71] and XENON100 [155] experiments, as well as counting results for a second R11410-20 PMT presented in [155] (referred to as "R11410 MOD" in that work). 187

7.13 Recent batch counting results for LZ R11410-20 PMTs. Each batch is comprised of five R11410-20 PMTs. All counting is performed at SOLO. Typical batch counting livetime is 12 days. 188

8.1 Alpha decay rate measurements for all ^{222}Rn chain radioisotopes, as well as the measured α rate from 210Po (from the 210Pb chain). Data is taken from [138]. Measured decay rates are compared with rate predictions based on a geometric series, using ^{222}Rn and 214Po measurements to fix the endpoints of the series. 212

8.2 Results from LUXSim neutron background studies (Sec. 5.5). Datasets correspond to neutron emission from bottom and top PMT arrays. Neutron emission rates are calculated in Sec. 5.5. Relative rates are calculated from the total fraction of neutrons interacting in the detector, multiplied by the neutron emission rate from each source. MS / SS ratios are calculated for MS events within a 180 kg ($R < 21$ cm, 7 cm $< Z <$ 52 cm) volume, and SS events with the standard 118 kg ($R < 18$ cm, $7 < Z < 47$ cm) or 100 kg ($R < 17$ cm, $9 < Z < 47$ cm) fiducial volumes. S1 estimates are taken from folding in NEST NR scintillation and ionization yields in post-processing, combined with analytic functions to fold in detector efficiencies. 218

8.3 NR SS upper limits from observed LUX data. The 118 kg fiducial is the standard WIMP search fiducial used in Run 3 ($R < 18$ cm, 7 cm $< Z <$ 47 cm). The 100 kg fiducial is defined as $R < 17$ cm, 9 cm $< Z <$ 47 cm, and is used for NR background projections for Run 4. Search efficiency is combined from all cuts listed in Sec. 8.7.3. MS / SS ratio is taken from LUXSim background studies, listed in Table 8.2. Upper limits are listed at 90% CL. 225

8.4 Low-energy ER background rate contributions from all sources measured in Run 3 data. Measurements and projections are averaged over the energy range 0.9–5.3 keV$_{\mathrm{ee}}$. Rates are calculated for three fiducial volumes: 118 kg (as used in the Run 3 WIMP search result); 100 kg (projected to be used for the Run 4 one year WIMP search run); and a 50 kg inner fiducial. Data is measured from April 22–August 8 in the "mean" row. The total observed early and late rows correspond to measurements in the date range April 22–June 13 and June 14–August 8, respectively. 227

8.5 Analytic model functions for all major low-energy ER background sources. Best-fit parameters are listed in Table 8.6. The functions are used in the WIMP search PLR analysis. 231

8.6 Best-fit analytic model function parameters. Parameters correspond to models listed in Table 8.5. For the ^{127}Xe model, $\tau_{^{127}\mathrm{Xe}} = 52.5$ days and $t = 0$ on May 1. 231

List of Figures

1.1 Measurements of radial star velocity in the NGC 3198 galaxy as a function of distance from the galactic center, obtained by observation of H 21 cm line emission. The measured rotation curve is shown (points), along with estimated curves corresponding to the contribution from gas only and stars+gas. Plot taken from [23]. 8

1.2 The generic diagram describing WIMP-SM interactions. Time axes are labeled for each different process. The interaction mechanism is generically described by the red circle. 12

1.3 Dark matter scattering rates for (a) 10 GeV and (b) 100 GeV WIMPs on various target elements. Scattering energy E_r is given in units of $\mathrm{keV_{nr}}$, where the "nr" subscript indicates energy deposition through a recoiling target nucleus (see discussion in Sec. 2.1.2). The differential recoil rate is shown as the solid curves, for scattering from Xe (green), Ge (red), and Ar (blue) nuclei. The integrals of the differential spectra from E_r to infinity are shown as the dashed curves for the same nuclei. A WIMP-nucleon SI cross section 10^{-45} cm^2 is used. Differential spectra assume a Helm nuclear form factor. Rates are calculated using Eq. 1.9, assuming $\rho_{local} = 0.3$ GeV cm^{-3}, $v_0 =$ 220 km s^{-1}, $v_{earth} = 245$ km s^{-1}, $v_{esc} = 544$ km s^{-1}. 17

1.4 WIMP dark matter direct detection parameter space, where the axes are the WIMP mass (horizontal) and spin-independent cross section (vertical). Plot taken from [46]. Solid lines are 90% exclusion curves from experiments reporting null results, including LUX 85.3 day [46] (blue, $\pm 1\sigma$ shaded), XENON100 100 day [54] (orange) and 225 day [49] (red) results, ZEPLIN-III [55] (magenta), CDMS II [56] (green), and Edelweiss II [57] (yellow). The inset shows allowed contours from DAMA/LIBRA [58, 59] (gray), CRESST II [60] (yellow), CDMS II Si detectors [61] (green, centroid denoted by the x), and CoGeNT annual modulation signals [62] (red). Further discussion of LUX results is given in Sec. 8.9. Limit and contour data available at [63]. . . . 19

1.5 A comparison of energy scales and background rates in several different particle detectors, illustrating the need for an instrument such as LUX for WIMP discovery. The background energy spectrum is given in units of $\mathrm{keV_{ee}}$, where the "ee" subscript refers to energy deposited by an electron in the detector (see Sec. 2.1.2 for further details). The LUX background energy spectrum (black) in the 100 kg fiducial volume is shown from the second half of the 85 day WIMP search run, after application of WIMP search cuts. Background energy spectra are shown for comparison for the following dark matter detectors: CDMS II Ge detectors (red, 241 kg days) [70], XENON10 (orange, 5.4 kg fiducial) [71], and XENON100 (yellow, 30 kg fiducial) [72]. Background spectra are also shown for the EXO (green, 175 kg) [73] and GERDA (cyan, 16.7 kg year) [74] double beta decay experiments, and the Borexino (blue, 154 ton years) [68] and SNO (magenta, 391 live days) [75] neutrino experiments. Overlaid is the projected p-p solar neutrino scattering spectrum on Xe (dark gray, dashed) [76, 77], which creates an electron energy deposition noise floor, and the spectrum from ^{136}Xe neutrinoless double β decay (light gray, dashed) [77], assuming no enrichment or depletion of ^{136}Xe in natural Xe. The projected ER background rate for Ar detectors from β decay of ^{39}Ar (purple dashed) is also given [78], assuming a reduction of ^{39}Ar levels to $\times 1/100$ their natural levels [79]. 22

2.1 Photon attenuation length (mean free path) for γ rays in liquid Xe, as a function of energy. The mean free path is broken down into various energy deposition processes. Data is taken from [87]. (LUX Matlab function gamma_length.m.) 25

2.2 (a) Number of detectable quanta generated for ER (solid) and NR (dashed) energy depositions in liquid Xe. Shown are the curves for scintillation photon n_ν (blue) and ionization electron n_e (red) average yields. (b) The ratio of ionization electrons to scintillation photons, as a function of photon yield, for ER (solid) and NR (dashed) energy depositions. The typical WIMP search range is shown in dashed green, corresponding to 3.4–25 keV$_{\mathrm{nr}}$. Data from [90]. 29

2.3 The LUX detector, shown in cross-section. Major detector features across all subsystems are highlighted. Figure is taken from [80]. 31

2.4 Snapshots of LUX detector construction and deployment. (Top left) The Cu top radiation shield and PMT array holders are mounted in the Ti strap frame, which is suspended from the inner cryostat dome. Assembly takes place in the Surface Lab clean room. (Top right) A bottom-up view of the detector after installation of the top PMT array, PTFE reflector panels, field shaping rings, and HDPE mounting panels. The bottom edges of the Xe heat exchanger and additional circulation lines are visible to the left and right of the active region respectively. Photo courtesy C. Faham. (Bottom left) The detector is lowered into position for the first technical run at the Surface Lab. Three flex conduits are visible, which contain HV and signal cables for the PMTs, electric grids, thermometry and level sensors. Connected to the flex conduits is the "breakout cart," on which are mounted feedthroughs for access to all cabling. In the background behind the breakout cart is the HV cart, containing HV for the PMTs and electric field grids, as well as the slow control master computer. (Bottom right) The LUX detector is fully installed in the water tank in the LUX Underground Lab. Twenty 10" Hamamatsu R7081 PMTs instrument the water tank as a Cherenkov veto for rejection of muon-induced background events. The tank is lined with Mylar to enhance Cherenkov signal collection. In the left background is the air conduit used for the D-D neutron generator calibration (Ch. 4). Photo courtesy M. Kapust. 32

2.5 Operating principle of a liquid Xe TPC. An energy deposition in the liquid Xe produces a prompt scintillation signal (S1) and an ionization electron cloud. This cloud is drifted by an electric field into the high-field gas Xe region, where it creates a proportional electroluminescence signal (S2). The relative sizes and shapes of the S1 and S2 pulses are diagrammed at the right. The S2 signal creates a narrowly focused hot spot on the top PMT array, used for XY position reconstruction of the event. The time between S1 and S2 fixes the Z position of the event. The figure is taken from Ref. [80]. 35

2.6 S1+S2 event from a γ interaction in the LUX drift region. The S1 and S2 pulses are expanded for detail. The S2 pulse hit pattern is shown in the upper right corner. The event is reconstructed with energy 4.2 keV$_{ee}$, scattering at the outer radial edge of the detector 24 cm above the bottom PMT array. The subsequent unmarked pulses are single electron S2s, used to calibrate the LUX ionization detection efficiency. Event trace credit [98]. 36

2.7 Sketch of the location and geometry of the low-radioactivity steel pyramid shield (red), built into the floor of the LUX Underground Lab directly below the water tank. The pyramid is constructed out of six octagonal low-radioactivity steel plates. The pyramid is used to augment the vertical water shielding, allowing the detector to sit closer to the cavern floor and increasing the water shield thickness above the detector. Image credit S. Fiorucci. . 42

2.8 Flux of γ rays and neutrons through a semi-infinite wall of water, as a function of wall thickness. Flux is defined as the fraction of particles traveling beyond a given depth. Curves are shown for γ rays from typical ^{238}U / ^{232}Th content in rock (blue), neutrons from typical ^{238}U / ^{232}Th content in rock (green), and high-energy neutrons from muon spallation in rock (red). Figure taken from [71]. 43

2.9 The LUX 0.1 detector. A 5 kg active region is instrumented by 3 top + 1 bottom R8778 PMTs. The active region is housed in a 230 kg displacer block made of Al, allowing the cryostat to be filled to the target liquid height (green) using only 50 kg of Xe. The liquid height in the detector is monitored by three parallel wire level sensors. The Xe is circulated through two heat exchangers, which were prototyped for deployment in LUX. The figure is taken from Ref. [105]. 47

2.10 (a) Measurement of S2 signal size as a function of depth in the LUX 0.1 detector. S2 signals are generated using a ^{57}Co 122 keV γ source, allowing the measured S2 size to map directly to electron drift length. Depth is determined by the S1-S2 timing separation, as described in Sec. 2.2.1. Data are shown from two measurements before (red) and after (blue) an early purification run. The datasets yield electron drift length measurements of 0.188 ± 0.001 cm and 12.4 ± 0.9 cm respectively. (b) Electron drift length in the LUX 0.1 detector, as a function of time. The drift length directly tracks the concentration of electronegative impurities in the active region. Xenon was circulated at 140 kg day^{-1} during the purification run. Figures are taken from [105]. 48

2.11 (a) LUX Surface Lab side profile. The Surface Lab was converted from a warehouse facility at Homestake in 2010. (b) LUX Surface Lab layout. The detector is deployed in a 3 m diameter water tank. The general layout of the Surface Lab closely follows the layout of the underground lab. The relative positions of the detector, water tank, breakout and HV carts, electronics racks, and clean room are the same. The gas system components were shifted to the second level of the underground lab to take advantage of multi-level occupancy. 51

2.12 Monte Carlo studies of the γ spectrum in the detector as a function of water shield thickness. Spectra are shown corresponding to the initial γ spectrum (blue), the γ spectrum in the active region using no water shield (cyan), and the active region γ spectrum for a 50 cm (green), 1 m (red), and 1.5 m (magenta) thickness water shield. Y axis units are counts $\mathrm{keV_{ee}}^{-1}$ (γ incident at the water tank wall)$^{-}$

3.1 Simulation of the fraction of photons detected, averaged over the full liquid Xe volume, as a function of PTFE reflectivity for TPCs of mass 13.5kg (red), 350 kg (magenta) and 20 tonnes (green). No grids are used, and light is collected from 100% absorbing end caps. Full active region coverage by PTFE is assumed. The detector aspect ratio is 0.9. The Rayleigh scattering length is 30 cm, and the absorption mean free path is infinite. Simulation is based on Geant4 [115]. 56

3.2 Grid geometric transparency as a function of photon angle of incidence, where 0° is normal to the grid plane. Curves are shown for strung (solid) and mesh (dashed) grids. l_{dia} and l_{space} are given in arbitrary units. 58

3.3 (a) Absorption spectra for O_2 and H_2O molecules (1 ppm concentration) at UV wavelengths, taken from Ref. [82]. The Xe scintillation spectrum is superposed. Y-axis units are corrected from [m^{-1}] to [cm^{-1}] from the original paper after correspondance with the author. (b) Calculated absorption lengths for scintillation photons using the spectra from (a). Absorption as a function of distance is shown over five orders of magnitude of H_2O concentration. 59

3.4 Illustration of the angular dependence of PMT QE. The apparent photocathode thickness is enhanced by ϵ/δ=1/cos(θ), where θ is the angle of incidence relative to the photocathode normal. Given a probability T of the photon transmitting through the layer at 0° incidence, the probability of photon transmission through the layer at angle θ is $T\left(\theta\right) = T_0^{\epsilon/\delta} = T_0^{1/\cos(\theta)}$. . . . 63

3.5 PMT QE vs. photon angle of incidence θ for the Hamamatsu R550 PMT [124]. The angle θ is defined relative to the PMT face normal. (a) Hamamatsu test data. Data was collected by rotating a test PMT through a wide 600 nm beam. Figure is taken from Ref. [121]. (b) Best-fit analytic curve given by Eq. 3.2, multiplied by $\cos\left(\theta\right)$ and window reflection terms (red dashed). Hamamatsu data (blue) is averaged about $\theta = 0°$. Best-fit results yield a value of $P_{loss,0} = 26\%$. Shown for comparison is a $\cos\left(\theta\right)$ dependence curve (black dashed), corresponding to QE independent of incidence angle. . . . 64

3.6 Angular dependence (with respect to PMT face normal) of R8778 QE, calculated from Eq. 3.2. $QE_{sim}(0°)$ is set to the standard LUX R8778 value of 35%. $P_{loss,0}$ is varied over the full allowed range of values, 0–65%. 64

3.7 Illustration of variation in light collection for top and bottom PMT arrays (black squares) with increasing event height. Light reaching the PMT arrays is shown in green. Light which escapes from the detector is shown in blue. Light reaching the PTFE reflector is shown in red. 66

3.8 A_i distribution for XENON10 R8520 PMTs, estimated using relative sensitivity measurements from [123]. Values are used for calculation of simulation scaling factors in Eq. 3.1. 68

3.9 Five closest simulation matches to XENON10 light collection data, and corresponding simulation reflectance parameters. The X axis is given in units of height (labeled H, corresponding to Z in Sec. 3.2.1). $H = 0$ mm corresponds to the liquid Xe surface. Upward (downward) arrows correspond to light collection at the top (bottom) PMT array. Measured data is taken from the homogeneous $^{131\mathrm{m}}$Xe 164 keV$_{\mathrm{ee}}$ line. Simulation data is shown with best-fit arbitrary scaling, before scaling with Eq. 3.4. 69

3.10 χ^2 probability distributions for XENON10 data matching in R_{PTFE}-R_{grid} space, using fixed optical parameters from Sec. 3.1. Color values are the χ^2/DOF p value in percentage units. (a) Distribution for arbitrary simulation scaling, matching only the slopes and relative separations of the top and bottom PMT array G curves. (b) Distribution using Eq. 3.4 to calculate the absolute simulation scaling factors. 70

3.11 Geometric collection efficiency G as a function of height for varying photon absorption length λ_a (labeled in the plot as λ_{abs}). Curves with high (low) collection efficiency at $Z = 10$ mm correspond to collection at the bottom (top) PMT array. The expected value of λ_a is $\gg$2 m. All XENON10 data fitting attempts use $\lambda_a \to \infty$. The simulation which begets the curves holds reflectivity values constant at $R_{PTFE} = 100\%$, $R_{grid} = 45\%$. 71

3.12 LUX geometric collection efficiency as a function of $R_{PTFE,liq}$. Curves are shown for low and high values of R_{grid}. Separate curves are also shown for $R_{PTFE,gas}$ values of 0% (down-pointing triangles) and 100% (up-pointing triangles). $R_{PTFE,gas}$ has been independently measured at 65%. (a) Results from using a point source for photon emission, located in the center of the active region. (b) Results from using a cylindrical emission volume occupying the entire drift region. No significant change is seen between the two different emission geometries in (a) and (b). 73

3.13 Simulated LUX light collection for 122 $\mathrm{keV_{ee}}$ energy depositions (zero field). Results are identical for point source and full drift emission geometries. G is calculated from LUXSim Monte Carlo. Scaling to phe/$\mathrm{keV_{ee}}$ is performed using Eq. 3.3 with the measured average LUX PMT D value. 74

3.14 Geometric collection efficiency as a function of PTFE reflectivity in liquid Xe, using a pure specular reflection model. Curves are the same as described for Fig. 3.12. 75

3.15 Photon angle-of-incidence distributions at the PMT photocathode. θ is defined with respect to PMT face normal. Separate curves are shown for low and high PTFE reflectivity datasets; no significant change in slope is seen. Curves are also shown separately for top and bottom PMTs. Photocathodes are modeled as quartz, to avoid reflection effects between the quartz and photocathode volumes. The spectrum is used in estimates for corrections to light collection curves, calculated in Sec. 3.1.7.1. Cutoffs in the angular spectra for the top PMT array result from the mismatch between the gas Xe and PMT windows ($n = 1.6$). 76

3.16 Relative gain in LUX light collection as a function of $P_{loss,0}$ for constant $R_{PTFE,liq}$ and $R_{PTFE,gas}$. The spectrum of photon incidence angles is not significantly affected by varying reflectivities, as shown in Fig. 3.15. The curve is calculated using the angular spectrum from Fig. 3.15 as input for Eq. 3.2. 77

4.1 LUX NR calibration strategy using a monoenergetic D-D neutron source and long air conduit for neutron beam collimation. The vector of the conduit is used in combination with the scatter vertex positions in the detector to reconstruct the neutron scattering angle. The corresponding energy is correlated with the detected signals, providing direct NR energy calibration in LUX. 81

4.2 (Top) The fully assembled neutron conduit in the LUX water tank. The PVC body measures 377 cm end-to-end, with 4.9 cm inner diameter. A stainless steel T-bar is used for ballast. Stainless steel hose clamps secure the pipe to the ballast in three locations to prevent bowing. Stainless steel wire connects the tube to winches at the top of the water tank, allowing operators to raise and lower the conduit during calibration operations. (Bottom Left) The 1 m prototype tube, used to test sealing, ballast and suspension techniques. The tube is immersed in the 1.8 m height water tank at Brown University. (Bottom Right) The DD-108M neutron generator, during initial testing at Brown. The generator head is located in the middle of the tee, in line with the turbopump. 84

4.3 Neutron energy spectrum at the active region boundary, for neutrons with initial energy 2.45 MeV launched isotropically from the neutron generator and arriving at the active region through the 5 cm diameter air conduit spanning the water tank. The energy spectrum for all neutrons is shown in black. Applied cuts are (red) an EM veto cut which removes all events with any EM deposition in the active region, (magenta) a position cut requiring the neutron to enter the active region in a 2.5 cm radius circle centered at the axis of the vacuum conduit, and (blue) both cuts combined. The cuts are described in detail in Sec. 4.3.3. 85

4.4 Radial distribution at the active region boundary, for neutrons with initial energy 2.45 MeV launched isotropically from the neutron generator and arriving at the active region through the 5 cm diameter air conduit spanning the water tank. Energy cuts are applied showing all events (black), E $>$ 1 MeV (red), E $>$ 1.5 MeV (magenta), E $>$ 2 MeV (green), and E $\simeq$ 2.45 MeV (blue), showing the dramatic clustering effect for full-energy neutrons in the line of the conduit. This effect allows for a large improvement in signal-to-noise by using a basic position cut on one of the scattering vertices. 86

4.5 Energy deposited as a function of scattering angle for double-scatter events, after application of the EM veto cut. The distribution is shown (a) before and (b) after applying the position cut. The full-energy peak is sharpened by the position cut, sharpening the correlation between NR energy and measured scattering angle. Cut definitions are given in Sec. 4.3.3. 90

4.6 Energy spectrum for scatters at (a) 10°–12° (0.5–0.8 $\mathrm{keV_{nr}}$), (b) 30°–32° (4.9–5.4 $\mathrm{keV_{nr}}$), and (c) 75°–77° (27.4–28.6 $\mathrm{keV_{nr}}$), with and without the position cut applied, for double-scatter events. Angle-energy relationship assumes $T = 2.45$ MeV. The vertex nearest the conduit axis is selected as the first vertex, with the other vertex assumed to be the second. The position cut selects neutrons which have not lost energy before entering the active region, precisely fixing the energy-angle relationship. Cut definitions are given in Sec. 4.3.3. 91

4.7 Neutron scatter multiplicity, before application of quality cuts listed in Sec. 4.3.3. The total fraction of useful events (N=2–4 scatters) is 31%. 16% of events are single-scatters, which can be used for Monte Carlo comparisons as a separate $\mathcal{L}_{eff}$ measurement. 92

4.8 Penetration distance of full-energy neutrons ($T > 2.3$ MeV) into the active region. Penetration distance is defined as the distance from the active region outer boundary (aligned with the conduit central axis) to the first scattering vertex. The exponential slope is 12 cm, agreeing with the 6 b cross-section for 2.45 MeV neutrons in Xe [132]. 93

5.1 Gamma Compton scattering spectra for γ energies 122 keV (black), 356 keV (red), 662 keV (green), 1200 keV (blue), and 2600 keV (cyan). Spectra are calculated by the Klein-Nishina equation (Eq. 5.2). 100

5.2 Probabilities $P_C(d, E_\gamma)$ (solid), $P_n(d, E_\gamma)$ (dashed) and $P_{BG}(d, E_\gamma)$ (dotted), plotted as a function of γ path length d for three typical γ energies. Probabilities are calculated from Eq. 5.3, 5.4 and 5.6, respectively. 100

5.3 (a) Distribution of scatters in the active region of a toy detector of 24 cm radius and 55 cm height, calculated for a 1 MeV isotropic γ source spread uniformly in area at the bottom of the detector. The calculation uses Eq. 5.8. Maximum source radius is 24 cm. (b) Analytic prediction for the ^{238}U background scaling factor as a function of detector position, calculated using Eq. 5.8 and the same geometry as in (a). Units are $\log_{10}(\mu\mathrm{DRU}_{\mathrm{ee}}\ \mathrm{mBq}^{-1})$. 101

5.4 Simulation spectra providing the best fit to observed high-energy γ peaks in data. The summed γ spectra in the 250 kg fiducial volume are shown for the top (red), bottom (blue), and side (green) radioisotopes, including ^{238}U, ^{232}Th, ^{40}K, and ^{60}Co. Spectra corresponding to ^{127}Xe (yellow), ^{222}Rn (gray) and ^{85}Kr (magenta) are also included. The ^{127}Xe spectrum normalization comes from measurements of 375 keV peak size during the WIMP search run (Sec. 8.4). The ^{214}Pb (^{222}Rn) normalization is 8 mBq in the active region. The ^{85}Kr normalization is 3.5 ppt $^{\mathrm{nat}}$Kr/Xe and 20 ppt ^{85}Kr/$^{\mathrm{nat}}$Kr. . . . 104

5.5 Simulated low-energy event rate from best-fit γ backgrounds, as a function of position in the detector. Simulation uses LUXSim Monte Carlo results for ^{238}U, ^{232}Th, ^{40}K, and ^{60}Co, with decay rates in different detector regions as listed in Table 5.1. Simulation uses energy range 0–50 keV$_{\mathrm{ee}}$ (flat spectrum, normalized per keV$_{\mathrm{ee}}$ with DRU units). 106

5.6 Energy deposition spectra from activated Xe isotopes. Spectra are shown for ^{127}Xe (cyan), $^{129\mathrm{m}}$Xe (green), $^{131\mathrm{m}}$Xe (red), and ^{133}Xe (dark blue). Decays are simualted inside a 100 kg cylindrical fiducial. 110

5.7 Decay scheme for ^{127}Xe. Scheme taken from [136]. Gamma decays are indicated at each of the arrows, along with their branching ratios and corresponding nuclear transitions. Internal conversion electrons comprise the fraction of de-excitations unaccounted for by γ emission in the diagram. The electrons generate an ER deposition at the original decay site. Of particular interest is the highlighted path in red, whereby the ^{127}I nucleus de-excites through emission of a single 375 keV γ. The undetected escape of this γ from the active region allows a naked EM cascade after ^{127}Xe electron capture, leading to a low-energy ER signature. 111

5.8 Decay schemes for (a) $^{129\mathrm{m}}$Xe, (b) $^{131\mathrm{m}}$Xe, and (c) ^{133}Xe. Schemes are taken from [136]. Decay scheme for ^{127}Xe, and general details on decay schemes, are given in Fig. 5.7. 112

5.9 LUXSim Monte Carlo simulation of naked x-ray rates from ^{127}Xe decay, as a function of position in the active region. Rate includes all x-ray events, including the 35 keV x-ray. Rate is normalized per unit mass and per decay. 113

5.10 Decay chain for ^{222}Rn. The chain is bounded at the lower end due to the very long (22 year) half-life of ^{210}Pb. 114

5.11 Energy deposition spectrum in the 100 kg cylindrical fiducial volume from ^{222}Rn isotope decays. Isotopes shown are ^{222}Rn (red), ^{218}Po (green), ^{214}Pb (cyan), ^{214}Bi (dark blue), and ^{214}Po (magenta). Spectrum includes deposition by γ rays, electrons, and α particles. Absolute energy deposition is shown, not translated to keV$_{\mathrm{ee}}$. Alpha energy depositions are quenched relative to γ or electron depositions, and an energy reconstruction based on electron-equivalent scaling would shift the α peak energies by a factor of ×0.75 [139]. 115

5.12 Energy spectrum in the 100 kg cylindrical fiducial volume from all summed ^{222}Rn isotope decays. The ^{214}Bi contribution is suppressed by 88% due to the inclusion of a time correlation cut, requiring events to occur >1 ms apart. Only γ and electron contributions to the energy spectrum are shown. The ^{222}Rn chain is assumed to be in equilibrium. 115

5.13 Decay scheme for ^{85}Kr. Scheme details are given in Fig. 5.7. 116

5.14 Two-neutrino double β decay spectrum for ^{136}Xe (black), shown in comparison with ^{214}Pb (blue) and ^{85}Kr (green) intrisic background sources in LUX. Also shown is the ER background rate from p-p solar neutrino scattering (red), discussed in Sec. 5.7 [76]. The ^{136}Xe lifetime is 2.1×10^{21} years, taken from measurements by the EXO experiment [73]. The detailed low-energy spectrum is adapted from the projected 10^{22} year lifetime curve in [77]. . 117

5.15 Qualitative representation of a gamma-X event. (Left) A γ scatters multiple times in the active region, with a single vertex in the drift region (small blue) and one or more vertices under the cathode (red). The resulting signal is shown at right as a function of time. The measured S1 signal is a composite signal from all vertices. Ionization is not collected from the vertices under the cathode. The resulting event has a single S2 which has a contribution only from the drift region vertex (large blue). (Right) The resulting waveform with detected S1 and S2 signals (black dashed). Shown are the contributions from the drift region vertex (blue) and RFR vertex (red). The reduced S2/S1 ratio for the event greatly lowers discrimination efficiency. 119

5.16 Analytic calculation of the ER event distribution in S2/S1 vs energy from Eq. 5.10 and 5.11, assuming $\alpha_{UC}/\alpha_{DR} = 1$. A flat energy deposition spectrum is assumed, appropriate to low-energy scatters. The nominal S2/S1 band location is at $\log_{10}$(S2/S1)=0 (black band). Variation in S2/S1 due to recombination fluctuations is not accounted for (i.e. the nominal band has 0 width in S2/S1). Density scale is normalized such that the sum of the bins is 1. 122

5.17 Gamma-X event rate in LUX from bottom PMT array radioactivity, with contributions from ^{238}U, ^{232}Th, ^{40}K, and ^{60}Co. Rates are normalized using PMT counting data in Table 7.3. Events consist of a scattering vertex in the drift region which passes the simulation single-scatter cut, combined with an energy deposition underneath the cathode. Energy depositions are convolved with light collection maps. The light collection maps account for geometric photon collection efficiency and variation in absolute photon yield with electric field magnitude. Histograms correspond to all gamma-X events (black), and events where the drift region vertex is found within a cylindrical fiducial volume of R $<$ 18.3 cm, ΔZ $<$ 32 cm, centered in the middle of the active region (red). The fiducial rate is fit with the linear function $y = \left(9 \times 10^{-6}\,\text{cts keV}_{\text{ee}}{}^{2}\ \text{day}^{-1}\right) \cdot E$. 124

5.18 Integrated WIMP-like gamma-X event rate in LUX in the 100 kg fiducial volume described in Fig. 5.17, as a function of WIMP search window energy bounds. The curve integrates the linear fit to simulation results in Fig. 5.17. Discrimination of gamma-X events is not included. The LUX WIMP search energy range from Run 3, 0.9–5.3 keV$_{\text{ee}}$, is marked with the black circle. . 125

5.19 Gamma-X spatial distribution in the detector, for (a) all gamma-X events and (b) gamma-X events with the drift region vertex falling inside the fiducial volume. The plots simulaneously display the locations of the drift region and under-cathode vertices for all events. 125

5.20 Neutrino scattering rates in liquid Xe. (a) ER scattering spectrum. Spectra are shown for neutrinos generated from p-p solar fusion (cyan) [76] and ^{7}Be(e-,ν)^{7}Li solar reactions (green) [77]. (b) NR scattering spectrum. Spectra are shown for neutrinos generated from ^{8}B solar decays, where the energy spectrum is convolved with an analytic Xe TPC Monte Carlo to estimate energy resolution (red) [147], proton-^{3}He solar collisions (blue), cosmic ray interactions in the upper atmosphere (magenta), and supernovae (green). Data is taken from [146]. 133

5.21 Fiducial shape optimization studies, based on projections for γ backgrounds from positive screening measurements. Event rates are shown as a function of radius and height in units of $\log_{10}(\mathrm{DRU_{ee}})$. Events are reflected across the Y axis with Poisson fluctuation in simulation statistics in order to aid the eye. Two cylindrical fiducial volumes are overlaid in red and green. An optimized ellipsoid shape is drawn in cyan. The unconstrained optimized shape, based on ordering mass bins by activity, is drawn in black. 134

5.22 Distributions in photon (n_{ph}) and electron (n_e) yields for (a) 1 $\mathrm{keV_{ee}}$ and (b) 5 $\mathrm{keV_{ee}}$ electrons. Distributions are calculated by NEST (v0.99β) / LUXSim. An electric field of 182 V $\mathrm{cm^{-1}}$ is used, the same as that for the 85 day LUX WIMP search run. 137

5.23 Distributions in S1 and S2 using NEST (v0.99β), for both background sources with flat energy spectra, and ^{127}Xe 1 $\mathrm{keV_{ee}}$ and 5 $\mathrm{keV_{ee}}$ x-ray peaks. (a) (S1,S2) distribution from a flat background spectrum. (b) (S1,S2) distribution for ^{127}Xe. (c) (S1,S2/S1) distribution from a flat background spectrum. (d) (S1,S2/S1) distribution for ^{127}Xe. The models are folded into energy deposition-only studies for direct comparison of simulation with measured low-energy spectra. S2/S1 widths predicted by NEST (v0.99β) are wider by 30% than observed widths in LUX data. 138

6.1 The decay chain for ^{238}U. The decay chain is broken into three sub-chains: the ^{238}U early sub-chain, the ^{226}Ra sub-chain, and the ^{210}Pb sub-chain. Isotopes are shown with their half-lives and probability for α or β emission, if not 100%. Decays with probability <1% are not shown. Alpha or β emission is listed under each isotope, with the mean α energy or β decay endpoint given. Energies and intensities are listed for γ emission with intensity >1%, with the exception of the ^{238}U early chain which lists γ rays with intensity >0.1%. Data from [135]. 142

6.2 The decay chains for (left) ^{235}U and (right) ^{232}Th. Isotopes are shown with their half- lives and probability for α or β emission, if not 100%. Decays with probability <1% are not shown. Alpha or β emission is listed under each isotope, with the mean α energy or β decay endpoint given. Energies and intensities are listed for γ emission with intensity >1%. Data from [135]. . 143

6.3 Alpha energies generated from ^{238}U decay chain isotopes, assuming full secular equilibrium. Alphas are shown corresponding to the ^{238}U early sub-chain (upward arrows), ^{226}Ra sub-chain (stars), and ^{210}Pb sub-chain (downward arrows). Data is taken from [135]. 150

6.4 Neutrons produced per incident α particle for various common elements in detector construction materials, as a function of α kinetic energy. Lines are shown for F (dark solid), Al (dark dashed), Ti (medium solid), C (medium dashed), Fe (light solid), and Cu (light dashed). 150

6.5 Neutron rate from (α,n) processes per ^{226}Ra sub-chain decay rate, as a function of ^{238}U early sub-chain / ^{226}Ra sub-chain ratio X, for various materials. Overlaid is the yield from ^{238}U spontaneous fission, assuming that fission yields single neutrons which cannot be vetoed by accompanying neutrons or γ rays. Lines are shown for F (dark solid), Al (dark dashed), Ti (medium solid), C (medium dashed), Fe (light solid), Cu (light dashed), and spontaneous fission (dark dash-dotted). Typical γ radioassay measurements limit the potential ^{238}U early fraction excess to ×20-60. 151

6.6 Neutrons produced per incident α particle for Ar (solid) and Xe (dashed), as a function of α kinetic energy. 152

6.7 Neutron emission energy spectra corresponding to ^{238}U spontaneous fission and (α,n) emission on F from the ^{238}U early sub-chain (upward arrows), ^{226}Ra sub-chain (stars), and ^{210}Pb sub-chain (downward arrows). Spectra were calculated from Eq. 6.1. 154

6.8 NR spectra in simulated one tonne (a) liquid Ar and (b) liquid Xe detectors, using geometry as described in Sec. 6.6. Recoil spectra correspond to neutrons generated from the ^{238}U early sub-chain (upward arrows), ^{226}Ra sub-chain (stars), and ^{210}Pb sub-chain (downward arrows), with incident neutron energy spectra given in Fig. 6.7. Black dashed vertical bars indicate typical WIMP search windows for both detectors, with gray bars indicating potential improvements in low-energy threshold. Rates are found in a 500 kg cylindrical fiducial volume. A cut removing multiple scatter events is applied. 154

6.9 WIMP signal and neutron rates as a function of WIMP mass M_χ in simulated one-tonne (a) liquid Ar and (b) liquid Xe detectors. A WIMP-nucleon spin-independent cross-section of 10^{-45} cm^2 is assumed. Neutron rates correspond to 1 Bq of ^{238}U early sub-chain (upward arrows), ^{226}Ra sub-chain (stars), and ^{210}Pb sub-chain (downward arrows). Note that ^{238}U early sub-chain and ^{210}Pb sub-chain NR rates overlap for the Ar detector, at 7×10^{-8}. Rates are calculated using NR energy windows of 50-100 keV$_{\text{nr}}$ for Ar and 5-30 keV$_{\text{nr}}$ for Xe. WIMP rates are shown as bands illustrating the effect of lowering the detection threshold to 30 keV$_{\text{nr}}$ for Ar and 2 keV$_{\text{nr}}$ for Xe, as shown in Fig. 6.8. 155

6.10 Gamma energy spectra generated from ^{238}U decay chain isotopes, assuming full-chain secular equilibrium. Gammas are shown corresponding to the ^{238}U early sub-chain (upward arrows), ^{226}Ra sub-chain (stars), and ^{210}Pb sub-chain (downward arrows). Data is taken from [135]. 157

6.11 Fiducial ER rate in simulated one tonne (a) liquid Ar and (b) liquid Xe detectors from ^{238}U sub-chain γ rays, as a function of fiducial mass. Three scenarios of ^{238}U early sub-chain / ^{226}Ra sub-chain ratio X are shown: $X = 1$ (solid), $X = 10$ (dashed), and $X = 100$ (dotted). The concentrations of ^{226}Ra sub-chain and ^{210}Pb sub-chain isotopes are held constant in all scenarios, while the concentration of ^{238}U early sub-chain isotopes is varied. Gammas depositing energy in the range 1-45 keV$_{\mathrm{ee}}$ are selected, and single-scatter cuts are applied which reject events with energy-weighted standard deviation above 2 cm in radius and 0.5 cm in height. 158

6.12 Fiducial ER rate in simulated one tonne (a) liquid Ar and (b) liquid Xe detectors from ^{238}U sub-chain γ rays, as a function of fiducial mass. Three scenarios of ^{210}Pb sub-chain to ^{226}Ra sub-chain rate are shown: ×1 (solid, corresponding to ^{238}U chain equilibrium), ×10 (dashed), and ×100 (dotted). The concentrations of ^{238}U early sub-chain and ^{226}Ra sub-chain isotopes are held constant in all scenarios, while the concentration of ^{210}Pb sub-chain isotopes is varied. Cuts are used as described in Fig.6.11. 158

6.13 Fraction of γ rays generating fiducial backgrounds in simulated one tonne (a) liquid Ar and (b) liquid Xe detectors, as a function of γ energy. Gamma rates are found in a 500 kg cylindrical fiducial mass with 1:1 aspect ratio is used. Single-scatter and energy cuts are applied as described in Fig. 6.11. 159

7.1 The open SOLO chamber, shown during construction of the shield in 2005. The 0.6 kg high-purity germanium detector is housed in a 1.5 mm thick Cu shield. The chamber is lined with >30 cm of lead shielding. The inner 5 cm lead layer was selected for its measured ^{210}Pb content (<50 mBq kg^{-1}) [164]. The inner chamber measures 25 cm × 20 cm × 30 cm. 167

7.2 Comparison of calibration Monte Carlo output (solid blue) with SOLO data from a ^{60}Co source (dashed red). Calibration Monte Carlo includes the detailed SOLO chamber and detector geometries, as well as faithful reconstruction of the source geometry to account for finite sample size and self-shielding. 167

7.3 SOLO counting spectra for R8778 (14 live days, blue) and R11410 MOD (19 live days, red) PMTs, superimposed with a sample background run (21 live days, black). ^{238}U is primarily identified by lines from late-chain daughters at 295, 352, and 609 keV. ^{232}Th is identified by lines at 239, 511, 582, and 2614 keV. ^{40}K is identified by a single line at 1460 keV. ^{60}Co yields twin peaks at 1173 and 1333 keV. Strong lines in the R8778 spectrum indicate the presence of ^{238}U, ^{232}Th, ^{40}K and ^{60}Co radionuclides. The reduced activity of the R11410 MOD is readily apparent from the lack of distinct features in comparison with the R8778, with the only activity significantly above background from the presence of ^{60}Co. Lines at 46.5 keV (^{210}Pb), 662 keV (^{137}Cs) and 1460 keV are used to periodically verify detector calibration. SOLO datasets shown are lux_5_pmts_batch_2 (R8778), R11410_v2_post_clean (R11410-20), and bg_combined_2011 (background). 168

7.4 Example background plot from ^{222}Rn leakage into the SOLO chamber (red, 4 days), compared with standard background (black, 21 days). Chamber includes only radiopure polyethylene material, which was recounted after the radon leak was sealed to verify its low radioisotope content. Peaks from ^{222}Rn daughter decays (^{214}Pb and ^{214}Bi, respectively) at 352 keV and 609 keV are clearly visible. SOLO dataset 'inner_poly' is used for the contaminated dataset. 169

7.5 SOLO measured σ/μ energy resolution as a function of energy. The measured points are characterized by the curve $\sigma^2 = 0.0033E + 1.2$. 169

7.6 Simulated full-energy γ depositions in the SOLO detector per γ emitted, as a function of γ energy. A point source emission geometry is used, located at the bottom of the chamber, directly beneath the front face of the detector (17 cm from the bottom edge of the detector). Curve is obtained from calibration Monte Carlo. 170

7.7 SOLO rate upper limits, as a function of counting livetime, for several common peaks. The DRU upper limit is calculated from measured background data. 170

7.8 Counting spectra for a 6.7 kg Ti sample, before (blue) and after (red) a six-month activation period at the Sanford Surface Laboratory during the LUX surface run. Comparison is shown with background (black). The sample was shipped by ground to and from SOLO to avoid spurious cosmogenic activation. Peaks are clearly found at 889 and 1121 keV, corresponding to γ emission from ^{46}Sc decay. 177

7.9 The Hamamatsu R8778 PMT, used in LUX (left), and the R11410-20 PMT, used in the upcoming LZ experiment (right). The R11410-20 features a 6.4 cm diameter photocathode, offering twice the surface area of the 4.5 cm diameter R8778 photocathode. 185

7.10 (a) LZ ER background spectra. Background spectra are shown from the PMTs (gray), p-p solar neutrino scattering (cyan) [76], ^{7}Be solar neutrino scattering (green) [77], and ^{136}Xe two-neutrino double β decay (magenta) [73]. The ^{136}Xe spectrum uses a 2.1×10^{21} yr lifetime. The average (flat spectrum) projected PMT ER background is overlaid from current LZ studies, assuming a conservative 3 ^{238}U / 3 ^{232}Th / 30 ^{40}K / 2.5 ^{60}Co mBq PMT^{-1} for the R11410-20 PMTs. No discrimination factor is applied. (b) LZ NR WIMP and background spectra. WIMP spectra are shown in black for m_χ = 100 GeV, assuming a spin-independent WIMP-nucleon cross-section of 10^{-47} (solid) and 10^{-48} (dashed) cm^2. Neutrino coherent scattering backgrounds are adapted from [146]. Overlaid are neutron background spectra for both (α,n) and fission contributions from the PMTs (gray). Neutrino coherent scattering backgrounds are shown from ^{8}B decays (red), proton-^{3}He collisions (blue), cosmic ray interactions in the atmosphere (magenta), and the diffuse supernova background (green). Further discussion of neutrino backgrounds is given in Sec. 5.7. 100% NR acceptance is shown. 189

8.1 Initial S1-only histogram from LUX underground running. Data was taken over a period of 1.2 hours on Feb. 12. A correction factor is applied to the data, normalizing total pulse area to detector midpoint. Clear peak features are visible, later matched to known features from γ spectra of radioisotopes and decay energies of activated Xe radioisotopes. 192

8.2 Data from Fig. 8.1, plotted in top PMT array vs bottom PMT array view. The top/bottom ratio acts as a proxy for event height in the detector. The addition of top and bottom signals acts as a proxy for energy. Gamma scattering continua are seen as the southwest–northeast hotspots, clustered at the top and bottom of the active region, forming the frame of the "ladder" feature. Activated Xe features are clearly visible as the ladder "rungs," as they are monoenergetic signals distributed uniformly in height throughout the active region. S1 signals equally distributed in the top and bottom PMT arrays fall on the dashed black line. 193

8.3 Fit to the activated Xe peaks from Fig. 8.1 (Feb. 12), using simulated spectra from Fig. 5.6. A resolution factor of 5% is applied to simulated spectra in order to match measured data. A fixed exponential baseline is used, which connects the bins at 30 $\mathrm{keV_{ee}}$ and 450 $\mathrm{keV_{ee}}$. Best-fit isotope decay rates are 2.7 ± 0.5 mBq kg^{-1} (^{127}Xe), 3.6 ± 0.7 mBq kg^{-1} ($^{129\mathrm{m}}$Xe), 4.4 ± 0.9 mBq kg^{-1} ($^{131\mathrm{m}}$Xe), and 3.6 ± 0.7 mBq kg^{-1} (^{133}Xe). 194

8.4 (S1,S2) space for early LUX data, showing the monoenergetic 164, 236, and 375 $\mathrm{keV_{ee}}$ signals from the $^{131\mathrm{m}}$Xe, $^{129\mathrm{m}}$Xe and ^{127}Xe respectively. S1 and S2 are corrected in Z relative to signals at the detector midpoint. The angle in S2 vs S1 space yields a measurement of the detection efficiencies for photons and electrons in the detector. 197

8.5 (a) S1 top vs bottom for all background data considered in this study. The large island is the main γ population, with energies extending to 3 MeV. The small island in the upper right corresponds to α events, excluded from this study. The island in the upper left corresponds to gas event S1s, also excluded from this study. (b) S1 top vs bottom, showing the S1 selection cut used for events in this study. The cut has negligible impact on energies $>$500 keV$_{ee}$, which is the region of primary interest for γ background fitting. 198

8.6 S2/S1 ratio vs energy for γ events in the active region. Event selection criteria using the S1 cut shown in Fig. 8.5 is used. Data is shown for (a) SS and (b) MS events, where MS cut criteria are described in Sec. 8.3.1.2. 199

8.7 Example of a MS event with unseparated S2s. X axis is time, in units of 10 ns samples (LUX PMT data is digitized at 100 MHz). Y axis is normalized to phe sample^{-1}. The event is reconstructed with energy 2.6 MeV, with Z positions ranging from 2 cm to 6 cm below the liquid surface. 200

8.8 S2 width vs drift time, measured from fits to background data. Black points indicate peak centers (error bars shown, tiny). Red dashed lines indicate measured $\pm 1\sigma$ on width distribution (NOT measurement error). An S2 width cut using this trend is used to distinguish MS events. The cut is shown as the blue dashed line. Events with width above the line are tagged as MS. 200

8.9 Calibration taken with a ^{228}Th source (black), compared with standard background data (red). Spectra are shown for (a) all events and (b) SS events. Energy reconstruction is performed as described in Sec. 8.3.2. The 2614 keV$_{ee}$ peak from ^{208}Tl is recreated at 2510$\pm$30 keV$_{ee}$. A position cut is used, requiring R $<$ 19 cm and 50 μs $<$ dt $<$ 250 μs. 203

8.10 LUX γ energy spectrum, with drift time cut applied requiring 20 $<$ dt $<$ 300 (3 cm removed from top and bottom of the drift region) and R $<$ 21 cm (3 cm removed from outer radius). The total Xe mass is 170 kg. The dashed line indicates the approximate low-energy threshold from the γ S1 cut (Sec. 8.3.1.1). Energy is reconstructed from S1+S2 for both SS and MS events as described in Sec. 8.3.2. 203

8.11 (a) Peak fits for γ lines at 403 keV, 609 keV, 1172 keV, 1461 keV, 1764 keV, and 2614 keV. The gray dashed line shows the Compton baseline, estimated by continuum activity around all visible peaks. The blue dashed line denotes the approximate energy cutoff due to the cutoff in S1 acceptance. Data is taken for SS+MS events, with 145 µs < dt < 175 µs, and R < 21 cm (b) Measured resolution vs energy, from peak fits shown in Fig. (a). Resolution is fit with the curve $0.59 \cdot (E)^{-1/2} + 0.03$. 205

8.12 SS cut efficiency as a function of energy, shown for data (black) and simulation (red). Shown for comparison is the ratio of photoelectric cross-section to photoelectric + Compton + pair production cross-section (blue dashed), which represents the SS cut expected in a detector with perfect position resolution for MS events. A fiducial cut with R < 20 cm and 50 μs < dt < 250 μs is used. 206

8.13 Drift region measured energy spectrum, compared with simulation best-fit scaling factors (red) and simulation projections based on positive screening results only (gray), giving the expected lower limit for γ activity. Scaling factors correspond to the "Best Fit" and "Screening" columns in Table 5.1, respectively. The lower bound used for fitting was 500 keV$_{\mathrm{ee}}$. The low-energy cutoff for the dataset is estimated at 200 keV$_{\mathrm{ee}}$ due to S1 selection cuts. Data includes both SS and MS events, with energy and position reconstruction explained in Sec. 8.3.2. A Z cut is used to remove 2 cm from the top and bottom of the drift region. No radial cut is used. The ^{127}Xe spectrum is added in to show the continued agreement between model and data at energies below 500 keV$_{\mathrm{ee}}$. 209

8.14 Drift region best-fit simulation energy spectra for 3.4 cm slices in Z, compared with data. All curves are shown as detailed in Fig. 8.13. The ^{127}Xe spectrum is not included in the Z slice histograms. 210

8.15 Measurement of peak rates at (a) 164 keV_{ee} from $^{131\text{m}}$Xe and (b) 410 keV_{ee} from ^{127}Xe, over the duration of the Run 3 WIMP search. Peak rates were measured in the energy range 150–175 keV_{ee} for the 164 keV_{ee} peak, and 350–450 keV_{ee} for the 410 keV_{ee} peak. The peak rates are fit with exponential functions with decay constants $\tau_{131m} = 17.1$ days and $\tau_{127} = 52.5$ days for $^{131\text{m}}$Xe and ^{127}Xe, respectively. t_0 corresponds to May 1. 211

8.16 Best-fit ^{214}Pb spectrum (red) for a 30 kg fiducial (R < 13 cm, 100 μs < dt < 220 μs), constrained in the range 310–340 keV_{ee}. Measured data is shown in black. A simple SS cut is used, requiring one S1 and one S2. No γ continuum contribution is assumed. Xenon-127 peak models are overlaid with measured data (green). Data and ^{127}Xe normalization is shown from June 20–August 8. . 214

8.17 Xenon flow patterns in the upper half of the active region (20 μs > dt > 160 μs). Flows are imaged by coincident ^{222}Rn-^{218}Po decays, occurring within 10 s of one another. Drift speeds are ascertained by the spatial and timing separation of the paired decay events. (a) XY velocity distribution, with Z velocity shown in color. Arrow length corresponds to XY speed, with the longest arrows corresponding to 3 cm s^{-1}. (b) XZ velocity distribution. Arrow length corresponds to XZ speed. The Y velocity component is not represented. . 216

8.18 S2/S1 vs S1 distributions for MS events, coupled in post-processing with NEST scintillation and ionization yields. The measured band mean and 90% contours (5%–95%, corresponding to 1.64σ) are drawn in cyan solid and dashed, respectively. Shown for reference is the mean of the S2/S1 vs S1 band for SS events in black. (a) NR distribution using the MS energy distribution from LUXSim neutron background studies. (b) ER MS distribution, using the random addition of two ER events which have an initial flat energy distribution. 220

8.19 S1 distributions using LUXSim / NEST data from Fig. 8.18. (a) ER distribution. S1 is characterized by a power law. (b) NR distribution. S1 is characterized by a double falling exponential. 221

8.20 Bad vs good area for MS events with corrected S1 $<$ 120 phe. Points are shown corresponding to all events (gray), events within the 180 kg search region (black), and events within the 118 kg WIMP search fiducial used for Run 3 (red). The bad area cut boundary used in this analysis is shown as the magenta line. The bad area cut requires events to fall below the line. The cut is defined as flat in the range 0–1700 phe good area, with a 10% slope for good area above 1700 phe. 224

8.21 $\log_{10}$(S2/S1) vs S1 for MS events. S1 and S2 correction and position definition are given in Sec. 8.7.2. Events are shown (a) before and (b) after application of the bad area cut defined in Sec. 8.7.3.5. Overlaid are the ER (blue) and NR (red) MS bands determined from LUXSim and NEST Monte Carlo studies. The band centroids are shown as the solid lines, and band widths are shown at 1.28σ (1.65σ) with dashed (dotted) lines. The NR band centroid sets the upper bound of the neutron MS search window. 226

8.22 Low-energy background distributions in RZ, from (a) measured data and (b) model predictions. Rates are taken in the range 0.9–5.3 keV$_{\mathrm{ee}}$ (2–30 S1 phe). Rates are shown in units of $\log_{10}$ (DRU$_{\mathrm{ee}}$). The 118 kg fiducial volume used in the 85 day WIMP search run is shown in dashed black. The model includes low-energy background contributions from γ Compton, ^{127}Xe, ^{214}Pb, and ^{85}Kr sources. The measured data at large radii includes a significant contribution from low-energy ^{210}Pb decays at the detector walls. These decays are not included in the background model in Fig. (b). 228

8.23 Low-energy background distributions in (a) radius, (b) height, and (c) S1, within the LUX 118 kg fiducial volume, measured over the full 85 liveday WIMP search run. Measured data are indicated by the black histogram with error bars. Simulation data are shown in red. Simulated distributions are reconstructed from high-energy background studies, and are not a fit to measured low energy data. The simulated S1 distribution folds in NEST (v0.99β) estimates of total photon yields and measured LUX light collection efficiency, detailed in Sec. 5.10. 229

8.24 S1 distribution observed in the first half (red) and second half (blue) of the WIMP search run. Data is shown in the 118 kg fiducial volume, with WIMP search cuts applied. The first half of the run spans from April 22–June 13, and the second half spans from June 14–August 8. 230

8.25 Percent variation per bin between simulated low-energy ER background event rates and analytic best-fit models for (a) time-independent (γ Compton + ^{214}Pb + ^{85}Kr) and (b) time-dependent (^{127}Xe) models. White bins have 0 simulation counts. Analytic functions are listed in Table 8.5. 232

8.26 WIMP search data from the LUX Run 3 85 liveday run. 160 events are found after data quality, SS and fiducial cuts in the range 2–30 phe. Overlaid are the measured ER band from ^{3}H calibration (blue), and the projected NR band from LUXSim / NEST (red), confirmed using external AmBe / ^{252}Cf calibration. Constant-energy contours are overlaid in gray, giving keV$_{\mathrm{ee}}$ energies above the ER band and keV$_{\mathrm{nr}}$ energies below the NR band. Plot taken from [46]. 234

8.27 WIMP search 90% exclusion limit set by the LUX Run 3 85 liveday run, in comparison with previous experimental exclusion limits and allowed regions [46]. The LUX limit is shown as the dark blue curve. The $\pm 1\sigma$ light blue band denotes the expected region for the actual curve, based on repeated trials of the PLR analysis using the parameterized background and signal models. 90% exclusion curves are also shown for XENON100 100 day [54] (orange) and 225 day [49] (red) results, ZEPLIN-III [55] (magenta), CDMS II [56] (green), and Edelweiss II [57] (yellow). The inset shows allowed contours from DAMA/LIBRA [58, 59] (gray), CRESST II [60] (yellow), CDMS II Si detectors [61] (green, centroid denoted by the x), and CoGeNT annual modulation signals [62] (red). Plot taken from [46]. 235

CHAPTER 1

DIRECT DETECTION OF DARK MATTER

Only 5% of the energy density in the universe is found in a form that is presently understood. This shockingly low number is based on a great number of cosmological observations made over the past 80 years. All of these measurements indicate that there is a high abundance of non-luminous, non-baryonic dark matter in the universe, and an even higher abundance of dark energy. The convergence of all of these measurements to a well-constrained set of values for the energy densities of baryonic matter, dark matter, and dark energy is known as Λ-CDM, or the Concordance Model.

The observed features of the universe, which paint the picture of the Concordance Model, include (but are not limited to) galactic rotation curves, velocity dispersion in galactic clusters, the cosmic microwave background, big bang nucleosynthesis, large scale structure, and evidence from weak and strong lensing measurements. The widespread acceptance of the concordance model is based on the strong statistical agreement of all of these measurements of the relative and absolute content of baryonic matter, non-baryonic matter, and total energy in the universe. The pertinent question in modern cosmology is no longer whether dark matter exists, but rather, what the identity of dark matter is. The magnitude of this question has generated an incredible effort to understand this missing component of the universe. Our efforts have paid off in providing a number of potential dark matter candidates.

In this work, we consider the existence and detection prospects of one particularly well-motivated candidate particle, called a weakly interacting massive particle, or WIMP. Not only are WIMP candidates motivated by several potential extensions of the particle physics standard model (SM), but the WIMP hypothesis is directly testable in the laboratory. WIMP searches are performed using a broad range of techniques, including production (using particle accelerators), annihilation (using γ ray telescopes and antimatter detectors), and scattering on baryonic matter (using low-background particle detectors). This chapter serves to motivate the latter category of searches, and to introduce the low-background class of experiments of which the LUX detector is the newest and most sensitive member.

1.1 The Concordance Model

A great triumph of the twentieth century is the establishment of a simple but powerful model describing cosmic dynamics with high accuracy. The model is referred to as Λ-CDM, where Λ refers to an energy density which drives the acceleration of the universe, and CDM refers to cold (non-relativistic) dark matter. The model is also referred to as the Concordance Model, in reference to the success of the model in explaining the observed expansion history of the universe with the observed abundances of matter and energy. An excellent primer on Λ-CDM is given in the text by Ryden [1].

Λ-CDM is built on relativistic kinematics and conservation of energy. At the foundation of the model are two equations which are expressions of these fundamentals. The first of these equations, the Friedmann equation, is derived from the conservation of gravitational potential energy and kinetic energy in the expanding universe. The Friedmann equation describes the rate of change of the scale of the universe as a function of energy density and curvature:

$$\left(\frac{\dot{a}}{a}\right)^2 = \frac{8\pi G}{3c^2}\rho\left(t\right) - \frac{\kappa c^2}{R_0^2 a^2} + \frac{\Lambda}{3}. \tag{1.1}$$

$a\left(t\right)$ is the time-dependent universal spatial scale factor; $\rho\left(t\right)$ is the energy density of the universe at time t; κ and R_0 describe the sign and magnitude of curvature of the universe, respectively; and Λ is the cosmological constant (not actually constant in some theories), which provides a time-invariant energy density that drives expansion of the universe. The Λ term is ascribed to a mysterious component of the universe referred to as dark energy, which is a subject of much study, but not in this work. Note that $H(t) \equiv (\dot{a}/a)$ is the Hubble parameter, measured at present day to be $H_0 = 67.3 \pm 1.2$ km s^{-1} Mpc^{-1} [2].

To be able to find unique solutions for both $a(t)$ and $\rho(t)$, further constraints are required on the model. The second key equation is the acceleration equation, derived from conservation of energy within a comoving volume:

$$\dot{\rho} + 3\frac{\dot{a}}{a}(\rho + P) = 0. \tag{1.2}$$

P describes pressure for a classical fluid. From Eq. 1.1 and 1.2, we provide two constraints on the two unknowns $a(t)$ and $\rho(t)$.

The thermodynamical equation of state for a classical gas is used to relate ρ and P:

$$P = w\rho. \tag{1.3}$$

w is the equation of state parameter, which differs depending on the component of the universe being described. $w = 0$ describes a gas of non-relativistic particles, e.g. cold (baryonic or non-baryonic) matter. $w = -1/3$ describes a relativistic gas, e.g. photons and neutrinos. $w = -1$ describes the dark energy component of the universe required for a non-zero, constant value of Λ in Eq. 1.1.

Equations 1.1–1.3 are adequate to uniquely describe the expansion history of the universe. One then requires measurements of the magnitudes of the energy densities contributing to ε, to set boundary conditions on the model. The energy density components can be written in the dimensionless form $\Omega(t) \equiv \varepsilon(t)/\varepsilon_c(t)$. ε_c is the critical energy density, above which the universe has a positive curvature and below which the curvature is negative. The energy density components of interest for measurement are those for matter Ω_m, dark energy Ω_Λ, and curvature Ω_K. (The matter term is dominated by cold matter; the formation of structure rules out a significant hot matter component [3])

Measurements leading to the determination of each of the energy density factors are

Parameter	**Measured Value**
Ω_b	0.0487 ± 0.0006
Ω_{DM}	0.265 ± 0.006
Ω_Λ	0.692 ± 0.010
Ω_K	$-0.0010^{+0.0062}_{-0.0065}$
w_{DE}	$-1.13^{+0.24}_{-0.25}$

Table 1.1: Component energy densities for the Λ-CDM model, as recently reported in [4]. Values are taken from Planck temperature power spectrum data. Uncertainties on Ω_b, Ω_{DM} and Ω_Λ are given at 68% CL (±34%). The constraint on Ω_K is taken from the combination of Planck, lensing, WMAP polarization, high-resolution CMB data, and BAO data constraints, with 95% (±47.5%) uncertainty. w_{DE} is constrained from Planck, WMAP polarization and BAO data, with 95% uncertainty.

taken from the latest cosmic microwave background (CMB) measurements from the Planck satellite [2, 4]. The matter term Ω_m can conveniently be divided into two components, Ω_b and Ω_{DM}, describing the baryonic matter and non-baryonic dark matter energy density components respectively. A selection of Λ-CDM parameter measurements are given in Table 1.1.

The measured energy density values paint a remarkable picture of the composition of the cosmos. The energy density from standard baryonic matter, comprised of all understood forms of stable matter in the SM, represents <5% of the energy density of the entire universe, and only 16% of the energy density of all of the matter in the universe. The remaining 84% of the matter is a non-baryonic matter component that is not currently understood. The remaining 70% of energy in the universe is in the form of dark energy. The constraints also find that the universe is flat to a remarkable 1% precision, and that the equation of state parameter w_{DE} for dark energy is also consistent with -1, as expected for a cosmological constant.

1.2 A Multitude of Measurements

The Concordance Model is so-named due to the wealth of measurements which qualtiatively and quantitatively agree: there is a significant non-baryonic component to the matter density of the universe, and a significant non-matter component to the energy density of the universe. A small subset of the cornucopia of cosmological measurements is given below, with a goal of motivating the current understanding of WIMP density and velocity in our local area of the galaxy. By far the strongest constraints on the dark matter content of the universe come from measurements of the CMB; the newest measurement results from the Planck satellite are reported in [2], and a well-rounded review is given in [5]. Strong supporting evidence and orthogonal constraints are found from measurements of big bang nucleosynthesis [6], gravitational lensing [7], supernovae [8], and large-scale matter distributions [9].

1.2.1 Dark Matter in Galaxies

The effects of dark matter on the rotation and orbits of galaxies are not only the oldest measurements of the existence of dark matter [10, 11], but are also of the most direct relevance to detection of dark matter interactions in the laboratory. Two pieces of information are used, that indicate that galaxies have much greater mass than can be accounted for by luminosity measurements alone: the rotational velocities of stars about galactic centers, and the velocities of galaxies about the center of mass in galaxy clusters. Measurements of galactic rotational velocity curves are used to constrain the predicted total mass of dark matter in our neighborhood of the Milky Way.

The first strong evidence of a non-luminous matter component in galaxies came from a peculiar observation by Franz Zwicky in 1933, forty years before the cosmological "missing mass" problem came to the forefront of discussions about models of the universe [12]. Zwicky studied the velocity dispersion of 19 galaxies in the Coma galaxy cluster, using it to infer the total cluster mass. The inferred mass was compared directly with the observed luminous mass. The study revealed that the average kinetic energies of the galaxies were too large by a factor $\times 400$ to be explained simply by the amount of luminous matter. Subsequent observations of the Coma Cluster, and revision of the Hubble parameter used in the distance estimate, have revised this factor to $\times 50$.

Around the same time, several measurements were reported for the velocities of stars orbiting the Milky Way and Andromeda galaxies, finding that their velocities were also too large to be explained by the measured luminous matter in the galaxy [12]. It was speculated that light from the galaxy was being absorbed by some unknown medium, explaining the deficit of mass in proportion to velocity. It was not until 1970 that firm evidence was published wherein the velocities of stars in galaxies as a function of radius were plotted in high resolution, showing a clear deviation from the Newtonian model [13]. Subsequent observations have further improved rotation curve measurements, tracing the rotational velocity in detail at all radii from the galactic center to the edge of the disk (see e.g. [14]).

The star number density in a galaxy falls off exponentially with distance from the center, with a typical length r_s of a few kpc (e.g. 4 kpc for the Milky Way) [1]. The dominant mass component of the galaxy sits inside a radius of that length, and the mass encompassed by higher radii becomes constant. The predicted velocities for orbiting objects at higher radii are estimated from Newton's gravitational law:

$$v = \sqrt{\frac{GM}{r}}, \tag{1.4}$$

where the numerator is fixed and the velocity simply falls with distance from the galactic center as $r^{-1/2}$. Data from [14] are plotted in comparison in Fig. 1.1. The measured velocity distribution clearly deviates from the Newtonian expectation (Eq. 1.4). The velocity curve is much closer to a constant function of distance.

A model for the mass in the galaxy that fits the measured curve in Fig. 1.1 must adjust Eq. 1.4 to create a constant velocity profile. Two possibilities are: (1) a position-varying value of G; or (2) a position-varying value of M. The former possibility, which is the basis of Modified Newtonian Dynamics (MOND), is not addressed here and is disfavored relative to the dark matter hypothesis (see e.g. Sec. 1.2.2, or tension between findings in [15] and [4]).

Assuming that M is varying with position, the functional form of $M(r)$ must then be proportional to r at distances $>r_s$. If one makes the assumption that the hidden mass is not constrained to the galactic disk, then the mass density $\rho(r) \propto r^{-2}$. The simplest realistic mass distribution model meeting the criteria follows the expression $\rho \propto \left(r^2 + r_c^2\right)^{-1}$, where r_c is a radial cutoff term which avoids a singularity at the galactic center (a mathematical singularity, anyway; it is too late to avoid an actual singularity at the galactic center [16]).

The dark matter mass distribution model implied by the rotation curves follows that of an isothermal halo of noninteracting particles, where "isothermal" refers to the origin of the model in Boltzmann statistics. The velocity distribution is written with the form

$$f\left(v, v_e\right) \propto \exp\left(-\left(v + v_e\right)^2 / v_0^2\right), \tag{1.5}$$

where v_e is the average speed of the Earth relative to the dark matter in the galaxy, and v_0 is a characteristic velocity. This distribution is used to estimate the energy spectra of dark matter signals in direct detection experiments, as detailed in Sec. 1.4.

Models of the Milky Way use this mass distribution, along with second-order corrections, to estimate the dark matter density in our area of the galaxy. This is the dark matter density directly relevant for direct detection measurements. Results vary widely in literature, dependent on measurement techniques and specific halo models (see e.g. [17, 18, 19, 20, 21]). A conservative assumption of $\rho_{local} \sim 0.3$ GeV cm^{-3} is generally used when projecting dark matter interaction rates, as well as a velocity profile following Eq. 1.5, in order to standardize dark matter search results. This value lies at $\sim\!-1\sigma$ of the distribution of estimated values of ρ_{local}.

There are two items worth noting explicitly. The first: ρ_{local} is the local density, not the average dark matter density in the universe. The second: any change in the assumed ρ_{local} affects the dark matter flux only, and leads to a simple scaling of dark matter interaction cross section limits set by direct detection experiments. If there is a change in the assumed velocity model, however, this affects the recoil spectrum in direct detection experiments, and scales the detection limits differently for different detectors [22].

1.2.2 The Bullet Cluster

The separation of the gravitational and luminous centers of mass in the Bullet Cluster is often given as evidence contradicting the theory of a scale-varying gravitational force (e.g. MOND), and further motivates the explanation of flattened galactic rotation curves with a non-baryonic matter component [24]. Weak lensing measurements of mass contours show an 8σ separation of the gravitational and baryonic centers of mass, with the gravitational contours centered around the non-interacting matter component. This is consistent with

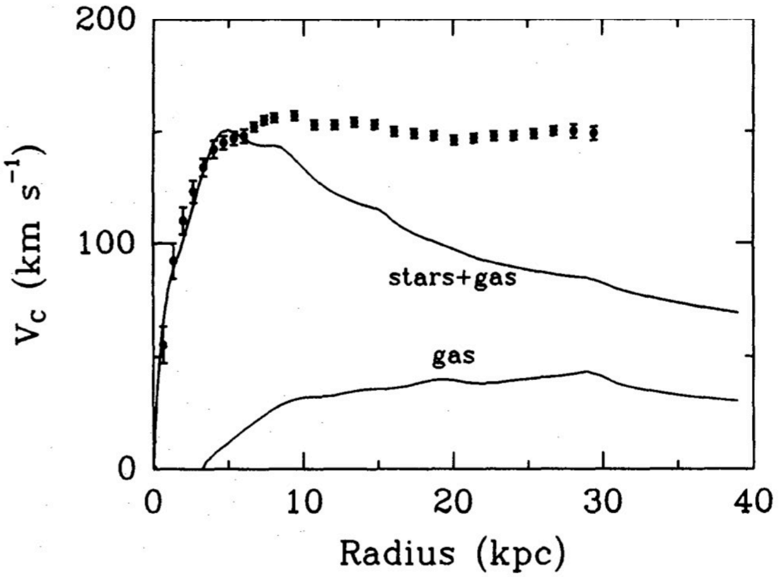

Figure 1.1: Measurements of radial star velocity in the NGC 3198 galaxy as a function of distance from the galactic center, obtained by observation of H 21 cm line emission. The measured rotation curve is shown (points), along with estimated curves corresponding to the contribution from gas only and stars+gas. Plot taken from [23].

a dark matter component in the clusters a factor ×4–5 greater than the baryonic component. It is also inconsistent with a theory which explains galactic rotation curves by a spatially-varying gravitational force, as any varying gravitational force without a dark matter component would remain centered over the baryonic center of mass. It should be noted that the Bullet Cluster observation is not the final word on modified gravity theories [25]. However, it strongly favors non-baryonic dark matter over modified gravity, and thereby motivates experimental detection efforts aimed at deducing the nature of dark matter.

1.3 WIMPs

Sec. 1.1 and 1.2 frame the hypothesis of the existence of dark matter, and provide an idea of its abundance both locally and universally. However, few insights are gleaned from those measurements as to the fundamental nature of dark matter. The WIMP, a leading dark matter particle candidate, is discussed here.

1.3.1 Freeze-Out and Relic Abundance

In the early universe, in the first nanosecond after the Big Bang, the incredible particle densities and temperatures were sufficient for the creation and destruction of all known particles. Dark matter particles, assuming coupling to SM particles, also underwent creation and annihilation processes, maintaining thermal equilibrium. The universe cooled as it expanded, and as the temperature fell the rates of creation and annihilation slowed. Eventually, the size of the universe diluted the dark matter density to the point where further dark matter interactions were essentially non-existent. This phenomenon is known as "freeze-out." An excellent review is found in [26].

The rate of change in the dark matter comoving number density as a function of time can be written as:

$$\frac{dn}{dt} = \langle \sigma v \rangle \left(n_{eq}^2 - n^2 \right) - 3Hn. \tag{1.6}$$

σ is the WIMP-WIMP annihilation cross section, v is the average WIMP velocity, and n_{eq} is the dark matter number density in equilibrium with the creation rate from SM particles. The equilibrium number density goes as $n_{eq} \propto (m_\chi T)^{3/2} \exp(-m_\chi / T)$.

Eq. 1.6 is broken into two terms on the right-hand side. The first term describes the rate of change of dark matter due to creation and annihilation. The two derived quantities in the first term, $\langle \sigma v \rangle n_{eq}^2$ and $\langle \sigma v \rangle n^2$, correspond to the gross dark matter creation and annihilation rates respectively. The second term, $-3Hn$, accounts for the dilution of dark matter particles due to the expansion of the universe. When the temperature of the universe falls below m_χ, SM particles no longer have sufficiently energetic collisions to produce dark matter particles, and the rate of change of the number density becomes locked to the annihilation and dilution terms, proportional to $\exp(-m_\chi / T)$. The WIMP number density is driven down until the condition $H = n \langle \sigma v \rangle$, where the scale of the universe becomes such that dark matter particles can no longer find each other to annihilate (note that both n and $\langle v \rangle$ decrease with time). At this point, the comoving number density is "frozen out," and the abundance of dark matter in the universe does not change significantly through present day.

The relic density after freeze-out can be expressed as [18]

$$\Omega_\chi h^2 = \frac{3 \times 10^{-27}\,\mathrm{cm}^3\,\mathrm{s}^{-1}}{\langle \sigma v \rangle}, \tag{1.7}$$

where $h = 0.673 \pm 0.012$ is the dimensionless Hubble parameter [4]. The most interesting part comes in when trying to match Eq. 1.7 with the observed abundance of dark matter (Table 1.1). If one assumes a dark matter particle with mass of the order of the weak scale (∼100 GeV), and assumes a weak scale coupling for the annihilation cross section, then the relic density is miraculously found to agree with the observed dark matter density, within potential model variations [26]. This is referred to as the "WIMP miracle," and provides one of the strongest motivations for a model of weakly interacting particle dark matter.

1.3.2 WIMP Candidates

The WIMP is a preferred dark matter candidate in part because its existence is strongly motivated across a wide range of minimal extensions of the SM. The most widely cited of these extensions is supersymmetry (SUSY). SUSY is a proposed theoretical extension of the SM that is meant to provide a natural answer to the gauge hierarchy problem, as well as to give rise to a convergence of the electromagnetic, strong and weak force couplings in a Grand Unified Theory.

Supersymmetry posits that all SM particles have a partner particle which carries the same characteristics, with the exception of a difference of $-1/2$ in spin. The theory introduces the concept of R-parity, which is a conservation of spin, baryon number and lepton number. Due to the difference in spin, SM (SUSY) particles have an R-parity of 1 (-1). SUSY is broken spontaneously, such that SUSY particles have a mass greater than those of their SM partners. The SUSY particle masses are constrained for various models by particle colliders.

Of interest to the dark matter search are the SUSY partners which are long-lived and electrically neutral. These SUSY particles (SM partners) include the bino (weak hypercharge), wino (W), two higginos (Higgs), gravitino (graviton), and the sneutrinos (neutrinos). The bino, wino and higgsinos, having the same quantum numbers, form four mass eigenstates called neutralinos. The lightest of the neutralinos is called the lightest supersymmetric partner (LSP), and, due to R-parity conservation, cannot decay into any other particle. The LSP could have a mass at the weak scale, neatly matching expectations from the relic abundance (Sec. 1.3.1). The LSP can also couple to SM particles through the W and Z bosons. All of these features make the LSP a strongly favored WIMP candidate.

A completely different WIMP candidate is offered by Kaluza-Klein (KK) theory, which is introduced to provide a unified model of gravity and electromagnetism. The theory posits that a number of compactified extra dimensions exist, in which the formation of "standing waves" creates the effect of a series of more massive cousins of each SM particle. This is analogous to the SUSY partners, except that the KK partners have the same spin as their SM cousins. Like SUSY, a lightest KK partner exists due to conservation of a new KK-related parity.

A large number of other SM extensions also lead light, stable particles that are WIMP candidates, not described here [18, 26, 27]. What is interesting is the common thread of the creation of a light particle, which is unable to decay into SM particles and thus lends itself naturally as a candidate for dark matter. The elegance of WIMP theory tests is that detection experiments are agnostic to the exact theory creating the WIMP, excepting the differing range of potential WIMP masses and WIMP-SM cross sections. As described in Sec. 1.3.3 and 1.4, detection experiments sweep wide sections of the WIMP parameter space and constrain many different WIMP models.

1.3.3 Detectability

The WIMP hypothesis lends itself to theory-independent testability. Regardless of the mechanism of generation of the WIMP, the WIMP (by definition) interacts with SM particles in the same fashion. This enables a generic set of detection experiments that can explore the WIMP parameter space, agnostic about the underlying theory. The three general detection schemes are those that search for signatures of annihilation, creation, or scattering, and are generally based on the diagram drawn in Fig. 1.2. Those three detection schemes are described below.

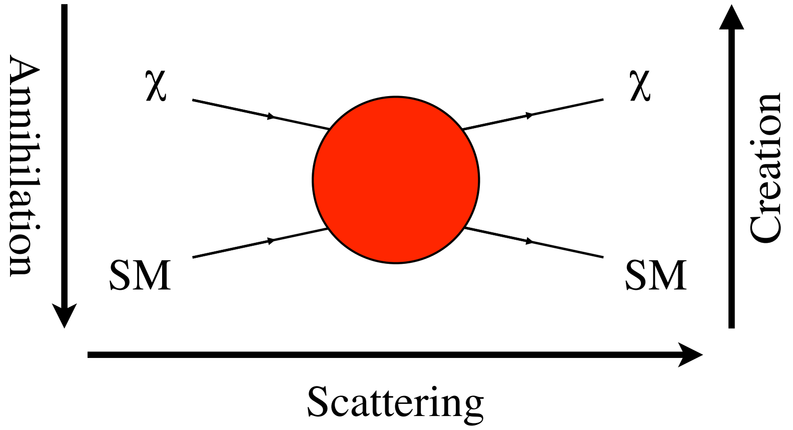

Figure 1.2: The generic diagram describing WIMP-SM interactions. Time axes are labeled for each different process. The interaction mechanism is generically described by the red circle.

1.3.3.1 Annihilation

The WIMP-SM process most directly understood from cosmological observations is the process of WIMP annihilation. Based on the required relic abundance of WIMPs in the universe, the requisite annihilation cross section is well established. Using knowledge of the annihilation cross section, one can undertake searches for signatures of SM particles in excess of standard cosmic backgrounds from known sources. This type of search is known as "indirect detection."

Indirect detection methods search for excess fluxes of γ rays (e.g. the Fermi Gamma-Ray Space Telescope [28, 29, 30, 31]) or antimatter (e.g. the Alpha Magnetic Spectrometer or AMS [32]) potentially attributable to WIMP annihilations. Fermi is able to probe the relic abundance annihilation cross section for WIMP masses below a few tens of GeV in selected decay channels, but the results are sensitive to uncertainties in the dark matter density function along the line of sight, and within the object of study. AMS reports a positron excess above 10 GeV, deviating from positron production models through SM processes. The excess can in principle be explained by dark matter annihilations producing e^+e^- pairs, where the positron energy spectrum would be peaked at the dark matter particle mass with a power law falloff toward low energies. It is unclear whether the rise can also be explained by a simple adjustment of SM background processes [33, 34]. Indirect detection efforts span a wide range of measurements. Measurements of unexplained excess line sources from the galactic center have prompted some dark matter signal claims, although the claims are not conclusive [35, 36, 37, 38, 39, 40].

1.3.3.2 Creation

The energies required for production are on the order of the typical WIMP mass, in the range of 10–1000 GeV. These energies are available in large-scale particle colliders, most notably the Large Hadron Collider (LHC). Searches for WIMP creation signatures hinge on locating “missing mass” in various particle collisions, where a significant amount of energy is unaccounted for based on the SM particles detected and known losses from e.g. neutrino production [41]. Missing mass searches in CMS result in a limit on WIMP-SM interaction that, although not competitive with direct detection experiments for WIMPs >10 GeV undergoing spin-independent interactions, has a relatively flat sensitivity as a function of WIMP mass down through 1 GeV, and can therefore exclude WIMPs much lighter than those detectable through current direct detection experiments [42]. Collider search limits are also particularly competitive in a spin-dependent parameter space, in which direct detection experiments are partially hobbled by the loss of the A^2 event rate enhancement, where A is the target nucleus atomic mass.

1.3.3.3 Scattering

The physics of WIMP annihilation into SM particles also leads to a description of WIMP-SM scattering. This forms the basis for all direct detection experiments. Direct detection is discussed in detail in Sec. 1.4.

1.4 Direct Detection

The process of WIMP direct detection is insensitive to the fine details of the motivating physical theory. Direct detection is robust in that it is sensitive to only two parameters describing the WIMP itself: the mass m_χ, and the nucleon interaction cross section σ_χ. Other parameters, such as number density and velocity distribution (Sec. 1.2.1), are determined independently from these particle-specific quantities. The results of direct detection experiments are therefore reported in (m_χ, σ_χ) space, using an underlying set of astrophysical assumptions to set the expectation for the interaction energy spectrum. The relevant parameters for a direct detection experiment are described in this section. The construction of the WIMP recoil spectrum follows the canonical review by Lewin and Smith [43].

1.4.1 WIMP / Nucleus Interactions

WIMP dark matter undergoes interactions with SM particles through both gravitational and weak interactions. While the gravitational forces from WIMP dark matter are responsible for all of the cosmological measurements of dark matter to date, this force is far too weak to be used for laboratory detection. The weak interactions between WIMPs and baryonic nuclei offer the most promise for yielding a direct observation of WIMPs.

The WIMP-nucleus interaction is coherent over the entire nucleus. For low-energy scatters, the WIMP de Broglie wavelength is much larger than the nuclear radius, giving the condition $h/q \gg r_n$, where h is Planck's constant, q is the momentum transfer and r_n is the nuclear radius. It is sufficient to represent the WIMP as undergoing s-wave scattering, isotropic in the center-of-mass frame [44]. As q increases, the coherent effect over the nucleus results in a drop in the scattering cross section, with a zero at intervals of $q = N \cdot h/r_n$ where N is an integer >0. (In practice, only the first zero is of any relevance, as the event rates for high momentum transfer are well below consideration.) The reduction in scattering rates due to coherence over the nucleus is represented by the nuclear form factor $F(q)$, which describes the spatial distribution of the nucleons in the target nucleus. The form factor acts on the scattering amplitude; as such, the overall WIMP event rate is multiplied by $F(q)^2$ to obtain the cross section correction.

The detailed form of $F(q)$ is the Fourier transform of the nucleon distribution, which is generally taken to be a solid sphere where only the nucleons in the outer shell contribute significantly to the scattering probability. An industry standard is the Helm form factor [45],

$$F\left(q\right) = 3\frac{j_1\left(qr_n\right)}{qr_n}\exp\Big(-\left(qs\right)^2/2\Big), \tag{1.8}$$

where $j_1\left(x\right) = x^{-2}\cdot\sin\left(x\right) - x^{-1}\cdot\cos\left(x\right)$ is the first order spherical Bessel function, and s is a skin thickness, describing the width of the outer edge of the nucleon distribution that contributes predominantly to the WIMP scattering amplitude. The values of r_n and s in Eq. 1.8 are empirically taken to be $r_n = 1.14\,A^{1/3}$, where A is the atomic mass, and $s = 0.9$ fm [43].

The simplest case of WIMP-nucleus interactions is a spin-independent (SI) interaction. In this case, the coherent addition of the scattering amplitudes over all nucleons creates the dependence $\sigma_\chi \propto A^2$. For this reason, heavy nuclei are generally favored for detection of WIMP SI interactions. Scattering models gain complexity under the assumptions that WIMPs couple to protons and neutrons differently, or the scattering amplitude takes the sign of the nucleon spin and the interaction becomes spin-dependent (SD). In the former case, the complexity of the model is taken into $F\left(q\right)$, as the dependence on the proton and neutron distributions in the nucleus becomes relevant. In the latter case, paired protons and neutrons do not contribute to the scattering amplitude, and only nuclei with odd numbers of protons and/or neutrons are sensitive to WIMP interactions. In practice, supersymmetric WIMP candidates are a mixture of particles with SI and SD couplings, and detection in both channels can aid in breaking the degeneracy betweeen various WIMP models.

1.4.2 Recoil Spectra

The actual or "true" recoil spectrum is calculated based on the assumed WIMP velocity distribution, given in Eq. 1.5, and the form factor $F\left(q\right)^2$ from Sec. 1.4.1. The general form of the differential recoil spectrum dR/dE_r, where R is the recoil rate and E_r is the energy imparted to the target nucleus by the WIMP, is given by

$$\frac{dR}{dE_r} = \frac{\sigma_0\rho_\chi}{2\mu^2 m_\chi}F^2\left(q\right)\int_{v_{\mathrm{min}}}^{v_{\mathrm{esc}}}\frac{f\left(v\right)}{v}\mathrm{d}v, \tag{1.9}$$

where σ_0 is the WIMP-nucleon interaction cross section, ρ_χ is the WIMP density, m_χ is the WIMP mass, μ is the reduced mass factor $4m_\chi m_n/\left(m_\chi + m_n\right)$, v_{min} is the minimum WIMP velocity required to generate recoil energy E_r [27], and v_{esc} is the velocity required for the WIMP to escape from the galaxy. The recoil spectrum is computed for three common detector targets (Xe, Ge and Ar, with $A = 131$, 73 and 40, respectively) in Fig. 1.3, using several assumptions for WIMP and astrophysical parameters. The mass and cross section used are close to the 100 GeV mass point on the 90% exclusion curve set by LUX [46].

The most relevant aspects to take away from Fig. 1.3 are the relative event rates in the different targets, and the energy ranges over which a significant number of WIMP recoils occur. The A^2 enhancement is apparent in the integrated event rates at $E_r = 0$. Even for the heaviest target (Xe), the raw number of dark matter scatters at all energies is only 7×10^{-4} kg^{-1} day^{-1}; a 100 kg detector operating for one year with zero energy threshold could potentially detect at most 26 WIMP recoils. Practical considerations reduce this number, due to the finite energy threshold and the <100% WIMP signal acceptance of real experiments. The presence of backgrounds can also limit the discovery potential of direct detection experiments. Due to the low signal rate, establishing a low-background experiment is essential for discovery.

In all targets, particularly in the case of Xe (used as the LUX target), the exponential form of the WIMP scattering spectrum dictates that a low detection threshold be established for the detector. The characteristic (e^{-1}) energy of the differential recoil spectrum at low E_r is 15 keV for the 100 GeV WIMP and 1.4 keV for the 10 GeV WIMP. The energy threshold for current Xe dark matter direct detection experiments is typically on the order of several keV$_{\text{nr}}$[47, 48, 49, 46]. A well-established low energy threshold is particularly important for the discovery of low-mass WIMPs, where the differential WIMP rate can vary by a factor of several for a keV$_{\text{nr}}$-scale change in threshold.

It is interesting to note that the velocity distribution $f(v)$ is influenced by the relative speed of the Earth and the WIMP wind, and that this speed fluctuates annually as the Earth orbits the Sun. This fluctuation creates a 6% peak-to-peak modulation in the average WIMP velocity, and a corresponding 3% modulation in rate, with an amplitude peaked around June 2. The annual modulation of the WIMP signal is an important technique for distinguishing WIMP events from constant backgrounds (e.g. neutron emission from materials), and is the basis for several positive detection claims [50, 51].

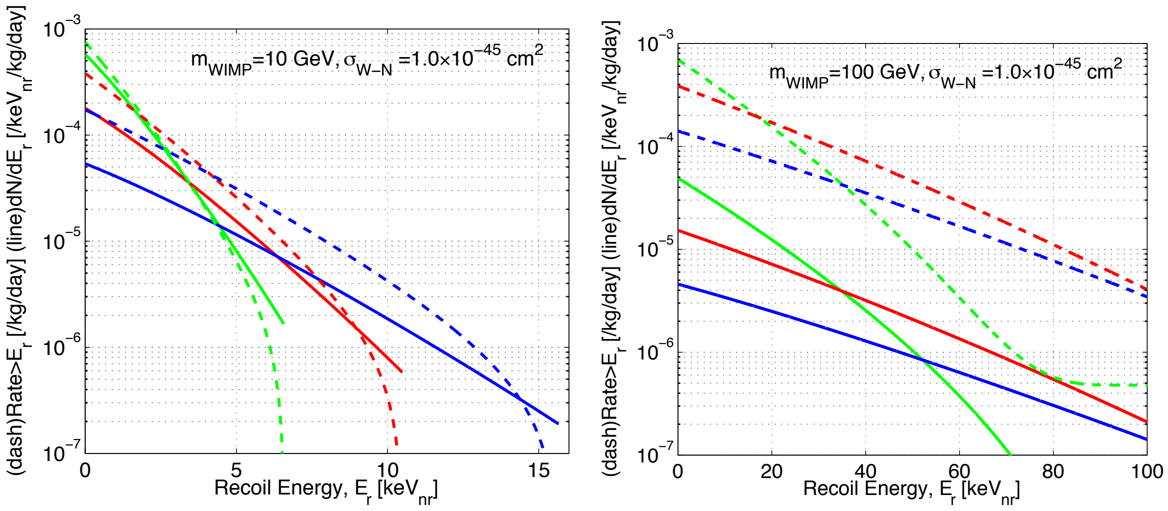

(a) (b)

Figure 1.3: Dark matter scattering rates for (a) 10 GeV and (b) 100 GeV WIMPs on various target elements. Scattering energy E_r is given in units of keV$_{\text{nr}}$, where the "nr" subscript indicates energy deposition through a recoiling target nucleus (see discussion in Sec. 2.1.2). The differential recoil rate is shown as the solid curves, for scattering from Xe (green), Ge (red), and Ar (blue) nuclei. The integrals of the differential spectra from E_r to infinity are shown as the dashed curves for the same nuclei. A WIMP-nucleon SI cross section 10^{-45} cm^2 is used. Differential spectra assume a Helm nuclear form factor. Rates are calculated using Eq. 1.9, assuming $\rho_{local} = 0.3$ GeV cm^{-3}, $v_0 = 220$ km s^{-1}, $v_{earth} = 245$ km s^{-1}, $v_{esc} = 544$ km s^{-1}.

1.4.3 Detection Parameter Space

Once the astrophysical and nuclear parameters for the WIMP recoil model are fixed, the results of a direct detection experiment are plotted in (m_χ, σ_χ) space. A sampling of the state-of-the-art in direct detection experimental results in the WIMP parameter space is shown in Fig. 1.4. For detectors reporting null results, an exclusion curve is drawn which rules out values of σ_χ above the curve with 90% confidence. The curve varies as a function of mass, limited on the low-mass end by detector threshold and on the high-mass end by WIMP number density, where the latter is proportional to m_χ^{-1}. For detectors reporting a potential positive WIMP signal, solid contours are drawn representing a 90% confidence interval.

Theoretical WIMP models are typically represented as 68% or 95% contours in the mass / cross section space. WIMP models span the full range of the parameter space shown in Fig. 1.4, and extend several orders of magnitude (higher and lower) in interaction cross section beyond what is shown in the figure, due to the number of different variations of the underlying theories, e.g. [26, 52, 53]. As dark matter experiments are agnostic to the specific details of the underlying WIMP theory, the experiments are able to test multiple theories simultaneously by sweeping a broad range of the parameter space. Experiments are able to maximize their coverage of the parameter space with a low energy threshold, a long exposure time and low background rates, as discussed in Sec. 1.4.4.

1.4.4 Establishing a Quiet Detector

Sections. 1.4.2 and 1.4.3 motivate the requirement for a direct detection experiment with a low energy threshold and very low background rate. The combination of these two requirements for dark matter discovery dictates the use of a particle detector that measures energies three to four orders of magnitude lower than those measured in other types of particle detectors. The background event rate must be comparably reduced to facilitate discovery of the exceptionally rare dark matter scattering events.

Dark matter experiments are commonly associated with their distant cousins: neutrino observation experiments. Both experiments share common characteristics in using massive

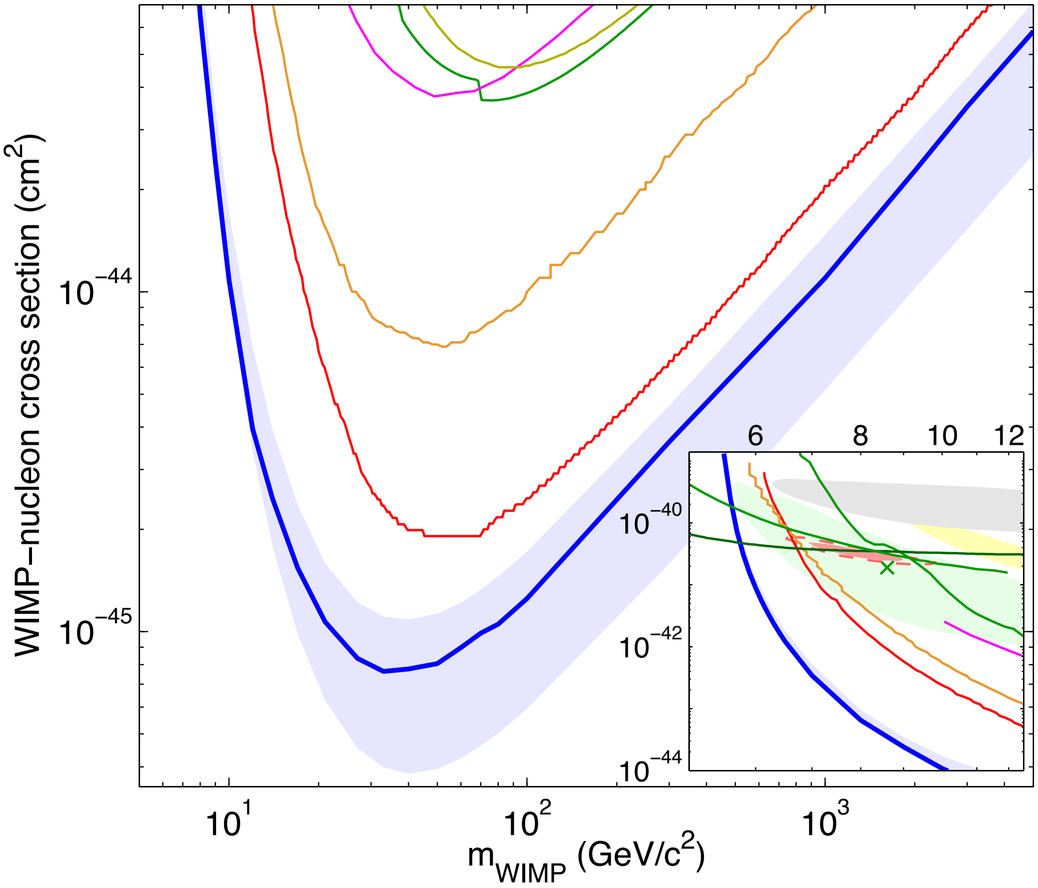

Figure 1.4: WIMP dark matter direct detection parameter space, where the axes are the WIMP mass (horizontal) and spin-independent cross section (vertical). Plot taken from [46]. Solid lines are 90% exclusion curves from experiments reporting null results, including LUX 85.3 day [46] (blue, $\pm 1\sigma$ shaded), XENON100 100 day [54] (orange) and 225 day [49] (red) results, ZEPLIN-III [55] (magenta), CDMS II [56] (green), and Edelweiss II [57] (yellow). The inset shows allowed contours from DAMA/LIBRA [58, 59] (gray), CRESST II [60] (yellow), CDMS II Si detectors [61] (green, centroid denoted by the x), and CoGeNT annual modulation signals [62] (red). Further discussion of LUX results is given in Sec. 8.9. Limit and contour data available at [63].

targets to observe interactions from particles with very low interaction cross sections. The similarities tend to end there, however. Neutrino experiments such as the Sudbury Neutrino Observatory [64] and Super-Kamiokande [65] search for neutrino interactions at MeV energy scales, by way of Cherenkov light production. The low-energy threshold of these experiments rolls off around 4 MeV due to photon generation and collection efficiency considerations. As shown in Fig. 1.3, this energy threshold is far too high to be useful for dark matter detection. The situation is much worse for the particle detectors which operate at accelerator facilities, where the energy thresholds are at e.g. ∼GeV for ECAL electron detection [66].

The Borexino experiment uses a liquid scintillator with a 200 keV energy threshold, below which β decay from ^{14}C (endpoint 156 keV) creates a background rate that limits neutrino searches [67]. Although this threshold is much improved relative to the water Cherenkov detectors, it is still two orders of magnitude too high for use in dark matter detection. The rate of ^{14}C low-energy decays, 100 decays s^{-1} in the 100 tonne search volume, would quickly overwhelm any potential low-energy dark matter signals [68].

Development of dark matter detectors has focused primarily on the use of materials which have high yields of scintillation photons, ionization electrons, and/or phonons at the 1–10 keV scale [27]. Early devices, high-purity Ge and Si detectors repurposed for dark matter signal detection in the 1980s, were gradually replaced by detectors that were bigger, better shielded, and carried lower intrinsic backgrounds [27]. The most powerful of these technologies, in a combination of background rates, scalability, and energy resolution, has proven to be the time projection chamber (TPC) [69]. TPC technology, with the LUX experiment as the example, is discussed in detail in Sec. 2.2.1.

Of the current TPC detectors purposed to dark matter detection, the LUX experiment has been demonstrated to be the most sensitive to dark matter signals [46]. LUX has made this remarkable achievement through a combination of ultra high signal collection (discussed in Ch. 3) and extreme background reduction (discussed in Ch. 5). The remainder of this work is devoted to a detailed analysis of these features, which give LUX the ability to place the greatest constraints on potential WIMP particle parameters to date. The LUX fiducial energy spectrum of background events is compared with the detected energy spectra after analysis cuts for several other experiments, including direct dark matter searches, neutrino scattering, and double beta decay experiments, in Fig. 1.5. The LUX background rate in the critical dark matter search energy range 1–10 keV is lower than any other experiment.

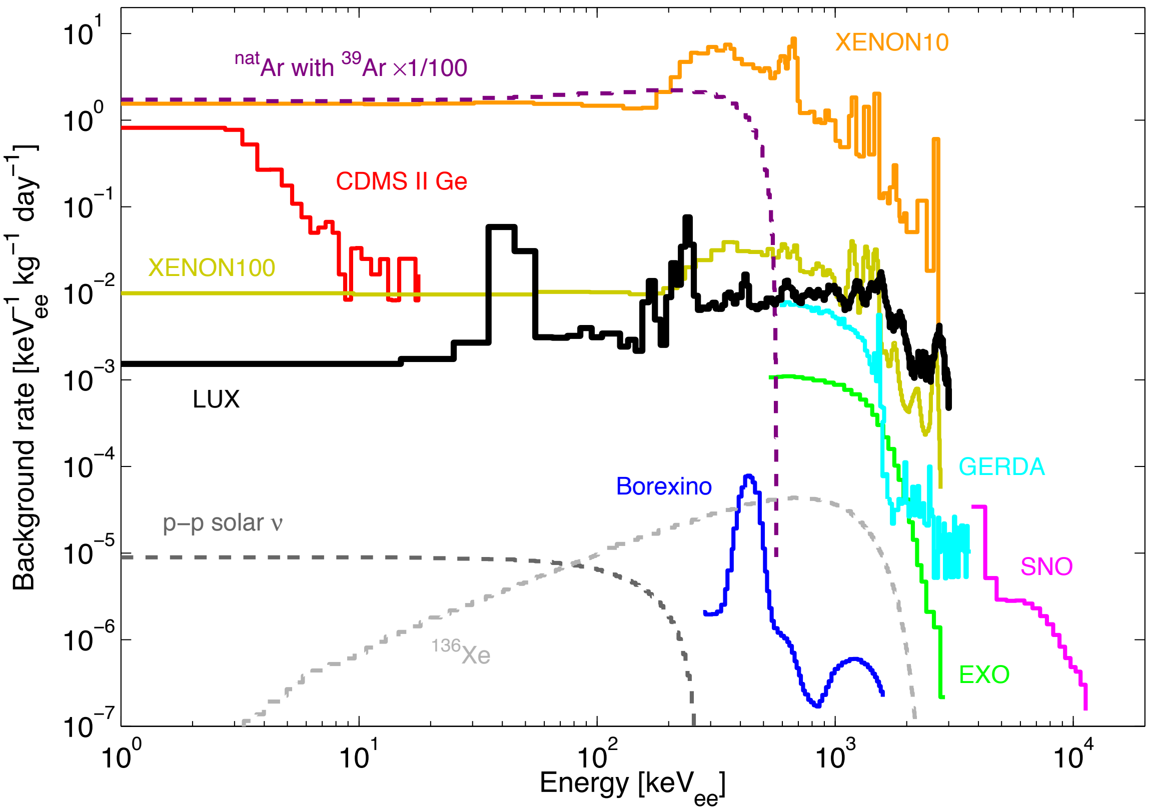

Figure 1.5: A comparison of energy scales and background rates in several different particle detectors, illustrating the need for an instrument such as LUX for WIMP discovery. The background energy spectrum is given in units of keV$_{ee}$, where the "ee" subscript refers to energy deposited by an electron in the detector (see Sec. 2.1.2 for further details). The LUX background energy spectrum (black) in the 100 kg fiducial volume is shown from the second half of the 85 day WIMP search run, after application of WIMP search cuts. Background energy spectra are shown for comparison for the following dark matter detectors: CDMS II Ge detectors (red, 241 kg days) [70], XENON10 (orange, 5.4 kg fiducial) [71], and XENON100 (yellow, 30 kg fiducial) [72]. Background spectra are also shown for the EXO (green, 175 kg) [73] and GERDA (cyan, 16.7 kg year) [74] double beta decay experiments, and the Borexino (blue, 154 ton years) [68] and SNO (magenta, 391 live days) [75] neutrino experiments. Overlaid is the projected p-p solar neutrino scattering spectrum on Xe (dark gray, dashed) [76, 77], which creates an electron energy deposition noise floor, and the spectrum from ^{136}Xe neutrinoless double β decay (light gray, dashed) [77], assuming no enrichment or depletion of ^{136}Xe in natural Xe. The projected ER background rate for Ar detectors from β decay of ^{39}Ar (purple dashed) is also given [78], assuming a reduction of ^{39}Ar levels to ×1/100 their natural levels [79].

CHAPTER 2

DIRECT DETECTION WITH THE LUX EXPERIMENT

The Large Underground Xenon (LUX) experiment uses 1/3 tonne of liquid Xe target to search for rare, low-energy nuclear recoil (NR) signatures from WIMP interactions. Liquid Xe offers excellent event calorimetry and background discrimination. This chapter details the use of liquid Xe for particle detection, and the details of the LUX detector construction and deployment at the Sanford Underground Research Facility (SURF) in Lead, SD. Further details about the LUX detector are published in [80].

2.1 Detection with Liquid Xenon

2.1.1 Xenon Properties

In the search for WIMP-baryon interactions, liquid Xe presents itself as a target of choice. A comprehensive review of Xe material characteristics is given in [81]. Xenon is a noble element with $Z = 54$ and $\langle A \rangle = 131$. Xenon can easily be liquified to create a suitable detector medium for dark matter searches. Xenon liquifies at temperatures in the range 165–185 K, which is a temperature range easily achievable using a wide variety of cooling systems. Liquid Xe has a density in the range 2.9–3.0 g cm^{-3}, allowing a large target mass to be contained in a relatively modest volume. Liquid Xe systems are also easily scalable with modest increases in containment and cooling systems, allowing rapid scaling from small prototype detectors to large-mass deployments.

The density and high Z of liquid Xe also provide suppression of backgrounds from γ rays, discussed in detail in Ch. 5. The mean free path of γ rays in liquid Xe is $\lesssim$cm scale, over a wide range of common γ energies, as shown in Fig. 2.1. The path length is dominated by photoelectric capture at γ energies below 300 keV, meaning that all energy is deposited immediately after capture. This means that Xe "self-shields," as the outer layers of the Xe absorb the majority of incoming γ rays. The center of the Xe is relatively free of γ interactions, creating a suitable region for rare-event searches. This region is referred to as the fiducial volume.

Natural Xe is comprised of several different isotopes, with atomic masses ranging from 124–136. Several isotopes have an odd number of neutrons, making Xe a suitable target for both spin-dependent and spin-independent interactions (see Sec. 1.4.1). Xenon also has no long-lived radioisotopes (excepting the incredibly rare double β decay of ^{136}Xe, discussed in Sec. 5.3.4), making Xe free of intrinsic backgrounds. The longest-lived unstable Xe radioisotope produced in appreciable quantities is ^{127}Xe, with a half-life of 36 days. A complete discussion of these isotopes is given in Sec. 5.3.1.

Xenon is virtually transparent to its own 7 eV (178 nm) scintillation light, allowing for high photon signal detection efficiency [82]. Scintillation light absorption lengths are therefore typically dominated by UV-absorbing impurities present in the Xe. These impurities can be removed with very high efficiency, leading to absorption path lengths much greater than the typical linear detector dimension ($\sim$m scale). Xenon scintillation light also undergoes coherent scattering, with measured path length 29 ± 2 cm [83, 84]. Detailed modeling of Xe optical physics is presented in Ch. 3.

Xenon is used in a variety of different applications. It is most commonly used in a variety of arc lamps. It can also be used as an anesthetic, in concentrations of $\sim$40% for loss of consciousness [85]. An interesting use of Xe is propellant in low-thrust ion engines. Xenon is an attractive ion engine fuel due to its high atomic mass, low ionization energy relative to many lighter elements, non-corrosive nature and environmental friendliness in case of spillage [86].

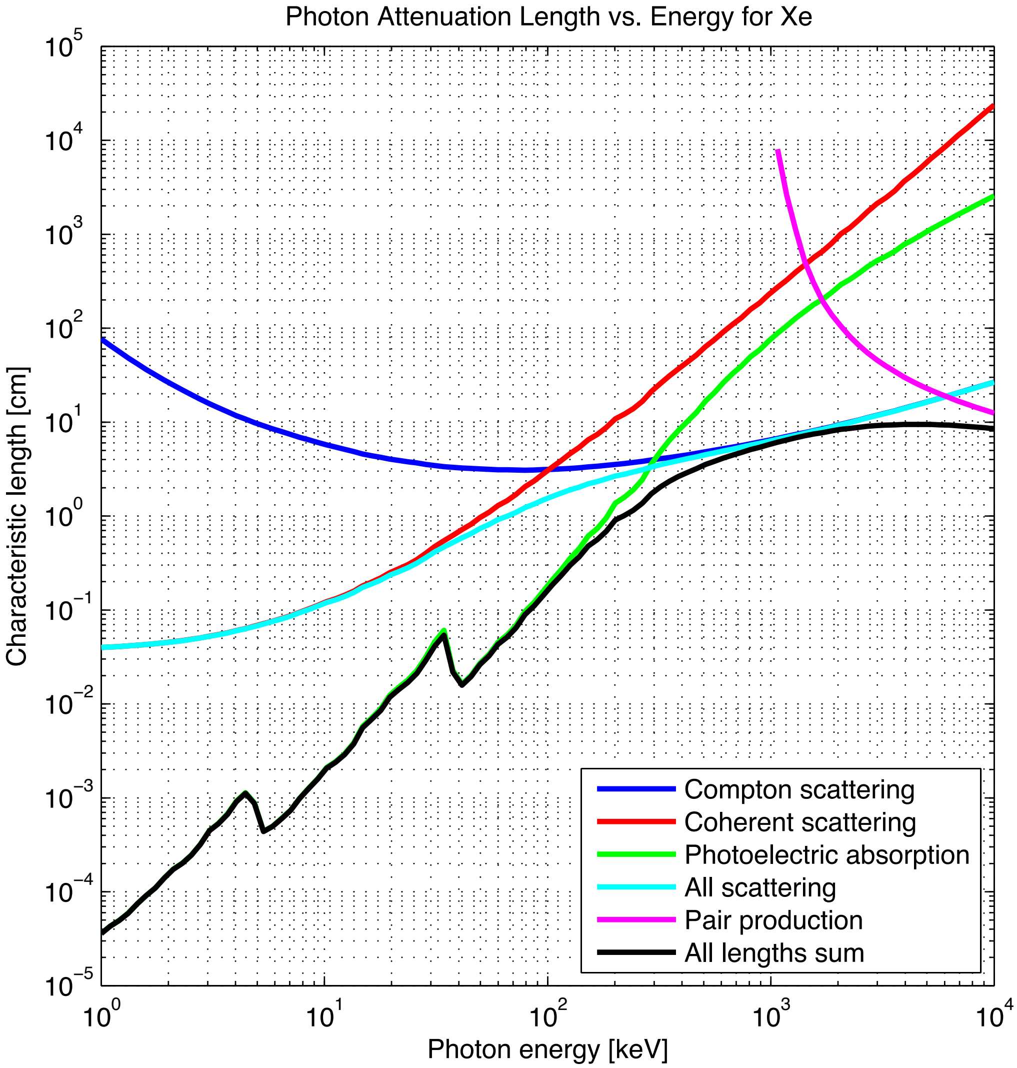

Figure 2.1: Photon attenuation length (mean free path) for γ rays in liquid Xe, as a function of energy. The mean free path is broken down into various energy deposition processes. Data is taken from [87]. (LUX Matlab function gamma_length.m.)

2.1.2 Energy Deposition Response

Energy depositions in liquid Xe produce a combination of scintillation photons, ionization electrons, and heat. The latter channel is insigificant in the case of electronic recoil (ER) events. Heat loss plays a significant role in energy reconstruction for NR events, and has been studied extensively.

A variety of technologies can be used to detect the 7 eV scintillation photons, with the most common being photomultiplier tubes (PMTs). The ionization electrons can be detected by collection at an anode or signal amplification region. Alternatively, the ionization electrons can be allowed to recombine with the ionized Xe atoms, resulting in a partial recovery of signal through additional scintillation. The ability to detect both the scintillation and ionization signals allows for very precise calorimetry of energy deposition events. The ratio of ionization to scintillation is also a powerful discriminant between ER and NR events.

A recoiling Xe nucleus or electron produces a µm-sized energy deposition track. Xenon atoms in the track are ionized or atomically excited through several different processes [71, 81]. The excited atoms de-excite through the emission of a 7 eV photon. In the absence of an electric field, the process of electron recombination, where ionization electrons re-fill the vacant atomic orbitals, dominates photon generation with a characteristic time of 45 ns. The application of an electric field suppresses the recombination process by extracting ionization electrons from the original interaction site. The de-excitation process is then dominated by the decay of dimers (Xe_2), with a 27 ns lifetime.

In the case of ER events, the total number of quanta generated (scintillation photons or ionization electrons) is linearly proportional to the total energy deposition in the Xe [88]. This relation is given by

$$E_{ER} = W \times (n_\nu + n_e)\,, \tag{2.1}$$

where E_{ER} is the energy deposited, W is the average energy required for generation of either a scintillation photon or ionization electron, and n_ν and n_e are the generated number of photons and electrons, respectively. W has been measured for liquid Xe to be 13.7 ± 0.2 eV

[89].

In the case of NR events, a significant fraction of the deposited energy is dissipated as heat. The energy fraction which is not lost to heat is quantified by the energy-dependent factor $\mathcal{L}\left(E_{NR}\right)$, colloquially known as the Lindhard factor. This factor describes the fraction of the initial energy deposition which results in a detectable electronic excitation (or, equivalently, the fraction of the initial energy deposition which results in the creation of a measurable signal, in scintillation photons and/or ionization electrons). The expression for NR energy deposition is

$$E_{NR} = \frac{W \times (n_{\nu} + n_e)}{\mathcal{L}\left(E_{NR}\right)}. \tag{2.2}$$

It is important to note that the partitioning between n_{ν} and n_e is both energy- and electric field-dependent, for both ER and NR . The average yields of these quanta for both ER and NR energy depositions are shown as a function of deposited energy in Fig. 2.2a, for the LUX Run 3 electric field of 182 V cm^{-1}. The curves are calculated using the Noble Element Simulation Technique (NEST) simulation code (v0.99β), which models the detailed physics of photon and electron generation in liquid noble gases [90]. The same data is shown in Fig. 2.2b as the ratio of the ionization to scintillation signal, as a function of the scintillation signal. This figure is an analog of the canonical ER/NR discrimination plot, discussed in Sec. 2.2.1.

It is apparent from Fig. 2.2a that the observable quanta per unit energy from ER and NR interactions differ dramatically as a function of energy. It is therefore important to establish the energy scale with which an event is reconstructed. We define the ER energy scale with the unit of $\mathrm{keV_{ee}}$, where the “ee” subscript stands for “electron-equivalent” and refers to energy deposited in the detector by an electron (e.g. a β ray, or an electron liberated from an atom by absorption of a γ ray). The NR energy scale is similarly defined with the unit $\mathrm{keV_{nr}}$, where the “nr” subscript stands for “nuclear recoil” and refers to energy deposited in the detector by a recoiling atom (characteristic of a WIMP or neutron interaction). The historical definition of the energy scales is given by the detected photon signal, compared to a given model of photon generation such as that shown in Fig. 2.2a. This definition, strictly speaking, does not accommodate information from using the ionization electron signal, as is used in Eq. 2.1 and 2.2. For this work, keV_{ee} and keV_{nr} will be used more literally, to refer directly to the type of interaction in the detector, and is independent of the exact energy reconstruction technique used.

The precise form of $\mathcal{L}\left(E_{NR}\right)$ is not well established for liquid Xe. A profusion of measurements in liquid Xe have been made, with a wide range of slopes reported at low energies. Reviews of all results are given in [90, 91]. The traditional technique for measurement of this quantity is the measurement of $\mathcal{L}\left(E_{NR}\right)$ relative to a fixed ER data point, typically the 122 keV_{ee} signal produced by a ^{57}Co source [92, 93]. This relative scintillation efficiency factor is known as $\mathcal{L}_{eff}$. Measurement techniques for $\mathcal{L}_{eff}$ use a neutron calibration source placed near the detector, and rely on a well-calibrated Monte Carlo simulation in order to predict the true energy deposition event rate in the detector. The value of $\mathcal{L}_{eff}$ is floated as a function of energy, allowing Monte Carlo NR energy spectra to be lined up with observed NR scintillation signals. This technique has been used to great effect in LUX and in past experiments. However, the most straightforward demonstration of sensitivity to low-energy signals comes from direct measurements in data alone. LUX aims to use a different technique to directly calibrate the NR signal as a function of energy deposition, which does not rely on a model of the energy deposition spectrum. This technique is discussed in Ch. 4.

2.2 The LUX Detector

The LUX detector is a Xe time projection chamber (TPC) designed for maximal collection of the scintillation photon (S1) and ionization electron (S2) signals [80]. LUX is shown in half cutaway in Fig. 2.3, with photos from construction given in Fig. 2.4. The detector contains 370 kg of liquid Xe. A volume of 280 kg[1] is lined with Hamamatsu R8778 PMTs, which collect the S1 and S2 signals with single-photon sensitivity. This 280 kg volume is referred to as the "active region", due to its instrumentation.

A series of electrostatic grids apply a vertical electric field to the active region, allowing

---

[1] Marked "300 kg" in Fig. 2.3, which was the original LUX specification before final detector construction was completed.

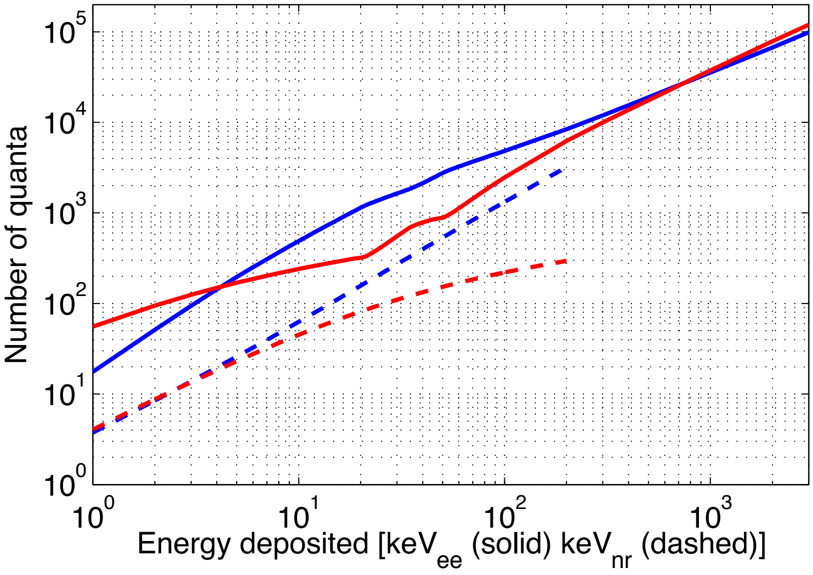

(a)

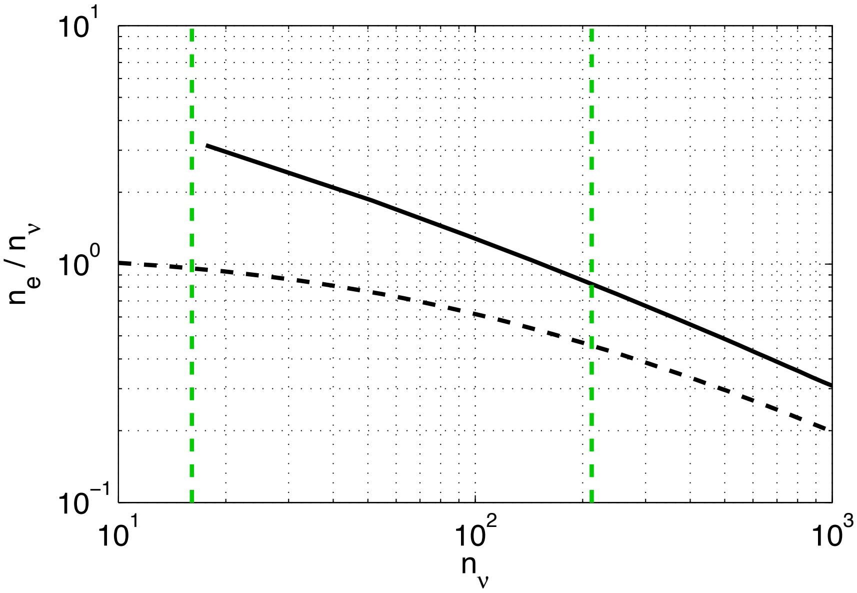

(b)

Figure 2.2: (a) Number of detectable quanta generated for ER (solid) and NR (dashed) energy depositions in liquid Xe. Shown are the curves for scintillation photon n_ν (blue) and ionization electron n_e (red) average yields. (b) The ratio of ionization electrons to scintillation photons, as a function of photon yield, for ER (solid) and NR (dashed) energy depositions. The typical WIMP search range is shown in dashed green, corresponding to 3.4–25 keV_{nr}. Data from [90].

for drift of ionization electrons and generation of the S2 signal. The section of the active region in which drift occurs, totalling 250 kg, is referred to as the "drift region." The drift region is created between the cathode grid, which stands 5.6 cm from the bottom PMT array, and the gate grid, which stands 49 cm away from the cathode grid and 0.5 cm below the liquid surface. The thin layer above the liquid surface in which electron extraction and secondary scintillation occurs is called the "extraction region," or "S2 region." The S2 region is created between the liquid surface and the anode grid, which stands in the gas layer 0.5 cm above the liquid surface.

Detector construction materials consist chiefly of low-radioactivity materials, including plastics, Cu, and low-activity stainless steel. A discussion of the radioactivity measurements for these materials is given in Ch. 7. The materials are housed in a low-radioactivity Ti cryostat. The cryostat is submerged in a 7.6 m (height) × 6.1 m (diameter) cylindrical water shield, which primarily serves to shield the detector from the γ and neutron flux from cavern rock.

Three steel flex conduits house the signal and high voltage lines which connect detector instrumentation to electronics outside of the water tank. Signals from the PMTs are amplified in a series of off-the-shelf and custom-made low-noise electronics modules. The amplifed signals are digitized at 100 MHz with a series of Struck ADC modules. The digitized waveforms are then paired with trigger signals and passed through a series of analysis software modules which characterize the pulses in each recorded detector event.

2.2.1 Observed Signals

LUX is a Xe TPC, which allows the detector to take advantage of the scintillation and ionization signals generated by liquid Xe to gain a nearly complete reconstruction of all aspects of an energy deposition event in the active region. The operating principle is shown in schematic in Fig. 2.5. The trace for a typical low-energy background event is shown in Fig. 2.6.

An energy deposition event produces a prompt burst of scintillation photons. These photons propagate through the active region, and are detected nearly instantly (on the timescale of ns) in the PMT arrays. The detected signal, known as S1, is proportional to

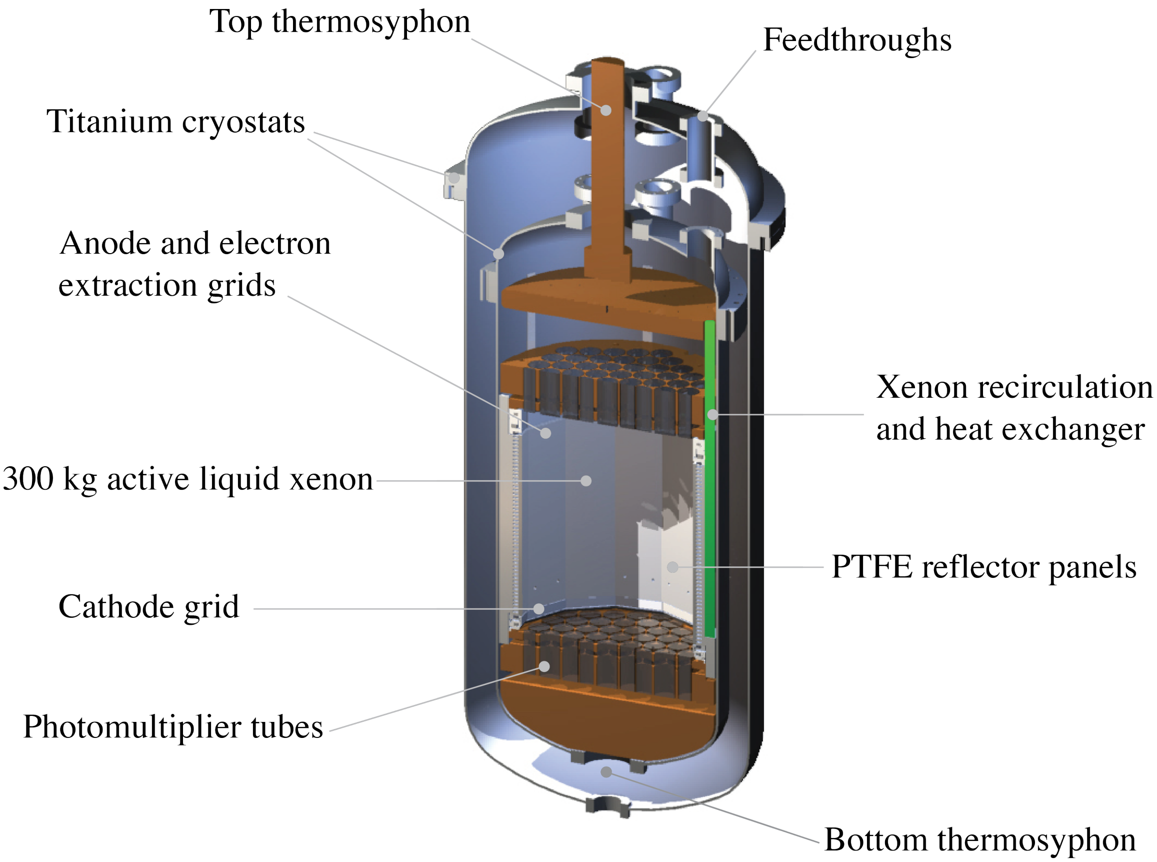
Top thermosyphon
Feedthroughs
Titanium cryostats
Anode and electron extraction grids
Xenon recirculation and heat exchanger
300 kg active liquid xenon
PTFE reflector panels
Cathode grid
Photomultiplier tubes
Bottom thermosyphon

Figure 2.3: The LUX detector, shown in cross-section. Major detector features across all subsystems are highlighted. Figure is taken from [80].

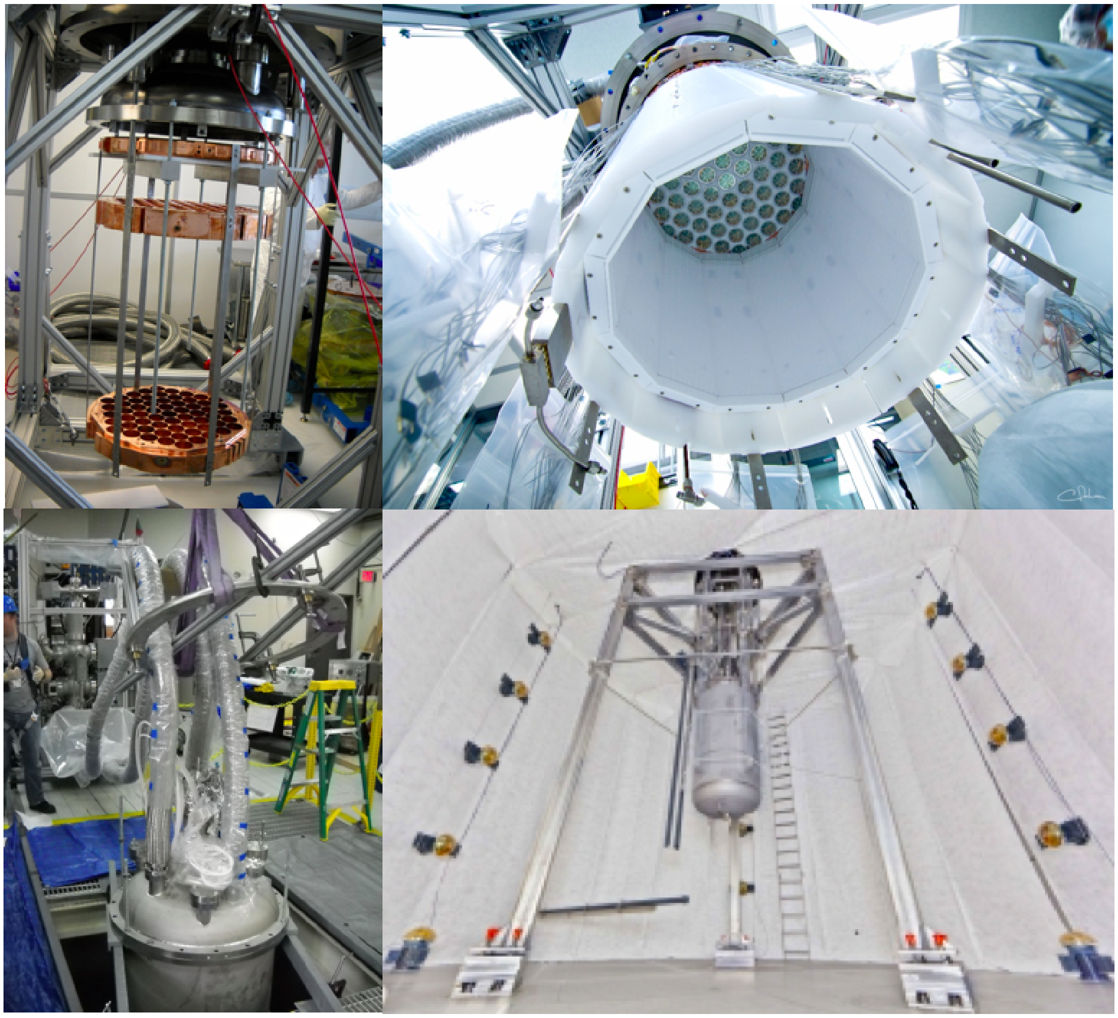

Figure 2.4: Snapshots of LUX detector construction and deployment. (Top left) The Cu top radiation shield and PMT array holders are mounted in the Ti strap frame, which is suspended from the inner cryostat dome. Assembly takes place in the Surface Lab clean room. (Top right) A bottom-up view of the detector after installation of the top PMT array, PTFE reflector panels, field shaping rings, and HDPE mounting panels. The bottom edges of the Xe heat exchanger and additional circulation lines are visible to the left and right of the active region respectively. Photo courtesy C. Faham. (Bottom left) The detector is lowered into position for the first technical run at the Surface Lab. Three flex conduits are visible, which contain HV and signal cables for the PMTs, electric grids, thermometry and level sensors. Connected to the flex conduits is the “breakout cart,” on which are mounted feedthroughs for access to all cabling. In the background behind the breakout cart is the HV cart, containing HV for the PMTs and electric field grids, as well as the slow control master computer. (Bottom right) The LUX detector is fully installed in the water tank in the LUX Underground Lab. Twenty 10” Hamamatsu R7081 PMTs instrument the water tank as a Cherenkov veto for rejection of muon-induced background events. The tank is lined with Mylar to enhance Cherenkov signal collection. In the left background is the air conduit used for the D-D neutron generator calibration (Ch. 4). Photo courtesy M. Kapust.

the number of photons generated (n_ν).

A cloud of ionization electrons is also created. These electrons are drifted vertically upward from the energy deposition site by a 182 V cm^{-1} electric field. When the electrons reach the liquid surface, they encounter a region of high electric field between the gate and anode grids. This field is 3.1 (6.0) kV cm^{-1} in the liquid (gas) in LUX. The high field imparts sufficient energy to the drifted ionization electrons that they are able to escape the liquid surface. The extracted electrons produce electroluminescence in the gas. The electroluminescence light, produced at the same wavelength as the S1 light, is collected by the PMTs. The detected signal from this event is referred to as S2. The total S2 signal is proportional to the number of ionization electrons (n_e).

The S1 and S2 signal from an event give excellent calorimetry, and are useful for several other types of event characterization. The three-dimensional position of the event can be localized to ∼cm accuracy through use of the S1 and S2 signal and time distributions. The Z coordinate can be found by the time separation between the S1 and S2, since the electron drift speed is constant (varying by 5% due to electric field variations). The XY position of the event can be found through analysis of the S2 signal pattern on the top PMT array, which is tightly localized around the S2 site. In the case of a γ or neutron which scatters multiple times in the detector, the scattering vertex locations and approximate relative energy depositions are easily resolved by the generation of multiple S2 pulses. The ability to discern multiple scatter events, and events which scatter in the outer Xe layers, is crucial to the rejection of ER backgrounds from γ rays. This is discussed in detail in Ch. 5.

The S1 and S2 signal sizes are also useful in distinguishing between ER and NR energy deposition events. From Fig. 2.2b, the ratio n_e/n_ν differs by a factor ×2–3 between ER and NR events in the low-energy nuclear recoil range where LUX conducts its WIMP search (3.4–25 keV$_{\mathrm{nr}}$). This serves as a powerful discriminant against low-energy ER backgrounds. Discrimination power from the S2/S1 ratio has been measured in the range 99–99.9% in several liquid Xe experiments. LUX background discrimination was measured during the first WIMP search run at 99.6% [46].

S1 and S2 signal sizes are measured in the number of photoelectrons detected, abbreviated “phe”. An example low-energy event is shown in Fig. 2.6. Typical WIMP signals generate a small number of S1 phe. From Fig. 2.2a, a 3.4 $\mathrm{keV_{nr}}$ energy deposition, roughly at the lower bound of the WIMP search range, generates an average of only 16 photons. Due to the finite efficiency of converting photons into phe at the PMT photocathode (Sec. 2.2.2), as well as imperfect reflecting surfaces in the detector (Ch. 3), the light collection efficiency for detection of a photon generated in the detector is $14.0 \pm 0.3\%$. This results in an average S1 signal of 2.2 phe at 3.4 $\mathrm{keV_{nr}}$. At 25 $\mathrm{keV_{nr}}$, which is the high end of the WIMP search range, the average S1 signal is 30 phe. It should be noted that, while the light collection efficiency may seem low in absolute terms, it is $> \times 2$ larger than the efficiency obtained in previous Xe experiments, and is dominated by finite detection efficiency (33% average [94]) for high UV photons.

S2 signals are much larger than S1 signals, since several photons are generated per ionization electron in the S2 region. The size of single-electron S2s was measured directly in LUX, yielding a size of 26 phe (extracted electron)$^{-1}$. From Fig. 2.2a, the average S2 signal size is 600 phe at 5 $\mathrm{keV_{nr}}$, and 2900 phe at 30 $\mathrm{keV_{nr}}$.

An expression for S2 photon generation per ionization electron extracted into the S2 region is found in [90], based on studies in [95]:

$$n_{\nu,S2} = \left(0.140\frac{\xi}{N} - 0.474\right) \cdot N \cdot x, \tag{2.3}$$

where the formula in Ref. [90] has been corrected after consultation with the authors. For Eq. 2.3, ξ is the electric field in units of kV cm^{-1}, N is the Xe number density in the gas region, and x is the size of the S2 region (the gap between the liquid surface and the anode grid). Using LUX values of $N = 6.9 \times 10^{19}$ cm^{-3}, $x = 0.5$ cm, and $\xi = 6.0$ kV cm^{-1}, the calculated S2 yield is 257 photons (extracted electron)$^{-1}$. The estimated S2 light collection efficiency is 9% [96], leading to an estimated 23 phe (extracted electron)$^{-1}$. This is in good agreement with the measured 26 phe (extracted electron)$^{-1}$ in LUX. The use of Eq. 2.3 leads to a substantial improvement over the S2 photon yield characterization in Ref. [97], which led to an observed factor ×6 discrepancy between the predicted and observed S2 yield in XENON10 [71].

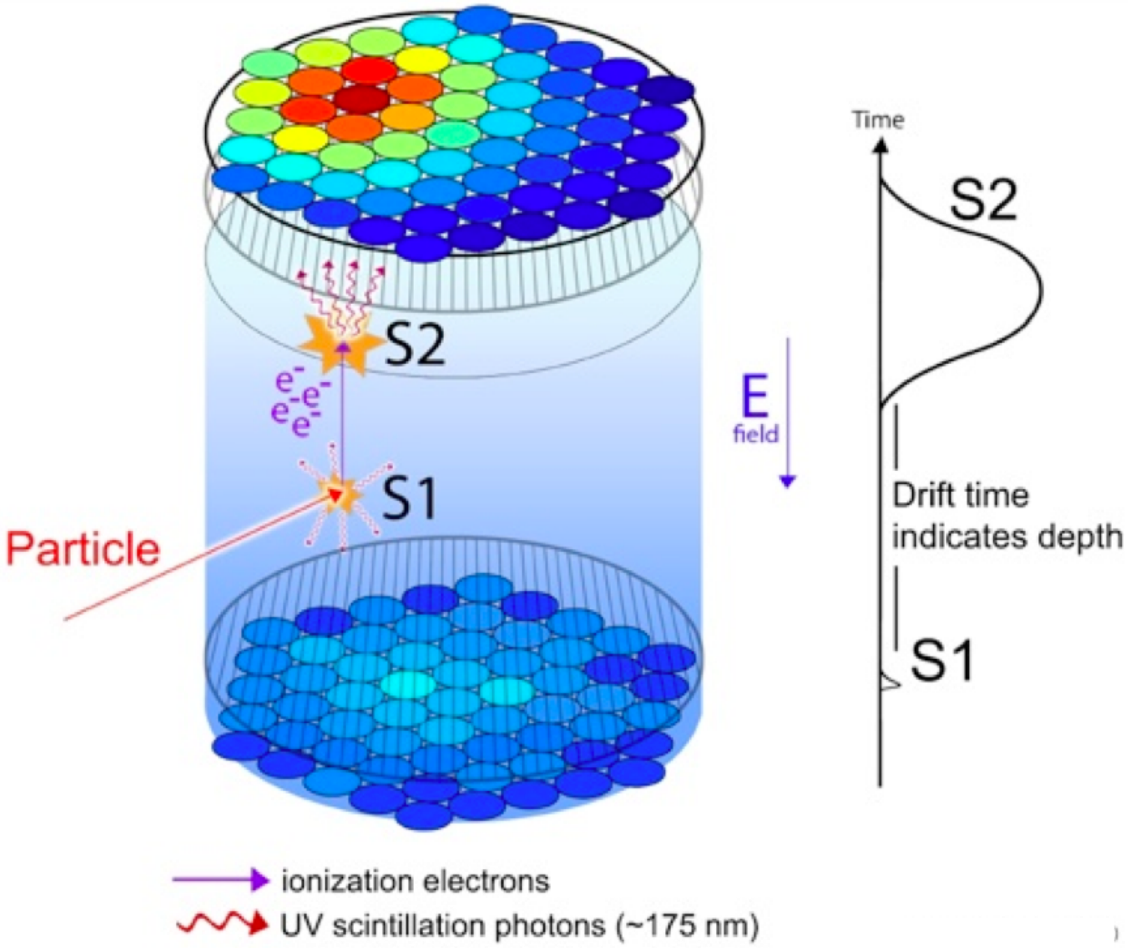
Time
S2
S2
e-
e-
e-
e-
e-
E
field
S1
Particle
Drift time
indicates depth
S1
ionization electrons
UV scintillation photons (~175 nm)

Figure 2.5: Operating principle of a liquid Xe TPC. An energy deposition in the liquid Xe produces a prompt scintillation signal (S1) and an ionization electron cloud. This cloud is drifted by an electric field into the high-field gas Xe region, where it creates a proportional electroluminescence signal (S2). The relative sizes and shapes of the S1 and S2 pulses are diagrammed at the right. The S2 signal creates a narrowly focused hot spot on the top PMT array, used for XY position reconstruction of the event. The time between S1 and S2 fixes the Z position of the event. The figure is taken from Ref. [80].

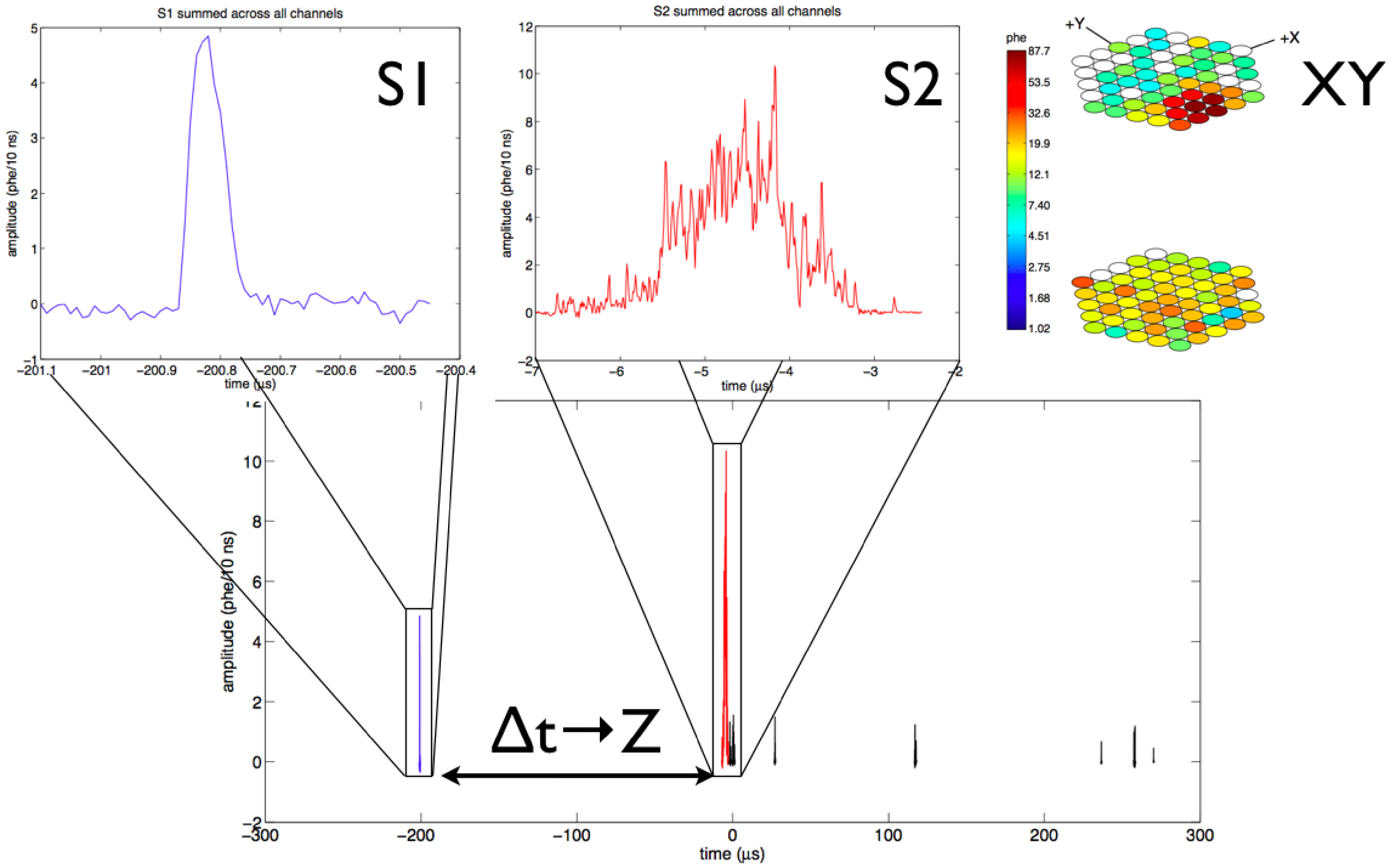

Figure 2.6: S1+S2 event from a γ interaction in the LUX drift region. The S1 and S2 pulses are expanded for detail. The S2 pulse hit pattern is shown in the upper right corner. The event is reconstructed with energy 4.2 keV$_{ee}$, scattering at the outer radial edge of the detector 24 cm above the bottom PMT array. The subsequent unmarked pulses are single electron S2s, used to calibrate the LUX ionization detection efficiency. Event trace credit [98].

2.2.2 PMTs and Light Collection

The active region is lined with one top and one bottom array of Hamamatsu R8778 PMTs, with 61 PMTs per array. The PMTs were tested extensively at Brown to characterize their response to Xe scintillation light. Full details of the PMT testing program are captured in [94].

The R8778 PMTs are well suited to operation in liquid Xe. The R8778 features an operating range from 160-320 K, encompassing the full range of liquid Xe operating temperatures (165–185 K). The PMTs are capable of operating in pressures up to 5 atm, well within LUX design specifications. The measured quantum efficiency (QE) for LUX R8778 PMTs, defined as the probability of conversion of a photon into a photoelectron at the PMT photocathode, is 33%. The collection efficiency, defined as the probability that a photoelectron is collected at the first dynode stage and subsequently produces a signal at the PMT anode, is 90%. LUX PMTs are operated at a gain of 4×10^6, where the gain represents the average number of electrons at the PMT anode per photoelectron which is successfully collected at the first PMT dynode. A more extensive definition of these terms is given in Ch. 3, for detailed characterization of the light collection model of the detector.

The R8778 PMTs used in LUX were selected after extensive testing of their radioactivity. The PMTs are projected to contribute the dominant radioactive background from detector construction materials. A full discussion of PMT background modeling is given in Ch. 5, and further details on radioactive screening are given in Ch. 7.

The Xe scintillation light is trapped with high efficiency inside the active region through the use of highly reflective panels at the active region boundaries. These panels are constructed out of polytetrafluoroethylene (PTFE, or Teflon®). These panels have repeatedly demonstrated an extremely high reflectance for liquid Xe scintillation light. Further details of light collection modeling are discussed in Ch. 3.

2.2.3 Electric Fields

The LUX detector uses five stainless steel electrostatic grids to generate a series of electric fields in the active region. Three of these grids (bottom, cathode, and gate) are in the liquid volume. The remaining two (anode, top) are in the gas. The drift region field, between the cathode and gate grids, is used to drift ionization electrons away from the energy deposition site. The extraction region, between the gate and anode grids, allows for generation of the S2 signal, enabling single-electron detection. The bottom and top grids are placed immediately in front of the PMT arrays, and serve to minimize the external electric field imparted on the PMTs. A series of 48 Cu field shaping rings are spaced uniformly around the outside of the active region, minimizing fringing of the electric field at the edges of the drift region.

The distance between the cathode grid and the bottom PMT array is 5 cm. The cathode grid is held at lower potential than the bottom grid and PMTs. This means that ionization electrons generated below the cathode grid will drift downward, away from the S2 generation region. For this reason, the region below the cathode grid is referred to as the reverse field region. Any energy deposition event in this region will generate a detected S1 signal, without an accompanying S2. A thorough study of this region for a potential systematic background contribution, known as "gamma-X," is given in Sec. 5.4.

2.2.4 Calibrations

Detector calibrations are vital to understanding ER and NR signals as a function of energy deposition. Previous Xe experiments have been calibrated through use of external radioactive sources, which generate γ rays at one or more known energies. The γ photocapture peak is found in data, setting the detector energy scale. Low-energy γ Compton scatters in the detector active region are used to populate the Xe discrimination plot ($\log_{10}$(S2/S1) vs S1), to provide a direct measurement of the shape of the ER band in this space.

The LUX detector is flanked by six equally spaced radioactive source delivery tubes. These tubes serve to provide a water-free path between the radioactive source and the detector, and guide the source housing to a precisely known position with reference to the active region. The source housing is constructed out of tungsten, which features $Z = 74$ and a density of 19 g cm^{-3}. Tungsten stops γ rays with a mean free path of 7.8 mm at 1 MeV. The housing can be fitted with collimation pieces of varying diameters, ranging from 0.5–17 mm. The orientation lock from the source tube and housing, in combination with the collimation, allow for the precise application of γ ray flux to any part of the detector.

The self-shielding of Xe against γ rays, crucial to the rejection of ER backgrounds in the fiducial volume, also serves to reject γ rays from external calibration sources. While low-energy γ scatters are relatively common at the edges of the detector, calibration signals must be delivered to the fiducial volume in order to properly reconstruct the S2/S1 band for WIMP search ER backgrounds. A full understanding of the limitations of the penetration power for these γ rays is given in Sec. 5.1.

In order to circumvent the problem of external γ penetration, the LUX detector makes use of several internal ER calibration sources. These sources consist of short-lived or removable radioisotopes that are mixed homogeneously with the Xe in the active region. The primary tool for ER calibration is $^{83\mathrm{m}}$Kr, which de-excites to ^{83}Kr with half-life 1.8 hours [99]. $^{83\mathrm{m}}$Kr has an excited energy level of 41 keV. It de-excites via a two-step process, first releasing a γ or conversion electron with energy 32 keV, followed by another γ or conversion electron at 9.4 keV. The two levels are separated by a characteristic time of 150 ns. This separation is wide enough to allow the identification of the two S1 signals, giving a photon yield calibration at the two energy levels. $^{83\mathrm{m}}$Kr is not removed by the purification system, because it is a noble element. However, the 1.8 hour half-life quickly reduces the $^{83\mathrm{m}}$Kr decay rate to negligible levels, making it an ideal source for periodic use during the dark matter search.

LUX also makes use of a tritiated methane source. Tritium is a low-energy β emitter, with endpoint 19 keV amd 12 year half-life. The endpoint is a factor $\times 4$ above the projected upper bound of the WIMP search window. Forty percent of the β spectrum will be contained within the WIMP search window, allowing for efficient calibration at modest event rates. The ^{3}H is bound to methane, which is largely inert and allows for efficient transport of the ^{3}H through the active region [100]. Due to the long half-life of ^{3}H, the purification system is relied upon for removal of the tritiated methane at the end of the calibration run.

The use of the LUX detector at the Sanford LUX Surface Facility resulted in the generation of several activated Xe isotopes with half-lives in the range 5–36 days. The most useful of these isotopes for energy calibration purposes are $^{129\mathrm{m}}$Xe and $^{131\mathrm{m}}$Xe, with half-lives of 8.9 days and 12 days, and de-excitation energies of 236 keV and 164 keV, respectively. Both isotopes decay through the release of low-energy γ rays and/or conversion electrons, which remain tightly localized around the decay site. This makes both isotopes well-suited to use as single-energy calibration sources. A full discussion of these and other activated isotopes is given in Sec. 5.3.1.

External neutron calibrations do not suffer the same penalties as external γ calibrations, as the mean free path of typical calibration source neutrons (with typical energy of several MeV) is 12 cm. The NR discrimination band is populated by use of external AmBe and ^{252}Cf sources. Subsequent studies of detector background data show no evidence of neutron activation of detector construction materials after several hours' exposure.

LUX will employ a novel calibration technique in order to directly measure the properties of scintillation and ionization for very low NR depositions. The technique uses a collimated, monoenergetic beam of neutrons, and relies on reconstruction of multiple-scatter events to determine signal yields as a function of energy deposition. The technique is described in detail in Ch. 4. This technique is available for the first time in a Xe detector due to the combination of the large size of LUX, the 300 tonne water shield, a high-yield D-D fusion neutron source, and a little forward planning.

2.2.5 Cryogenics

The LUX detector uses a novel thermosyphon-based cooling system to maintain the Xe in the detector at the liquid phase. Thermosyphons are closed loops of gaseous N_2, which exchange heat between the detector and a liquid nitrogen (LN) bath mounted vertically above the detector. Nitrogen gas condenses in the lines inside the LN bath. This condensed gas drips down the thermosyphon lines and encounters an evaporator head, in contact with the detector. The LN evaporates, removing heat from the detector. The thermosyphon assembly in LUX is capable of delivering $>$1 kW cooling power, more than sufficient for maintaining the 370 kg payload at -100°C. The thermosyphon assembly was intentionally overpowered for LUX, as the assembly will be used to cool the 7 tonne LZ detector following LUX decommissioning.

LUX is instrumented with four thermosyphons, with one cold head located at the top of the detector, one at the bottom, and two on the sides. An additional fifth thermosyphon is installed for testing purposes. All thermosyphon cold heads are attached to Cu internals, taking advantage of their high thermal conductivity and large mass to deliver fast uniform cooling to the Xe. The cold heads are instrumented with heaters in order to allow fine temperature control, and to assist in detector warmup during Xe recovery operations. The temperature of the internals is monitored by 40 thermometers mounted in the Xe space, while the temperature of the cryostat vacuum and thermosyphons are monitored by 23 thermometers.

2.2.6 Circulation and Purification

Xenon in the LUX detector is continuously circulated in order to remove impurities with high electron affinity or UV absorption coefficients. Liquid Xe is removed from the active region through a weir, which sets the liquid level in the detector and provides a buffer against large swings in liquid surface position. The removed liquid enters a two-phase heat exchanger, where the liquid Xe evaporates, and then a single-phase concentric-cylinder heat exchanger, which warms the Xe to room temperature. Prototypes of the heat exchangers, developed during the LUX 0.1 program, achieved >94% cooling efficiency (Sec. 2.3.1).

The Xe is circulated out of the detector by a double-diaphragm pump. Purification of the Xe is achieved with a SAES MonoTorr hot metal getter, which is projected to remove non-noble impurities to <ppb levels [101]. The purified Xe is circulated back into the detector, through the heat exchangers, and through the large-mass Cu internals, equilibrating the purified Xe temperature with the temperature of the active region. The purified Xe is reintroduced to the active region through a return line at the bottom edge.

2.2.7 Water Shield

The LUX cryostat is submerged in a cylindrical water tank, which has radius 3.8 m and total height 6.1 m. The water tank is used as a shield against γ and neutron backgrounds from sources outside of the detector, particularly radioactivity and muon interactions in cavern rock. The finite size of the detector results in a minimum shielding thickness of 2.75 m on the top and sides of the detector. The bottom water shielding thickness is 1.2 m, augmented by use of a low-radioactivity inverted steel “pyramid” shield built into the

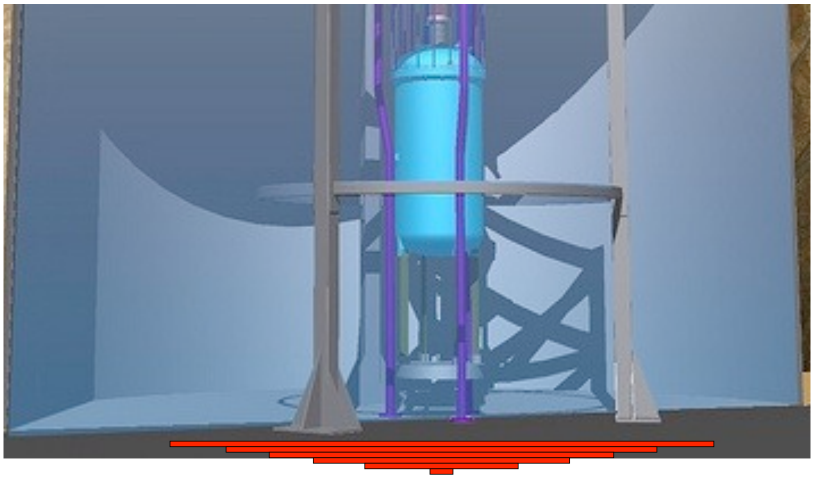

Figure 2.7: Sketch of the location and geometry of the low-radioactivity steel pyramid shield (red), built into the floor of the LUX Underground Lab directly below the water tank. The pyramid is constructed out of six octagonal low-radioactivity steel plates. The pyramid is used to augment the vertical water shielding, allowing the detector to sit closer to the cavern floor and increasing the water shield thickness above the detector. Image credit S. Fiorucci.

cavern floor below the water tank. The location and geometry of the pyramid are sketched in Fig. 2.7. Projections of γ and neutron flux through a semi-infinite water shield are shown in Fig. 2.8. The water shield is projected to reduce external γ backgrounds in LUX by a factor $\times 10^{-7}$, and high-energy neutron backgrounds by a factor 3×10^{-3}.

The water shield is instrumented to detect the Cherenkov light generated by throughgoing muons. Muons interacting in the cavern rock and water shield can potentially generate high-energy neutrons [71]. Detection of muon Cherenkov light enables the water shield to be used as a veto against background events generated by these neutrons. Cherenkov signals are detected by 20 10" diameter Hamamatsu R7081 PMTs spaced in five groups of four around the water tank.

2.2.8 Data Acquisition

The LUX data acquisition system is described in detail in [98, 102]. The 122 R8778 PMTs instrumenting the active region provide a gain of 4×10^6 for detected photoelectrons. The boosted signal is collected at the PMT anode and transferred through a dedicated cable out of the detector and water shield. The signal is then passed through a chain of analog electronics. The analog chain consists first of a preamplifier stage, custom-made for the

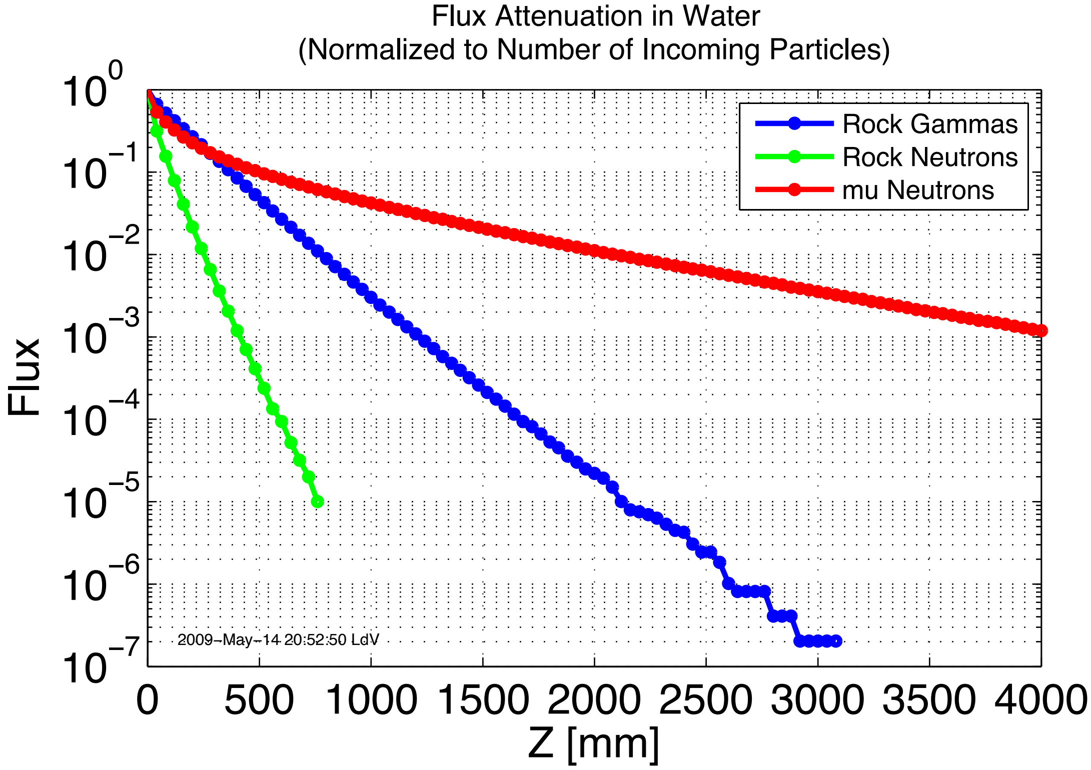

Figure 2.8: Flux of γ rays and neutrons through a semi-infinite wall of water, as a function of wall thickness. Flux is defined as the fraction of particles traveling beyond a given depth. Curves are shown for γ rays from typical ^{238}U / ^{232}Th content in rock (blue), neutrons from typical ^{238}U / ^{232}Th content in rock (green), and high-energy neutrons from muon spallation in rock (red). Figure taken from [71].

LUX experiment at the University of California, Davis. The preamplifier stage provides a ×5 signal height amplification, with an optional ×1/10 attenuator built in-line after the amplifier. The signal is then passed through a postamplifier, custom-made by Harvard University, which provides a further ×1.5 area gain. The PMT channel signals are individually digitized by Struck ADCs, with digitization speeds of 100 MHz.

The Struck modules feature a pulse-only digitization (POD) mode. Digitization in POD mode results in traces which are free of baseline between pulses. Baseline information for each event is separately recorded as a single average value. Baseline suppression changes the size of a typical event in the dark matter search region (assuming only a single S1 and S2 are digitized) by a factor ×1/50, allowing for a massive savings in storage and post-processing computing power.

LUX makes use of a digital trigger to reject spurious signals. The trigger is the DDC-8DSP system, designed by LUX collaborators at University of Rochester. The DDC-8 digitizes PMT signals output from the postamplifiers. The FPGA firmware can be programmed to recognize various pulse shapes, thereby allowing rough identification of S1 and S2 signals. Triggering conditions can then be set to identify events which contain preselected signal topologies, e.g. low-energy events, or single-S1 + single-S2 events. The trigger signal is digitized through a Struck channel, and is integrated into the data stream during post-processing.

The analog and digitization systems are optimized for low-energy signal detection. The S1 signals exhibit a 27 ns decay time constant. After all amplification stages, the pulse from a single photoelectron has a height of 2.0 mV, giving an integrated area of 16 mV ns. The ADC boards saturate at a 1.9 V signal height, corresponding to 950 phe or 6800 S1 photons collected in a single PMT. Approximately 80% of the S1 light is spread over the bottom array, and has a uniform distribution over all bottom tubes. The saturation limit then corresponds to 5.2×10^5 S1 photons generated, a factor ×5 higher than the largest γ signal in the detector. Note that, while S2 pulses have an area $\sim\times 100$ larger than corresponding S1 pulses, they have a FWHM of ~ 2 μs, and therefore have comparable or lower heights.

More stringent limits on signal sizes are placed by PMT saturation effects. A 2% deviation in reconstructed event energy from the true energy, for the addition of S1 and S2 signals, occurs for 500 $\mathrm{keV_{ee}}$ events; the deviation rises to 10% for events at 2.6 MeV. A full treatment of PMT saturation effects and measurements is given in [94].

2.2.9 Data Processing

Digitized signals from the Struck ADC units are saved into files on a dedicated acquisition computer on site. These files, known as DAT files, contain the digitized waveform trace data, saved as data points in (samples, mV), where samples are ADC samples (10 ns intervals) and mV is the signal height. The DAT files also contain timestamps for all digitized pulses.

The DAT files are transferred to a second on-site computer, dedicated to pairing trigger information with the acquired waveforms, and removing data points which fall outside of a preset time window around the trigger signals. This is known as "event building," where an "event" includes any pulses within the time window around a trigger. Event building removes all pulse information that clearly does not correspond to an interesting detector event, i.e. small noise events, single-electron S2s, etc. The resulting event waveform files are called EVT files. The time window spans 500 µs both before and after the trigger signal. This allows pulse identity determination to be made during post-processing, while still capturing the other pulses from the event, regardless of the identity of the triggering pulse. The measured maximum drift time in LUX is 320 µs, and is fully encapsulated in the event time window. The EVT files are transferred off-site to the primary data mirror at Brown University, where the files are available for consumption by the collaboration.

A copy of the EVT files is transferred to the Oscar cluster at the Brown University Center for Computing and Visualization [103]. There, the waveforms are passed through a series of software modules which quantify the relevant descriptive qualities of the pulses, e.g. pulse identity, area, height, width, etc. Final decisions regarding the pairing of S1 and S2 pulses are also made, allowing for identification of XYZ position(s) of the event, position-dependent pulse area corrections, and event energy reconstruction. The relevant quantities, known as RQs, are stored in separate files and transferred back to the primary mirror. The author, regretfully citing brevity, refers readers to upcoming LUX publications describing the data analysis pipeline for detailed information on all analysis algorithms. The XY position reconstruction algorithm used for LUX is described in [104].

2.3 LUX Timeline

2.3.1 LUX 0.1

LUX hardware and software development efforts were started in 2007 with the LUX 0.1 program. Results from the program are published in [105], and are covered in detail in [94]. The LUX 0.1 detector was used as a testbed for several different heat exchanger technologies. The detector geometry is shown in Fig. 2.9. The detector used 50 kg of Xe, of which 5 kg filled a fully-instrumented active region. Four R8778 PMTs, identical to those used in LUX, observed the active region, with three tubes at the top (to allow basic position reconstruction) and one on bottom. A 5 cm drift region was established by cathode, gate and anode grids, allowing for generation of S2 signals. The circulation, heat exchange, and purification systems for LUX were deployed for testing in the LUX 0.1 detector. A 230 kg Al displacer mass surrounding the active region was used to approximate the heat load of a full 350 kg Xe payload. The entire assembly sat inside a cryostat identical in dimension to that used on LUX.

The LUX 0.1 program was successful in demonstrating the capabilities of the LUX circulation and purification systems. The LUX heat exchanger was shown to operate at >94% efficiency for heat transfer between incoming and outgoing Xe, while circulating at flow rates of 380 kg day^{-1} (over one LUX Xe payload per day). The circulation and purification resulted in an electron drift length that was measured to be >1 m at 90% confidence level. Purification data are shown in Fig. 2.10. The analysis was performed by direct measurement of S2 size as a function of depth, using a ^{57}Co 122 keV γ source next to the active region. The measurement upper limit is set by the small size of the active region. The LUX 0.1 detector was decommissioned in 2010, in order to support operations at the LUX Surface Facility at SURF.

2.3.2 LUX Surface Facility

The full LUX detector was commissioned at the LUX Surface Facility, commonly referred to in this work and others as the Surface Lab. LUX personnel gained beneficial occupancy

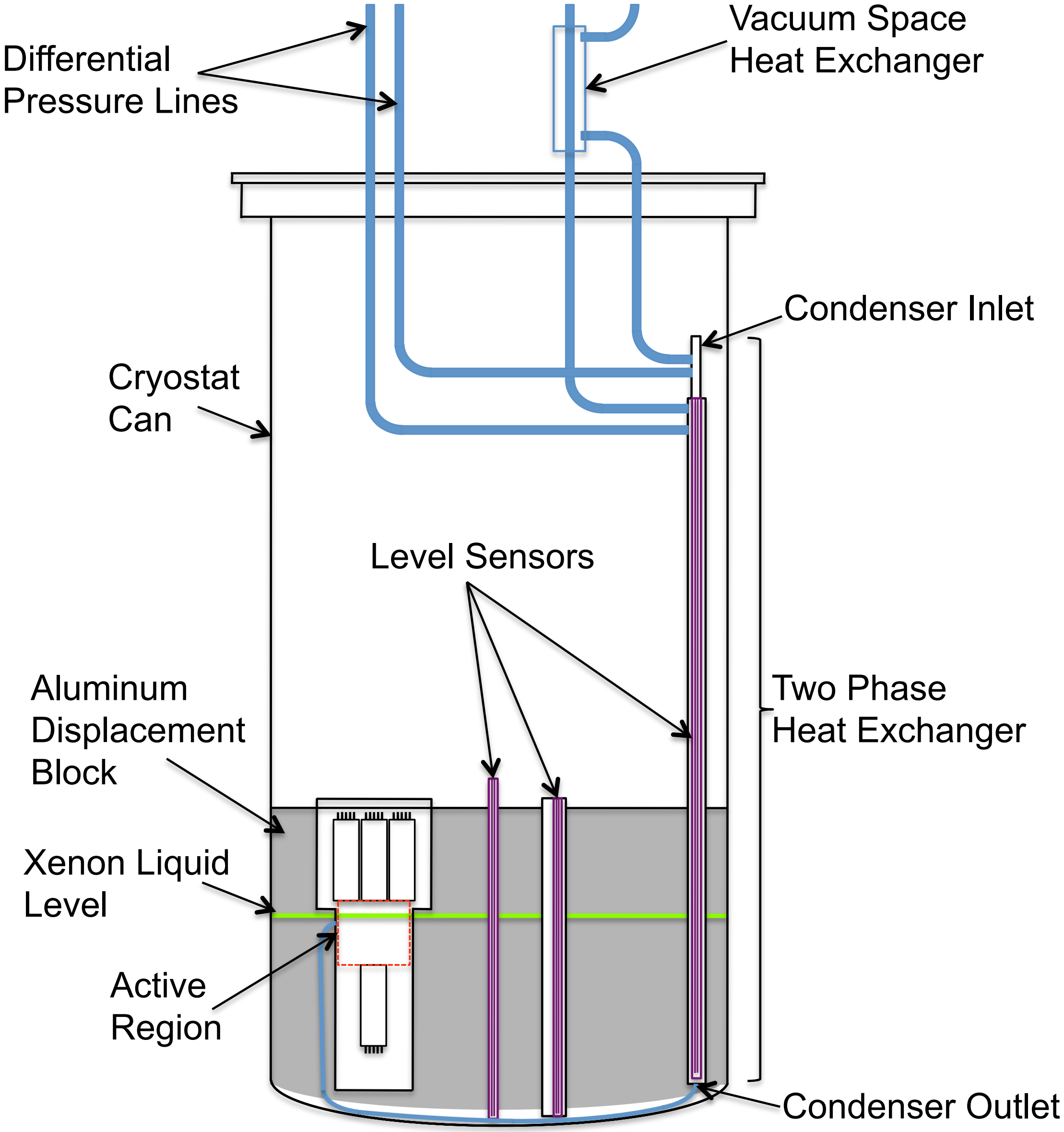
Differential
Pressure Lines
Vacuum Space
Heat Exchanger
Condenser Inlet
Cryostat
Can
Level Sensors
Aluminum
Displacement
Block
Two Phase
Heat Exchanger
Xenon Liquid
Level
Active
Region
Condenser Outlet

Figure 2.9: The LUX 0.1 detector. A 5 kg active region is instrumented by 3 top + 1 bottom R8778 PMTs. The active region is housed in a 230 kg displacer block made of Al, allowing the cryostat to be filled to the target liquid height (green) using only 50 kg of Xe. The liquid height in the detector is monitored by three parallel wire level sensors. The Xe is circulated through two heat exchangers, which were prototyped for deployment in LUX. The figure is taken from Ref. [105].

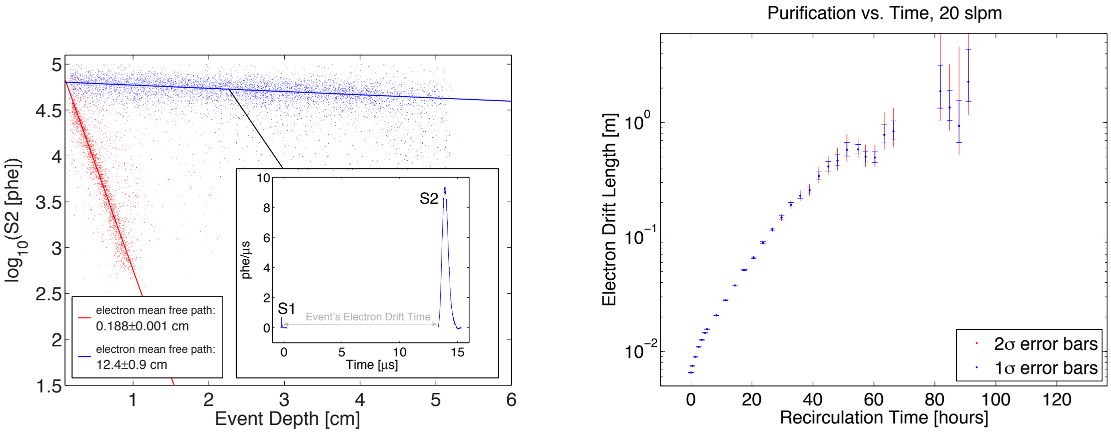

(a)

(b)

Figure 2.10: (a) Measurement of S2 signal size as a function of depth in the LUX 0.1 detector. S2 signals are generated using a ^{57}Co 122 keV γ source, allowing the measured S2 size to map directly to electron drift length. Depth is determined by the S1-S2 timing separation, as described in Sec. 2.2.1. Data are shown from two measurements before (red) and after (blue) an early purification run. The datasets yield electron drift length measurements of 0.188 ± 0.001 cm and 12.4 ± 0.9 cm respectively. (b) Electron drift length in the LUX 0.1 detector, as a function of time. The drift length directly tracks the concentration of electronegative impurities in the active region. Xenon was circulated at 140 kg day^{-1} during the purification run. Figures are taken from [105].

of the Surface Lab in October 2009. The LUX detector underwent construction and two calibration runs at the Surface Lab until February 2012, when Surface Lab operations were discontinued in support of the beginning of operations underground. Technical results from the Surface Lab data runs are published in [106].

The Surface Lab was constructed with a layout closely matching that of the underground laboratory. A schematic is shown in Fig. 2.11. The detector is deployed in a 3 m diameter water tank. Electronics, Xe circulation, and thermosyphon lines are fed through conduits and a tree structure directly above the water tank, on the top floor, as is done for the underground deployment. All electronics are accessed through a breakout cart adjacent to the tree. The detector can be removed from the water tank via crane and transported by rail cart into the clean room for maintenance.

A class 1000 clean room was used during the construction phase of the detector. Personnel were required to fully cover body parts which could potentially contact the detector. Required garb included Tyvek suits, boot covers, double-layered gloves sealed with tape, hair nets, and face masks. This eliminates the introduction of body oils to detector parts during construction, maximizing Xe purification efficiency and reducing potential radioactive contamination.

The Surface Lab water shield was designed to reduce ambient γ and neutron background event rates, enabling the use of γ calibration sources. The requisite water shield thickness was estimated using Geant4-based Monte Carlo, with a 50 cm × 60 cm liquid Xe volume enclosed by 2 cm of Ti. The γ spectrum at the Surface Lab was taken from measurements by LUX collaborators at University of South Dakota. The γ energy spectrum in the detector is shown for several water shield thicknesses in Fig. 2.12. Initial Monte Carlo studies of aboveground backgrounds projected a total detector γ background rate of 10 kHz during liquid Xe operation, with no water shield present. This rate is far too high for LUX data taking, causing virtually 100% event overlap and drowning out any calibration signal from 100 Hz external radioactive sources. Simulation studies predicted a γ background rate reduction of over two orders of magnitude by the use of a 1 m water shield, allowing for a clear signal to be seen from the monoenergetic calibration sources. This prediction was found to be in good agreement with measurements taken during surface running.

The detector was fully commissioned during the aboveground run, beginning with an initial run using argon gas (Run 1), followed by a run with the full 370 kg Xe payload (Run 2). The runs allowed a full characterization of all 122 PMTs, the electronics chain, and the data processing chain. Use of γ calibration sources allowed a measurement of LUX light collection, measured at 8.4 phe $\text{keV}_{\text{ee}}{}^{-1}$ at 662 keV_{ee}. Best-fit results with Monte Carlo studies, combined with separate measurements of S2 light collection, found best-fit agreement with a PTFE reflectivity >95% in liquid Xe. Two species of activated Xe, $^{129\text{m}}$Xe and $^{131\text{m}}$Xe, were also identified due to their homogeneous, monoenergetic signal throughout the active region. Two other species were later discovered in the low-background environment of the Davis Underground Laboratory (Sec. 8.4).

Xenon flow imaging was accomplished by injection of ^{222}Rn into the Xe circulation lines. ^{222}Rn decay is covered in detail in Sec. 5.3.2. 3D imaging of the ^{222}Rn α decay rate over time clearly identified a break in the Xe circulation lines, resulting in the introduction of Xe into the top of the detector, above the two-phase heat exchanger and near the location of the weir. Daughter decay rate ratios reached a steady state after 24 hours, decaying with the ^{222}Rn 3.8 day half-life. The ratios of the daughter decays were well-matched by a model in which the daughters were swept from the active region with a 10 minute time constant. Neutron generation from ^{210}Pb decay (α,n) on PTFE was estimated to generate <3.2 n yr^{-1}, well below the neutron generation rate from the PMTs (Sec. 5.5).

2.3.3 Underground Deployment

LUX was deployed to the Davis Underground Laboratory at SURF beginning in July 2012, with assembly and subsystem tests carried out through February 2013. The underground lab occupies the Davis Cavern, on the 4850 ft level of the former Homestake gold mine. The cavern is named after Raymond Davis Jr, who used the same cavern to deploy the "Homestake experiment" solar neutrino detector in 1970 [107, 108].

The 4850 ft level at SURF affords a factor 4×10^{6} reduction in muon flux relative to sea level [109]. This is essential in attaining low-background detector operations for WIMP search running. The estimated Homestake muon flux is 4.4×10^{-9} cm^{-2} s^{-1}, equivalent to 2 muons week^{-1} passing through the detector.

The detector was readied for liquid Xe running in February 2013, with the first hour of S1-only data taken on February 20 (see Sec. 8.1). S1+S2 running mode was begun a month later. The initial deployment featured frequent use of ER and NR sources for energy calibration and characterization of the detector in low-background running mode. The ER sources included $^{83\mathrm{m}}$Kr and ^{3}H, as well as external ^{137}Cs and ^{228}Th γ sources. NR response was calibrated using an AmBe neutron source. The official start of the WIMP search run was April 22.

2.4 Dark Matter Search

The initial LUX dark matter search, published in [46], is known as Run 3. Run 3 is an 85 liveday non-blind run of the detector. The search is non-blind in that analysis and data quality cuts are developed during the WIMP search run in response to evolving models of detector backgrounds and data artifacts. Non-blind running during initial detector oper-

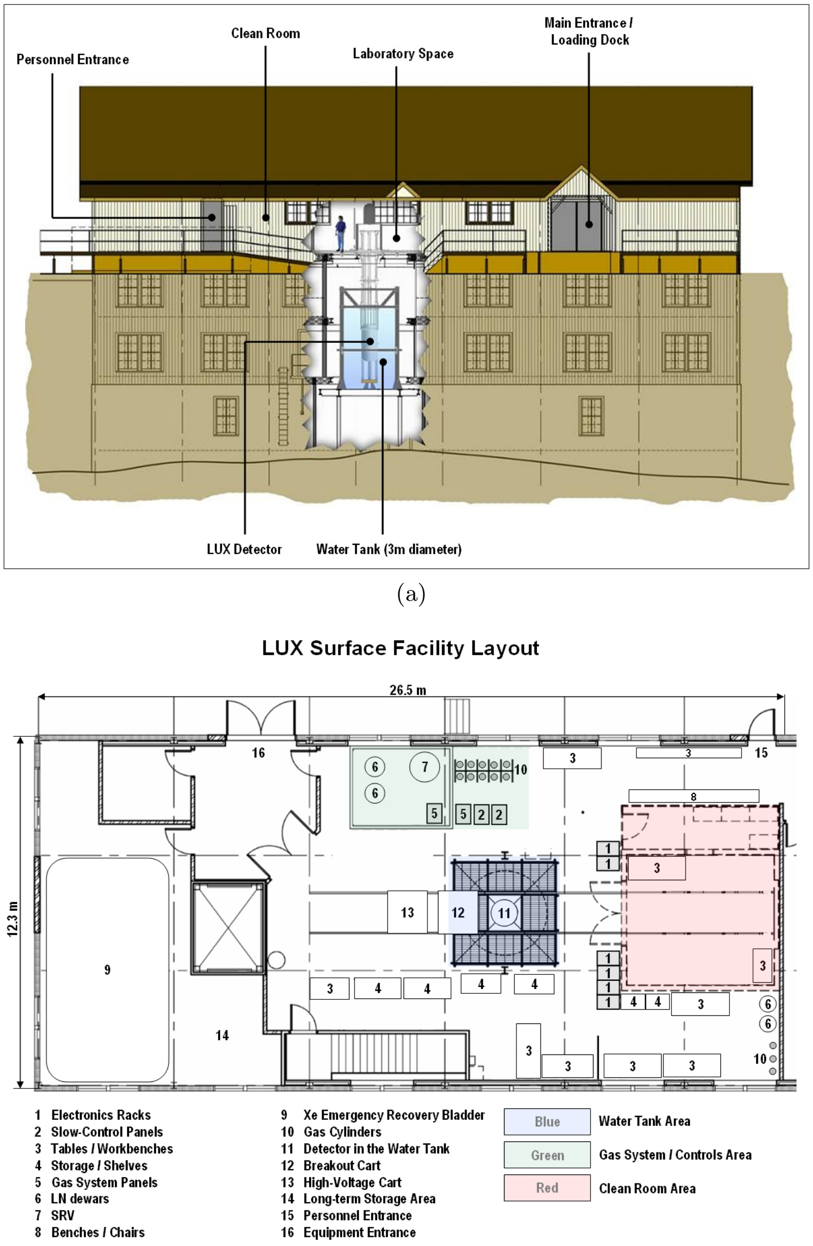
Personnel Entrance
Clean Room
Laboratory Space
Main Entrance / Loading Dock
LUX Detector
Water Tank (3m diameter)
LUX Surface Facility Layout
26.5 m
12.3 m
1 Electronics Racks
2 Slow-Control Panels
3 Tables / Workbenches
4 Storage / Shelves
5 Gas System Panels
6 LN dewars
7 SRV
8 Benches / Chairs
9 Xe Emergency Recovery Bladder
10 Gas Cylinders
11 Detector in the Water Tank
12 Breakout Cart
13 High-Voltage Cart
14 Long-term Storage Area
15 Personnel Entrance
16 Equipment Entrance
Blue Water Tank Area
Green Gas System / Controls Area
Red Clean Room Area

(a)

(b)

Figure 2.11: (a) LUX Surface Lab side profile. The Surface Lab was converted from a warehouse facility at Homestake in 2010. (b) LUX Surface Lab layout. The detector is deployed in a 3 m diameter water tank. The general layout of the Surface Lab closely follows the layout of the underground lab. The relative positions of the detector, water tank, breakout and HV carts, electronics racks, and clean room are the same. The gas system components were shifted to the second level of the underground lab to take advantage of multi-level occupancy.

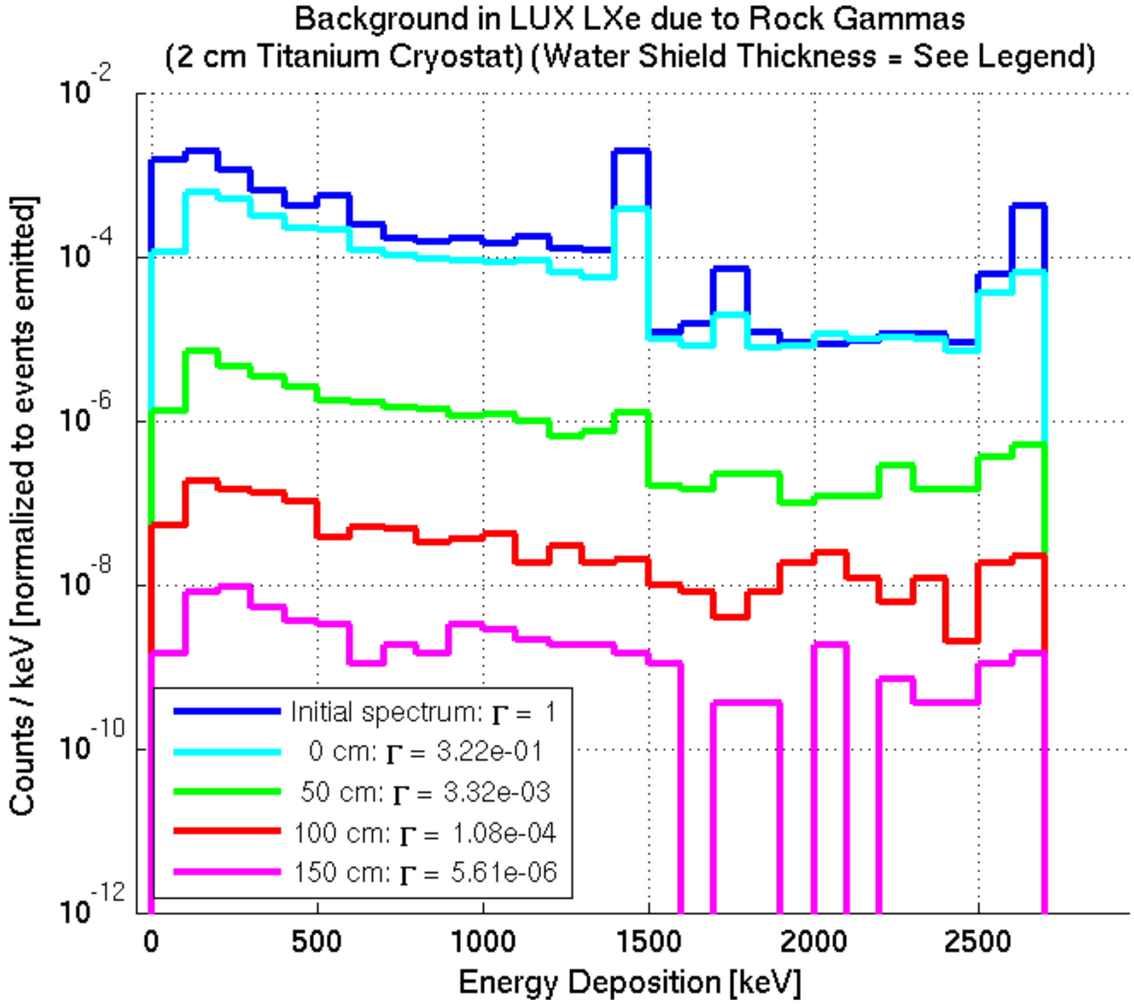

Figure 2.12: Monte Carlo studies of the γ spectrum in the detector as a function of water shield thickness. Spectra are shown corresponding to the initial γ spectrum (blue), the γ spectrum in the active region using no water shield (cyan), and the active region γ spectrum for a 50 cm (green), 1 m (red), and 1.5 m (magenta) thickness water shield. Y axis units are counts $\mathrm{keV_{ee}}^{-1}$ (γ incident at the water tank wall)$^{-1}$.

ation is necessary to characterize the functionality of the detector and accurately model detector backgrounds, before the initiation of a long-duration blind search run. Since the run was non-blind, strong emphasis was placed on minimizing the number of data quality cuts required, thereby minimizing the human bias introduced to the search results. A full discussion of Run 3 analysis results, with particular emphasis on studies pertaining to background modeling, is given in Ch. 8. Dark matter search results from Run 3 are presented in Sec. 8.9.

The ultimate goal of the LUX experiment is to conduct a one year blind WIMP search run [110]. This run will use periodic calibrations during the run, as well as analysis cuts developed during Run 3. Results from Run 3 have been used to great effect in projecting detector performance and backgrounds for the one year run. Background modeling performed for LUX, discussed in Ch. 5, shows that the detector will be able to establish a dark matter limit in 100 kg × one year with <1 WIMP-like low-energy background event expected. LUX will also be capable of reporting a WIMP signal discovery at interaction cross sections that have not been explored at the time of this writing.

Chapter 3

Xenon TPC Optical Modeling

The LUX experiment is able to achieve world-leading dark matter sensitivity in part because of its high light collection efficiency. As discussed in Sec. 1.4, the number of WIMP scatters in the detector falls exponentially as a function of scatter energy, making a low energy threshold crucial for WIMP sensitivity. For this reason, Xe TPCs, and LUX in particular, are constructed using materials known to have high reflectivity to 178 nm Xe scintillation photons [111]. The most common of these materials is polytetrafluoroethylene (PTFE).

This chapter details studies performed to model light collection for the XENON10 detector, a Xe TPC with similar characteristics to LUX, operated by the XENON collaboration at the Gran Sasso laboratory from 2006–2007 [112]. XENON10 modeling compares measured light collection curves with simulation predictions. Curves are matched to data by varying material reflectivity and absorption parameters. This allows for an estimate of the reflectance characteristics of materials used in the experiment. The results are broadly applicable to all Xe TPCs which use similar construction materials, including LUX.

3.1 Xenon TPC Light Collection Model

Several construction aspects of Xe TPCs must be modeled in detail to build a reasonable light collection simulation. Materials used in TPC construction are reviewed in Sec. 2.2. The PTFE reflector panels play the dominant role in light collection efficiency for the experiment. Other materials exposed to the active region play a lesser role in influencing light collection, due to their relatively low surface areas in the active region. These other materials include the electric field grids and PMT windows. The gas-liquid interface reflects a significant fraction of light generated in the liquid target, preventing the photons from reaching the top PMT array and increasing their path length in the detector. Photons also elastically scatter in the Xe, or are absorbed by impurities in the Xe, creating finite scattering and absorption mean free paths. Each of these effects is discussed in detail below.

An understanding of the photon collection efficiencies of the PMTs themselves is required in order to set an absolute light collection scale from simulation data. PMT detective efficiency (D) is determined primarily by the quantum efficiency (QE) of the photocathode, and is influenced to second order by photoelectron collection efficiency and performance variation with temperature. A clear definition of these efficiencies and a detailed model of their behaviors is given in Sec. 3.1.7.

3.1.1 PTFE Reflectors

Xenon TPCs typically bound the active Xe volume with PTFE paneling. This reflector maximizes the amount of S1 and S2 light detected from an event in the active region. The reflector also shields the active region from external photons, which may be generated from energy depositions in pockets of "dead" (uninstrumented) Xe or in other detector materials. For an idealized Xe detector surrounded in 4π by reflector material, use of a high-reflectivity reflector material can increase the amount of light collected from an S1 event by up to $\times 5$, independent of detector mass. Light collection as a function of PTFE reflectivity for the ideal detector is shown in Fig. 3.1.

PTFE is generally modeled with zero specular reflectivity, due to its rough microfaceted surface composition [113]. The roughness of the surface suggests that PTFE should act as a highly Lambertian reflector, meaning that photons are reflected at angle θ_R with probability $\propto \cos(\theta_R)$. For the optical simulations in this note, PTFE is given this reflectivity characteristic. Measurements performed on PTFE in Xe gas indicate a more detailed model for PTFE reflection, involving non-zero specular lobe and spike constants [114]. The specular components are estimated to become dominant at angles of incidence on the PTFE

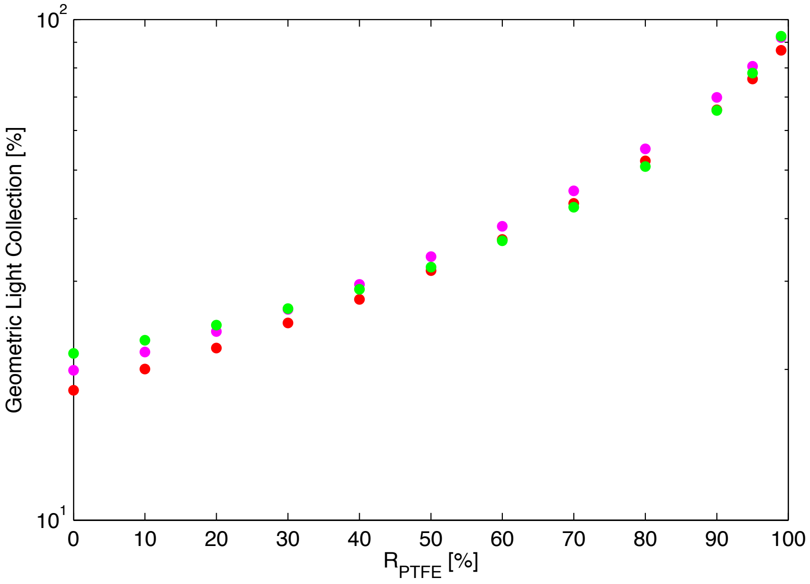

Figure 3.1: Simulation of the fraction of photons detected, averaged over the full liquid Xe volume, as a function of PTFE reflectivity for TPCs of mass 13.5kg (red), 350 kg (magenta) and 20 tonnes (green). No grids are used, and light is collected from 100% absorbing end caps. Full active region coverage by PTFE is assumed. The detector aspect ratio is 0.9. The Rayleigh scattering length is 30 cm, and the absorption mean free path is infinite. Simulation is based on Geant4 [115].

which are >65°. The impact of using a specular or diffuse reflection model is negligible, as discussed in Sec. 3.3.3.

3.1.2 Electric Field Grids

Electric field grids are typically strung wire or mesh designs with steel construction, as used in the XENON and LUX detectors. Stainless steel reflectivity is not well measured in Xe, with one reported measurement of ∼60% in vacuum [116]. During construction, the grids are chosen to have the smallest wire diameter and largest wire spacing possible, while maintaining a uniform electric field for position-independent electron drift. This maximizes the grid transparency to scintillation photons, independent of considerations of photon reflection from the grid wires. Transparency without consideration of reflection is referred to in this work as “geometric transparency.”

Previous Xe TPC optical simulations have assumed a semi-transparent “wafer” approximation to model the effects of the electric field grids on incident photons [117]. The wafer assumed a transparency calculated from the geometric transparency of the grid at 0° angle of incidence with respect to the normal of the grid plane. This approximation is flawed, in that this model ignores both the transparency dependence on photon angle-of-incidence and the reflectivity characteristics of the grid wires.

Due to the finite wire diameter, geometric transparency varies with photon angle of incidence. The geometric transparency is calculated as

$$\begin{aligned} T_{strung} &= \frac{l_{space} \cdot \cos(\theta) - l_{dia}}{l_{space} \cdot \cos(\theta)}, \\ T_{mesh} &= \frac{\left(l_{space} \cdot \cos(\theta) - l_{dia}\right)\left(l_{space} - l_{dia}\right)}{l_{space}^2 \cdot \cos(\theta)}, \end{aligned}$$

where l_{dia} is the grid wire diameter, l_{space} is the separation between grid wires (measured between the wire centers), and θ is the incident angle of the photon, where 0° is normal to the plane of the grid. T_{strung} is for a strung grid, where the wires run parallel in one dimension only. T_{mesh} is for a mesh grid, where the wires run in two dimensions and intersect at 90° angles. As photon angle of incidence increases, grid geometric transparency decreases. The decrease of geometric transparency increases the importance of grid material reflectivity in the light collection model. Geometric transparency as a function of angle for both grid types is shown in Fig. 3.2.

3.1.3 Gas-Liquid Boundary Refraction and Reflection

The change in refractive index between gas and liquid Xe volumes results in refraction and reflection of photons encountering the gas-liquid boundary. The refractive index of liquid Xe is a sensitive function of energy, and at Xe scintillation energies (7 eV) has been reported as $n = 1.69 \pm 0.02$ [118]. This index results in a critical angle $\theta_c = 36°$ at the gas-liquid boundary. Light incident on the boundary with $\theta_i > 36°$ will be reflected downward toward the PTFE, liquid phase grids, and bottom PMT array, creating further sensitivity of light collection to the reflectance characteristics of these components. Reflection at the boundary also significantly influences the ratio of light collected on the top and bottom arrays, which is a crucial parameter in reflectance studies.

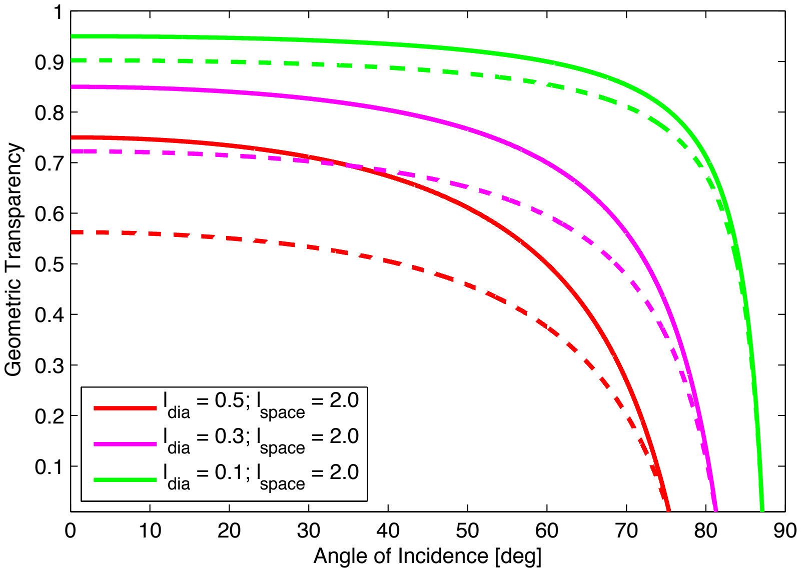

Figure 3.2: Grid geometric transparency as a function of photon angle of incidence, where 0° is normal to the grid plane. Curves are shown for strung (solid) and mesh (dashed) grids. l_{dia} and l_{space} are given in arbitrary units.

3.1.4 Xenon Rayleigh Scattering Length

Scintillation photons undergo elastic (Rayleigh) scattering within the liquid Xe volume. The photons change direction by $\Delta\theta$, with probability $P(\Delta\theta) \propto 1 + \cos^2(\theta)$. The characteristic length λ_R for this scattering process is a function of $\lambda_s^{-4}((n^2-1)(n^2+2))^2$, where n is the refractive index and λ_s is the Xe scintillation light wavelength [119]. The scattering length is therefore extremely sensitive to the refractive index of the material. λ_R has been calculated to be 30 cm and is measured as 29 ± 2 cm [83, 84]. These values are averaged over the Xe scintillation spectrum, shown in Fig. 3.3a. In optical simulations, $\lambda_R = 30$ cm is used.

For a liquid Xe TPC of order 10 kg or larger, typical track lengths for optical photons exceed λ_R. A significant fraction of photons will undergo one or more Rayleigh scatters in larger detectors. The scattered photons have an increased path through the detector, and become more likely to interact with construction materials lining the active region.

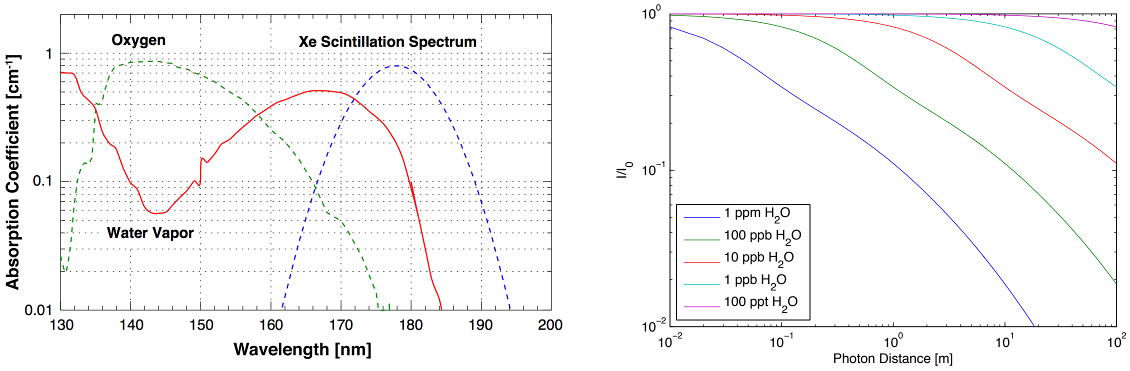

(a) (b)

Figure 3.3: (a) Absorption spectra for O_2 and H_2O molecules (1 ppm concentration) at UV wavelengths, taken from Ref. [82]. The Xe scintillation spectrum is superposed. Y-axis units are corrected from [m^{-1}] to [cm^{-1}] from the original paper after correspondance with the author. (b) Calculated absorption lengths for scintillation photons using the spectra from (a). Absorption as a function of distance is shown over five orders of magnitude of H_2O concentration.

3.1.5 Xenon Scintillation Photon Absorption Length

Pure Xe is believed to have an extremely long characteristic length associated with absorption of scintillation photons (λ_a), as the first free exciton absorption band is 10.3 eV and the scintillation photon energy is narrowly peaked at 7 eV [82, 120]. However, UV-opaque impurities are known to exist in commercial Xe gases, particularly O_2 and H_2O molecules left from the distillation process during Xe production. These molecules can significantly limit Xe photoconductivity. The absorption spectra of O_2 and H_2O, as well as the Xe scintillation photon attenuation curves as a function of H_2O concentration, are shown in Fig. 3.3. It is believed that current purification technology is sufficient to remove these impurities to concentrations <1 ppb H_2O and O_2 [101]. In the optical simulations described in this work, λ_a is taken to be much larger than the mean free path of optical photons in the modeled detectors, and is taken to infinity unless stated otherwise.

3.1.6 PMT Windows

PMTs used in liquid Xe detectors typically employ windows constructed from quartz (SiO_2) [121]. Quartz is chosen for its high transmissivity of VUV photons. This allows the photocathode material to be deposited on the inside of the window, protecting it from physical degradation. The refractive index of fused silica quartz is measured as 1.57 at 190 nm [122]. The value is less than that of liquid Xe. This results in a critical angle between liquid Xe and PMT windows of $\theta_c = 68°$. The diffuse photon wash created by PTFE and grid reflections accentuate the importance of factoring this extra reflection into simulations.

3.1.7 PMT Detective Efficiency

It is important to be clear on the various definitions of PMT detection efficiencies. A thorough discussion on PMT efficiencies and measurements is given in [94]. PMT detective efficiency D is defined as

$$D = QE \cdot CE \cdot H\left(T\right). \tag{3.1}$$

The PMT quantum efficiency QE is defined as the probability for a photon which is incident at the PMT front face to be converted into a photoelectron (phe). QE is determined by the photocathode material, and is wavelength- and angle-dependent. Further discussion on QE is given in the following subsections. The QE term is the dominant efficiency factor contributing to D, and to first order the other contributing terms can be neglected. QE is defined at room temperature, unless stated otherwise.

The PMT collection efficiency CE is defined as the probability for a phe generated at the photocathode to reach the first dynode stage of the PMT. This term is dependent on the PMT bias, and is flat within the range of biases used for standard PMT operation. $H\left(T\right)$ is a temperature-dependent efficiency gain from operating the PMTs at $-100°$C liquid Xe temperatures, measured relative to the efficiency at room temperature. CE and $H\left(T\right)$ are both of order 10% variations and largely cancel each other, contributing to the dominance of the QE term in Eq. 3.1.

3.1.7.1 Definition of Quantum Efficiency

The Hamamatsu definition of QE is the efficiency with which a photon incident on the PMT quartz face (at 0° angle of incidence) is converted into a phe. At Xe scintillation light wavelengths, typical PMT QE measurements (as defined by Hamamatsu) range from 25%–35% [121]. XENON10 Hamamatsu R8520 PMTs were measured to have an average QE of 24% [123]. LUX R8778 PMTs were measured to have an average 33% QE [94]. These values are used in simulation modeling.

It must be made clear that the Hamamatsu QE definition includes the probability of a photon being successfully transmitted across the quartz window to reach the photocathode, as well as the probability of conversion of the photon into a phe. It does not, however, include the probability of measuring the resulting phe; this is captured by CE. This definition is incompatible with a simple multiplication of Monte Carlo results, as the Monte Carlo also includes the effects of photons being transmitted through the quartz window. Multiplication of simulation results by the Hamamatsu QE definition double-counts the probability of photon transmission through the PMT window. The simulation must include the probability of photon transmission through the window, as this is an angle-dependent quantity. A redefinition of QE is therefore required for compatibility with simulation results.

For this work, QE_{sim} is defined to be the Hamamatsu-measured QE divided by the probability of photon transmission at the quartz window at 0° incidence. The definition of QE_{sim} is the probability of a photon which has been transmitted through the glass being converted into a phe, which is suitable for multiplication with simulation results. Additional factors, including CE, are also separately included.

3.1.7.2 Variation of QE with Angle

Measurements of PMT QE show a dependence on photon incidence angle [121]. PMT QE varies due to the apparent increase in photocathode thickness at nonzero angles of incidence. For a photon incident on an infinite-plane photocathode, the QE should be a function of $\cos(\theta)$, as illustrated in Fig. 3.4. Hamamatsu test data for PMT response as a function of angle is not available for LUX R8778 PMTs, but is available for the R550 PMT. The R550 PMT is a 5 cm diameter tube, with similar physical characteristics to the R8778 used in LUX, but a lower nominal gain (7×10^5) and a minimum detected wavelength of 300 nm.

The R550 PMT signal response as a function of angle is shown in Fig. 3.5a [121]. The measurement is performed using a wide 600 nm wavelength beam illuminating the PMT face. As the PMT is rotated, the effective area of the photocathode is reduced by $\cos(\theta)$. For a “flat” QE, PMT output should closely follow this curve. The data points deviate significantly from the simple $\cos(\theta)$ model, showing a QE enhancement as a function of angle.

QE as a function of photon incidence angle follows Eq. 3.2 below. The functional form of QE with incidence angle is derived based on two parameters: the probability of the photocathode absorbing a photon which is traversing its length, and the probability of an absorbed photon in the photocathode becoming a phe. The model must break these two probabilities apart, since both quantities are unknown, and they influence the model differently.

QE as a function of angle is expressed as

$$QE_{sim}(\theta) = \frac{QE_{sim,0}}{QE_{sim,0} + P_{loss,0}} \times \left(1 - (1 - P_{loss,0} - QE_{sim,0})^{1/\cos(\theta)}\right). \tag{3.2}$$

For a photocathode thickness δ, the photon transmission probability is $T = 1 - P_{abs} = 1 - P_{phe} - P_{loss}$, where P_{abs} is the probability for a photon to be absorbed in length δ, P_{phe} is the probability for an absorbed photon to convert into a phe, and P_{loss} is the probability of any other conversion type after absorption. (Note that, at 0° angle of incidence, $P_{phe} = QE_{sim}$.) For a photon incident at the photocathode at angle θ from the normal (see Fig. 3.4), the zero-angle transmission probability is multiplied a number of times ϵ/δ, where $\epsilon = \delta/\cos(\theta)$ is the apparent thickness of the photocathode. The probability of transmission of the photon is then $T(\theta) = (1 - P_{abs,0})^{\epsilon/\delta} = (1 - P_{loss,0} - QE_{sim,0})^{1/\cos(\theta)}$, where the 0 subscript represents 0° angle of incidence. The absorption probability is $P_{abs}(\theta) = 1 - T(\theta)$. The absorption probability is then multiplied by the probability of an absorbed photon producing a phe, equal to $P(phe|abs) = P(abs|phe)\,P(phe)/P(abs) = P_{phe}/P_{abs}$ $= QE_{sim,0}/(QE_{sim,0} + P_{loss,0})$, to yield Eq. 3.2.

As an example, the value of $P_{loss,0}$ for the R550 multialkali photocathode, at 600 nm, can be estimated from Fig. 3.5. The predicted output curve for the R550 can be computed using Eq. 3.2 and the average measured R550 QE at 600 nm of 6.5% [124]. A best-fit curve is computed by multiplying Eq. 3.2 by the $\cos(\theta)$ photocathode area dependence term, as

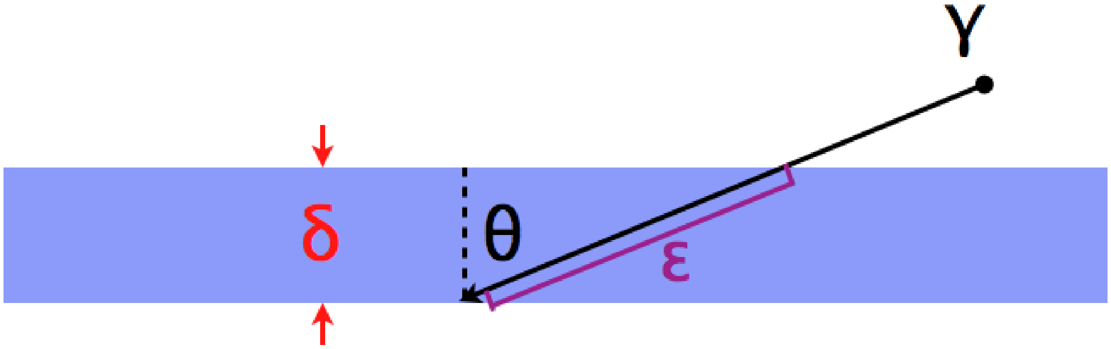

Figure 3.4: Illustration of the angular dependence of PMT QE. The apparent photocathode thickness is enhanced by ϵ/δ=$1/\cos(\theta)$, where θ is the angle of incidence relative to the photocathode normal. Given a probability T of the photon transmitting through the layer at 0° incidence, the probability of photon transmission through the layer at angle θ is $T(\theta) = T_0^{\epsilon/\delta} = T_0^{1/\cos(\theta)}$.

well as the Fresnel reflection coefficient for photons reflecting off of the PMT window. The best-fit parameter yields an estimate of $P_{loss,0} = 0.26$ with fitting results shown in Fig. 3.5b.

The value of $P_{loss,0}$ was not measured by Hamamatsu for the R8520 or R8778. The measurement taken from Hamamatsu test data for the R550 PMT is taken for a different photocathode type, at a much longer wavelength than Xe scintillation light. It is unreasonable to apply this same factor to the R8520 or R8778 PMTs for 178 nm wavelength photons. QE dependence on angle is not incorporated into simulations for XENON10 data. For LUX modeling, the impact on QE from variation of the $P_{loss,0}$ parameter is shown in Fig. 3.6. $P_{loss,0}$ is varied from 0–65%, where 0% corresponds to QE dependent only on the probability of a photon absorbing at the photocathode, and 65% corresponds to the maximum possible value (corresponding to a QE independent of incidence angle, meaning that no photons are transmitted through the photocathode at 0° incidence). Tests performed by LUX collaborators at LIP Coimbra were used to back out the estimated value of $P_{loss,0}$ in Sec. 3.3.4.2.

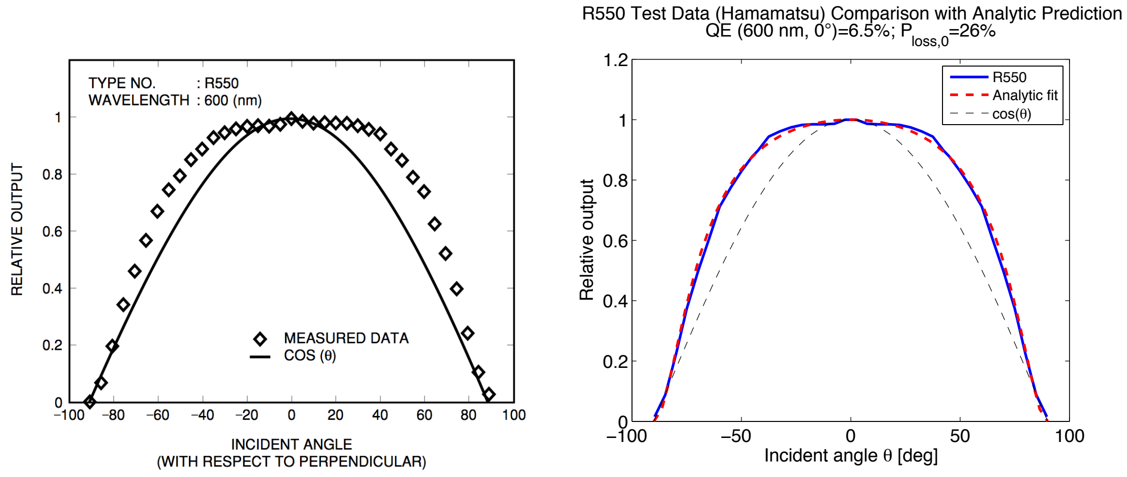

(a)

(b)

Figure 3.5: PMT QE vs. photon angle of incidence θ for the Hamamatsu R550 PMT [124]. The angle θ is defined relative to the PMT face normal. (a) Hamamatsu test data. Data was collected by rotating a test PMT through a wide 600 nm beam. Figure is taken from Ref. [121]. (b) Best-fit analytic curve given by Eq. 3.2, multiplied by $\cos(\theta)$ and window reflection terms (red dashed). Hamamatsu data (blue) is averaged about $\theta = 0°$. Best-fit results yield a value of $P_{loss,0} = 26\%$. Shown for comparison is a $\cos(\theta)$ dependence curve (black dashed), corresponding to QE independent of incidence angle.

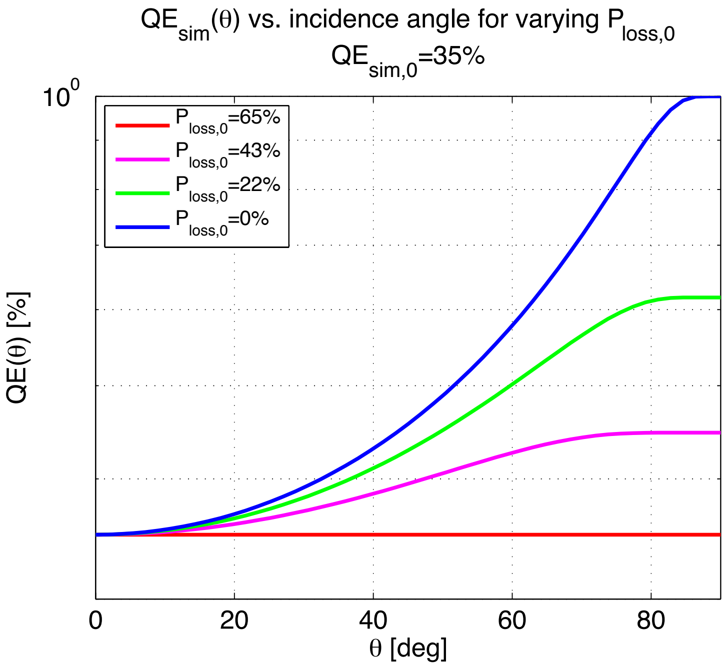

Figure 3.6: Angular dependence (with respect to PMT face normal) of R8778 QE, calculated from Eq. 3.2. $QE_{sim}(0°)$ is set to the standard LUX R8778 value of 35%. $P_{loss,0}$ is varied over the full allowed range of values, 0–65%.

3.2 Fitting XENON10 Data

Before the beginning of LUX construction, existing Xe TPC data was used to try to constrain the range of reflectivity values of PTFE and other common detector materials in liquid Xe. Studies of PTFE reflectivity and its effects on light collection were used to inform LUX and LZ detector designs. The study data was taken from the XENON10 experiment. XENON10 is a liquid Xe TPC, featuring a 13.5 kg active region and 5.4 kg fiducial volume. The construction of XENON10 is similar to that of LUX, where PTFE is used to line the active region, and stainless steel electric field grids are present at the top and bottom of the active region. This section details the use of XENON10 calibration data and Monte Carlo simulations to find the reflectances of PTFE and stainless steel at 178 nm in liquid Xe.

3.2.1 Methodology

Monte Carlo simulations of scintillation photon collection efficiency were performed using a Geant4-based representation of the XENON10 detector. The simulation featured a faithful recreation of the XENON10 geometry, based on CAD drawings, and included all materials adjacent to the active region. The XENON10 geometry and data used in this study are documented in [123].

The sensitivity of event light collection to Z position and PTFE reflectivity is sketched in Fig. 3.7. The Z coordinate is defined such that Z increases when moving from the bottom PMT array toward the liquid surface. An event very near the bottom of the liquid Xe volume will deposit ∼50% of its S1 signal in the bottom PMT array immediately. Of the up-going light, a fraction will encounter the PTFE panels, and the remainder will encounter the gas-liquid interface. Of the light encountering the interface, there are a further three populations: photons which encounter the top PMTs; photons which are refracted outward and away from the top PMTs; and photons which are reflected back into the liquid volume. A large fraction of the photons in this latter population will encounter the PTFE reflector in the liquid volume, and be scattered at random angles. As event height increases, the light collected by the bottom (top) PMT array goes as Z^{-2} (Z^{2}), with an offset from a

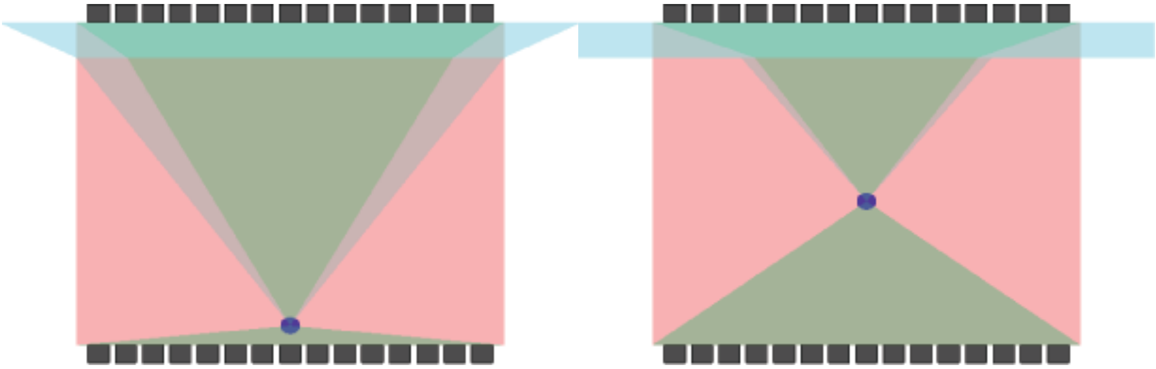

Figure 3.7: Illustration of variation in light collection for top and bottom PMT arrays (black squares) with increasing event height. Light reaching the PMT arrays is shown in green. Light which escapes from the detector is shown in blue. Light reaching the PTFE reflector is shown in red.

diffuse photon population which has reflected off of detector materials.

In the limit of very poor PTFE reflectivity, the light collected at the bottom PMT array primarily comes directly from the event site, without having scattered from detector materials. The light collection curve as a function of height is therefore a function of Z^{-2}. In the limit of very high PTFE reflectivity, photons encountering the PTFE reflector are recycled back into the active volume, independent of event height. The fraction of recycled photons collected by the PMTs is largely independent of event height. The slopes of the light collection curves as a function of height in the high PTFE reflectivity limit are therefore much flatter than the simple Z^2 case.

Slope changes with event height for the top and bottom PMT array light collection curves are of great importance for reflectivity matching. The slope changes are independent of the assumed absolute photon yield from energy depositions in the Xe, and are solely a function of reflectivity and path length parameters. Absolute scaling matches between simulations and detector data can be made by estimating the efficiencies of the PMTs, and estimating the absolute scintillation photon yield in liquid Xe.

3.2.2 Scaling Factor Calculations

To match the absolute light collection values calculated from simulation and measured data, a scaling factor is required which converts energy deposition into a measured number of phe. This scaling factor is

$$N\left(\frac{phe}{keV_{ee}}\right) = \sum_i A_i \cdot G_i\left(\vec{x}\right), \tag{3.3}$$

where N is the number of phe generated per $\mathrm{keV_{ee}}$ energy deposited. $G_i\left(\vec{x}\right)$ is the geometric collection efficiency for PMT i, which is calculated by Monte Carlo. $G_i\left(\vec{x}\right)$ is defined as the probability for a photon emitted at position $\vec{x}$ to encounter the photocathode of PMT i (not including QE). The detector geometric collection efficiency is defined as $G\left(\vec{x}\right) \equiv \sum_i G_i\left(\vec{x}\right)$.

The term A_i rolls in all effects which are not accounted for in the Monte Carlo, and are used to scale between the simulation and measured data. A_i is expressed as

$$A_i = \frac{QF\left(\varepsilon\right) \cdot D_i}{w_\nu\left(E\right)}. \tag{3.4}$$

$w_\nu\left(E\right)$ is the average energy required to generate a scintillation photon at zero electric field, as a function of energy deposition E; QF is the quenching factor, which is the scintillation efficiency of an energy deposition at electric field ε relative to zero field; and D_i is the detective efficiency of PMT i, given by Eq. 3.1.

It is important to note that w_ν is different from W as defined in Sec. 2.1.2. W is the average energy required to produce either an ion or exciton in liquid Xe, yielding either a scintillation photon or ionization electron. w_ν is the average energy required to produce a scintillation photon in liquid Xe: $w_\nu\left(E\right) = \langle E/n_\nu\left(E\right)\rangle$.

$w_\nu\left(E\right)$ was directly estimated from measured XENON10 data for 164 $\mathrm{keV_{ee}}$ energy depositions. The value of w_ν for generation of a photon at 122 $\mathrm{keV_{ee}}$ has been measured as 15.2 ± 0.3 eV [125]. For photon generation at 164 $\mathrm{keV_{ee}}$, the work function is calculated based on the relative measured XENON10 light yields at 164 $\mathrm{keV_{ee}}$ and 122 $\mathrm{keV_{ee}}$ [123]. The estimate of w_ν at 164 $\mathrm{keV_{ee}}$ is 16.6 ± 1.2 eV. $QF\left(\varepsilon\right)$ is taken from measurements of ER scintillation yield as a function of electric field published in [126]. At the XENON10 operating field of 0.73 kV $\mathrm{cm^{-1}}$, $QF = 0.53 \pm 0.02$.

The terms listed above create a single scaling factor between photon generation and signal detection, with uncertainties propagated from the constituent terms. Average values for each term are listed in Table 3.1. These values result in an average collection efficiency factor $\langle A_i\rangle$ of 0.0065 ± 0.0009 $\mathrm{eV^{-1}}$.

Term	Value
w_ν (164 $\mathrm{keV_{ee}}$)	16.6 ± 1.2 eV [89, 123]
QF (0.73 kV/cm)	0.53 ± 0.02 [126]
$\langle QE_i \rangle$	0.237 ± 0.019 [123]
CE	0.75 ± 0.05 [123]
H_T	1.15 ± 0.03 [123]
$\langle A_i \rangle$	0.0065 ± 0.0009 $\mathrm{eV^{-1}}$

Table 3.1: Average values for the efficiency terms used in Eq. 3.1.

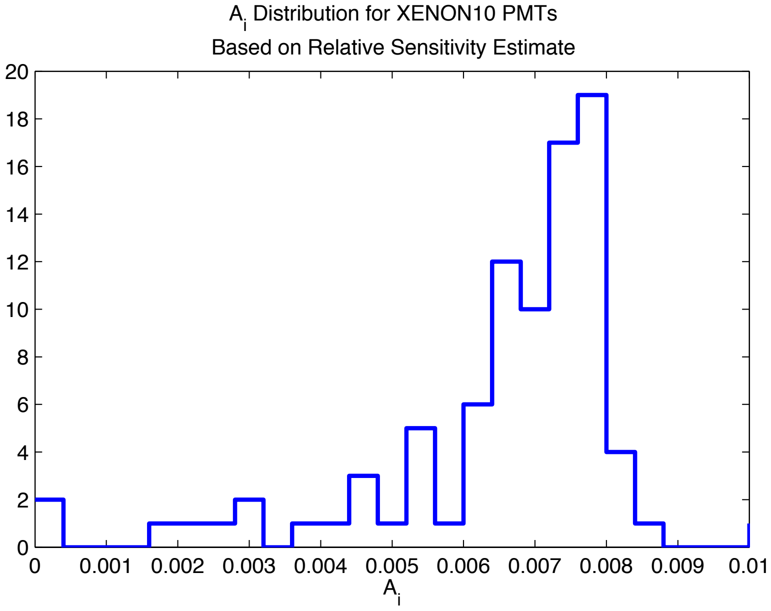

Figure 3.8: A_i distribution for XENON10 R8520 PMTs, estimated using relative sensitivity measurements from [123]. Values are used for calculation of simulation scaling factors in Eq. 3.1.

For comparison of simulation results with detector data, PMT D values are individually estimated based on relative sensitivity maps created for XENON10 [123]. These relative efficiency fractions are then multiplied by $\langle D \rangle$ to obtain individual models for A_i. The distribution of the final A_i values is shown in Fig. 3.8.

3.2.3 Results

The XENON10 Monte Carlo simulation was run over a grid of PTFE reflectivity (R_{PTFE}) and electric field grid reflectivity (R_{grid}) values. Simulated geometric collection efficiency curves for each R_{PTFE}-R_{grid} dataset are scaled by Eq. 3.4, and the p value of the χ^2 score is computed for each dataset. The top five results with the highest p values are shown in

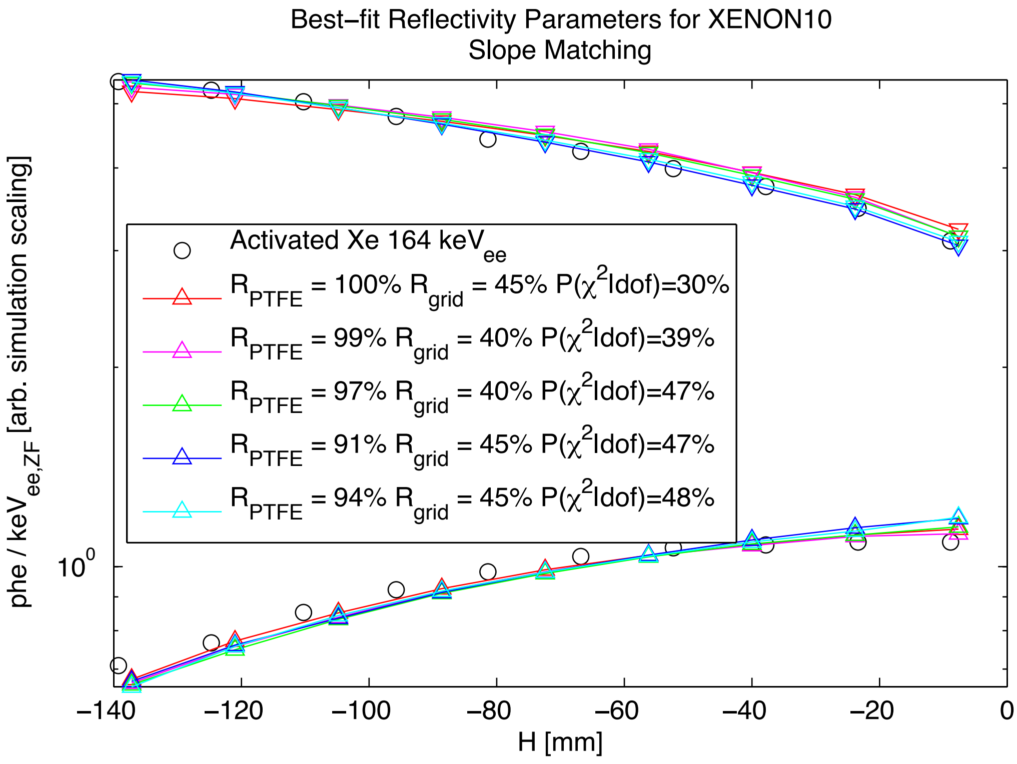

Figure 3.9: Five closest simulation matches to XENON10 light collection data, and corresponding simulation reflectance parameters. The X axis is given in units of height (labeled H, corresponding to Z in Sec. 3.2.1). $H = 0$ mm corresponds to the liquid Xe surface. Upward (downward) arrows correspond to light collection at the top (bottom) PMT array. Measured data is taken from the homogeneous ^{131m}Xe 164 keV$_{ee}$ line. Simulation data is shown with best-fit arbitrary scaling, before scaling with Eq. 3.4.

Fig. 3.9. The χ^2 distribution of the R$_{PTFE}$-R$_{grid}$ space is shown in Fig. 3.10. The contour in (R_{PTFE}, R_{grid}) space is centered at $R_{PTFE} \to 100\%$, and shows consistency with measured data for $R_{PTFE} > 95\%$. The lower-limit measurement is in agreement with Ref. [127]. The most likely value for R_{grid} is found to be $45 \pm 5\%$, lower than the measurement (with unquoted error) reported in Ref. [116].

A brief investigation was made into incorporating absorption effects into the XENON10 optical model. The light collection curves asymptote at $\lambda_a > 2$ m, as shown in Fig. 3.11. The χ^2 fit values show significant deterioration for $\lambda_a < 2$ m. It is assumed that for XENON10 $\lambda_a \gg 2$ m, based on projected performance of the XENON10 purification system and the photon mean free paths computed from Fig. 3.3b.

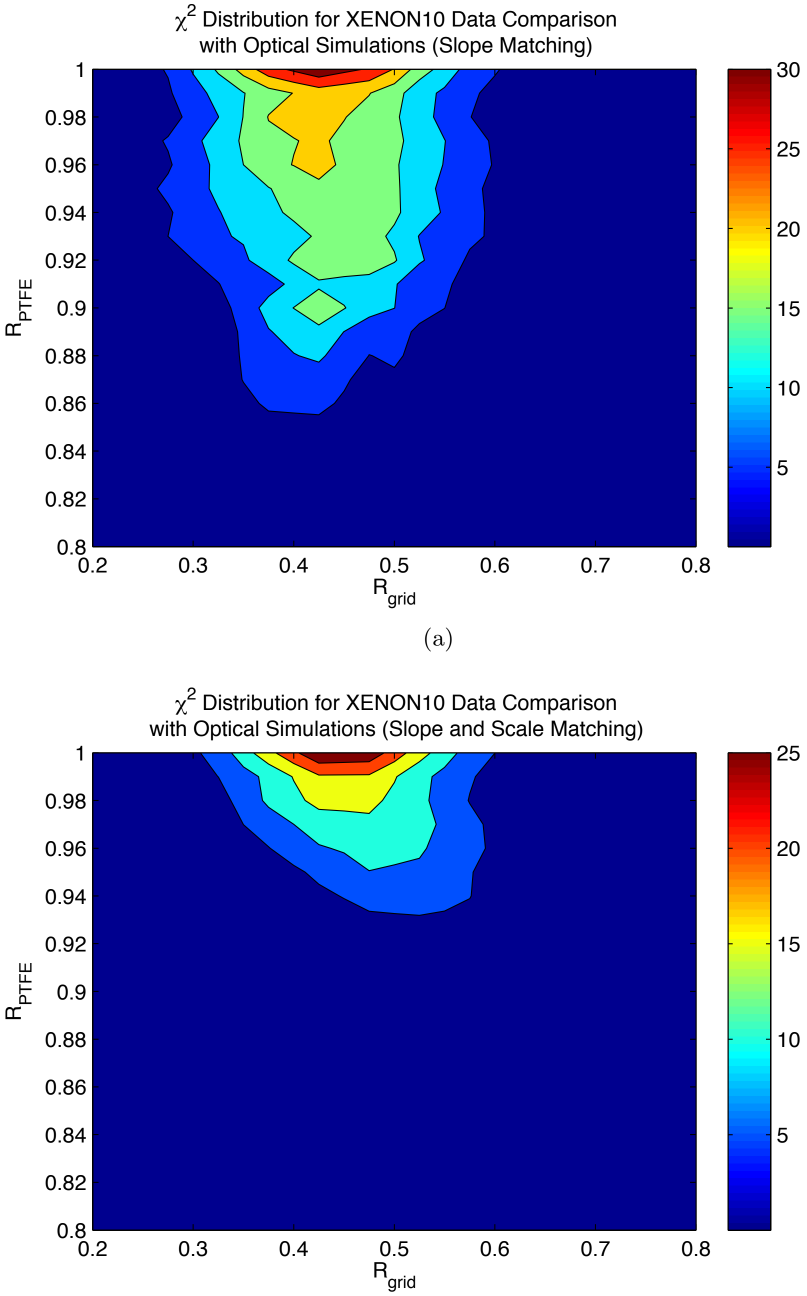

(a)

(b)

Figure 3.10: χ^2 probability distributions for XENON10 data matching in R_{PTFE}-R_{grid} space, using fixed optical parameters from Sec. 3.1. Color values are the χ^2/DOF p value in percentage units. (a) Distribution for arbitrary simulation scaling, matching only the slopes and relative separations of the top and bottom PMT array G curves. (b) Distribution using Eq. 3.4 to calculate the absolute simulation scaling factors.

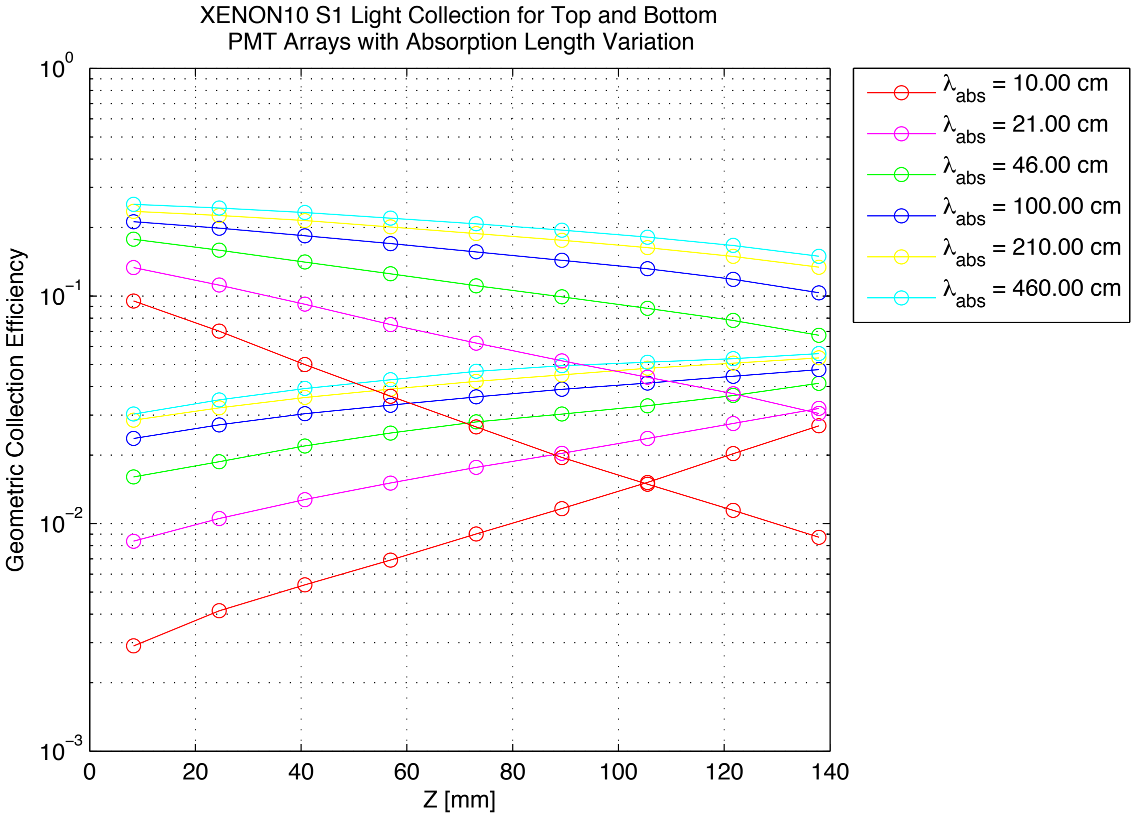

Figure 3.11: Geometric collection efficiency G as a function of height for varying photon absorption length λ_a (labeled in the plot as λ_{abs}). Curves with high (low) collection efficiency at $Z = 10$ mm correspond to collection at the bottom (top) PMT array. The expected value of λ_a is $\gg$2 m. All XENON10 data fitting attempts use $\lambda_a \to \infty$. The simulation which begets the curves holds reflectivity values constant at $R_{PTFE} = 100\%$, $R_{grid} = 45\%$.

3.3 Predicting LUX Light Collection

LUX light collection was modeled using the Geant4-based LUXSim Monte Carlo package, described in Sec. 5.2 [128]. LUXSim features a precise replication of all significant detector components, including all Xe TPC characteristics outlined in Sec. 3.1. Optical photons were generated homogeneously within the simulated active region, and given random isotropic directions. Light collection is averaged across XY for all Z bins. Studies of detector light collection efficiency were performed by varying PTFE and electric field grid reflectivities, as done for XENON10 data matching (Sec. 3.2).

Results of comparisons of average LUX light collection with model predictions are discussed in Sec. 8.2. Light collection values measured from WIMP search data are consistent with 100% PTFE reflectivity. The studies in this section were used for projections of LUX light collection, before detector data was available. These studies have since been superceded by more detailed models, using in-situ measured LUX PMT efficiencies and light collection curves. The updated studies will be available in upcoming LUX publications.

3.3.1 Geometric Collection Efficiency for Varying PTFE Reflectivities

Detailed studies of PTFE reflectance indicate a significant difference in PTFE reflectivity between gas and liquid Xe media [113]. To accommodate this effect, and to remain agnostic about the reflectivity values for LUX construction materials, LUX PTFE reflectivity was varied independently at the liquid ($R_{PTFE,liq}$) and gas ($R_{PTFE,gas}$) interfaces. Values of $R_{PTFE,liq}$ were varied from 50–100%. For each value of $R_{PTFE,liq}$, values of $R_{PTFE,gas}$ were swept from 0–100%. The reflection model used was 100% diffuse. Geometric collection efficiency G was measured for each data point. Variation in G is also investigated for varying values of electric field grid reflectivity (R_{grid}).

Geometric collection as a function of $R_{PTFE,liq}$ is shown in Fig. 3.12. Results are shown using two emission geometries: a point source located at the middle of the drift region, and a cylindrical volume encompassing the entire drift region. No significant change in the curves is seen between the two emission geometries. Results also include the effect of varying the corresponding $R_{PTFE,gas}$ in the range 0–100%. Due to the majority of S1 light being

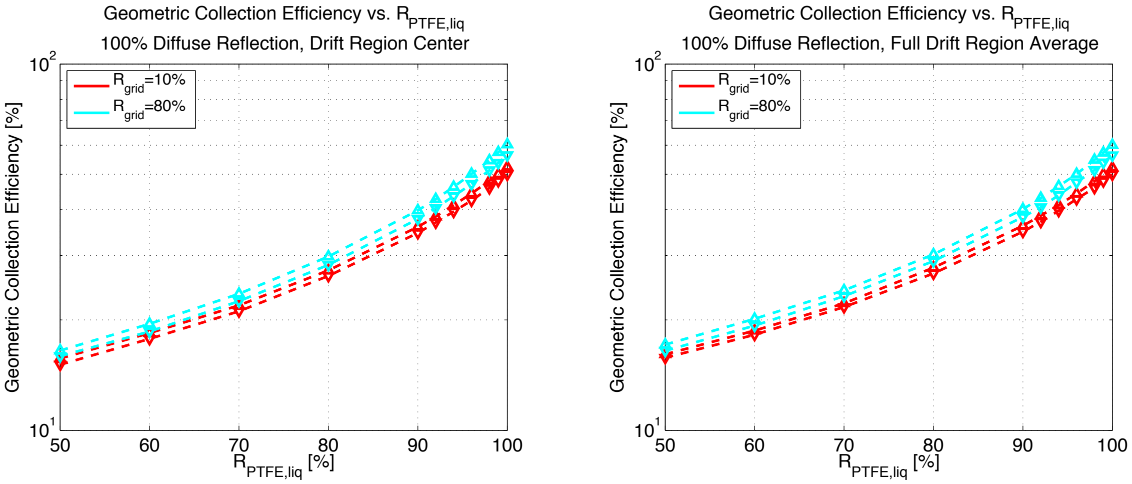

(a) (b)

Figure 3.12: LUX geometric collection efficiency as a function of $R_{PTFE,liq}$. Curves are shown for low and high values of R_{grid}. Separate curves are also shown for $R_{PTFE,gas}$ values of 0% (down-pointing triangles) and 100% (up-pointing triangles). $R_{PTFE,gas}$ has been independently measured at 65%. (a) Results from using a point source for photon emission, located in the center of the active region. (b) Results from using a cylindrical emission volume occupying the entire drift region. No significant change is seen between the two different emission geometries in (a) and (b).

reflected within the liquid volume (see discussion in Sec. 3.1), G is relatively insensitive to $R_{PTFE,gas}$.

3.3.2 Measured Light Collection Efficiency for Varying PTFE Reflectivities

Measured light collection is calculated in units of phe/keV$_{\mathrm{ee}}$ (zero field) following Eq. 3.3. The QE used is QE_{sim} as defined in Sec. 3.1.7.1. The average LUX R8778 QE value, as measured by Hamamatsu, is 33% [129]. This value multiplies the probability of photon transmission through the PMT quartz window with the probability of conversion into a phe. Using the Fresnel equation for reflection, the transmission probability for a photon incident from air (in which the measurement was made) into quartz is 95%. The value of QE_{sim} is then 33%/0.95 = 35%. The average R8778 collection efficiency CE is measured to be 90% for R8778 PMTs [94]. $w_{\nu}(E)$ is taken at 122 keVee, at 15.3 eV (Sec. 3.2.2). Curves from Fig. 3.12 are multiplied by the factors calculated with Eq. 3.4, using LUX efficiency

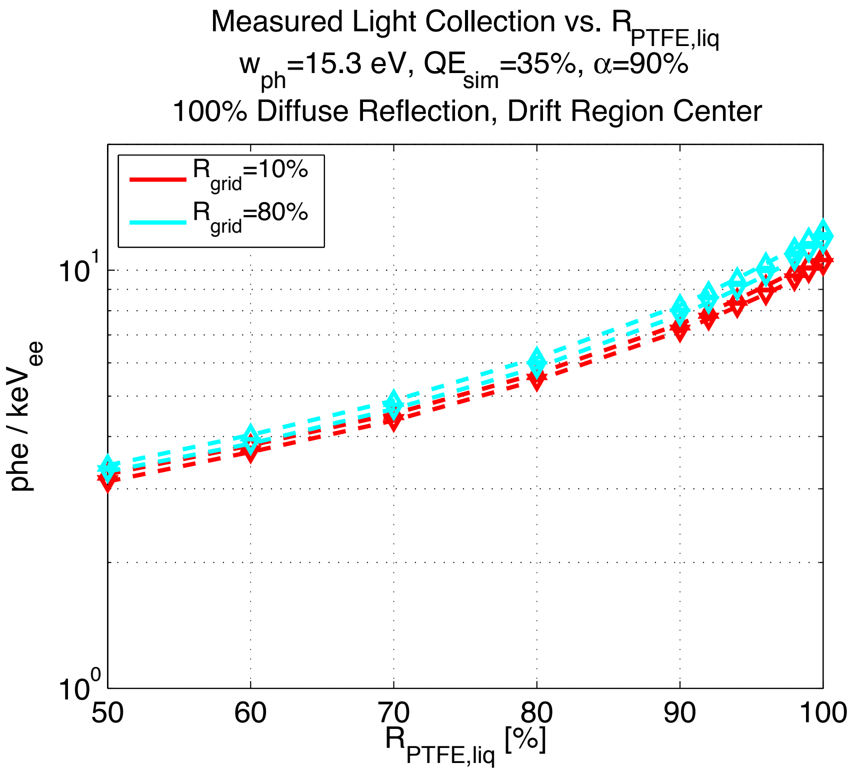

Figure 3.13: Simulated LUX light collection for 122 keV_{ee} energy depositions (zero field). Results are identical for point source and full drift emission geometries. G is calculated from LUXSim Monte Carlo. Scaling to $\text{phe}/\text{keV}_{\text{ee}}$ is performed using Eq. 3.3 with the measured average LUX PMT D value.

values. Results are shown in Fig. 3.13.

3.3.3 Specular vs. Diffuse Reflection and Impact on Geometric Collection Efficiency

The use of a diffuse reflection model is well motivated by arguments about the microfaceted composition of PTFE surfaces [113]. Direct measurements of PTFE reflectance spectra in gas indicate an angle-dependent specular reflection component for $R_{PTFE,gas}$ [114]. The angular reflection spectrum in liquid Xe is not currently measured.

The Geant4 optical physics processes do not support variable reflectance parameters as a function of angle, as was directly measured for the LUX PTFE in gas. To place a bound on the potential systematic error in the Monte Carlo associated with use of a pure diffuse reflection model, the studies from Sec. 3.3.1 were repeated using a pure specular reflection model. Results are shown in Fig. 3.14.

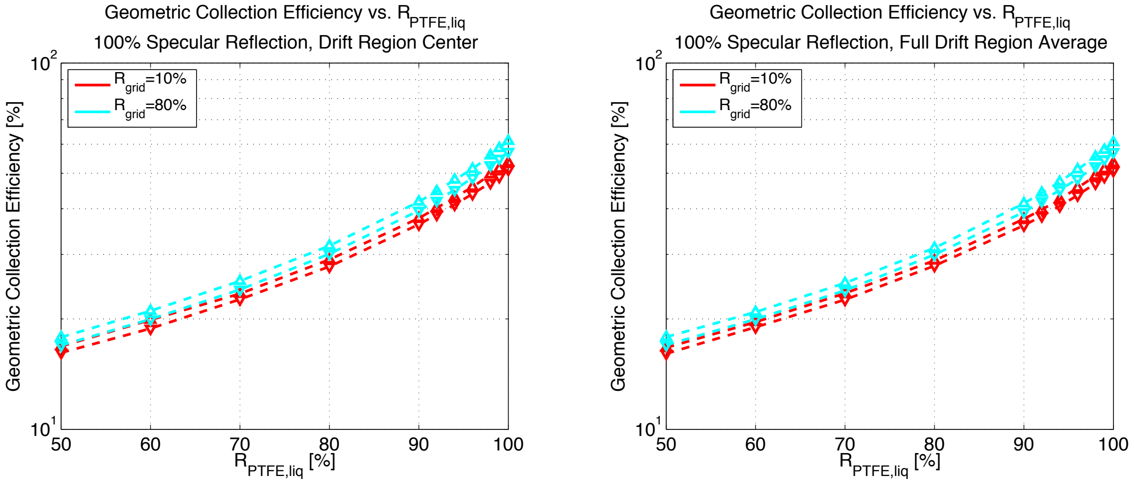

(a) (b)

Figure 3.14: Geometric collection efficiency as a function of PTFE reflectivity in liquid Xe, using a pure specular reflection model. Curves are the same as described for Fig. 3.12.

The choice of a pure specular or pure diffuse reflection model changes S1 light collection by <5%. The limited magnitude of the change in efficiency is due to the effects of Rayleigh scattering within the liquid Xe. As the characteristic scattering length is significantly lower than the photon mean free path, all photons undergo multiple scatters within the liquid Xe volume, essentially randomizing their trajectories regardless of their reflection angle from the PTFE. Scattering from field grids, the liquid surface, and PMT quartz windows further randomizes photon directions.

3.3.4 Photon Angle-of-Incidence Distributions and Corrections to PMT QE Estimates

3.3.4.1 Photon Incidence Angles at the Photocathode

The distribution of photon incidence angles at the photocathode is shown in Fig. 3.15, for two PTFE reflectivity values, using a photon point source at the detector center. The photocathode is modeled as a quartz object, in order to eliminate reflections of incident photons from the quartz / photocathode boundary. Some reflection likely exists in reality. However, the quantity is unknown, and is not included in the model. To highlight the importance of knowing the $P_{loss,0}$ parameter for the R8778 at 178 nm, Fig. 3.16 gives

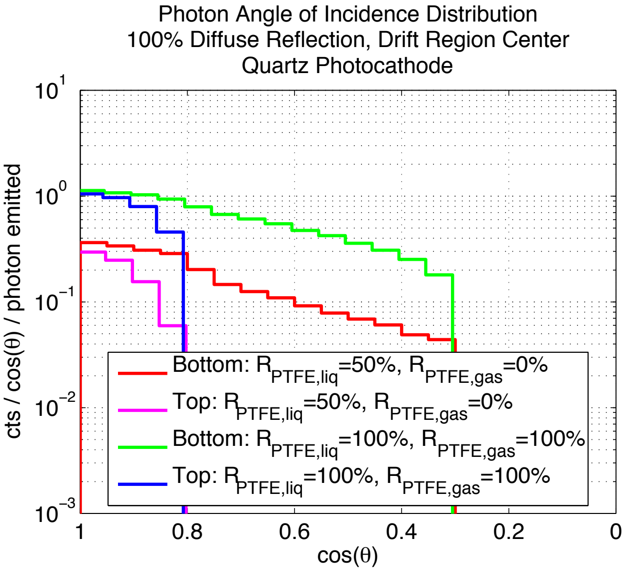

Figure 3.15: Photon angle-of-incidence distributions at the PMT photocathode. θ is defined with respect to PMT face normal. Separate curves are shown for low and high PTFE reflectivity datasets; no significant change in slope is seen. Curves are also shown separately for top and bottom PMTs. Photocathodes are modeled as quartz, to avoid reflection effects between the quartz and photocathode volumes. The spectrum is used in estimates for corrections to light collection curves, calculated in Sec. 3.1.7.1. Cutoffs in the angular spectra for the top PMT array result from the mismatch between the gas Xe and PMT windows ($n = 1.6$).

the potential gain in measured light collection vs. $P_{loss,0}$ for constant PTFE and grid reflectivities.

3.3.4.2 Measurements of $P_{loss,0}$

LUX collaborators at LIP Coimbra performed a direct measurement of R8778 QE vs angle-of-incidence in 2011. Three R8778 PMTs were tested, using both blue and UV light from a Xe lamp. The incident light was collimated with an iris of 1.3 mm diameter, and the PMT was rotated about the center of its front face. Results were collected as single phe spectra at several angles.

The VUV lamp data for absorption probability was fit with the function $P_{abs}(\theta) = 1 - \exp(1.6 \cdot \sec(\theta))$. From Sec. 3.1.7, $P_{loss,0} = P_{abs,0} - QE_{sim,0}$. Taking the measured value of P_{abs} at 0°, $P_{loss,0} = 0.45$. From Fig. 3.16, this value of $P_{loss,0}$ yields an estimated 8% increase in predicted LUX light collection above the flat-QE model.

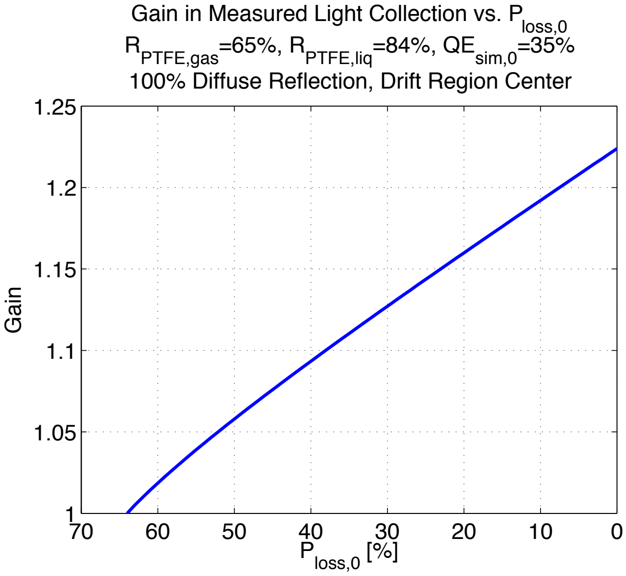

Figure 3.16: Relative gain in LUX light collection as a function of $P_{loss,0}$ for constant $R_{PTFE,liq}$ and $R_{PTFE,gas}$. The spectrum of photon incidence angles is not significantly affected by varying reflectivities, as shown in Fig. 3.15. The curve is calculated using the angular spectrum from Fig. 3.15 as input for Eq. 3.2.

CHAPTER 4

DIRECT MEASUREMENT OF NUCLEAR RECOIL SCINTILLATION EFFICIENCY

The LUX detector will be the first Xe TPC to use a novel NR signal calibration strategy that allows a direct, unambiguous measurement of signal yields from NR events. The measurement takes advantage of the 2.5 m thick LUX water shield, the large linear dimensions of the LUX active region, a moveable air conduit which was built into the water shield, and a high-yield deuterium-deuterium (D-D) fusion source. The modeling and simulation work for the calibration technique, used to evaluate the merit of this calibration and to develop analysis cuts which maximize signal-to-noise, are described in this chapter. Calibration data taking and analysis results will be described in future publications [130].

4.1 Strategy

For any radiation source to be useful for detector energy calibrations, independent knowledge of the incident particle energy is required. Gamma sources are well understood in terms of their energy spectra, and the γ rays are emitted at discrete energies, enabling easy correlation of energy deposition with observed S1 and S2 peaks. Neutrons are emitted from radioactive decay processes with very wide energy spectra (see e.g. Fig. 6.7). This limits the potential usefulness of radioactive neutron sources for energy calibrations. Furthermore, whereas γ rays provide observable ER peaks through photoelectric capture, there is no comparable process for neutrons with reasonable cross-section. (Even if there were, the incident neutron energy is much too high to provide a useful calibration of the dark matter search region.) Neutrons instead produce a continuous energy deposition spectrum through scattering.

A NR calibration can be established if both the neutron scattering angle and the incident neutron energy are well known. The NR energy deposited by a neutron with order MeV energy is well characterized by non-relativistic kinematics, as the speed of a 1 MeV neutron is $0.03c$ (0.9 cm/ns, 55 ns to cross the LUX active region). For a neutron with kinetic energy T, the expression for the total energy imparted to a Xe nucleus (with mean atomic mass $A = 131$) is

$$E = T \times \frac{4m_1m_2}{(m_1+m_2)^2}\left(\frac{1+\cos(\theta)}{2}\right) \approx T \times \frac{4}{131}\left(\frac{1+\cos(\theta)}{2}\right), \tag{4.1}$$

where θ is the neutron scattering angle in the center-of-mass frame.

The incident neutron energy from radioactive sources is generally not well understood because of two effects: the width of the emitted neutron energy spectrum, and the scattering of the neutrons in passive construction materials before reaching the active region. For LUX NR calibrations, it is proposed to circumvent the first of these problems through the use of a D-D fusion source, which generates monoenergetic 2.45 MeV neutrons. The D-D reaction is

$$^{2}\mathrm{H} + {}^{2}\mathrm{H} \quad \rightarrow \quad \begin{cases} {}^{3}\mathrm{He} + \mathrm{n}, \\ {}^{3}\mathrm{H} + \mathrm{p}, \end{cases}$$

where either reaction is 50% probable. Protons are quickly captured in surrounding generator components, and do not influence measurements. ^{3}H undergoes β decay, with a 12 year half-life and Q-value 18.6 keV; the low-energy β is also quickly stopped in generator materials. The only detectable product of the D-D reaction is the neutron.

The D-D fusion process is generated by imparting a low speed to one of the ^{2}H nuclei, sufficient to enable tunneling through the Coulomb barrier of the second ^{2}H nucleus. The ^{2}H nuclei can be modeled as being at rest before the fusion reaction. The neutron energy can then be calculated from the rest masses of ^{2}H and ^{3}He, and momentum conservation requirements between the ^{3}He nucleus and the neutron. The rest masses of ^{2}H, ^{3}He and the neutron are 2.0141 u, 1.00866 u, and 3.01603 u respectively. This leaves a total leftover mass of 0.00351 u = 3.27 MeV. As the ^{3}He nucleus is three times more massive than the neutron, the energy is partitioned such that the neutron obtains 3/4 of the leftover energy. This leaves 2.45 MeV for the neutron.

In practice, the neutron energies emitted from the generator head have a small angular dependence due to the high-field acceleration of the ionized ^{2}H nuclei when initiating fusion. The energy range is expected to vary by 0.6 MeV when sweeping from 0–π around the generator. Choosing a fixed angle for the generator head relative to the detector largely mitigates the energy variation.

The problem of neutron scattering in materials is addressed in LUX by using a long air-filled conduit, which penetrates the water shield between the neutron generator and the detector. This provides a tightly collimated beam of neutrons entering the detector, which have scattered minimally in other materials during their flight. A neutron which scatters in the water enough to significantly change its kinetic energy will also deviate significantly from the conduit path; this will effectively remove it from the neutron beam, and it will quickly capture in the water shield. A large fraction of the neutrons surviving to reach the active region will therefore have their original kinetic energy from the generator, and will have momentum aligned with the conduit axis. Further analysis cuts described in Sec. 4.3.3 remove neutrons which scatter in detector construction materials.

The tight collimation of the neutrons entering the detector also enables a measurement of the scattering angle θ. This is illustrated in Fig. 4.1. LUX is capable of detecting multiple scatter vertices in a single event, through identification of multiple S2 signals. In the example of a double-scatter event, the vertex which is well-aligned with the beam path is known to be the first scattering vertex in the detector. The next vertex is therefore the second scatter vertex, which fixes the vector of the neutron after it initially scattered. The value of θ can be calculated based on the vector of the conduit and the vector between the

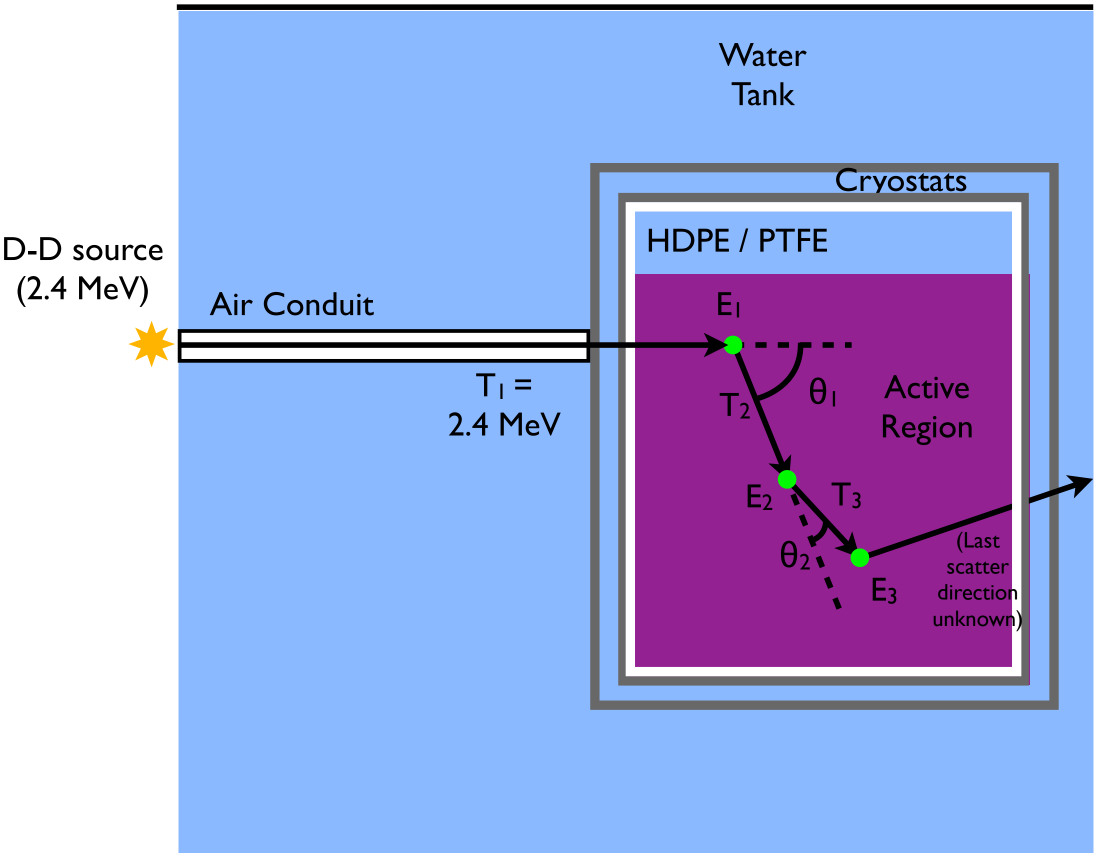

Figure 4.1: LUX NR calibration strategy using a monoenergetic D-D neutron source and long air conduit for neutron beam collimation. The vector of the conduit is used in combination with the scatter vertex positions in the detector to reconstruct the neutron scattering angle. The corresponding energy is correlated with the detected signals, providing direct NR energy calibration in LUX.

scatter vertices. The same scheme can be used for the measurement of θ for events with >2 scatters. Ambiguity in the ordering of the secondary scattering vertices can be overcome through the relative S2 sizes from the vertices, pairing lower (higher) energy scatters and therefore smaller (larger) scattering angles with smaller (larger) S2 signals.

Knowledge of the incident energy T and measurement of θ allow calculation of the total NR energy deposited via Eq. 4.1. This energy can be correlated with the size of the S2 signal observed from each vertex, enabling a direct measurement of ionization yield as a function of energy. Direct calibration of the S1 signal for each vertex cannot be performed due to the overlap of the S1s from all vertices. A likelihood analysis from observation of a wide range of scattering profiles can potentially be used to estimate the scintillation yield.

4.2 Materials

The LUX neutron conduit is constructed out of PVC pipe, sealed at either end against water using PVC pipe cement (McMaster ID 18815K61). The conduit is shown as installed in the LUX water tank in Fig. 4.2 (top). The conduit measures 377 cm end-to-end, with a 4.9 cm inner diameter. The conduit is suspended from two stainless steel cords, affixed to the outer top cover of the water shield by two hand winches. A stainless steel T-bar is strapped to the bottom of the conduit to provide ballast, and to prevent conduit bowing during submersion. During neutron calibration operations, two operators use the winches to raise the conduit into alignment with the active region. When neutron calibration is not in progress, the conduit is lowered to the bottom of the water tank, in order to close off line-of-sight to the detector for γ rays and neutrons from cavern radioactivity. The position of the conduit has been shown to be reproducable to $\sim$cm accuracy using a calibration of height as a function of winch rotations.

The conduit was prototyped at Brown University in a 1.8 m height water tank, before deploying the conduit in the LUX water tank. A 1 m prototype tube was used to gauge the effectiveness of the PVC cement in sealing the tube against water during full submersion. Prototype submersion is shown in Fig. 4.2 (bottom left). The tube was filled with paper towels with ink markings, used to show any indications of water buildup after submersion. The tube was sealed and affixed to the stainless steel ballast, with segments of stainless steel wire used for suspension. The tube was submerged in the Brown water tank for three days. After submersion, the tube was opened, and the paper towels and ink were checked for signs of water absorption, with none found.

Corrosion was noted on the stainless steel components after submersion tests at Brown. As a precautionary measure, all stainless steel components were subjected to passivation on site at SURF using a nitric acid bath. The acid formed an oxide layer over the steel components, preventing further corrosion during submersion in the LUX water tank. Observations of the stainless steel cords used to suspend the tube operation indicate that passivation successfully prevented corrosion of these components after the water tank was filled.

The neutron generator is made by Adelphi Technology, model DD-108M [131]. The DD-108M is shown during initial testing and characterization at Brown in Fig. 4.2 (bottom right). The DD-108M is capable of producing up to 10^8 n s^{-1}. During calibration operations, the generator is lifted into place adjacent to the water tank, with the generator head aligned with the conduit. Results from generator testing, including characterization of the neutron energy spectrum, is reported in future LUX theses and publications.

4.3 Calibration Simulations

4.3.1 Simulation Parameters

The LUXSim package was used to estimate the neutron flux incident on the active region during generator operation, and to develop a set of analysis cuts designed to reject neutrons which had scattered before reaching the active region. The simulation uses the LUX water tank and full detector geometry. A 5 cm diameter air conduit is added, spanning between the water tank wall and the edge of the cryostat. The conduit is positioned 10 cm below the liquid Xe surface. The conduit is flush against both the detector and the tank wall.

Neutrons with energy 2.45 MeV are launched from a point source immediately outside of the water tank, aligned with the conduit. The neutrons are launched from the point source isotropically, as they are launched from the D-D generator[1]. The neutrons are propagated through the conduit, scattering and capturing in the water tank and liquid Xe. Although capture physics is implemented in Geant4, this is not studied in detail, as the capture cross-sections for all relevant elements were not verified before the study. Scatter vertex energy depositions and positions in the liquid Xe were recorded. The simulation did not incorporate Xe scintillation and ionization physics, and energy depositions alone were used to characterize events. The total number of NR vertices for each event was found in post-processing, as well as the sum total ER energy deposition (without position information). ER information was recorded for calculation of total detector event rates, as well as inelastic

---

[1] A considerable savings on computation was realized by only launching neutrons in a narrow cone centered on the conduit axis. The fraction of neutrons scattering early in the conduit and reaching the detector are assumed to be negligible.

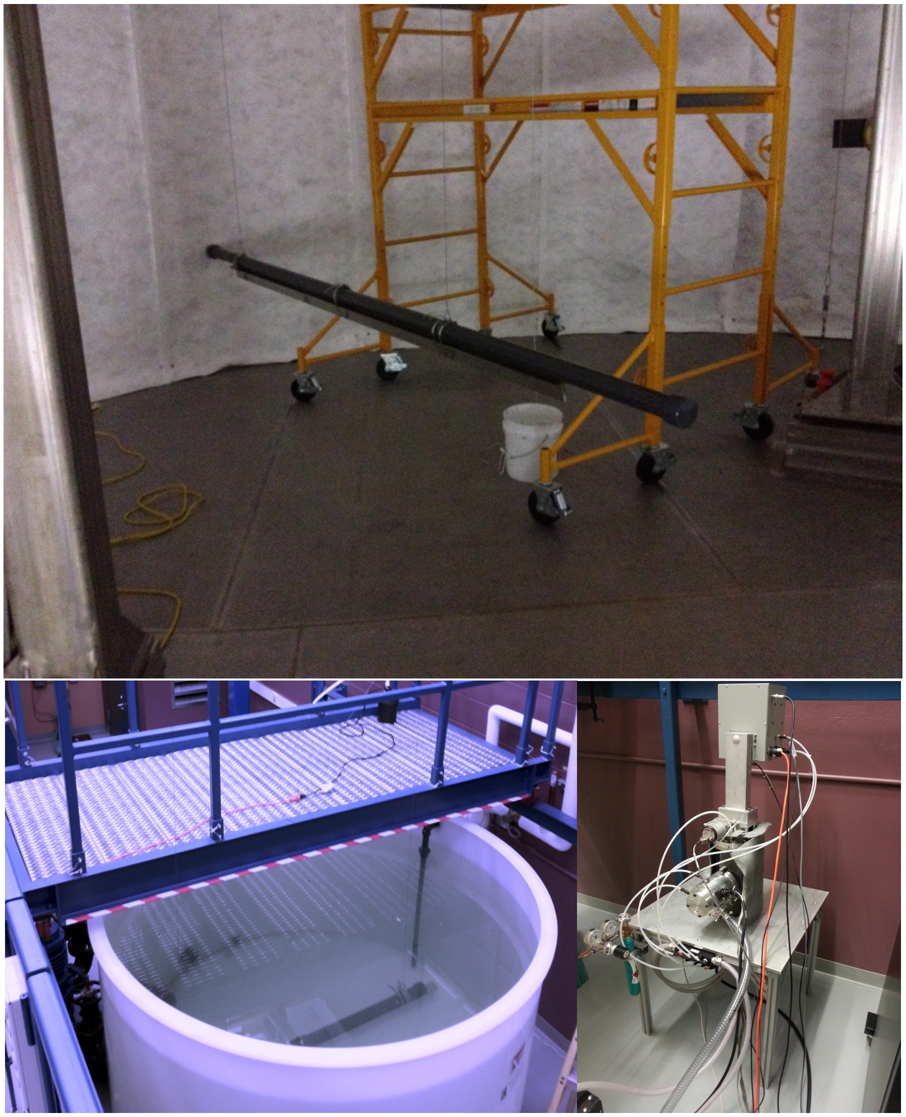

Figure 4.2: (Top) The fully assembled neutron conduit in the LUX water tank. The PVC body measures 377 cm end-to-end, with 4.9 cm inner diameter. A stainless steel T-bar is used for ballast. Stainless steel hose clamps secure the pipe to the ballast in three locations to prevent bowing. Stainless steel wire connects the tube to winches at the top of the water tank, allowing operators to raise and lower the conduit during calibration operations. (Bottom Left) The 1 m prototype tube, used to test sealing, ballast and suspension techniques. The tube is immersed in the 1.8 m height water tank at Brown University. (Bottom Right) The DD-108M neutron generator, during initial testing at Brown. The generator head is located in the middle of the tee, in line with the turbopump.

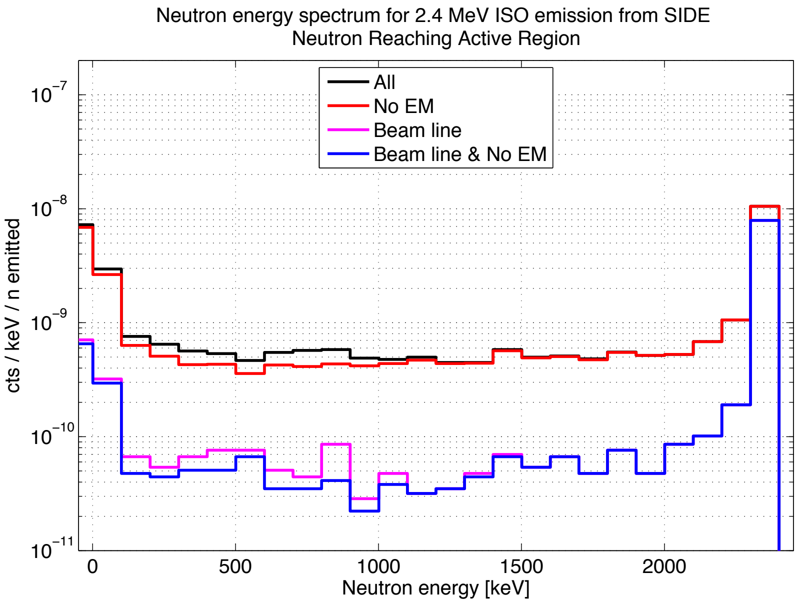

Figure 4.3: Neutron energy spectrum at the active region boundary, for neutrons with initial energy 2.45 MeV launched isotropically from the neutron generator and arriving at the active region through the 5 cm diameter air conduit spanning the water tank. The energy spectrum for all neutrons is shown in black. Applied cuts are (red) an EM veto cut which removes all events with any EM deposition in the active region, (magenta) a position cut requiring the neutron to enter the active region in a 2.5 cm radius circle centered at the axis of the vacuum conduit, and (blue) both cuts combined. The cuts are described in detail in Sec. 4.3.3.

scatter rejection.

4.3.2 Neutron Energy Spectrum

The energy spectrum of neutrons incident on the active region is shown in Fig. 4.3. Without application of analysis cuts, the fraction of neutrons near full energy (>2.3 MeV) is 21%. Applying a position cut on the scattering vertices (discussed in Sec. 4.3.3) boosts this fraction to 76%. The EM veto cut, discussed in Sec. 4.3.3, negligibly impacts this fraction.

The radial distribution of neutrons relative to the conduit central axis is shown in Fig. 4.4. Neutrons which scatter in the water shield or detector internals are thrown significantly off from the conduit axis. This forms the basis for the position cut discussed in Sec. 4.3.3.

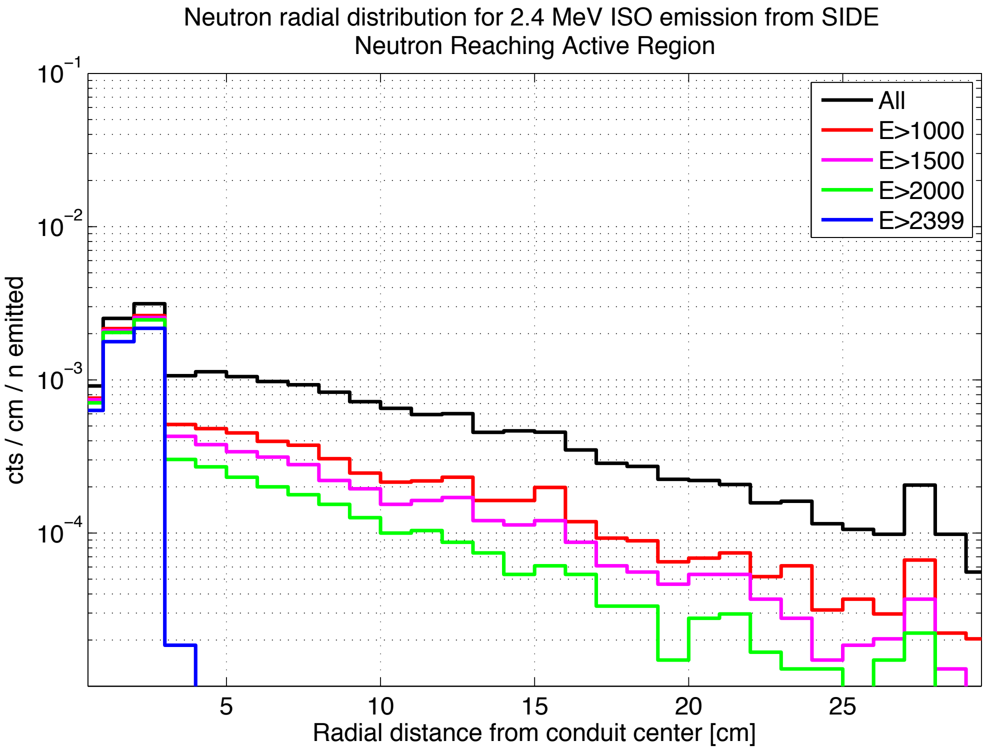

Figure 4.4: Radial distribution at the active region boundary, for neutrons with initial energy 2.45 MeV launched isotropically from the neutron generator and arriving at the active region through the 5 cm diameter air conduit spanning the water tank. Energy cuts are applied showing all events (black), E $>$ 1 MeV (red), E $>$ 1.5 MeV (magenta), E $>$ 2 MeV (green), and E $\simeq$ 2.45 MeV (blue), showing the dramatic clustering effect for full-energy neutrons in the line of the conduit. This effect allows for a large improvement in signal-to-noise by using a basic position cut on one of the scattering vertices.

4.3.3 Cut Definitions

4.3.3.1 Position Cut

A position cut is applied for each event, in order to screen out events where the incoming neutron has scattered in the water tank or detector internals and deviated significantly from its original trajectory. The cut allows events to pass where any vertex is within 2.5 cm of the conduit central axis, and all vertices are >15 cm from the edge of the active region where the neutron entered. The latter requirement is imposed to remove neutrons which scatter in materials immediately adjacent to the active region, where the path length between the passive material scatter and the first Xe scatter vertex is not long enough to remove the neutron from the beam path.

Note that the maximum angle of neutrons entering the active region from the conduit, assuming a point-like emission source at the end of the tube, is 0.4°. Using a 2.5 cm cylinder to approximate this cone therefore does not cut out any potentially legitimate events. 95% of neutrons with scatters passing this cut have kinetic energy in the range 2.3–2.45 MeV. The position cut removes 93% of all events with one or more NR scatters in the active region.

4.3.3.2 EM Veto Cut

It is assumed that the S2/S1 analysis is insufficient for removing events with an EM component, since the overall S2/S1 of the event is weighted by multiple NR scatters. However, a cut on S2 size for individual vertices can easily remove events with an EM component. The maximum energy deposited by a 2.4 MeV neutron incident on Xe is 75 keV_{nr}. Using the ER and NR ionization electron yields from Fig. 2.2a, this means that a high-S2 veto could be set at 6 keV_{ee} in order to reject events which must come from EM depositions. The simulations used a more conservative 15 keV_{ee}, due to a more conservative estimate of the ionization yield ratio for ER and NR events. The 15 keV_{ee} cut removes 99.9% of all events with an EM component. The rejection factor of the cut is 99.6% at 39 keV_{ee}; above this energy, the rejection efficiency drops due to 40 keV γ rays from inelastic scatters on ^{129}Xe. Application of the EM veto cut reduces the fraction of the neutron energy spectrum in the range 2.3–2.45 MeV to 92%, but greatly aids in tightening the energy vs. scattering angle distribution. The EM veto cut removes 63% of all NR events. When combined with the position cut, 98% of NR events are removed.

4.3.3.3 Energy Cut

Energy cuts are used to isolate both the full WIMP search energy range (taken generously as 1–30 keV_{nr}), and the low-energy NR detector threshold (1–5 keV_{nr}). The energy cut requires, for an event with N total scattering vertices, that any of the 1, 2, ..., $(N-1)$ vertices results in an energy deposition within the specified range. The final vertex is not included, as the determination of energy deposition for a given vertex requires a subsequent vertex to be present to determine the scattering angle.

4.3.4 Event Rates

Rates for all events in the active region are listed in Table 4.1. The fraction of emitted neutrons generating any signal in the active region is 7.5×10^{-6}. The fraction of emitted neutrons passing the position and EM veto cuts is 1.2×10^{-7}. 92% of neutrons passing the position and EM veto cuts (1.1×10^{-7} of all emitted neutrons) have $T > 2.3$ MeV.

The breakdown of N-scattering event rates for various cuts, assuming operation of the D-D generator at 10^7 n s^{-1} and no water in the beam path, is given in Table 4.2. Cut definitions are described in Sec. 4.3.3, and are used to screen out neutrons which either scatter before reaching the active region or undergo inelastic scattering in the active region. For a 10^7 n s^{-1} D-D source outside the water tank, the corresponding raw signal rate in the detector (any event type) is 75 Hz. The signal rate for events in the energy range 1–30 keV_{nr} using 2–4 scatter events would be 36 min^{-1}, decreasing to 24 min^{-1} for the 1–5 keV_{nr} energy range.

The effectiveness of the position cut is demonstrated in Fig. 4.5, before and after application of the position cut. The smear in incident neutron energies due to scattering on detector internals or in the water degrades the quality of the energy-angle correlation. Use of the position cut ensures that at least one of the scattering vertices occurred directly in the neutron beam line, with a high probability that one of the vertices near the central line

Cut	**Neutron Kinetic Energy Range**	
	All	**2.3 MeV $< T <$ 2.45 MeV**
Any ER or NR	7.5×10^{-6}	2.5×10^{-6}
NR Event	5.6×10^{-6}	2.5×10^{-6}
NR & Position Cut	4.0×10^{-7}	3.8×10^{-7}
NR & EM Veto	2.1×10^{-6}	5.9×10^{-7}
NR & Position Cut & EM Veto	1.2×10^{-7}	1.1×10^{-7}

Table 4.1: Event rates normalized per neutron emitted from the source. Rates are listed both for all incoming neutrons and for neutrons with energy >2.3 MeV when entering the active region. Cut definitions are listed in Sec. 4.3.3.

was the first vertex. Neutrons which have not scattered outside of the detector will have full energy, enhancing the ratio of full-energy neutrons to reduced-energy neutrons as described in Sec. 4.3.3. The spread of neutron energies as a function of angle is shown for three cases in Fig. 4.6.

Scatter multiplicity is shown in Fig. 4.7. The total fraction of interacting events with 2–4 multiple scatters is 34%, a significant fraction of all incoming events. It should also be noted that there is a 16% fraction of single-scatter events, reduced to 2.4% after application of EM veto and position cuts. As the position cut isolates full-energy neutrons with high efficiency, the spectrum of these single-scatter events can be compared to Monte Carlo results for a separate $\mathcal{L}_{eff}$ measurement (see Sec. 2.1.2 for a discussion of $\mathcal{L}_{eff}$). Single-scatter events passing the position and EM veto cuts will accumulate at a rate of 24 min^{-1} using a 10^7 n s^{-1} source, assuming no water in the beam path.

Neutron penetration distance is shown in Fig. 4.8 for neutrons with energy >2.3 MeV. The penetration distance is defined as the distance from the active region outer boundary (aligned with the conduit central axis) to the first scattering vertex. The mean free path through liquid Xe is measured to be 12 cm as expected [71].

4.4 Optimization of Conduit Placement

The air conduit was determined from simulations to have an optimal placement 10 cm below the liquid surface. This placement allows for a significant mass of Xe on all sides of the beam path, maximizing the number of multiple scatter events, and reduces the number of

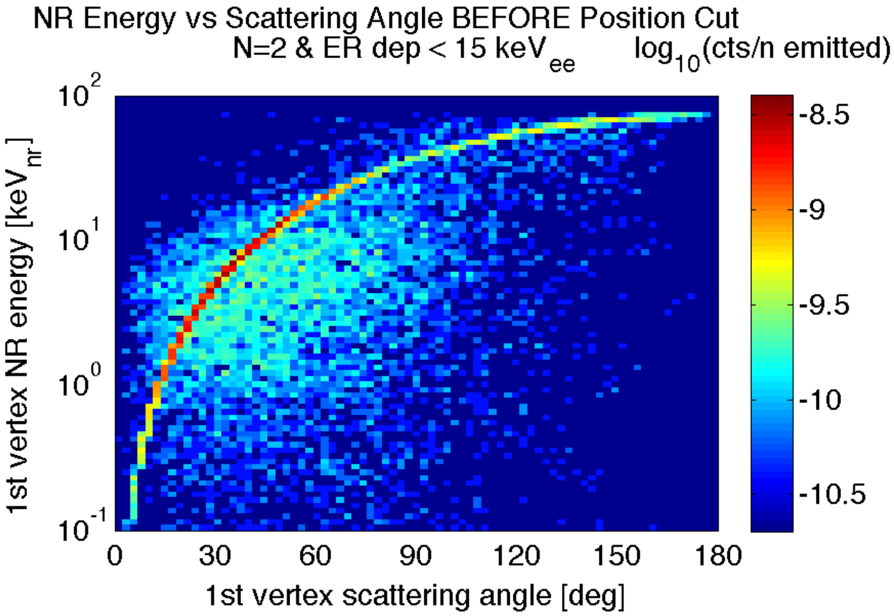

(a)

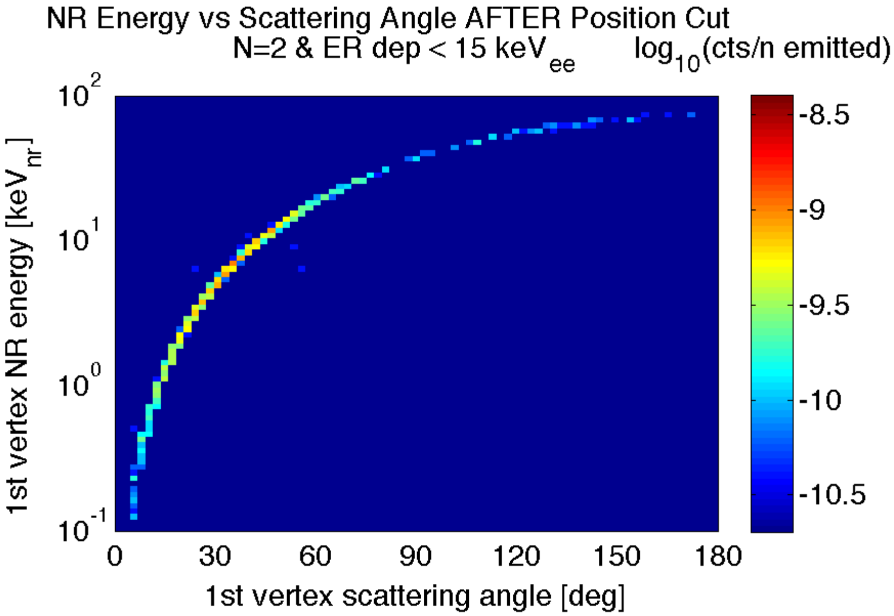

(b)

Figure 4.5: Energy deposited as a function of scattering angle for double-scatter events, after application of the EM veto cut. The distribution is shown (a) before and (b) after applying the position cut. The full-energy peak is sharpened by the position cut, sharpening the correlation between NR energy and measured scattering angle. Cut definitions are given in Sec. 4.3.3.

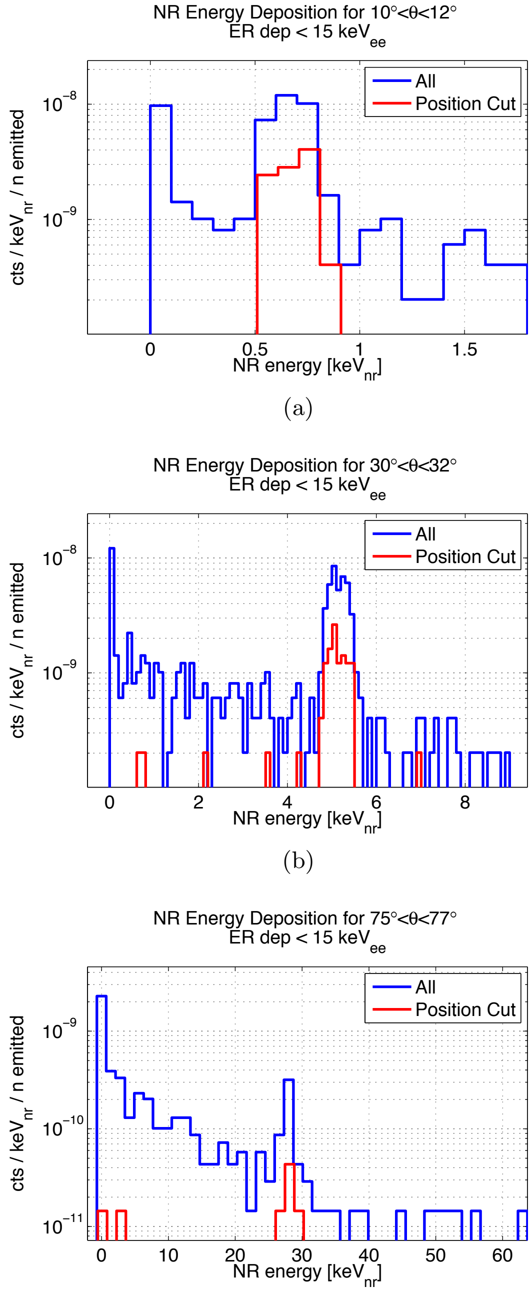

(a)

(b)

(c)

Figure 4.6: Energy spectrum for scatters at (a) 10°–12° (0.5–0.8 keV$_{\rm nr}$), (b) 30°–32° (4.9–5.4 keV$_{\rm nr}$), and (c) 75°–77° (27.4–28.6 keV$_{\rm nr}$), with and without the position cut applied, for double-scatter events. Angle-energy relationship assumes $T = 2.45$ MeV. The vertex nearest the conduit axis is selected as the first vertex, with the other vertex assumed to be the second. The position cut selects neutrons which have not lost energy before entering the active region, precisely fixing the energy-angle relationship. Cut definitions are given in Sec. 4.3.3.

Number of Neutron Scatters N in Active Region	Rate of All Events in Active Region [min^{-1}]	Rate of All Events in Active Region After EM Veto & Position Cut [min^{-1}]	Rate of All Events in Active Region After EM Veto, Position & Energy Cut [min^{-1}]	
			1-30 keV$_{nr}$	**1-5 keV$_{nr}$**
0 (ER only)	110	–	–	–
1	71	24	18	7.4
2	58	20	19	11
3	45	11	11	7.8
4	34	6.3	5.9	4.7
$\geq$5	130	9.3	8.1	7.1

Table 4.2: Event rates with N neutron scatters after application of various cuts, for all incoming neutron energies, assuming use of a 10^7 n s^{-1} D-D source outside of the water tank. Cut definitions are given in Sec. 4.3.3.

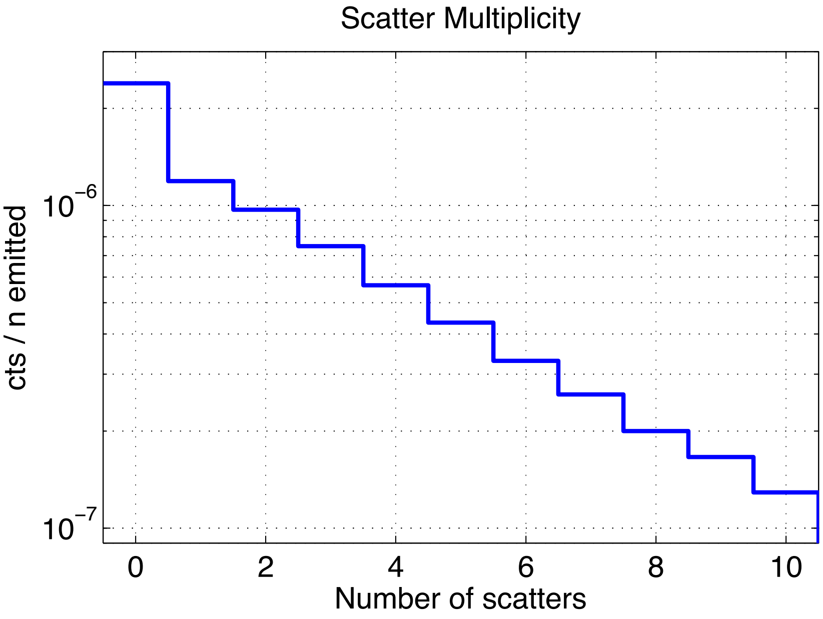

Figure 4.7: Neutron scatter multiplicity, before application of quality cuts listed in Sec. 4.3.3. The total fraction of useful events (N=2–4 scatters) is 31%. 16% of events are single-scatters, which can be used for Monte Carlo comparisons as a separate $\mathcal{L}_{eff}$ measurement.

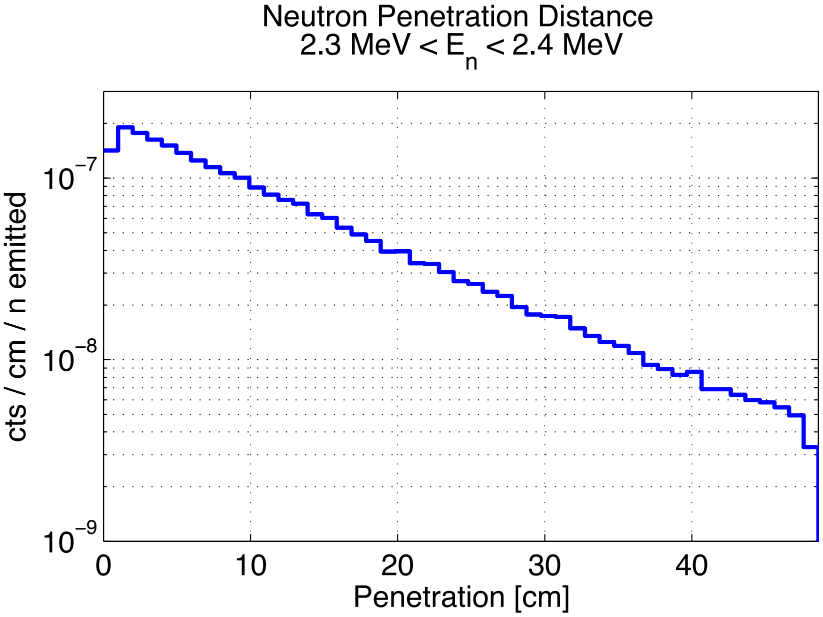

Figure 4.8: Penetration distance of full-energy neutrons ($T > 2.3$ MeV) into the active region. Penetration distance is defined as the distance from the active region outer boundary (aligned with the conduit central axis) to the first scattering vertex. The exponential slope is 12 cm, agreeing with the 6 b cross-section for 2.45 MeV neutrons in Xe [132].

high-order scatter events by allowing neutrons to escape more easily from the top of the active region. The movement of the conduit toward the top of the detector also significantly reduces the number of "neutron-X" events, wherein at least one scatter occurs below the cathode grid and does not produce an S2 signal. (These events are an analog to gamma-X events, discussed in Sec. 5.4.) An off-axis alignment of the conduit could further enhance the number of low-order multiple scatter events, by reducing the mass of Xe on one lateral side of the beam. It is expected that the conduit will naturally have a slight off-axis alignment due to the logistics of conduit and detector installation, so off-axis alignment of the conduit was not intentionally introduced.

Geometries were also considered where the beam was introduced to the detector through the top, using a vertical pipe. This method has several disadvantages. The primary disadvantage is the use of XY position reconstruction to determine the angle of very small-angle scatters. Position resolution in Z is several times higher than resolution in XY. For neutrons introduced laterally to the detector, and which undergo a scatter in which the neutron scatters upward, Z position reconstruction enables fine measurement of the scattering angle. In the scenario of neutrons fed in vertically, the angular measurement resolution is dominated by XY position measurement resolution for both vertices. The superior Z resolution lends a significantly smaller reconstruction systematic to the lateral neutron beam scenario. Other disadvantages of vertical conduit placement include logistics of the neutron conduit installation in the necessary position, and placement of the generator in a location much closer to populated areas of the lab.

4.5 Data Analysis

Data analysis techniques for reconstruction of the neutron multiple scatter events have been explored for LUX WIMP search data (Sec. 8.7). These techniques are currently being implemented for analysis of neutron generator calibration data. For the simulation study in this chapter, data analysis efficiencies were not incorporated into the modeling. Multiple scatter neutron analysis for WIMP search data used a photon generation model based on NEST yields, discussed in Sec. 8.7. The analysis of the D-D NR calibration signals ought not rely on this model, since this is the very model that one seeks to verify with the calibration.

Correlation of S2 size with neutron scattering angle at each vertex is expected to be relatively straightforward, due to the wide separation of measured S2s in data for multiple scatter events. The S1 signal analysis has additional complexity due to the S1 overlap for all vertices in the event. The S1 analysis is afflicted with an extra degree of freedom introduced by the last scattering vertex, which has indeterminate energy (recall that energy for vertex N is fixed by measurement of the position of scattering vertex $N+1$). It is likely that an initial analysis of S2 as a function of energy, performed for all vertices up to the $(N-1)$th vertex, will be required in order to establish the $S2\,(E)$ curve. This yield curve would then have to be used in a re-analysis of the calibration data in order to fix an energy for the last scattering vertex. This would eliminate the extra degree of freedom in the S1 analysis, and allow a less-ambiguous measurement of S1 as a function of energy. Although the S2 is measured independently of the composite S1, any errors in ionization signal reconstruction or systematics from the S2-energy correlation would be propagated to the S1 signal calibration. It is conservatively assumed that only the S2 signal will be unambiguously resolved by this calibration technique.

The calibration is potentially able to probe NR energies far below the 3.4 $\mathrm{keV_{nr}}$ LUX WIMP search threshold used for the 85 liveday run [46]. An example is calculated for a double-scatter event. Assuming a 30 cm lateral separation between the scatter vertices, and a 3 cm vertical separation (minimizing systematics from multiple S2 reconstruction in data), one can measure the ionization yield from NR events with energy 0.2 $\mathrm{keV_{nr}}$. This energy is an order of magnitude lower than the lowest-energy data points in recent published $\mathcal{L}_{eff}$ measurements [90, 93].

Extrapolating from Fig. 2.2a, the ionization yield from 0.2 $\mathrm{keV_{nr}}$ events is in the single electron regime. The high single-electron detection efficiency of LUX can potentially facilitate measurements of these low-energy events. The measurement will also be able to detect significant deviations of the NEST ionization yield model from reality. The direct efficiency measurement from this calibration technique can greatly enhance the power of a low-energy S2-only WIMP search in LUX, such as that performed for the XENON10 experiment [133].

Chapter 5

The LUX Background Modeling Program

The most significant background in LUX for the dark matter search is from low-energy scatters from γ rays. A smaller but significant background component arises from β or x-ray emission from intrinsic radioisotopes. A detailed model of all γ, β and neutron emission within the detector was constructed in order to predict and verify observed WIMP search backgrounds. Modeling of γ emission was based primarily on LUX screening results, discussed in Ch. 7. Intrinsic backgrounds were modeled after *in situ* measurements with LUX underground data. All background measurements are discussed in Ch. 8.

The LUX background modeling program is based on Monte Carlo simulation of γ, β and neutron propagation through the active region, based on screening results and *in situ* measurements. Emission energy spectra are taken from literature or independent calculations. Background rate predictions are made by creating cuts on event topologies that emulate cuts used on real LUX WIMP search data. This chapter describes the Monte Carlo and analytic background modeling efforts in detail.

5.1 Analytic Model of Gamma Backgrounds

The physical model of γ backgrounds can be calculated analytically, to support simulation predictions. Gamma backgrounds are suppressed by several orders of magnitude in the fiducial volume through a process referred to as "self-shielding." Self-shielding exploits the relatively small γ mean free path through Xe, and rejects events in which the incident γ scatters multiple times in the active region. This model will faithfully recreate the effect of self-shielding, which is the greatest ER background rejection feature of liquid Xe detectors.

A γ with energy E_γ, which scatters from an electron with angle θ, will deposit an energy E_d following the Compton scattering formula

$$E_d = E_\gamma - \frac{(511\,\mathrm{keV_{ee}})\,(E_\gamma)}{(511\,\mathrm{keV_{ee}}) + E_\gamma\,(1-\cos(\theta))}. \tag{5.1}$$

For a 1 MeV γ, characteristic of typical γ energies from radioactive decays, an energy deposition in the range $0.5\,\mathrm{keV_{ee}} < E_d < 5\,\mathrm{keV_{ee}}$ corresponds to $1.3^\circ < \theta < 4.1^\circ$. This angular deviation represents a negligible change to the γ trajectory through the detector. It is thus reasonable to approximate γ rays traversing the active region and undergoing small energy deposition as moving in a straight line.

The probability for a γ to scatter through angle θ is given by the Klein-Nishina formula. The unnormalized probability is given by

$$\frac{d\sigma}{d\Omega}(E_\gamma,\theta) \propto P(E_\gamma,\theta)^2 \left[P(E_\gamma,\theta) + P(E_\gamma,\theta)^{-1} - 1 + \cos^2(\theta)\right], \tag{5.2}$$

where $\frac{d\sigma}{d\Omega}(E_\gamma,\theta)$ is the differential cross-section at scattering solid angle $\mathrm{d}\Omega$, and $P(E_\gamma,\theta) = 1/\left(1 + (E_\gamma/511\,\mathrm{keV})\,(1-\cos(\theta))\right)$. For a 1 MeV γ scattering between $1.3^\circ < \theta < 4.1^\circ$, the scattering probability varies by 1.1%. This is essentially flat, as the 1% variation does not significantly change the signal-to-noise ratio for WIMPs across the search energy range. $\mathrm{d}\sigma/\mathrm{d}E$ is shown for several common γ energies in Fig. 5.1.

Given that the γ moves in a straight line through the detector, the probability of energy deposition for a given path through the active region can be calculated in a straightforward manner. The probability of the γ undergoing a single Compton scatter in the active region,

$P_C\left(d, E_\gamma\right)$, is given by the Poisson probability for observing one event, as

$$P_C\left(d, E_\gamma\right) = \frac{d}{\lambda_C\left(E_\gamma\right)} e^{-d/\lambda_C\left(E_\gamma\right)}, \tag{5.3}$$

where d is the total path length of the γ through the active region and $\lambda_C\left(E_\gamma\right)$ is the energy-dependent Compton mean free path. The γ is also required not to undergo any other energy deposition process in the active region (i.e. photoelectric absorption or pair production). The probability of not undergoing these processes, $P_n\left(d, E_\gamma\right)$, is given by

$$P_n\left(d, E_\gamma\right) = e^{-d/\lambda_n\left(E_\gamma\right)}, \tag{5.4}$$

where $\lambda_n\left(E_\gamma\right)$ is the combined mean free path for photoelectric absorption $\lambda_a\left(E_\gamma\right)$ and pair production $\lambda_p\left(E_\gamma\right)$, calculated as $\lambda_n\left(E_\gamma\right) = \left(\lambda_a\left(E_\gamma\right)^{-1} + \lambda_p\left(E_\gamma\right)^{-1}\right)^{-1}$.

The γ is furthermore required to deposit only energy within the range of interest. This probability is given by an integration of the normalized angular scattering probability, over the range of interest:

$$P_l\left(E_\gamma\right) = \frac{\int_{\cos(\theta_1)}^{\cos(\theta_2)} \frac{d\sigma}{d\Omega}\left(E_\gamma, \theta\right) \mathrm{d}\Omega}{\int_{1}^{-1} \frac{d\sigma}{d\Omega}\left(E_\gamma, \theta\right) \mathrm{d}\Omega}, \tag{5.5}$$

where $\frac{d\sigma}{d\Omega}\left(E_\gamma, \theta\right)$ is given by Eq. 5.2.

The total probability for a γ to generate a background ER event in the active region is calculated by multiplying Eq. 5.3, 5.4 and 5.5,

$$P_{BG}\left(d, E_\gamma\right) = P_C\left(d, E_\gamma\right) \times P_n\left(d, E_\gamma\right) \times P_l\left(E_\gamma\right). \tag{5.6}$$

For a 1 MeV γ, and a 25 cm path (corresponding to the typical path of a γ incident on a LUX-sized detector), $P_{BG}\left(d, E_\gamma\right)$ is dominated by $P_C\left(d, E_\gamma\right)$. This follows from Fig. 2.1, as the Compton cross-section dominates the total interaction probability at this γ energy. $P_C\left(d, E_\gamma\right)$, $P_n\left(d, E_\gamma\right)$ and $P_{BG}\left(d, E_\gamma\right)$ are shown as functions of path length d in Fig. 5.2.

The probability of generating a low-energy event in a small volume $\mathrm{d}V$ can be calculated for an isotropic γ point source at distance x from the volume. $\mathrm{d}V$ is most easily calculated in spherical coordinates from the point source, subtending solid angle $\mathrm{d}\Omega$ and having thickness $\mathrm{d}x$. $\mathrm{d}V$ is then calculated as $\mathrm{d}V = \mathrm{d}\Omega x^2 \mathrm{d}x$. The probability of an event in $\mathrm{d}V$ is given by

$$\mathrm{d}P\left(d, E_\gamma\right) = \frac{\mathrm{d}\Omega \mathrm{d}x}{4\pi d} P_{BG}\left(d, E_\gamma\right). \tag{5.7}$$

The probability of an event per unit volume is then calculated as

$$\frac{\mathrm{d}P}{\mathrm{d}V}\left(d, E_\gamma\right) = \frac{P_{BG}\left(d, E_\gamma\right)}{4\pi d x^2}. \tag{5.8}$$

Unfortunately $P_{BG}\left(d, E_\gamma\right)$ cannot be easily solved analytically for real detector configurations, as d is dependent on detector geometry and the distribution of radioisotopes. The validity of the model was instead investigated by creating a simple cylindrical detector, choosing γ emission points distributed homogeneously around the periphery of the detector, and calculating $\frac{\mathrm{d}P}{\mathrm{d}V}$ in a fine mesh of volume coordinates through the detector.

Fig. 5.3a shows the results of a calculation using Eq. 5.6 for a 1 MeV isotropic γ source spread uniformly across the bottom of the detector. The powerful self-shielding effect of Xe is apparent in the factor 10^{-4} drop in event rate from the outer detector corners to the center. The effect is dominated by the factor $P_C\left(d, E_\gamma\right)$, which falls by 10^4 between $0 \text{ cm} < d < 70 \text{ cm}$.

For a direct comparison with Monte Carlo results, Eq. 5.8 is used to generate probability maps over the full range of γ rays emitted by the ^{238}U and ^{232}Th chains, in increments of 100 keV$_{\mathrm{ee}}$. Probability maps for ^{238}U and ^{232}Th γ rays are then found by interpolation, and added together. Results are shown in Fig. 5.3b. Background rate estimates within a 100 kg cylindrical fiducial volume are within a factor $\times 2$ compared to full Monte Carlo predictions. Second-order model corrections can bring the two predictions into closer agreement. At this point, however, it is more efficient to address all second-order corrections through the use of Monte Carlo techniques to build a much more accurate model of detector backgrounds.

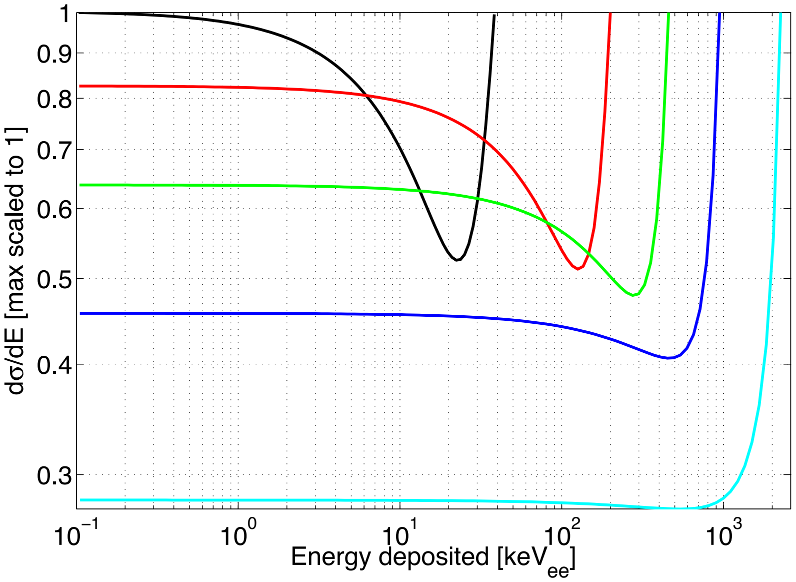

Figure 5.1: Gamma Compton scattering spectra for γ energies 122 keV (black), 356 keV (red), 662 keV (green), 1200 keV (blue), and 2600 keV (cyan). Spectra are calculated by the Klein-Nishina equation (Eq. 5.2).

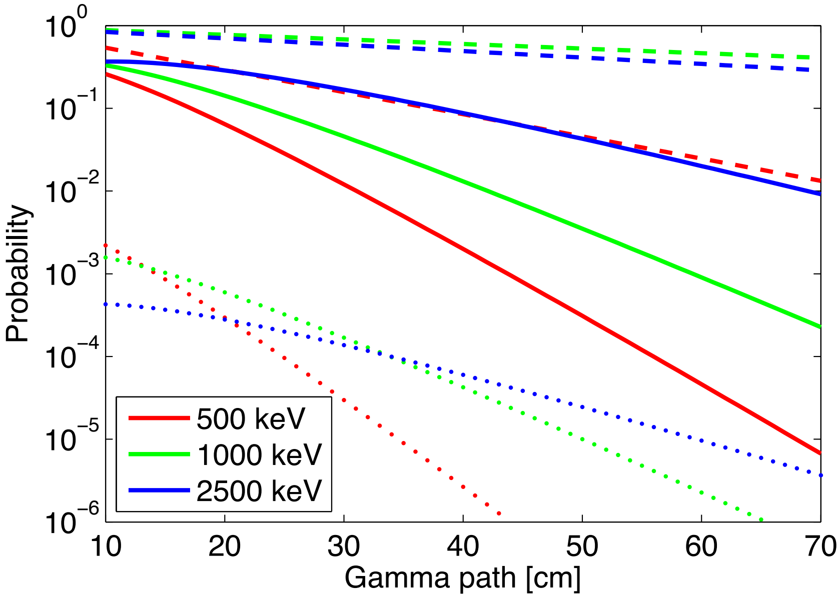

Figure 5.2: Probabilities $P_C(d, E_\gamma)$ (solid), $P_n(d, E_\gamma)$ (dashed) and $P_{BG}(d, E_\gamma)$ (dotted), plotted as a function of γ path length d for three typical γ energies. Probabilities are calculated from Eq. 5.3, 5.4 and 5.6, respectively.

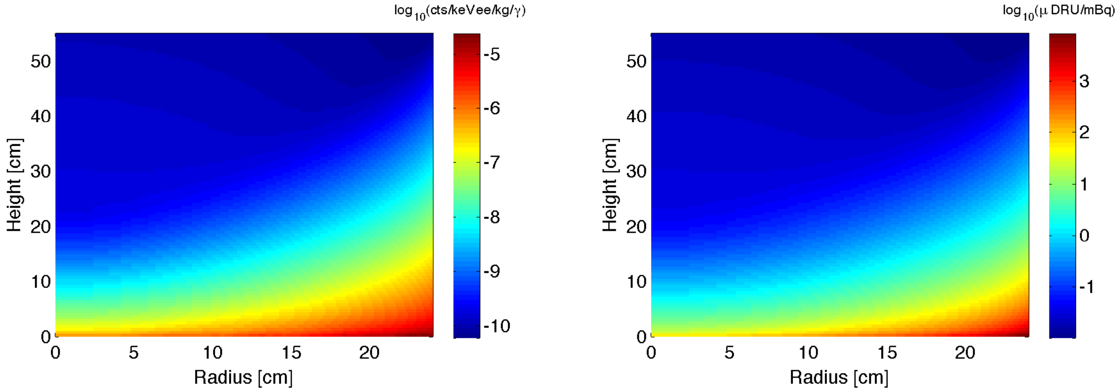

(a) (b)

Figure 5.3: (a) Distribution of scatters in the active region of a toy detector of 24 cm radius and 55 cm height, calculated for a 1 MeV isotropic γ source spread uniformly in area at the bottom of the detector. The calculation uses Eq. 5.8. Maximum source radius is 24 cm. (b) Analytic prediction for the ^{238}U background scaling factor as a function of detector position, calculated using Eq. 5.8 and the same geometry as in (a). Units are $\log_{10}(\mu\mathrm{DRU}_{\mathrm{ee}}\ \mathrm{mBq}^{-1})$.

5.2 Monte Carlo Modeling of Gamma Backgrounds

The analytic model presented in Sec. 5.1 demonstrates the power of Xe self-shielding against γ ER backgrounds. However, the absolute scaling of the model is subject to simple assumptions made about the physical processes occurring inside of the detector. For accurate modeling of the detector, a Monte Carlo simulation containing a faithful description of the detector geometry, radioactive loads, and physics processes pertinent to γ interactions in the active region was used. The simulation is the LUXSim package, the details of which are published in [128]. LUXSim is based on the Geant4 physics toolkit [115, 134].

Gamma rays were thrown within the simulation, with their resulting energy depositions and hit vertices in the active region recorded. The γ generation locations corresponded to specific major internal construction materials. This allows an estimate to be made of background rates per unit contamination for different construction components. The γ rays were generated using the Geant4 radioactive decay generator, which faithfully reproduces the γ energies, intensities, and correlations for all isotopes of interest to this work. In the cases of ^{238}U and ^{232}Th, the LUXSim decay chain generator was used, which randomly draws from a pool of all isotopes in the chains with proper weighting by parent decay branching fraction. This implicitly assumes that the decay chains are in secular equilibrium. The effects of chain disequilibrium on γ and neutron production are discussed in Ch. 6.

For the results presented in this chapter, only energy depositions were recorded in the liquid Xe volume. The simulation did not propagate the deposited energies through the generation of scintillation light or ionization electrons, and drift physics was not incorporated. This provides the most basic, assumption-free model of detector backgrounds, which can later be convolved with measured detector efficiencies and resolutions to produce corrections to background rates.

5.2.1 Analysis Cuts

During analysis of simulation results, cuts were applied to simulation output in emulation of cuts applied during analysis of real detector data. These cuts include a single-scatter cut, a low-energy cut, and a fiducialization cut. These cuts identify all events which will pass background rejection cuts during real data analysis. The fraction of events passing the cuts gives a predicted background rate within the detector fiducial volume, scaled by the amount of contamination of each isotope in each detector component. The typical unit of this factor is $\mu\text{DRU}_{\text{ee}}$ mBq^{-1}, where DRU $\equiv$ cts keV^{-1} kg^{-1} day^{-1}, and the "ee" subscript follows the convention in Sec. 2.1.2.

The single-scatter cut used an energy-weighted position resolution of 0.5 cm in XY (based on early projections from position resolution tests), and 0.2 cm in Z (based on typical S2 width and electron drift velocity). The single-scatter cut efficiency is not affected in the WIMP search energy range for any reasonable variation in resolution. The low-energy cut assumes a WIMP search energy window of 0–5 keV_{ee}. There is no significant difference in DRU event rate between this window and the 0.9–5.3 keVee window used during LUX Run 3, due to the flatness of the low-energy γ spectrum (Sec. 5.1). The fiducialization cut removes events outside of a 118 kg (Run 3) or 100 kg (expected for the LUX one year run) cylindrical volume in the detector center. The 118 kg volume has dimensions R = 18 cm, 7 cm $<$ Z $<$ 47 cm, where Z = 0 cm is defined as the bottom PMT faces. The 100 kg volume has dimensions R = 17 cm, 9 cm $<$ Z $<$ 47 cm. A reference 50 kg inner fiducial volume is also given, with dimensions R = 15 cm and 15 cm $<$ Z $<$ 40 cm.

5.2.2 Fitting High-Energy Data

Observed high-energy detector data provides a calibration of the γ energy spectrum incident at the active region. The peaks corresponding to major γ lines can be fitted to simulation predictions. By fitting the peaks simultaneously over different parts of the detector, the radioisotope decay rates in different detector construction materials can be constrained. This allows for a refined projection of low-energy γ backgrounds, using high-energy data well above the WIMP search range.

The LUXSim package is able to simulate radioactive decays from any component of the detector. This capability is immensely useful for generating projections of LUX backgrounds. However, the observed detector data is relatively insensitive to the precise locations of each different material, as many materials are layered radially, or have sizes comparable to the path length of typical γ rays, e.g. the PMTs. The model of ER contributions to detector backgrounds was therefore simplified for comparison with measured data. Materials can be grouped into three areas in the detector: top, bottom, and side. Contributions from ^{238}U, ^{232}Th, ^{40}K, and ^{60}Co were modeled from the top, bottom, and side regions, creating 12 energy spectra with which to compare measured high-energy peaks. The spectra were then given floating normalizations (units of mBq), and simultaneously fit to the measured γ energy spectrum in the detector. The best-fit spectra, along with the detector data, are shown in Fig. 5.4. The measured high-energy data used for comparison with the model is described in detail in Sec. 8.3.

The use of averaged spectra in the top, bottom and sides fits conveniently with the projected backgrounds from screening results. The PMTs and thermal insulation were found to have the dominant rates of ^{238}U, ^{232}Th, ^{40}K, and ^{60}Co decays during screening. These internals also span the top, bottom, and sides of the detector individually. These components were used as the emission geometry for the γ rays used in the study.

The best-fit radioisotope decay rates are listed next to the expectations based on screening in Table 5.1. The total isotope decay rate is found to be consistent with that predicted from screening, with an additional ^{60}Co component from activation of Cu in the detector. The amount of ^{60}Co in Cu is estimated by subtracting the known ^{60}Co concentration

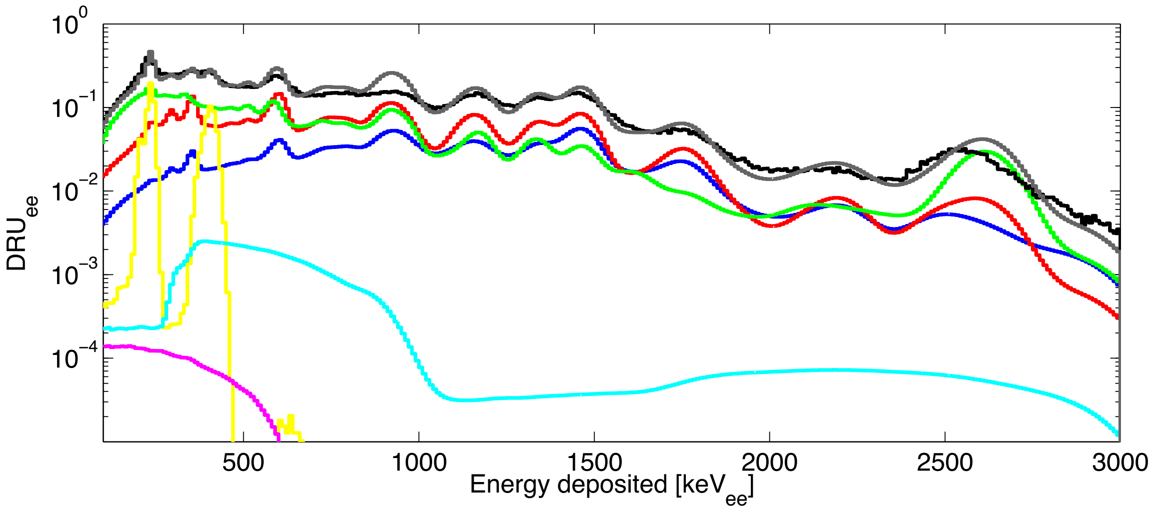

Figure 5.4: Simulation spectra providing the best fit to observed high-energy γ peaks in data. The summed γ spectra in the 250 kg fiducial volume are shown for the top (red), bottom (blue), and side (green) radioisotopes, including ^{238}U, ^{232}Th, ^{40}K, and ^{60}Co. Spectra corresponding to ^{127}Xe (yellow), ^{222}Rn (gray) and ^{85}Kr (magenta) are also included. The ^{127}Xe spectrum normalization comes from measurements of 375 keV peak size during the WIMP search run (Sec. 8.4). The ^{214}Pb (^{222}Rn) normalization is 8 mBq in the active region. The ^{85}Kr normalization is 3.5 ppt ^{nat}Kr/Xe and 20 ppt ^{85}Kr/^{nat}Kr.

in the PMTs from the total best-fit value, and multiplying the remainder of the ^{60}Co by (DRU mBq^{-1} PMT) / (DRU mBq^{-1} Cu). The estimated decay rate of ^{60}Co in Cu is 1.7 ± 1.0 mBq kg^{-1}. This is consistent with cosmogenic activation predictions in Sec. 7.3.1.

5.2.3 Low-Energy Fiducial Background Rates

Low-energy γ scatter rates in the fiducial volume were calculated from the best-fit radioisotope decay rates in Sec. 5.2.2, and from LUXSim Monte Carlo. The RZ distribution from the Monte Carlo is shown in Fig. 5.5. The individual radioisotope contributions to low-energy backgrounds in the 118 kg, 100 kg and 50 kg fiducial volumes are given in Table 5.1.

The low-energy γ background contributions from individual construction components are inferred from PMT screening results and estimates of ^{60}Co cosmogenic activation. The PMT background contribution is estimated using the PMT screening results in Table 7.3. The cosmogenic background component is estimated as described in Sec. 5.2.2. The backgrounds from the PMTs and cosmogenic ^{60}Co, along with the remainder of backgrounds attributed to radioactivity in other detector materials, are summarized in Table 5.2.

Region	**Isotope**	**Decay Rate [Bq]**		**Background Rate [mDRU$_{\mathbf{ee}}$]**	
		Screening	**Best Fit**	**118 kg**	**100 kg**
Top	^{238}U	0.58 ± 0.04	0.62 ± 0.16	0.45 ± 0.03	0.19 ± 0.02
	^{232}Th	0.16 ± 0.02	0.23 ± 0.06	0.085 ± 0.008	0.040 ± 0.006
	^{40}K	4.0 ± 0.4	2.7 ± 0.7	0.130 ± 0.009	0.066 ± 0.007
	^{60}Co	0.16 ± 0.01	0.22 ± 0.06	0.15 ± 0.01	0.074 ± 0.009
Bottom	^{238}U	0.58 ± 0.04	0.87 ± 0.22	0.28 ± 0.01	0.12 ± 0.01
	^{232}Th	0.16 ± 0.02	0.25 ± 0.06	0.075 ± 0.007	0.036 ± 0.006
	^{40}K	4.0 ± 0.4	3.8 ± 1.0	0.127 ± 0.008	0.056 ± 0.005
	^{60}Co	0.16 ± 0.01	0.30 ± 0.08	0.076 ± 0.008	0.033 ± 0.006
Side	^{238}U	0.94 ± 0.14	0.22 ± 0.06	0.059 ± 0.007	0.041 ± 0.006
	^{232}Th	0.36 ± 0.07	1.5 ± 0.38	0.22 ± 0.01	0.15 ± 0.01
	^{40}K	1.4 ± 0.1	2.4 ± 0.6	0.046 ± 0.002	0.032 ± 0.002
	^{60}Co	–	0.36 ± 0.09	0.09 ± 0.01	0.07 ± 0.01
Total				1.8 ± 0.3	0.9 ± 0.1

Table 5.1: Results from fitting averaged radioisotope spectra to measured high-energy detector data. Screening values are taken from SOLO measurements of the PMTs (corresponding to top and bottom regions), and superinsulation and plastic thermal insulation (side region). Errors on the best fit decay rate values are estimated to be 25% based on variation of fitting parameters across expected ranges. Corresponding low-energy background rates are given for the 118 kg (Run 3) and 100 kg (Run 4) fiducial volumes in the range 0.9–5.3 keV$_{\mathrm{ee}}$. Errors on low-energy background rates are statistical from simulation results only, and do not propagate errors from decay rate estimates. Total background rate errors incorporate error from both rate estimates and simulation statistics.

Component	**Background Rate [mDRU$_{\mathbf{ee}}$]**	
	118 kg	**100 kg**
PMTs	1.2	0.54
Cosmogenic ^{60}Co (Cu)	0.17	0.11
Other	0.43	0.27

Table 5.2: Gamma backgrounds from PMTs, cosmogenic ^{60}Co, and other construction materials, for the Run 3 118 kg fiducial volume and a 100 kg fiducial volume. PMT contributions are estimated from screening results (Sec. 7.3.2). Cosmogenic contributions are estimated from assuming that the dominant ^{60}Co background, after subtraction of ^{60}Co backgrounds from PMTs, comes from activated Cu construction components. The background rate from other construction materials is calculated by subtraction of the PMT and cosmogenic background rates from the total observed background rate.

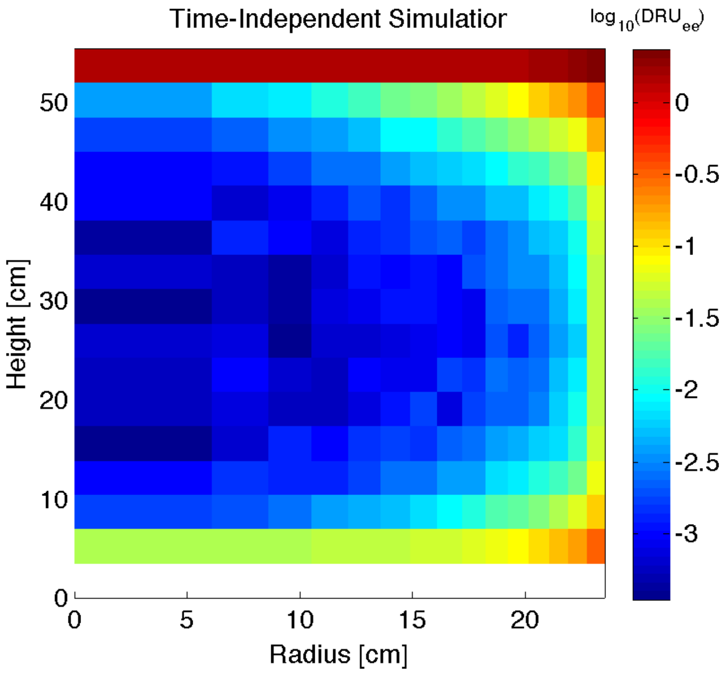

Figure 5.5: Simulated low-energy event rate from best-fit γ backgrounds, as a function of position in the detector. Simulation uses LUXSim Monte Carlo results for ^{238}U, ^{232}Th, ^{40}K, and ^{60}Co, with decay rates in different detector regions as listed in Table 5.1. Simulation uses energy range 0–50 keV$_{ee}$ (flat spectrum, normalized per keV$_{ee}$ with DRU units).

5.3 Intrinsic Background Modeling

LUX Xe is kept virtually impurity-free by the gas getter through which it circulates. The getter removes common non-noble impurities to sub-ppb levels [101]. However, there are several noble element radioisotopes which can be mixed with the Xe, and will not be removed by the getter. Several of these isotopes are modeled in this section. These isotopes have either been identified before the underground run (in the cases of ^{85}Kr, $^{129\text{m}}$Xe, and $^{131\text{m}}$Xe), or from *in situ* measurement after underground running began (in the cases of ^{220}Rn, ^{222}Rn, ^{127}Xe, and ^{133}Xe).

Intrinsic radioisotopes create a much higher ER background per decay than radioisotopes external to the active region. The two classes of decay which can generate a low-energy internal background are naked decays and semi-naked decays. Naked decays are decays in which a single low-energy emission occurs, with no complimentary photon or electron emission to veto the event. Semi-naked decays are characterized by a single low-energy emission, complimented by emission of a high-energy γ; this γ can potentially escape the active region without depositing its energy, making the decay effectively naked. In the case of a semi-naked decay, the probability of escape of the γ is proportional to $e^{-x/\lambda}$, where x is the shortest distance from the decay site to the edge of the active region, and λ is the mean free path of the γ. This can be compared to the probability of generating a background as described in Sec. 5.1. As external γ rays must penetrate into the detector and then escape again in order to generate a low-energy background, the typical path length for external γ rays is at least twice the path length for intrinsic γ rays. The background generated per intrinsic isotope decay is greatly enhanced relative to backgrounds from isotopes outside of the active region.

5.3.1 Activated Xenon Isotopes

Xenon benefits from having no long-lived (year-timescale or greater) unstable isotopes[1]. Xenon radioisotopes have half-lives on the timescale of days or weeks. The longest-lived Xe isotope is ^{127}Xe, with a half-life of 36 days. Although the Xe radioisotope half-lives are short, their signatures are still visible in LUX underground data, due to the relatively fast turnaround time between the LUX surface and underground runs.

In situ measurement from low-background underground data shows the clear signatures of four Xe isotopes: ^{127}Xe, $^{129\mathrm{m}}$Xe, $^{131\mathrm{m}}$Xe, and ^{133}Xe (see Sec. 8.4). The decay signatures of $^{129\mathrm{m}}$Xe and $^{131\mathrm{m}}$Xe are such that they are virtually incapable of creating a low-energy background. ^{127}Xe and ^{133}Xe, however, possess finite probabilities of depositing small amounts of energy through various channels. Activated Xe signatures are summarized in Table 5.3. The energy spectra for all four isotopes are shown in Fig. 5.6.

The $^{129\mathrm{m}}$Xe and $^{131\mathrm{m}}$Xe isotopes undergo isomeric transition decays, during which energy is released in a cascade of γ rays and/or conversion electrons. The low energy of the γ rays keeps them confined within the active region. The entire parent level energy is deposited, elevating the total event energy well above the upper bound of the WIMP search window. These isotopes are used as very convenient homogeneous energy calibration points at 236 $\mathrm{keV_{ee}}$ and 164 $\mathrm{keV_{ee}}$ respectively.

---

[1] The exception is ^{136}Xe, which undergoes double β decay with a half-life of 2.1×10^{21} years. The process is rare, to the point of requiring enrichment of $^{\mathrm{nat}}$Xe with ^{136}Xe in order to study the process in detail [73]. Backgrounds from ^{136}Xe are discussed further in Sec. 5.3.4.

Xenon-133 undergoes β decay to an excited state of ^{133}Cs. There is an overall 0.1% chance for ^{133}Xe to decay to the 161 keV level, and for the excited ^{133}Cs atom to then decay to ground via emission of a 161 keV γ. If this γ escapes the active region, then only the β (with effective endpoint 266 keV) remains in the active region. Fortunately, the 5.2 day half-life of ^{133}Xe quickly reduces the isotope decay rate after moving the Xe underground. The probability of low-energy background from ^{133}Xe is also subdominant to ^{127}Xe, and is not shown in Fig. 5.6.

Xenon-127 remains in the active region for much longer than ^{133}Xe due to its 36 day half-life. Xenon-127 atoms decay through electron capture, which results in an x-ray and/or Auger electron cascade. The most probable shell from which to capture an electron is the K shell, with energy 35 keV and probability 80%. If the electron is captured from the *s* orbital of the L or M shells, then the resulting cascade will have a total energy of 5.5 keV or 1.1 keV respectively. Both x-rays fall into the WIMP search window, after application of detector resolution.

The ^{127}Xe decay scheme is shown in Fig. 5.7. For most events, the x-ray / Auger electron signal is complimented by a high-energy deposition from the de-excitation of the daughter ^{127}I nucleus. However, if the ^{127}I nucleus decays via emission of a single high-energy γ, there is a finite chance of this γ escaping the active region without depositing any veto energy, creating a semi-naked x-ray event. The most probable scenario for escape of the ^{127}I de-excitation γ is when the ^{127}I nucleus is left in the 375 keV excited state, and decays via emission of a single 375 keV γ to ground. This γ has a mean free path of 2.6 cm in liquid Xe, allowing the γ sufficient mobility to escape the active region when generated near the edge of the fiducial volume. This decay path has a global 8.2% probability.

Detector backgrounds due to ^{127}Xe were modeled using LUXSim, after verification of the Monte Carlo model of the intensities and coincidences of all photon and electron emission. The backgrounds are shown as a function of position in Fig. 5.9. The background can be seen to fall off as a function of distance from the edge of the active region, tracking the 2.6 cm mean free path of the 375 keV γ for $R < 22$ cm. Fig. 5.9 includes 35 keV x-ray

Isotope	Half-Life [days]	Decay Mode	Q-Value or Parent Level [$\mathrm{keV_{ee}}$]	Decay Scheme Fig. No.	Low-Energy Background
127	36	ε	662	5.7	Semi-naked x-ray
129m	8.9	IT	236	5.8	–
131m	12	IT	164	5.8	–
133	5.2	β	427	5.8	Semi-naked β

Table 5.3: Activated Xe isotopes and their characteristic signatures. Only long-lived (>1 day) isotopes with significant abundances identified in LUX data are listed. Data is taken from [135, 136].

events, as well as the lower-energy x-rays. Note that the ^{127}I decay path is independent of the x-ray energy generated from the electron cascade.

The total ^{127}Xe decay rate in LUX was measured at 510 μBq kg^{-1} as of the beginning of the WIMP search run, on April 26. The measurement was made initially using S1-only data (Sec. 8.1), and later verified using the decay of the 375 $\mathrm{keV_{ee}}$ peak over the WIMP search run (Sec. 8.4). Xenon-127 is projected to give a background rate of 0.1 counts day^{-1} from M shell captures (1.1 $\mathrm{keV_{ee}}$), and 0.4 counts day^{-1} from L shell captures (5.5 $\mathrm{keV_{ee}}$) with the LUX Run 3 118 kg fiducial volume. The 35 keV x-ray can also be used to trace the activity, as it yields 2 counts day^{-1} in the 118 kg fiducial volume. The background contribution from ^{127}Xe is added to Table 5.6.

5.3.2 Radon

Radon is a well-known radioactive gas, commonly found seeping into households through cracks in walls and floors [137]. The most common radon isotope is ^{222}Rn, a 3.8 day radioisotope generated as part of the ^{238}U decay chain. Another common radon isotope is ^{220}Rn, part of the ^{232}Th decay chain. The half-life of ^{220}Rn is 56 s, much shorter than that of ^{222}Rn, which suppresses its observed count rate relative to that of ^{222}Rn. Radon enters the detector active region through exposed radium sources, typically resulting from manufacturing processes.

The ^{222}Rn chain is shown in Fig. 5.10. The chain consists of ^{222}Rn and four daughters, ending with ^{214}Po. The chain ends above ^{210}Pb due to the very long ^{210}Pb half-life, which

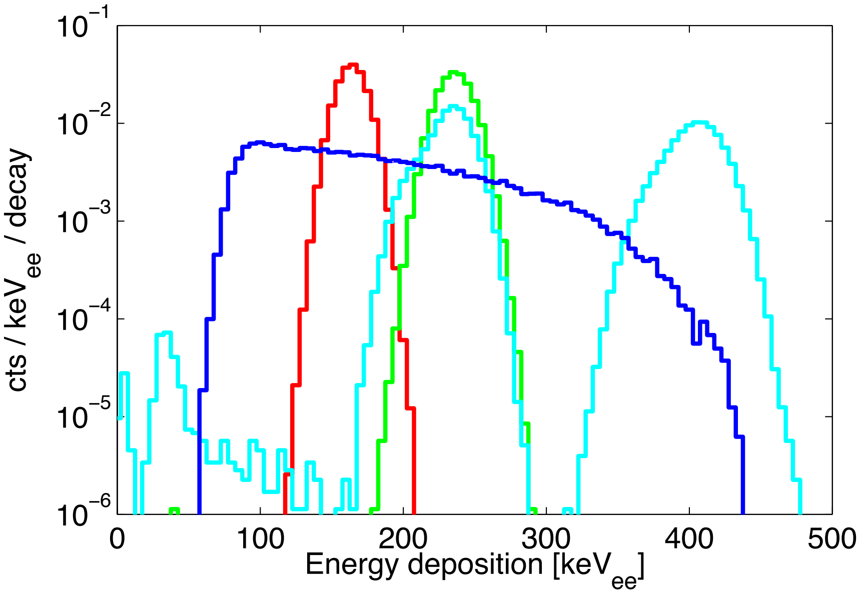

Figure 5.6: Energy deposition spectra from activated Xe isotopes. Spectra are shown for ^{127}Xe (cyan), $^{129\text{m}}$Xe (green), $^{131\text{m}}$Xe (red), and ^{133}Xe (dark blue). Decays are simualted inside a 100 kg cylindrical fiducial.

suppresses the observed ^{210}Pb rate by a factor of 3×10^6.

Of all radioisotopes in the ^{222}Rn chain, only ^{214}Pb and ^{214}Bi can potentially generate low-energy backgrounds. Both isotopes undergo β decay, with 11% and 19% probability of decaying directly to the ground state, respectively. This enables both isotopes as naked β emitters. Backgrounds from ^{214}Bi are easily mitigated through the very short half-life of its daughter, ^{214}Po, which lives for only 160 μs and decays through the unmissable emission of a 7.8 MeV α. The dominant ER background from the ^{222}Rn chain is therefore generated solely by ^{214}Pb.

The energy deposition spectrum from all ^{222}Rn chain daughters in the 100 kg cylindrical fiducial region is shown in Fig. 5.11, including energy depositions from α particles as well as γ rays and electrons. The combined energy spectrum for all ^{222}Rn chain γ rays and electrons is shown in Fig. 5.12, folding in a time coincidence cut with a 500 μs window. This suppresses the ^{214}Bi contribution by 88% due to its coincidence with ^{214}Po. The decay rates of ^{222}Rn and daughters are assumed to be equal, i.e. the chain is in equilibrium.

Measurements of ^{222}Rn α rates in LUX data indicate a departure from equilibrium condition, with an average α rate of 17.9 ± 0.2 mHz ^{222}Rn and 14.4 ± 0.2 mHz ^{218}Po in the

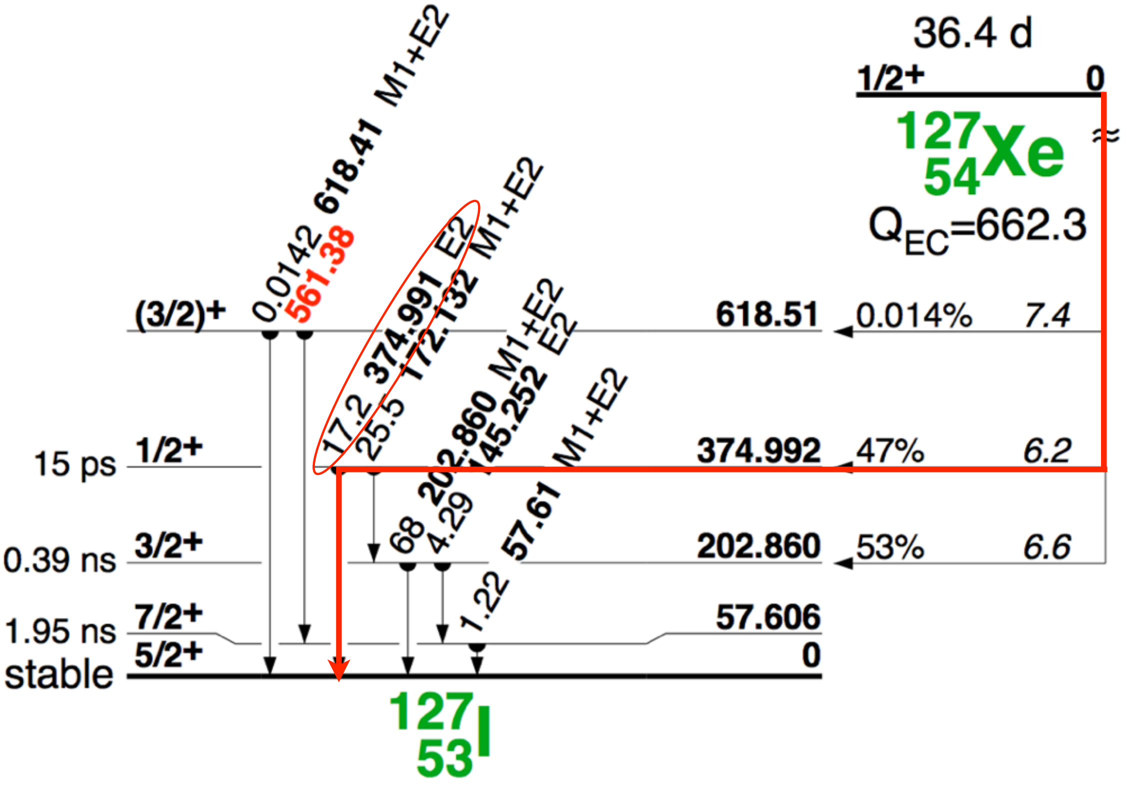
36.4 d
1/2+
0
$^{127}_{54}$Xe
Q_{EC}=662.3
0.0142 618.41 M1+E2
561.38
17.2 374.991 E2
25.5 172.132 M1+E2
68 202.860 M1+E2
4.29 145.252 E2
1.22 57.61 M1+E2
(3/2)+
618.51
0.014%
7.4
15 ps
1/2+
374.992
47%
6.2
0.39 ns
3/2+
202.860
53%
6.6
1.95 ns
7/2+
57.606
stable
5/2+
0
$^{127}_{53}$I

Figure 5.7: Decay scheme for ^{127}Xe. Scheme taken from [136]. Gamma decays are indicated at each of the arrows, along with their branching ratios and corresponding nuclear transitions. Internal conversion electrons comprise the fraction of de-excitations unaccounted for by γ emission in the diagram. The electrons generate an ER deposition at the original decay site. Of particular interest is the highlighted path in red, whereby the ^{127}I nucleus de-excites through emission of a single 375 keV γ. The undetected escape of this γ from the active region allows a naked EM cascade after ^{127}Xe electron capture, leading to a low-energy ER signature.

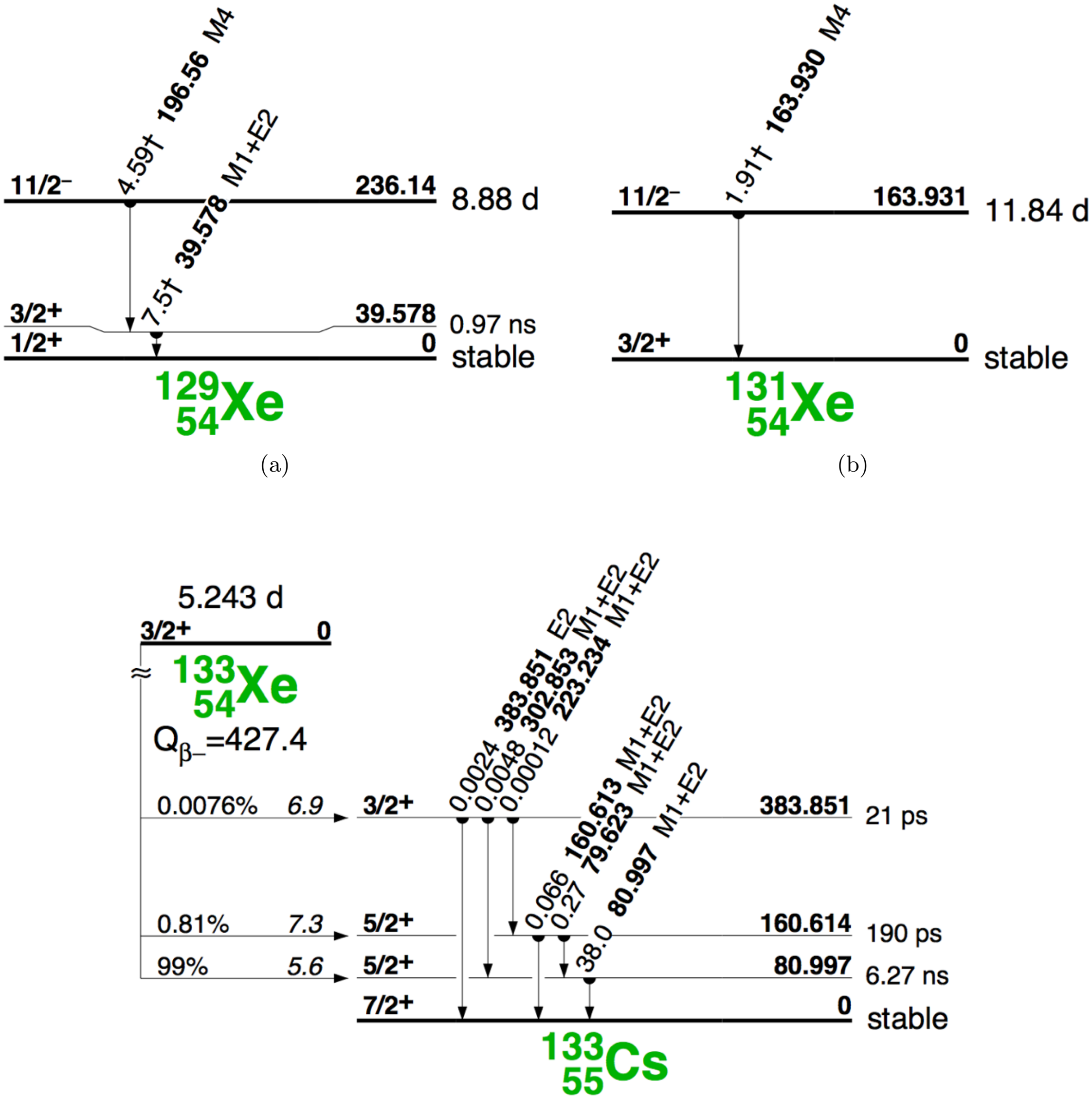
4.59† 196.56 M4
7.5† 39.578 M1+E2
11/2−
236.14
8.88 d
3/2+
39.578
0.97 ns
1/2+
0
stable
$^{129}_{54}$Xe
1.91† 163.930 M4
11/2−
163.931
11.84 d
3/2+
0
stable
$^{131}_{54}$Xe
5.243 d
3/2+
0
$^{133}_{54}$Xe
$Q_{\beta-}$=427.4
0.0076% 6.9
0.81% 7.3
99% 5.6
0.0024 383.851 E2
0.0048 302.853 M1+E2
0.00012 223.234 M1+E2
0.066 160.613 M1+E2
0.27 79.623 M1+E2
38.0 80.997 M1+E2
3/2+
383.851
21 ps
5/2+
160.614
190 ps
5/2+
80.997
6.27 ns
7/2+
0
stable
$^{133}_{55}$Cs

(a) (b)

(c)

Figure 5.8: Decay schemes for (a) $^{129\mathrm{m}}$Xe, (b) $^{131\mathrm{m}}$Xe, and (c) ^{133}Xe. Schemes are taken from [136]. Decay scheme for ^{127}Xe, and general details on decay schemes, are given in Fig. 5.7.

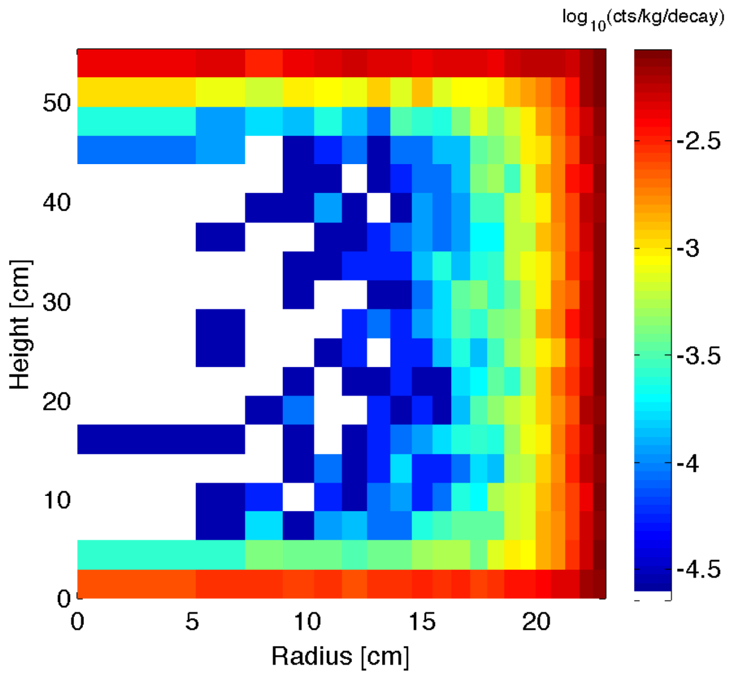

Figure 5.9: LUXSim Monte Carlo simulation of naked x-ray rates from ^{127}Xe decay, as a function of position in the active region. Rate includes all x-ray events, including the 35 keV x-ray. Rate is normalized per unit mass and per decay.

full drift region, sampled periodically over the WIMP search run [138]. There is no direct measurement of ^{214}Pb, as the β decay signature from this isotope is difficult to isolate from background, and the 30 min half-life is too long for time coincidence measurements given the background γ rate in the detector and the mobility of the ions in the active region (see Sec. 8.6). The ^{214}Pb rate in the drift region is given an upper bound of $<$8.3 mBq (90% CL) from high-energy ER spectrum measurements in a 30 kg fiducial, discussed in detail in Sec. 8.5.2. The expected ^{214}Pb rate based on a geometric series model of α decay rates is 8 mBq, discussed in Sec. 8.5.3. The lower bound on the rate is 3.5 ± 0.1 mBq in the drift region, taken from ^{214}Po decay counting. The 8 mBq and 8.3 mBq figures are added to the low-energy estimate in Table 5.6.

5.3.3 ^{85}Kr

Commercial grade Xe contains a residual concentration of Kr from atmospheric processing. Atmospheric Kr (referred to as $^{\text{nat}}$Kr) contains the manmade radioisotope ^{85}Kr, with an 11 year half-life. Krypton-85 levels in $^{\text{nat}}$Kr are $\sim$1 MBq kg^{-1} [110]. Krypton-85 undergoes

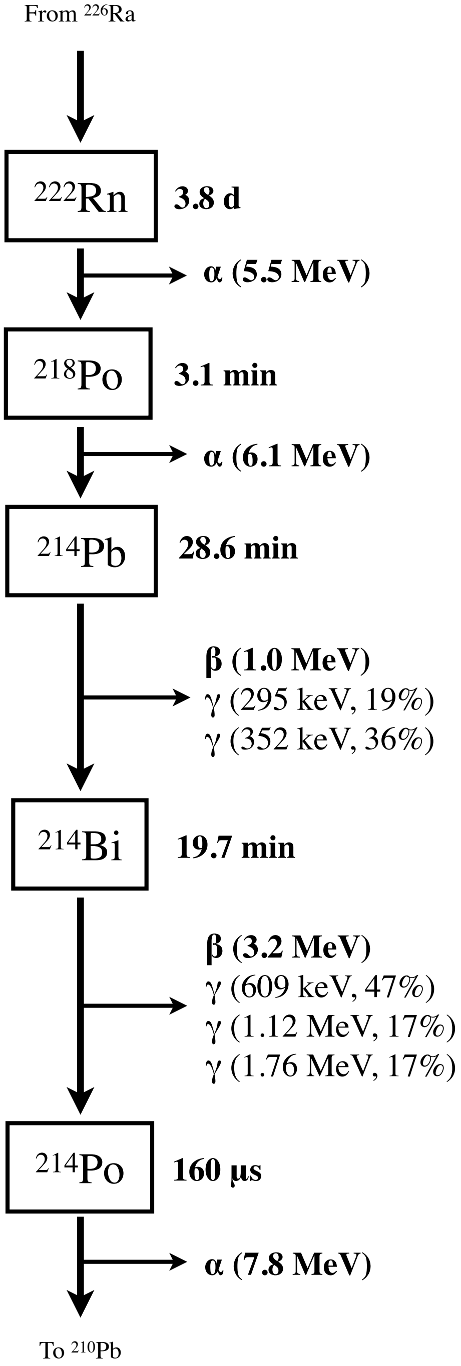

From ^{226}Ra
^{222}Rn
3.8 d
α (5.5 MeV)
^{218}Po
3.1 min
α (6.1 MeV)
^{214}Pb
28.6 min
β (1.0 MeV)
γ (295 keV, 19%)
γ (352 keV, 36%)
^{214}Bi
19.7 min
β (3.2 MeV)
γ (609 keV, 47%)
γ (1.12 MeV, 17%)
γ (1.76 MeV, 17%)
^{214}Po
160 µs
α (7.8 MeV)
To ^{210}Pb

Figure 5.10: Decay chain for ^{222}Rn. The chain is bounded at the lower end due to the very long (22 year) half-life of ^{210}Pb.

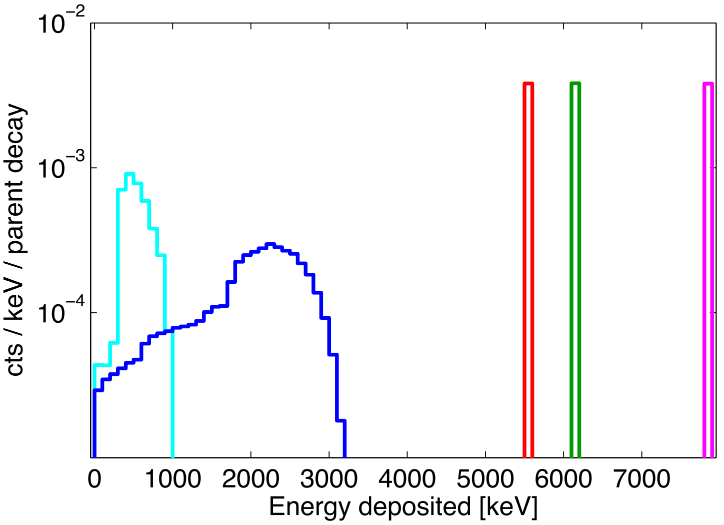

Figure 5.11: Energy deposition spectrum in the 100 kg cylindrical fiducial volume from ^{222}Rn isotope decays. Isotopes shown are ^{222}Rn (red), ^{218}Po (green), ^{214}Pb (cyan), ^{214}Bi (dark blue), and ^{214}Po (magenta). Spectrum includes deposition by γ rays, electrons, and α particles. Absolute energy deposition is shown, not translated to keV$_{\mathrm{ee}}$. Alpha energy depositions are quenched relative to γ or electron depositions, and an energy reconstruction based on electron-equivalent scaling would shift the α peak energies by a factor of ×0.75 [139].

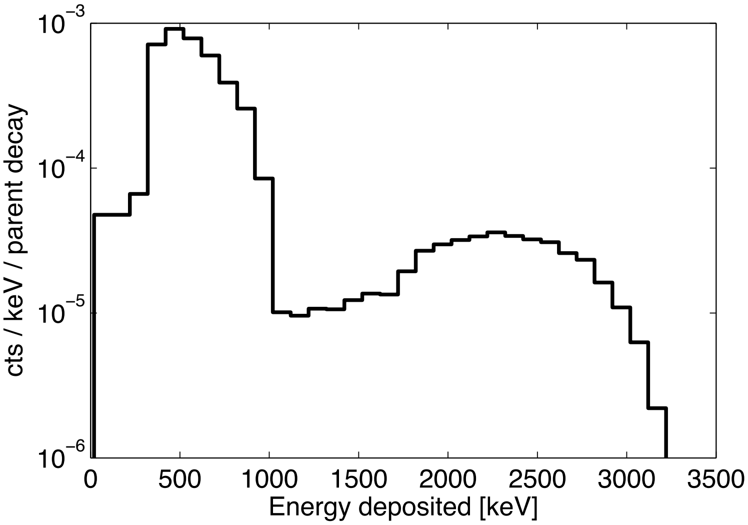

Figure 5.12: Energy spectrum in the 100 kg cylindrical fiducial volume from all summed ^{222}Rn isotope decays. The ^{214}Bi contribution is suppressed by 88% due to the inclusion of a time correlation cut, requiring events to occur >1 ms apart. Only γ and electron contributions to the energy spectrum are shown. The ^{222}Rn chain is assumed to be in equilibrium.

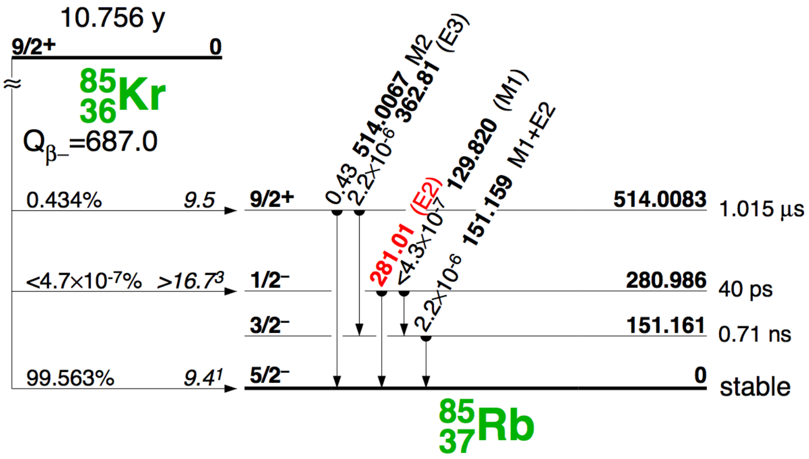
10.756 y
9/2+
0
85
36
Kr
Qβ–=687.0
0.434%
9.5
9/2+
<4.7×10-7%
>16.73
1/2–
3/2–
99.563%
9.41
5/2–
0.43
514.0067 M2
2.2×10-6
362.81 (E3)
129.820 (M1)
281.01 (E2)
<4.3×10-7
151.159 M1+E2
2.2×10-6
514.0083
1.015 µs
280.986
40 ps
151.161
0.71 ns
0
stable
85
37
Rb

Figure 5.13: Decay scheme for ^{85}Kr. Scheme details are given in Fig. 5.7.

β decay with a 687 keV endpoint and 99.6% branching ratio directly to the daughter ground state. The probability of a low-energy β event is 2×10^{-3} keV^{-1} decay [78]. The ^{85}Kr decay scheme is given in Fig. 5.13.

LUX Xe was processed with a special charcoal-based distillation column. After the final distillation process was completed, levels of $^{\text{nat}}$Kr were directly measured at 4 ppt. The average level throughout Run 3 was 3.5 ± 1.0 ppt. At this level, the low-energy differential rate in the detector is calculated to be 150 ± 50 µDRU$_{\text{ee}}$, with errors contributed both by the Kr level in the detector and by the ratio of ^{85}Kr to $^{\text{nat}}$Kr. These results are added to Table 5.6.

The ^{85}Kr signature in LUX data can potentially be measured directly, or have an upper limit set, by exploiting the 0.4% probability of β decay to the 514 keV excited state of the ^{85}Rb. LUX features 0.04 decays kg^{-1} day^{-1} of ^{85}Kr, yielding an estimated 3.6 decays from the 514 keV state in the full drift region in 90 days. The decay half-life of the state is 1 µs, leading to a "double-bang" signature (first bang from the β, second bang from the 514 keV de-excitation) which is well separated in data. The measurement will be detailed in upcoming LUX publications.

5.3.4 ^{136}Xe

Xenon-136 undergoes double β decay with a measured half-life of $(2.11 \pm 0.21) \times 10^{21}$ yrs [73]. The low-energy component of the ^{136}Xe two-neutrino double β spectrum is shown in

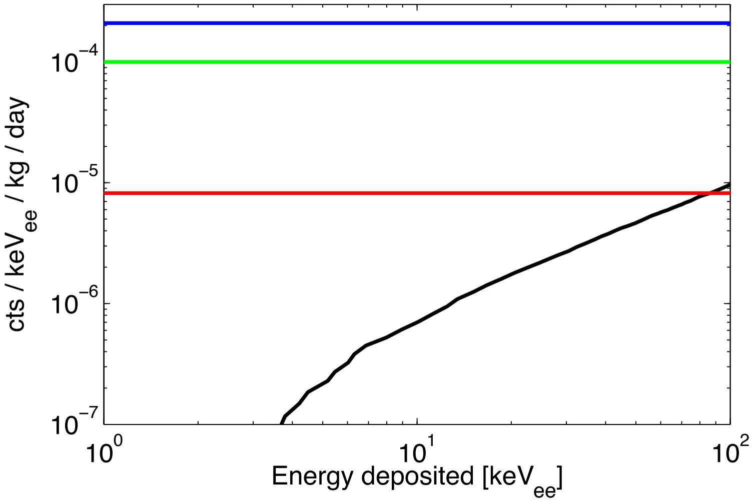

Figure 5.14: Two-neutrino double β decay spectrum for ^{136}Xe (black), shown in comparison with ^{214}Pb (blue) and ^{85}Kr (green) intrisic background sources in LUX. Also shown is the ER background rate from p-p solar neutrino scattering (red), discussed in Sec. 5.7 [76]. The ^{136}Xe lifetime is 2.1×10^{21} years, taken from measurements by the EXO experiment [73]. The detailed low-energy spectrum is adapted from the projected 10^{22} year lifetime curve in [77].

Fig. 5.14. The ER spectra for the other intrinsic background sources in LUX are shown for comparison. The low-energy component of the spectrum does not produce a significant background for dark matter search in LUX. The high-energy portion of the spectrum (>100 keV) is potentially visible in tonne-scale Xe experiments such as LZ, after suppression of ^{222}Rn and ^{85}Kr signatures. This portion of the spectrum does not create a dark matter search background.

5.4 Gamma-X Background Modeling

A "gamma-X" event is defined as a multiple-scatter γ event within the active region, with only one vertex in the drift region. The resulting signal has a composite S1 from all vertices, but S2 signal from only the drift region vertex. The event escapes the standard multiple scatter cuts, as only one S2 vertex is found. The event will also have a reduced S2/S1 ratio, greatly reducing ER discrimination efficiency. This is illustrated in Fig. 5.15.

The most likely scenario for the generation of a gamma-X event is a γ emitted from underneath the cathode grid, scattering once in the drift region and one or more times in the reverse field region (RFR, defined in Sec. 2.2.3). The reversed field orientation underneath the cathode grid will push electrons away from the drift region, resulting in only the drift region ionization signal being detected. The most likely emission source for γ rays scattering in the reverse field region is the bottom PMT array, given that γ emission in the detector is dominated by the PMTs.

The PMT radioactivity simulations described in Sec. 5.2 were analyzed for the rate of coincident scatters above and below the cathode grid. Scatters were counted in three separate regions: the drift region, the RFR (between the cathode grid and the bottom grid, where the electric field is $\sim$4 kV cm^{-1} upward), and the zero-field region or ZFR (between the bottom grid and bottom PMTs, where the electric field is $\sim$0). The regions were partitioned in this manner to account for their significantly different electric fields, which influences scintillation yield [126]. A gamma-X event is considered to be an event in which (a) energy deposition in the drift region is non-zero and passes standard multiple-scatter cuts, and (b) energy deposition in either the RFR or ZFR is non-zero. The effects of non-uniform photon yield and light collection were convolved with each event to obtain a realistic estimate of the resulting signal size.

For the results presented in this work, energy depositions were not recorded in the liquid Xe space contained between the bottom trifoils, directly above the bottom PMTs. A basic cut on S1 hit pattern will be able to discriminate against these events with high efficiency. A PMT with a scatter directly in front of it will collect a large fraction of the generated photons, in sharp contrast to the uniformly-distributed S1 hit pattern typical of drift region scatters.

5.4.1 Model of Spectral Shape and Position Distribution

Gamma-X events are the result of two or more scatters. Gamma-X events become a background when the reconstructed energy of the event falls in the WIMP search energy range. The low-energy end of the distribution is expected to be dominated by events with two scatters, as the probability of scattering more than twice with the total energy deposited still within the low-energy regime is very low (see Sec. 5.1). The energy deposited in each vertex is independent and randomly distributed. The parameter space resulting in a total energy

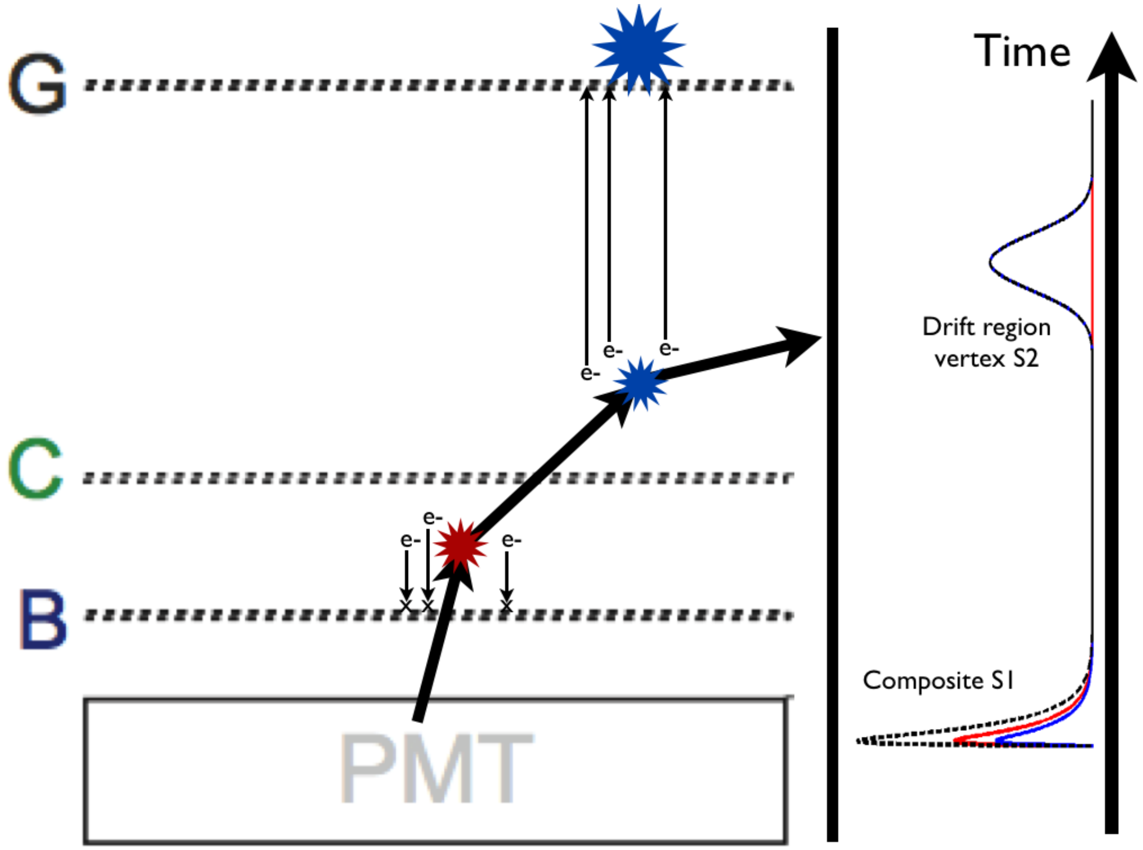

Figure 5.15: Qualitative representation of a gamma-X event. (Left) A γ scatters multiple times in the active region, with a single vertex in the drift region (small blue) and one or more vertices under the cathode (red). The resulting signal is shown at right as a function of time. The measured S1 signal is a composite signal from all vertices. Ionization is not collected from the vertices under the cathode. The resulting event has a single S2 which has a contribution only from the drift region vertex (large blue). (Right) The resulting waveform with detected S1 and S2 signals (black dashed). Shown are the contributions from the drift region vertex (blue) and RFR vertex (red). The reduced S2/S1 ratio for the event greatly lowers discrimination efficiency.

deposition in the range E to $E + dE$ is therefore defined by the addition of two independent, uniformly distributed random variables, the distribution of which increases linearly with energy in the low-energy regime. Note that this distribution is well distinguished from the typical falling exponential WIMP spectrum.

The most likely physical location for gamma-X events follows the shortest path of the γ through the active region. In the low-energy limit, γ rays deviate insignificantly from their original trajectory after scattering, and the probability of scattering at any point along the track is constant. It is therefore expected that, for a given gamma-X event, the under-cathode vertex is located randomly anywhere along the track between the bottom PMTs and the cathode, and the drift region vertex is located randomly anywhere along the track above the cathode. For low-energy events the most probable overall γ trajectories are near the corner of the detector, where the total amount of Xe to be traversed is minimized.

For gamma-X events with a vertex in the fiducial volume, the most likely γ trajectory is one which diagonally traverses the active region, radially outward. This minimizes the total γ path length while still allowing the γ to clip the corner of the cylindrical fiducial region. The highest concentration of under-cathode vertices is therefore expected to be clustered toward the center PMTs.

5.4.2 Estimating Signal Size

For a gamma-X event, the S1 signal size is the sum of signals from all vertices. Each vertex has a different light collection factor associated with it, as well as a different light yield. The composite S1 signal is calculated as

$$S1 = \sum_j E_j \times Y_j \left(E_j, \epsilon_j\right) \times \alpha_j \left(\vec{x}_j\right), \tag{5.9}$$

where, for the jth vertex in the event, E_j is the energy deposited at that vertex; $Y_j \left(E_j, \epsilon_j\right)$ is the light yield, in units of photons generated per unit energy deposition; and $\alpha_j \left(\vec{x}_j\right)$ is the geometric light collection efficiency, in units of photoelectrons detected per photon generated, at position $\vec{x}_j$. $Y_j \left(E_j, \epsilon_j\right)$ is a function both of the energy deposited at the vertex and the electric field in the local area of the vertex, defined as ϵ_j.

For this study, it is taken as a simple assumption that energy is reconstructed proportional to S1. Recombination fluctuations are also neglected in the model. Under these assumptions, the reconstructed energy E_{rec} is proportional to the total detected S1 signal, from all gamma-X vertices. E_{rec} is calculated from the true energy deposits at each vertex as

$$E_{rec} = \sum_j E_j \times \frac{\alpha_j}{\alpha_{DR}} \times \frac{Y\left(E_j, \epsilon\right)}{Y\left(E_{DR}, \epsilon\right)}, \tag{5.10}$$

where E_j is the energy deposited at vertex j, and the DR subscript denotes the vertex in the drift region. It is further assumed that the S2 signal can be calculated by similar methods, proportional to the total energy deposited at the drift region vertex. This enables a model of the S2/S1 band to be calculated as

$$S2/S1 = \frac{E_{DR}}{E_{rec}}. \tag{5.11}$$

In the case of completely uniform light collection (i.e. α is a single constant for the whole detector), and ignoring the 20% variation in light generation per unit energy from 0–5 keV$_{\mathrm{ee}}$, the S2/S1 band is skewed as shown in Fig. 5.16. The effects of light yield variation are incorporated into simulation results, discussed in Sec. 5.4.3.

5.4.3 Simulation Results

Simulations of radioactivity from the bottom PMT array are used to evalute the total expected gamma-X event rate in LUX. The simulations use 3000 livedays' worth of events for decays of ^{238}U, ^{232}Th, ^{40}K, and ^{60}Co, where the length of time represented is based on PMT screening results (Table 7.3). These are the same simulations performed for the analysis in Sec. 5.2, where an additional analysis was performed to track energy depositions in the RFR and ZFR regions for each event. Data tables for $Y_j\left(E_j, \epsilon_j\right)$ are taken from work based on [90], using LUX electric field values in each region.

$\alpha_j\left(\vec{x}_j\right)$ is computed from LUXSim optical photon simulations. The simulations were performed by launching optical photons homogeneously and isotropically throughout the

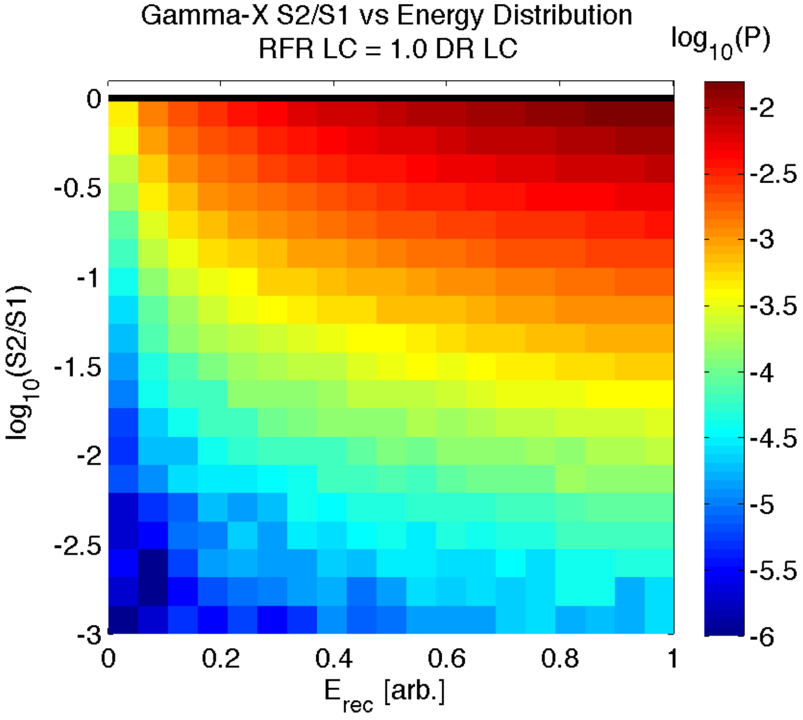

Figure 5.16: Analytic calculation of the ER event distribution in S2/S1 vs energy from Eq. 5.10 and 5.11, assuming $\alpha_{UC}/\alpha_{DR} = 1$. A flat energy deposition spectrum is assumed, appropriate to low-energy scatters. The nominal S2/S1 band location is at $\log_{10}$(S2/S1)=0 (black band). Variation in S2/S1 due to recombination fluctuations is not accounted for (i.e. the nominal band has 0 width in S2/S1). Density scale is normalized such that the sum of the bins is 1.

entire active region, as was done in the study described in Sec. 3.2 and 3.3. The geometric light collection efficiency map $\alpha_j\left(\vec{x}_j\right)$ is built by partitioning the active region into cuboid cells, and counting photoelectron signals in each PMT per photon generated in each cell. This provides a three dimensional map of geometric light collection efficiency, with statistical errors <1%.

The rate of all gamma-X events in the detector is shown in Fig. 5.17. The measured rate of events in both the full drift region and fiducial region is well-matched by a linear function, as predicted in Sec. 5.4.1. The linear function is extrapolated down to very low energies, where no simulation statistics are available due to the rare nature of fiducial gamma-X events. An integration of this event rate over the LUX WIMP search range as a function of WIMP search window energy bounds is shown in Fig. 5.18. For the LUX WIMP search range 0.9–5.3 $\mathrm{keV_{ee}}$, and the cylindrical 100 kg fiducial, the projected WIMP-like gamma-X event rate is 1.2×10^{-4} counts day^{-1}. This rate is before considerations of ER/NR discrimination, or application of any gamma-X veto analysis cuts. This rate is subdominant to background contributions from single-scattering γ rays considered in Sec. 5.2. The rate is added to the background summary in Table 5.6.

The spatial distribution of gamma-X events from the simulation is shown in Fig. 5.19. The density plots simulaneously display the locations of the drift region and under-cathode vertices for all events. From the plot in Fig. 5.19b, an obvious spatial correlation is seen for events where the drift region vertex falls within the fiducial volume. The events under the cathode are clustered at the center of the detector, matching γ shortest-path arguments discussed in Sec. 5.4.1.

5.5 Internal Neutrons

5.5.1 Neutron Yield Rates

5.5.1.1 PMTs

Neutrons are commonly generated from three sources. These sources include (α,n) processes, ^{238}U spontaneous fission, and muon spallation / capture. The first two sources are discussed

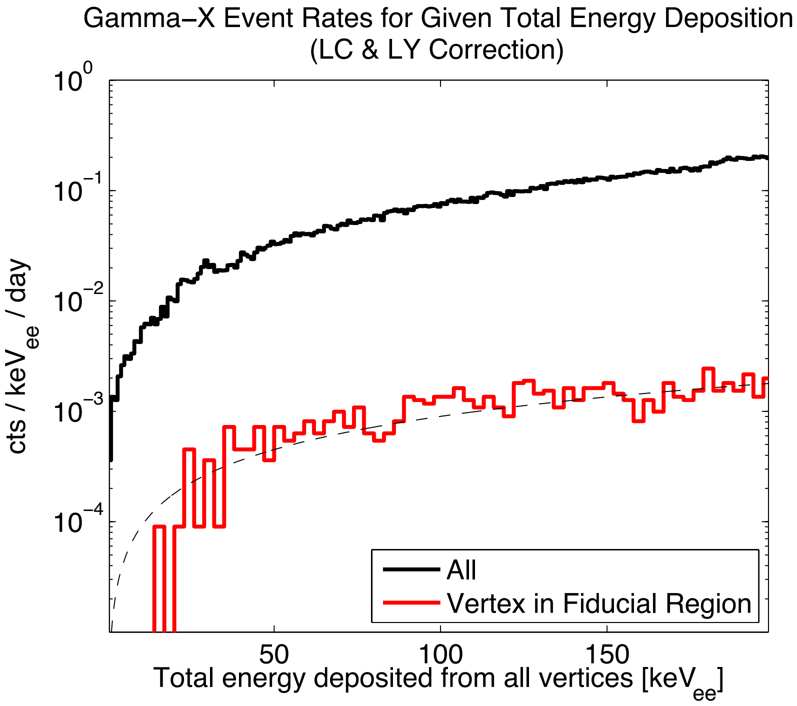

Figure 5.17: Gamma-X event rate in LUX from bottom PMT array radioactivity, with contributions from ^{238}U, ^{232}Th, ^{40}K, and ^{60}Co. Rates are normalized using PMT counting data in Table 7.3. Events consist of a scattering vertex in the drift region which passes the simulation single-scatter cut, combined with an energy deposition underneath the cathode. Energy depositions are convolved with light collection maps. The light collection maps account for geometric photon collection efficiency and variation in absolute photon yield with electric field magnitude. Histograms correspond to all gamma-X events (black), and events where the drift region vertex is found within a cylindrical fiducial volume of R < 18.3 cm, ΔZ < 32 cm, centered in the middle of the active region (red). The fiducial rate is fit with the linear function $y = \left(9 \times 10^{-6}\,\text{cts}\ \text{keV}_{\text{ee}}{}^{2}\ \text{day}^{-1}\right) \cdot E$.

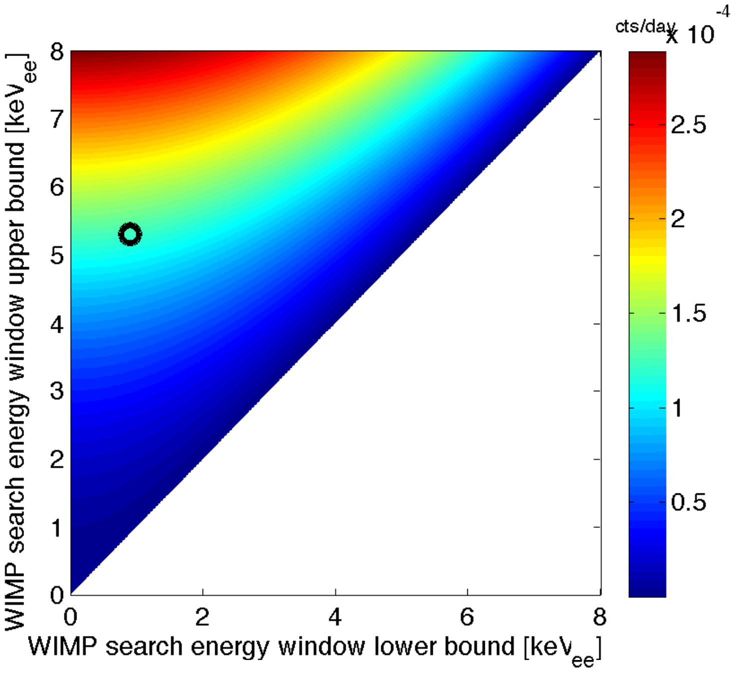

Figure 5.18: Integrated WIMP-like gamma-X event rate in LUX in the 100 kg fiducial volume described in Fig. 5.17, as a function of WIMP search window energy bounds. The curve integrates the linear fit to simulation results in Fig. 5.17. Discrimination of gamma-X events is not included. The LUX WIMP search energy range from Run 3, 0.9–5.3 keV$_{\text{ee}}$, is marked with the black circle.

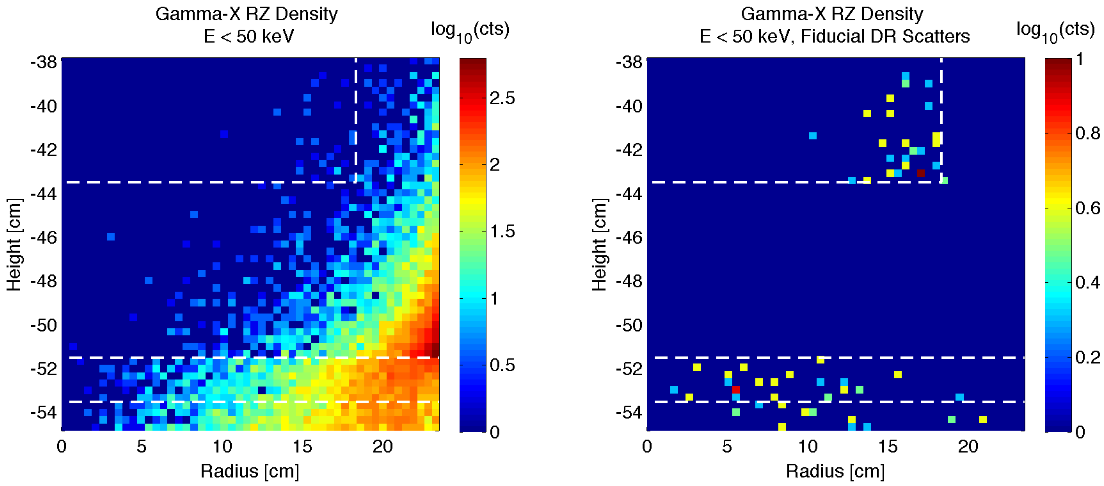

(a)

(b)

Figure 5.19: Gamma-X spatial distribution in the detector, for (a) all gamma-X events and (b) gamma-X events with the drift region vertex falling inside the fiducial volume. The plots simulaneously display the locations of the drift region and under-cathode vertices for all events.

in this section. The neutron yield from muon processes is discussed in Sec. 5.6.

Neutrons in LUX are generated primarily through (α,n) processes in detector materials. Alpha particles are generated from radioisotope decays. These particles interact in surrounding detector materials, generating neutrons. The most common radioisotopes generating α particles in detector construction materials are those found in the ^{238}U and ^{232}Th decay chains. A full discussion of (α,n) neutron yields from ^{238}U decays in common detector materials is given in Sec. 6.5.

Neutrons are also generated through spontaneous fission of ^{238}U. Under this process, the ^{238}U nucleus splits into two or more fragments, and releases of order 10 MeV in the form of neutrons and/or γ rays. The branching ratio for this decay process is 5.4×10^{-7} fissions per ^{238}U decay [78]. The average neutron yield is 2.07 n decay^{-1} [140]. In modeling work, it is conservatively assumed that neutrons are individually detected from all fission events. In reality, multiple neutrons and/or γ rays would greatly reduce the NR background prediction from this source, as the interaction of multiple secondary particles in the detector would serve as an immediate veto of the event.

The (α,n) yield from LUX PMTs has been calculated for two scenarios. The first scenario is the LUX neutron yield baseline case, where it is assumed that the measured ^{238}U and ^{232}Th contamination per PMT is evenly distributed by mass amongst all PMT construction components. The second, most-conservative scenario assumes that all contamination is concentrated in the construction component which gives the highest (α,n) yield.

Neutron yields were calculated using the PMT construction material compounds and masses supplied by Hamamatsu in a confidential communication. The calculated neutron yield values for the baseline contamination scenario are given in Table 5.4. The summed neutron yields are listed with and without the additional conservative contribution from ^{238}U spontaneous fission neutrons. The baseline neutron yield from LUX PMTs is 1.2 n PMT^{-1} yr^{-1}.

The (α,n) yield from the PMTs is significantly enhanced if all ^{238}U chain radioisotopes are concentrated in the Al construction material. Al is present in pure form in the seal between the PMT windows and bodies. It should be noted that Al does not have the highest (α,n) yield per compound; however, all compounds with higher (α,n) yields than Al are mixed

	(α,n) Neutron Rate [n/PMT/yr]		Total (α,n) Neutron Rate [n/PMT/yr]
	^{238}U	^{232}Th	
Sum ((α,n) only)	0.60	0.21	0.81
Sum ((α,n) + fission)	0.93	0.21	1.15

Table 5.4: (α,n) yields for each PMT construction component, sorted by total neutron contribution. Yields for ^{238}U and ^{232}Th are calculated using the USD Neutron Yield Tool [141, 142] Normalized yields integrate over all neutron energies above 100 keV. Values for several lighter elements are cross-checked with (α,n) yields from [143], and are found to agree within 10%. PMT construction components were obtained by confidential communication with Hamamatsu Photonics K.K.

with compounds with very low (α,n) yields in construction materials. This dilutes the total neutron yield from those construction materials, rendering their background contributions lower than that from the Al seals. The neutron yield in the scenario of contamination only in the Al is 4.2 n PMT^{-1} yr^{-1} from ^{238}U and 1.4 n PMT^{-1} yr^{-1} from ^{232}Th. The total is a factor ×5 above the rate predicted from the baseline scenario.

5.5.1.2 ^{210}Pb Daughters

Accumulation of ^{210}Pb on detector surfaces, in particular the PTFE reflector panels, contributes to the neutron background in LUX. Lead-210 is deposited on the PTFE surfaces as a result of plate-out of airborne ^{222}Rn daughters during construction. Lead-210 undergoes a three-stage decay to stable ^{206}Pb, limited by the ^{210}Pb 22 year half-life. This decay chain includes ^{210}Po, which generates a 5.3 MeV α, which can undergo (α,n) processes in fluroine. The ^{210}Pb decay chain is shown in Fig. 6.1 in the righthand column.

Fluorine is of particular concern for (α,n) production, since it has the highest (α,n) yield of all large-mass detector materials present in LUX construction. The neutron yield curve as a function of incident α energy is shown in Fig. 6.4. At 5.3 MeV, the neutron yield from from fluorine is 10^{-5} n α^{-1}. PTFE is expected to be extremely radiopure, supported by counting results listed in Table 7.5. The ^{210}Po decays on the PTFE surface are therefore expected to dominate the neutron production rate from PTFE.

Alpha rate measurements from Run 3 yield a clear measurement of ^{210}Po on the PTFE reflector panels [138]. The measured ^{210}Po decay rate is 14 mHz. This rate corresponds to the measurable decays on PTFE, which are assumed to correspond to α particles which are emitted toward the active region and deposit all of their energy in the liquid Xe. Under this assumption, the actual ^{210}Po decay rate is 28 mHz. It is further assumed that there are a factor ×2 more ^{210}Po decays occurring on the back side of the PTFE panels (on the face pointing radially outward from the detector center), which are unmeasurable. This yields a total decay rate of 56 mBq, conservatively rounded up to 60 mBq to include miscellaneous PTFE surfaces in the detector.

The fraction of α particles interacting in the PTFE is assumed to be ×1/2 the total number generated, yielding a 30 mHz rate of α particles incident on PTFE. Taking the figure 10^{-5} n α^{-1}, this corresponds to 9.5 n yr^{-1} from PTFE. This is 6% of the total neutron generation number from the PMTs, under the baseline neutron yield assumption.

5.5.1.3 Cryostats

The LUX cryostats were selected from a batch of extremely low-radioactivity titanium [144]. One of the material batches was identified by γ screening to have a ^{238}U chain imbalance, with a measured 6.2 ± 1.2 mBq kg^{-1} ^{238}U early sub-chain concentration, and <0.19 mBq kg^{-1} ^{226}Ra sub-chain concentration. As discussed in Ch. 6, the ^{238}U early sub-chain yields substantially fewer neutrons per decay than does the ^{226}Ra sub-chain. Assuming a negligible concentration of ^{226}Ra sub-chain in the cryostats, the neutron yield from the cryostats is dominated by ^{238}U spontaneous fission. At the measured 6.2 ± 1.2 mBq kg^{-1} ^{238}U early sub-chain concentration, assuming that both cryostats were made from the batch showing the positive measurement, the cryostats generate a total of 45 n yr^{-1}, 30% of the neutron yield from the PMTs under the baseline yield scenario. The background rate in the fiducial region per neutron generated from the cryostats is also significantly lower than the rate per neutron generated from the PMTs, due to the greater distance of the cryostats from the active region, and the intervening construction materials.

5.5.2 Neutron Backgrounds

LUXSim Monte Carlo simulations were used to predict the background contribution from each of the neutron sources listed in Sec. 5.5.1. The rates are found after application of single-scatter, fiducial, and energy cuts as outlined in Sec. 5.2.1. In addition, an EM veto cut is imposed, which vetoes inelastic neutron scatters. The EM veto cut requires that the absolute energy deposited by NR from the neutron scatter is less than the absolute energy deposited by ER. In practice, this discards all inelastic events within the 5–25 keV_{nr} WIMP search range, as the lowest γ energy from neutron inelastic scattering is 40 keV_{ee} from ^{129}Xe.

NR background rates are projected for a 100 kg fiducial and 5–25 keV_{nr} energy range. NR background rates from the neutron sources outlined in Sec. 5.5.1 are listed in Table 5.5. Only relevant scaling factors are calculated, based on neutron generation mechanism expected for each source. The total NR rate in the 5–25 keV_{nr} WIMP search range, projected from all sources, is 150 ± 20 nDRU_{nr}. This rate translates to 3×10^{-4} WIMP-like NR events per day passing all analysis cuts.

5.6 External Gamma and Neutron Backgrounds

Gamma and neutron fluxes from outside of the LUX detector were investigated in [71]. The background contributions from all external sources were found to be rendered subdominant to ER backgrounds from internal sources. External sources are very effectively moderated by the LUX water shield, which provides >2.5 m of shielding on all sides of the detector.

There is no significant γ flux from cavern rock into the active region, due to the presence of the water shield. Gammas from ^{232}Th chain decays with energy 2.6 MeV are attenuated in the water shield with a characteristic length of 23 cm. The water shield is 2.5 m thick at minimum, giving a suppression of nearly five orders of magnitude for these γ rays. The full γ energy spectrum from cavern rock γ rays was used in the water shield Monte Carlo study which generated the data for Fig. 2.8. The study shows an additional γ suppression factor of $\times 1/5$ below the consevative estimate based on 2.6 MeV γ rays. This is due to the shorter mean free path of γ rays with lower energy, which comprise the majority of the incident γ energy spectrum. Using a conservative figure for the total γ flux in the cavern based on the assumption of 100% rhyolite rock, the estimated low-energy background contribution from external γ rays is 27 nDRU_{ee} [71]. This figure is over four orders of magnitude below the PMT background contribution.

Component	**NR Scaling Factors [nDRU$_{\text{nr}}$ mBq^{-1}]** ^{238}**U Fission**	^{238}**U (α,n)**	^{232}**Th (α,n)**	**Total Background Rate [nDRU$_{\text{nr}}$]**
PMTs	$(4.7 \pm 0.8) \times 10^{-2}$	$(5.0 \pm 0.9) \times 10^{-2}$	$(7.7 \pm 0.14) \times 10^{-2}$	140 ± 20
PTFE (^{210}Pb)		$(3.7 \pm 0.1) \times 10^{-2}$		4.0 ± 0.1
Cryostats	$(0.74 \pm 0.12) \times 10^{-2}$			11 ± 2
Total				**150±20**

Table 5.5: Predicted low-energy NR rates in a 100 kg cylindrical fiducial volume, from neutrons generated in LUX internals. Fiducial and single-scatter cuts are applied as described in Sec. 5.2.1, as well as an EM veto cut described in Sec. 5.5. Rates are taken over the NR energy range 5–25 keV$_{\text{nr}}$.

High-energy muon spallation or muon capture events in the cavern provide a third source of neutrons, in addition to (α,n) and spontaneous fission processes discussed in Sec. 5.5. Neutrons generated in the cavern through (α,n) and spontaneous fission processes have energy on the scale of MeV, and are moderated below consideration by the water shield, as discussed in Sec. 2.2.7. Neutrons generated from muon interactions in cavern rock have average energies on the scale of 100 MeV, with a high-energy tail extending through several GeV [109]. The neutrons in this high-energy tail are able to penetrate the water shield at rates sufficient to generate a non-negligible NR event rate in the detector. The estimated rate of low-energy NR events passing the standard single-scatter, fiducial, low-energy and EM veto cuts due to muon-induced neutrons from cavern rock is 54 $\mathrm{nDRU_{nr}}$ [71]. This rate is a factor ×1/3 that expected from the PMTs, assuming the baseline PMT neutron yield scenario.

Muon interactions in the water shield can also act as a source of neutrons near the LUX detector. Muon capture or spallation on O nuclei in the water shield can lead to hadronic showers, creating a neutron flux originating in the water shield itself. The estimated rate of low-energy NR events from muon interactions in the water shield, which pass the standard single-scatter, fiducial, low-energy and EM veto cuts, is 120 $\mathrm{nDRU_{nr}}$ [71]. This rate is comparable to the neutron rate from the PMTs, assuming the baseline PMT neutron yield scenario.

5.7 Neutrino Backgrounds

Neutrinos create a sensitivity floor for dark matter direct detection experiments. Neutrinos with energies on the order of MeV generate an ER scattering signature. Higher-energy neutrinos, with energies on the order of 10–100 MeV, generate NR signatures. As the neutrino interaction cross-section is extremely small, dark matter experiments cannot be shielded from neutrinos. Fiducial and single-scatter techniques do not reject these events; the events are always single-scatter, and are distributed homogeneously in the active region. Neutrino signatures therefore represent the “ultimate sensitivity” of direct detection experiments using technologies such as those in LUX[2]. The ER and NR signatures from neutrinos are too rare to be seen in the LUX fiducial volume; however, their signatures will be apparent in tonne-scale detectors such as LZ.

Neutrinos from the p-p solar chain dominate the neutrino ER event rate, with a subdominant contribution from neutrinos generated in ^{7}Be(e-,ν)^{7}Li solar reactions. The scattering spectra are shown in Fig. 5.20a. The p-p ER spectrum is flat through 100 keV$_{\text{ee}}$, with a maximum energy deposition of 260 keV$_{\text{ee}}$. The flat low-energy rate is 8×10^{-6} DRU$_{\text{ee}}$. The ER signature from these neutrinos can only be rejected by S2/S1 discrimination. LUX is portentiously already reaching the limit of p-p neutrino detection. The Run 3 WIMP search data is estimated to have 0.7 p-p neutrino events in the full 250 kg drift region, within the WIMP search energy range. The 118 kg fiducial region expectation integrated over the full energy spectrum is 6 events.

Neutrinos with energies on the order of 10–100 MeV generate NR signatures in significant rates for large dark matter experiments, with energies on the order of 1–100 keV$_{\text{nr}}$ [146]. These high-energy neutrinos are sourced from ^{8}B solar decays; high-energy proton-^{3}He collisions in the sun; cosmic ray interactions in the upper atmosphere; and the diffuse supernova background, generated from the past history of all supernova decays in the universe. These sources form a NR rate floor across all relevant energies for WIMP dark matter searches. The spectra are shown in Fig. 5.20b. As these recoils are NR signatures, there is no means with which to distinguish their scattering signatures from those of WIMPs.

5.8 Fiducial Volume Optimization

The fiducial volume definitions used in Run 3 and for Run 4 projections were simply defined as cylinders, where the observed background rate is minimized. From observations of the low-energy contours from non-homogeneous sources, it is clear that the optimal fiducial shape is not cylindrical.

---

[2] The presence of a neutrino background does not strictly preclude WIMP detection with a liquid noble TPC. If the neutrino background spectrum is well understood, then subtraction of the background is possible. However, the sensitivity of the experiment would then scale as $\sqrt{Mt}$, rather than Mt in the background-free case projected for current and near-future detectors [145]. This creates a significant impediment to gains in detector sensitivity.

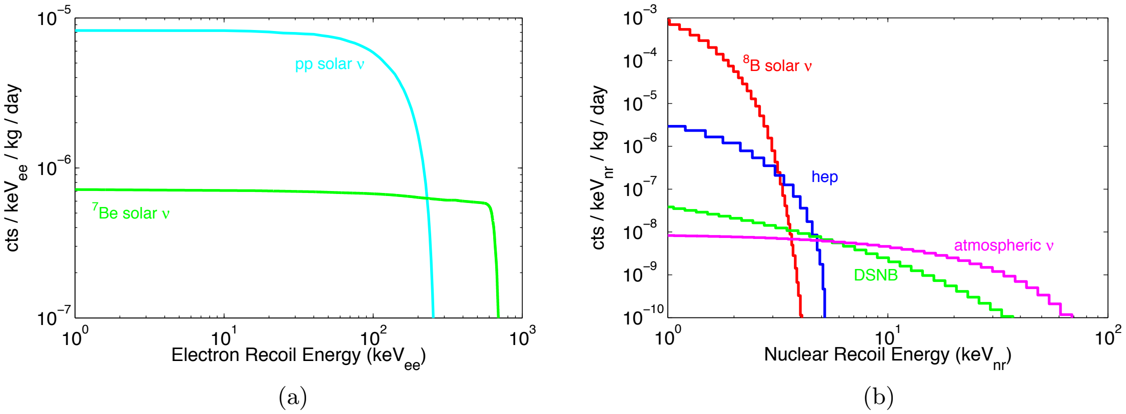

Figure 5.20: Neutrino scattering rates in liquid Xe. (a) ER scattering spectrum. Spectra are shown for neutrinos generated from p-p solar fusion (cyan) [76] and ^{7}Be(e-,ν)^{7}Li solar reactions (green) [77]. (b) NR scattering spectrum. Spectra are shown for neutrinos generated from ^{8}B solar decays, where the energy spectrum is convolved with an analytic Xe TPC Monte Carlo to estimate energy resolution (red) [147], proton-^{3}He solar collisions (blue), cosmic ray interactions in the upper atmosphere (magenta), and supernovae (green). Data is taken from [146].

An exercise was undertaken with γ background simulation data to find the optimal fiducial shape in the detector. The optimal shape was found using the requirement that the shape was centered in the middle of the detector, and that the shape was convex. The optimal shape is shown in Fig. 5.21, overlaid with cylindrical and ellipsoid fiducial volumes. The optimal shape is seen to be very close to an ellipsoid. The observed background event rate is lower by a factor ×0.6.

The ellipsoid fiducial is not used in Run 3. Low-energy events occuring at the edges of the active region were observed to be reconstructed at lower radii, contaminating the edges of the ellipsoid fiducial volume. For this reason, Run 3 featured a cylindrical fiducial volume. Run 4 can potentially benefit from the use of an ellipsoid fiducial shape, dependent on the results of efforts to reduce the misreconstruction of low-energy edge events.

5.9 Predicted Low-Energy ER Background Event Rates

The total predicted ER backgrounds for both Run 3 and the projected Run 4 WIMP search runs are listed in Table 5.6. The results summarize projected event rates from the previous sections in this chapter.

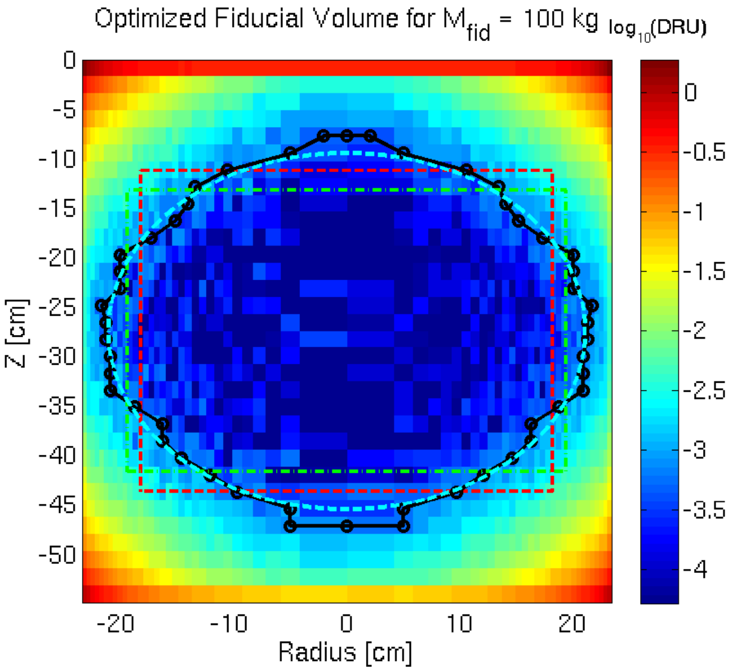

Figure 5.21: Fiducial shape optimization studies, based on projections for γ backgrounds from positive screening measurements. Event rates are shown as a function of radius and height in units of $\log_{10}(\mathrm{DRU_{ee}})$. Events are reflected across the Y axis with Poisson fluctuation in simulation statistics in order to aid the eye. Two cylindrical fiducial volumes are overlaid in red and green. An optimized ellipsoid shape is drawn in cyan. The unconstrained optimized shape, based on ordering mass bins by activity, is drawn in black.

Source	**Background Rate (0.9–5.3 keV$_{\mathbf{ee}}$) [mDRU$_{\mathbf{ee}}$]** **Run 3 (118 kg)**	**Run 4 (100 kg)**	**50 kg**
γ	$1.8 \pm 0.2_{\text{stat}} \pm 0.3_{\text{sys}}$	$0.9 \pm 0.1_{\text{stat}} \pm 0.1_{\text{sys}}$	0.47 ± 0.1
^{127}Xe	$0.5 \pm 0.02_{\text{stat}} \pm 0.1_{\text{sys}}$	–	–
^{214}Pb (^{222}Rn)	0.11–0.22 (0.2 expected)	0.2	0.2
^{85}Kr	$0.17 \pm 0.10_{\text{sys}}$	$0.17 \pm 0.10_{\text{sys}}$	$0.17 \pm 0.10_{\text{sys}}$
Gamma-X	5×10^{-4}	2.7×10^{-4}	1.3×10^{-4}
^{136}Xe	10^{-3}	10^{-3}	10^{-3}
Neutrino	8×10^{-3}	8×10^{-3}	8×10^{-3}
Total	$2.6 \pm 0.2_{\text{stat}} \pm 0.4_{\text{sys}}$	1.3 ± 0.2	0.85 ± 0.1

Table 5.6: Projected low-energy event rates for LUX WIMP search runs. Rates are listed for Run 3, with 118 kg fiducial volume, and the projected Run 4, with a 100 kg fiducial volume. A 50 kg inner fiducial volume is also included, assuming no ^{127}Xe contamination. Fiducial volumes are cylindrical, and are unoptimized for background rejection. Fiducial volume physical definitions are listed in Sec. 5.2.1.

The main differences between the Run 3 and Run 4 background rate projections are the γ and ^{127}Xe contributions. Gamma contributions fall by 50% when scaling from the Run 3 118 kg fiducial volume to the 100 kg fiducial. The rate of ^{127}Xe decay is such that any background from this source will be $<\times 0.1$ the background from the γ rays, by the start of Run 4. The only other fiducial-dependent differential background rate is that of gamma-X events. There was no explicit study of gamma-X events performed for the Run 3 fiducial volume. The gamma-X background rate is assumed to scale with the γ background rate, using the 100 kg estimated rate from Sec. 5.4 as the estimated rate for Run 4. The predicted background rates are compared explicitly with measured data in Sec. 8.8.

5.10 S1 and S2 Distributions from Energy Depositions

The modeling work performed in this chapter is based on simulations which end with energy depositions in the active region. The LUXSim package, using NEST, is able continue the simulation past the energy deposition stage. NEST calculates the photon and electron yield for a given ER or NR energy deposition and electric field, based on a semi-empirical model. LUXSim then uses Geant4 physics processes to propagate the generated photons through to the PMT photocathodes. The generated electrons are made to undergo scintillation processes in the detector gas volume, and the resulting S2 photons are also propagated through to the PMT photocathodes. The actual simulation of S1 and S2 processes allows the resulting signals to be passed through the LUX data processing chain, which allows the convolution of detector and analysis efficiencies with simulation results. Unfortunately, the generation of S1 and S2 signals is extremely CPU-intensive, particularly for events with energies above the WIMP search range. For this reason, a method was developed to approximate the S1 and S2 distributions for a given event in post-processing.

NEST (v0.99β) was used to generate a library of photon and electron distributions as a function of ER energy deposition. These libraries were taken directly from LUXSim. The data was generated by launching low-energy electrons in the middle of the active region, with the LUX electric field input into the simulation to get the correct photon and electron partitioning. Examples of the (S1,S2) distributions are given in Fig. 5.22. The difference in photon and electron yields between a γ and an electron launched in the liquid Xe is negligible below 10 $\mathrm{keV_{ee}}$.

The NEST v0.99β band centroid is well matched to observed LUX data. However, the S2/S1 band width is wider than that observed in LUX by an additional 30%. S1 spectra generated using this data have a higher (worse) σ/μ energy resolution than that expected for real data. Signal PDFs for ^{127}Xe for the profile likelihood WIMP search analysis are corrected against the measured ^{3}H band [148].

The photon and electron yields are converted into S1 and S2 signals through convolution of the distribution of photoelectrons for a given number of generated photons. The detection efficiency factors are summarized in Table 5.7. For the S1 signal, this distribution is binomial, where the probability is the measured average photoelectron signal per generated photon, equal to 0.14 as calculated in Sec. 8.2. For the S2 signal, two efficiency factors are applied. The first is the efficiency with which electrons are removed from the liquid Xe, which is described by a binomial with $p = 0.64$. The second is the number of photoelectrons detected per electron extracted from the liquid, which is measured at 10.5 phe per extracted electron for S2 signals in the bottom PMT array. The distribution is Gaussian with measured $\sigma = 4.5$ phe per extracted electron. For small signals, the PMT resolution on single photoelectrons is applied as a Gaussian with 30% σ [129]. The single photoelectron resolution has no significant effect on S1 distributions. Note that the variation in light and

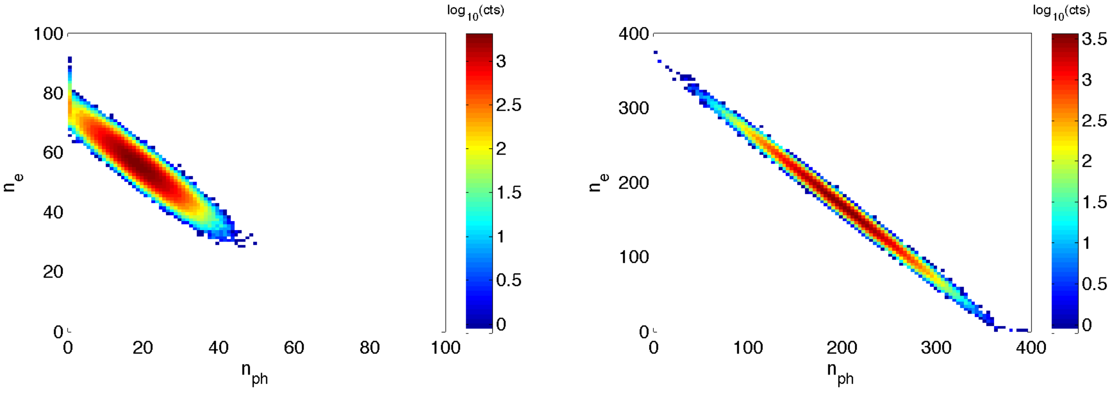

(a) (b)

Figure 5.22: Distributions in photon (n_{ph}) and electron (n_e) yields for (a) 1 keV$_{\text{ee}}$ and (b) 5 keV$_{\text{ee}}$ electrons. Distributions are calculated by NEST (v0.99β) / LUXSim. An electric field of 182 V cm^{-1} is used, the same as that for the 85 day LUX WIMP search run.

charge collection with position is not folded into the model. It is assumed that fluctuations in S1 and S2 due to position variation are subdominant to fluctuations from photon and electron generation.

The corresponding predicted distributions for S1 and S2 signals for ^{127}Xe and for backgrounds with flat energy spectra are shown in Fig. 5.23. The semi-analytic distributions were compared with distributions generated by LUXSim propagation of photon and electron signals. The distributions were seen to agree to within 5% for the band mean. Distribution widths were found to be in agreement to within 15%.

The predicted S1 spectra for various background sources are used to directly compare simulations with measured S1 data, in Sec. 8.8. The (S1,S2) distributions can also be added linearly to simulate the resulting distributions for multiple scatter events, as done in Sec. 8.7. The use of a NEST library from simple simulation results decreases the computing power required to find (S1,S2) distributions by several orders of magnitude, relative to the brute-force approach of generating scintillation events in the simulation. The brute force approach is still useful for generating simulation data which can be processed with the LUX data processing chain, yielding a direct comparison with measured data for efficiency studies.

Parameter	Value
Single phe resolution	0.46
S1 phe per photon	0.14
Ionization electron extraction efficiency	0.64
S2 phe per single extracted e^- mean	10.45 phe per extracted electron
S2 phe per single extracted e^- sigma	4.5 phe per extracted electron

Table 5.7: Parameters used in conversion of NEST (v0.99β) scintillation and ionization yields to S1 and S2 signals. All quantities are measured from LUX data during the 85 day WIMP search run.

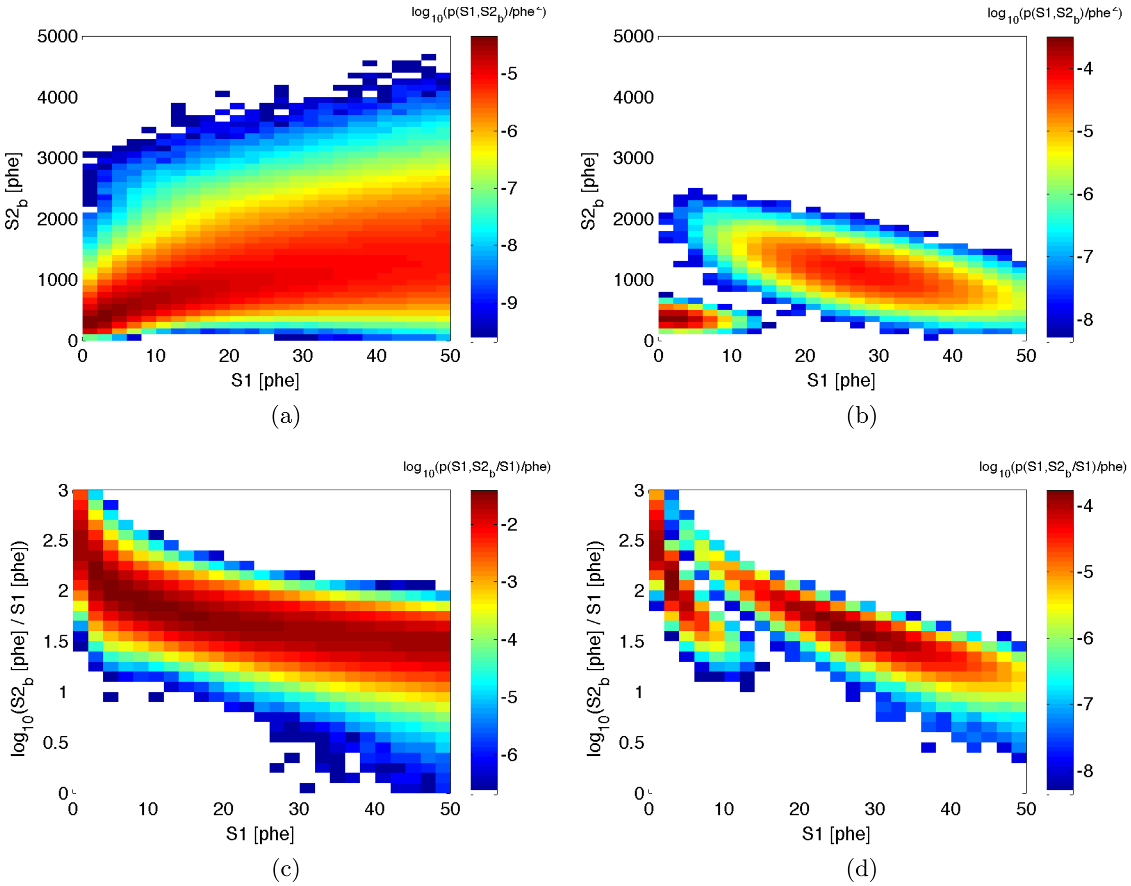

(a) (b) (c) (d)

Figure 5.23: Distributions in S1 and S2 using NEST (v0.99β), for both background sources with flat energy spectra, and ^{127}Xe 1 keV$_{ee}$ and 5 keV$_{ee}$ x-ray peaks. (a) (S1,S2) distribution from a flat background spectrum. (b) (S1,S2) distribution for ^{127}Xe. (c) (S1,S2/S1) distribution from a flat background spectrum. (d) (S1,S2/S1) distribution for ^{127}Xe. The models are folded into energy deposition-only studies for direct comparison of simulation with measured low-energy spectra. S2/S1 widths predicted by NEST (v0.99β) are wider by 30% than observed widths in LUX data.

CHAPTER 6

DARK MATTER SEARCH BACKGROUNDS FROM PRIMORDIAL RADIONUCLIDE CHAIN DISEQUILIBRIUM

The following work was developed in the course of neutron background modeling, and was submitted for publication in 2013 [149]. The work investigates the ER and NR background contributions from different segments of the ^{238}U and ^{232}Th decay chains, for generic one tonne Ar and Xe detectors. The material is presented with only minor alteration for incorporation into this document.

6.1 Abstract

Dark matter direct-detection searches for weakly interacting massive particles (WIMPs) are commonly limited in sensitivity by neutron and gamma backgrounds from the decay of radioactive isotopes. Several common radioisotopes in detector construction materials are found in long decay chains, notably those headed by ^{238}U, ^{235}U, and ^{232}Th. Gamma radioassay using Ge detectors identifies decay rates of a few of the radioisotopes in each

chain, and typically assumes that the chain is in secular equilibrium. If the chains are out of equilibrium, detector background rates can be elevated significantly above expectation. In this work we quantify the increase in neutron and gamma production rates from an excess of various sub-chains of the ^{238}U decay chain. We find that the ^{226}Ra sub-chain generates x10 higher neutron flux per decay than the ^{238}U early sub-chain and ^{210}Pb sub-chain, in materials with high (α,n) neutron yields. Typical gamma screening results limit potential ^{238}U early sub-chain activity to ×20–60 higher than ^{226}Ra sub-chain activity. Monte Carlo simulation is used to quantify the contribution of the sub-chains of ^{238}U to low-energy nuclear recoil (NR) and electron recoil (ER) backgrounds in simplified one tonne liquid Ar and liquid Xe detectors. NR and ER rates generated by ^{238}U sub-chains in the Ar and Xe detectors are found after comparable fiducial and multiple-scatter cuts. The Xe detector is found to have ×12 higher signal-to-background for 100 GeV WIMPs over neutrons than the Ar detector. ER backgrounds in both detectors are found to increase weakly for excesses of ^{238}U early sub-chain and ^{210}Pb sub-chain relative to ^{226}Ra sub-chain. Experiments in which backgrounds are NR-dominated are sensitive to undetected excesses of ^{238}U early sub-chain and ^{210}Pb sub-chain concentrations. Experiments with ER-dominated backgrounds are relatively insensitive to these excesses.

6.2 Introduction

Direct WIMP dark matter searches are typically limited by backgrounds caused by neutron and γ interactions in the target material. The primary source of these particles is radioactive decay from contaminants in detector materials or the laboratory. The most common of these contaminants which produce notable backgrounds are the primordial radioisotopes ^{238}U, ^{235}U and ^{232}Th. These radioisotopes are the parents of lengthy decay chains, shown in Fig. 6.1 and 6.2. Decay chain data is taken from [135].

Several isotopes from these chains decay with half-lives much longer than the typical lifetimes of dark matter experiments ($\gg$10 years). The removal of these long-lived isotopes from the decay chains, e.g. from chemical processing, can lead to quasi-permanent breaks in secular equilibrium. If chain breakage results in the removal of radioisotopes used during

γ radioassay, then assay results will lead to an underrepresentation of the total number of radionuclides present in the material.

In this work, we quantify the effects of primordial radioisotope chain disequilibrium on neutron and γ emission. Monte Carlo is used to estimate the impact of these changes on a liquid Xe detector similar to the current LUX and XENON TPC designs [80, 150, 151, 152]. A model liquid Ar detector of equal mass, similar to the ArDM and DarkSide designs [153, 154], is used to estimate the impact of chain disequilibrium on Ar targets.

6.3 Screening Methodologies

The most common method for measuring radioisotope concentrations in construction materials is to expose material samples to a high-sensitivity Ge detector [155, 156, 157, 158, 129]. This method yields a direct measurement of the γ energy spectrum emitted by all radioisotopes in the material. This method is well-suited to screening large quantities of construction materials in a single screening run, which is crucial for experiments which use very large quantities of these materials in close proximity to their active targets. This also enables γ screeners to average over any variations in radioisotope concentration with position in the sample. Gamma screening yields comparable sensitivity per γ emitted for all radioisotopes. For these reasons, γ radioassay is widely used as the primary radioassay method for material screening programs in low background experiments.

Isotopes with low γ emission probability per decay are identified with relatively high upper limits. This means that γ screening is relatively insensitive to several radioisotopes shown in the decay chains in Fig. 6.1 and 6.2. Typical γ detectors also have backgrounds which fall exponentially with increasing energy, with an order of magnitude or greater change in background rate between 100 keV and 1000 keV. This generally leads to the preferential use of high-energy γ lines for radioisotope identification. Standard identification of the ^{238}U and ^{232}Th chains uses γ lines >300 keV.

Mass spectrometry techniques can also be used to identify radioisotopes in material samples [155, 156]. In principle, this technique can be useful for distinguishing radioisotopes which have a low γ emission intensity, and would therefore escape detection by Ge screeners.

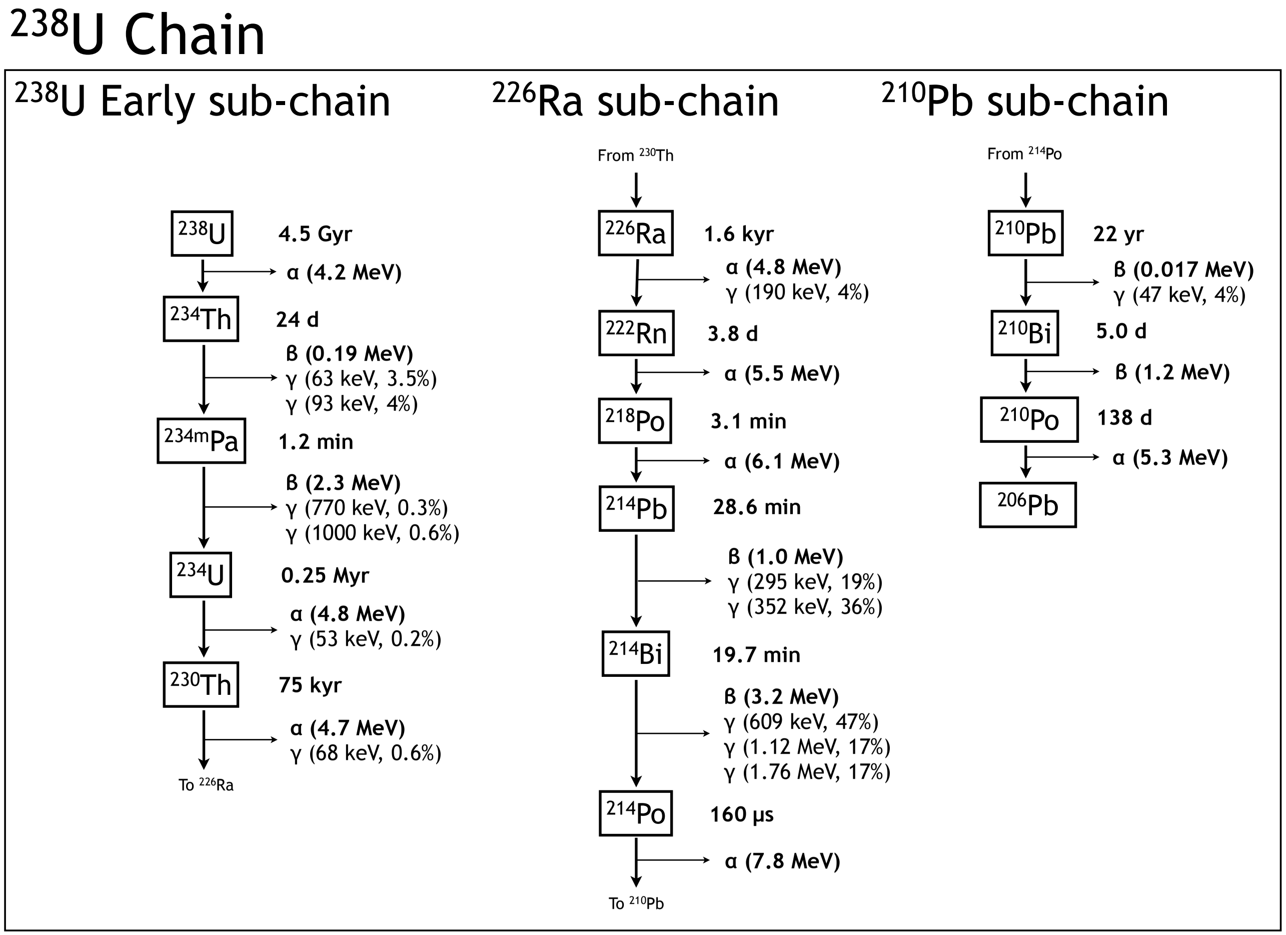
^{238}U Chain
^{238}U Early sub-chain
^{226}Ra sub-chain
^{210}Pb sub-chain
^{238}U
4.5 Gyr
α (4.2 MeV)
^{234}Th
24 d
β (0.19 MeV)
γ (63 keV, 3.5%)
γ (93 keV, 4%)
^{234m}Pa
1.2 min
β (2.3 MeV)
γ (770 keV, 0.3%)
γ (1000 keV, 0.6%)
^{234}U
0.25 Myr
α (4.8 MeV)
γ (53 keV, 0.2%)
^{230}Th
75 kyr
α (4.7 MeV)
γ (68 keV, 0.6%)
To ^{226}Ra
From ^{230}Th
^{226}Ra
1.6 kyr
α (4.8 MeV)
γ (190 keV, 4%)
^{222}Rn
3.8 d
α (5.5 MeV)
^{218}Po
3.1 min
α (6.1 MeV)
^{214}Pb
28.6 min
β (1.0 MeV)
γ (295 keV, 19%)
γ (352 keV, 36%)
^{214}Bi
19.7 min
β (3.2 MeV)
γ (609 keV, 47%)
γ (1.12 MeV, 17%)
γ (1.76 MeV, 17%)
^{214}Po
160 μs
α (7.8 MeV)
To ^{210}Pb
From ^{214}Po
^{210}Pb
22 yr
β (0.017 MeV)
γ (47 keV, 4%)
^{210}Bi
5.0 d
β (1.2 MeV)
^{210}Po
138 d
α (5.3 MeV)
^{206}Pb

Figure 6.1: The decay chain for ^{238}U. The decay chain is broken into three sub-chains: the ^{238}U early sub-chain, the ^{226}Ra sub-chain, and the ^{210}Pb sub-chain. Isotopes are shown with their half-lives and probability for α or β emission, if not 100%. Decays with probability <1% are not shown. Alpha or β emission is listed under each isotope, with the mean α energy or β decay endpoint given. Energies and intensities are listed for γ emission with intensity >1%, with the exception of the ^{238}U early chain which lists γ rays with intensity >0.1%. Data from [135].

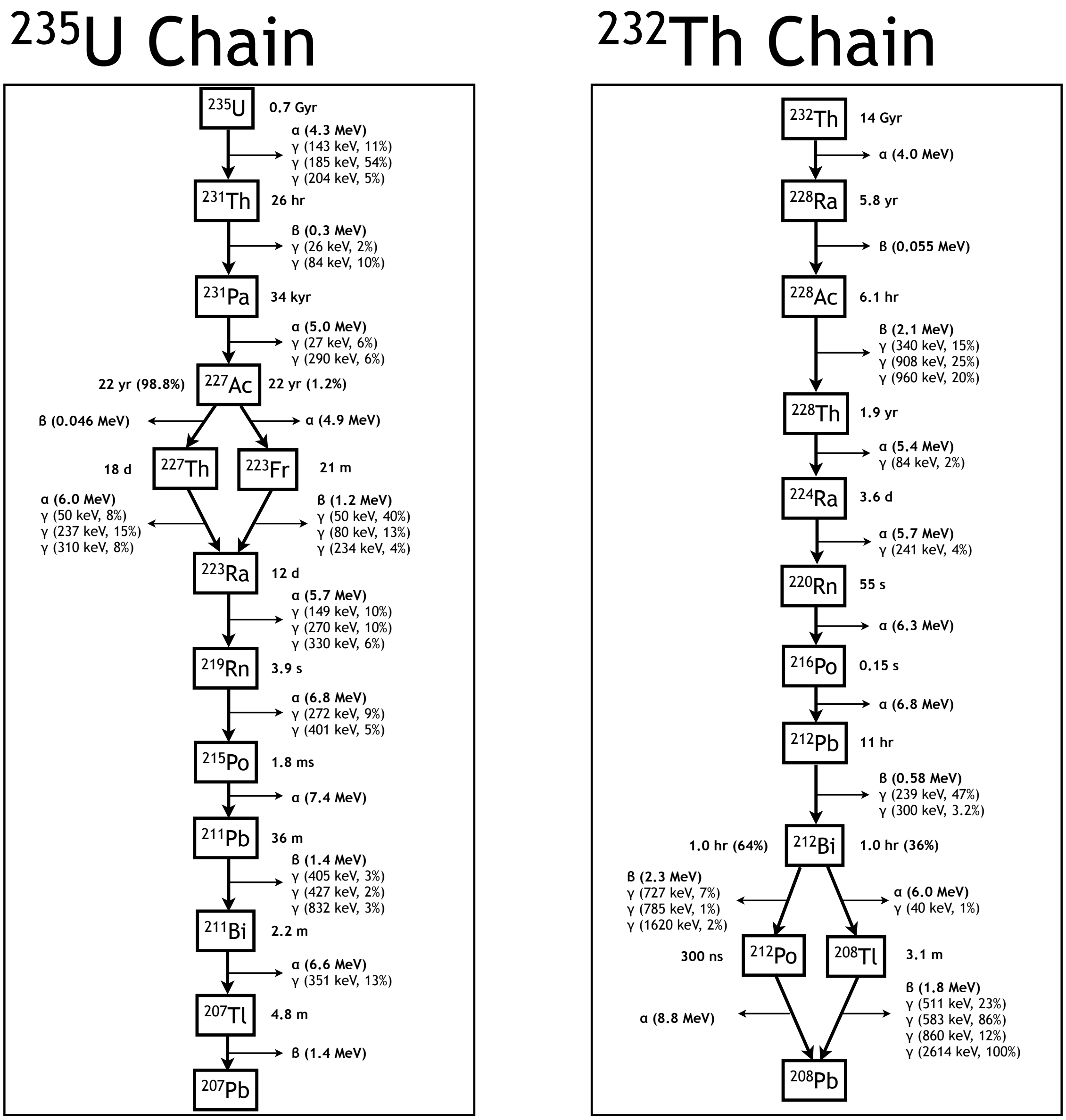
235U Chain
235U
0.7 Gyr
α (4.3 MeV)
γ (143 keV, 11%)
γ (185 keV, 54%)
γ (204 keV, 5%)
231Th
26 hr
β (0.3 MeV)
γ (26 keV, 2%)
γ (84 keV, 10%)
231Pa
34 kyr
α (5.0 MeV)
γ (27 keV, 6%)
γ (290 keV, 6%)
22 yr (98.8%)
227Ac
22 yr (1.2%)
β (0.046 MeV)
α (4.9 MeV)
18 d
227Th
223Fr
21 m
α (6.0 MeV)
γ (50 keV, 8%)
γ (237 keV, 15%)
γ (310 keV, 8%)
β (1.2 MeV)
γ (50 keV, 40%)
γ (80 keV, 13%)
γ (234 keV, 4%)
223Ra
12 d
α (5.7 MeV)
γ (149 keV, 10%)
γ (270 keV, 10%)
γ (330 keV, 6%)
219Rn
3.9 s
α (6.8 MeV)
γ (272 keV, 9%)
γ (401 keV, 5%)
215Po
1.8 ms
α (7.4 MeV)
211Pb
36 m
β (1.4 MeV)
γ (405 keV, 3%)
γ (427 keV, 2%)
γ (832 keV, 3%)
211Bi
2.2 m
α (6.6 MeV)
γ (351 keV, 13%)
207Tl
4.8 m
β (1.4 MeV)
207Pb
232Th Chain
232Th
14 Gyr
α (4.0 MeV)
228Ra
5.8 yr
β (0.055 MeV)
228Ac
6.1 hr
β (2.1 MeV)
γ (340 keV, 15%)
γ (908 keV, 25%)
γ (960 keV, 20%)
228Th
1.9 yr
α (5.4 MeV)
γ (84 keV, 2%)
224Ra
3.6 d
α (5.7 MeV)
γ (241 keV, 4%)
220Rn
55 s
α (6.3 MeV)
216Po
0.15 s
α (6.8 MeV)
212Pb
11 hr
β (0.58 MeV)
γ (239 keV, 47%)
γ (300 keV, 3.2%)
1.0 hr (64%)
212Bi
1.0 hr (36%)
β (2.3 MeV)
γ (727 keV, 7%)
γ (785 keV, 1%)
γ (1620 keV, 2%)
α (6.0 MeV)
γ (40 keV, 1%)
300 ns
212Po
208Tl
3.1 m
α (8.8 MeV)
β (1.8 MeV)
γ (511 keV, 23%)
γ (583 keV, 86%)
γ (860 keV, 12%)
γ (2614 keV, 100%)
208Pb

Figure 6.2: The decay chains for (left) ^{235}U and (right) ^{232}Th. Isotopes are shown with their half- lives and probability for α or β emission, if not 100%. Decays with probability <1% are not shown. Alpha or β emission is listed under each isotope, with the mean α energy or β decay endpoint given. Energies and intensities are listed for γ emission with intensity >1%. Data from [135].

However, these techniques are limited in their ability to detect daughter nuclei in long decay chains. In secular equilibrium, the ratios of daughter isotope to head isotope half-lives determines the concentrations of the daughter isotopes. In the case of the decay chains in Fig. 6.1 and 6.2, the parent half-lives are higher than those of the daughters by 4–25 orders of magnitude. Mass spectrometry can therefore set meaningful upper limits only on the head isotopes of the decay chains. Mass spectrometry also samples very small quantities of material in a given run, which leads to potential error in inhomogeneous samples.

6.4 Chain Disequilibrium for Primordial Radionuclides

6.4.1 ^{238}U Chain

In principle, disequilibrium can be introduced at any stage in a decay chain. However, disequilibrium is only relevant to dark matter experiments in the case that disequilibrium occurs by removing an isotope with a half-life comparable to or greater than the timescale of the experiment. This timescale is typically measured in years. From Fig. 6.1 and 6.2, the decay chain most likely to yield a relevant break in equilibrium is that of ^{238}U, which has several isotopes with half-lives significantly longer than this limit. For this work, we define three ^{238}U sub-chains based on the relatively long half-lives of their parent isotopes: the ^{238}U early sub-chain, including isotopes from ^{238}U to ^{230}Th; the ^{226}Ra sub-chain, including isotopes from ^{226}Ra to ^{214}Po; and the ^{210}Pb sub-chain, including ^{210}Pb and its daughters.

The definition of the ^{226}Ra sub-chain is conservative for this study. If breakage occurs below ^{226}Ra, the relatively short half-lives of the daughters (set by ^{222}Rn at 3.8 days) will lead to re-establishment of equilibrium well before radioassay measurements are performed. Breakage above ^{226}Ra will lessen the effect of disequilibrium on detector backgrounds, since there will be fewer unaccounted radioisotopes in excess. Setting ^{226}Ra as the parent of the middle sub-chain therefore leads to the greatest potential for impact of the sub-chain on detector backgrounds. The specific details of equilibrium breakage are dependent on the chemical processes used in the treatment of materials. We do not address these processes in this work, but instead make simple conservative assumptions about the disequilibrium scenario.

Although γ rays from the ^{238}U early sub-chain have considerably lower branching ratios than those from the ^{226}Ra sub-chain, typical γ counters can still place useful upper limits on ^{238}U early sub-chain activity. The ratio of ^{238}U early sub-chain limits to ^{226}Ra sub-chain limits set by γ counting is comparable to the ratio of the intensities of the γ rays used to identify these sub-chains. For the ^{226}Ra sub-chain, the typical energies used for identification are the 352 keV and 609 keV lines, with branching ratios of 36% and 47% respectively. The ^{238}U early sub-chain is generally identified by the 1.0 MeV line from ^{234}Pa, which has an intensity a factor $\times 1/60$ and $\times 1/80$ that of the 352 keV and 609 keV lines, respectively. Variability in detection efficiency and detector backgrounds can result in a wide range of upper limits for the ^{238}U early sub-chain relative to the ^{226}Ra sub-chain, with typical ratios ranging from ×20–60 [155, 156, 157, 158, 129, 144].

The ^{238}U chain contains one long-lived radioisotope after the ^{226}Ra sub-chain, ^{210}Pb, with a half-life of 22 years. The ^{210}Pb chain contains no high-energy γ rays with high branching ratios, so the expected increase in detector ER backgrounds is minimal. However, one of the ^{210}Pb sub-chain daughters undergoes α decay, potentially leading to neutron generation. This work also considers neutron generation from the ^{210}Pb sub-chain.

It should be noted that ^{210}Pb and its daughters do not produce γ rays which are easily observable in typical radioassay Ge detectors. Gamma emission comes primarily from ^{210}Pb decay, with a 4% branching ratio for generation of a 46 keV γ. The mean free path of this γ is 4 cm in H_2O. The γ is easily absorbed within bulk samples before reaching the Ge detector, thereby heavily suppressing its signal and greatly raising upper limits on its activity. Gamma screening backgrounds are also typically high in the energy range around 46 keV, further weakening upper limit activity measurements. Screening results for ^{210}Pb are therefore typically not reported in γ radioassays. We do not attempt to quantify likely concentrations of the ^{210}Pb sub-chain in this work.

6.4.2 ^{235}U Chain

The concentration of ^{235}U in nature is 0.7% that of ^{238}U. Standard chemical processes do not alter the ^{235}U / ^{238}U ratio in materials. It is therefore common to assume that screened materials have a natural ratio of ^{235}U / ^{238}U, which sets a much lower limit on the amount of ^{235}U than does direct counting. Since ^{235}U and its daughters are not directly measured, ^{235}U chain disequilibrium is not addressed in this work.

If γ screening misidentifies the amount of ^{238}U in a material due to a factor ×1/60 deficit in the ^{226}Ra sub-chain, then the amount of ^{235}U will be misidentified by the same factor. In this scenario, the ^{235}U decay rate could potentially be 50% of the ^{226}Ra sub-chain decay rate. However, the ^{235}U chain has one less α emission per parent decay than the ^{238}U chain, a comparable mean α energy, and lower-energy γ rays with lower intensities. ^{235}U will contribute neutron and γ backgrounds no larger than those already present from existing ^{226}Ra in the experiment, as discussed in Sec. 6.6 and 6.7. It is also notable that, in this scenario, the ^{235}U chain would be detectable in γ radioassay by the 185 keV γ line from ^{235}U decay.

6.4.3 ^{232}Th Chain

The ^{232}Th chain can only be broken on a timescale of years, matching the common lifetime of current and future dark matter experiments. The longest-lived daughter below ^{232}Th is ^{228}Ra, with a half-life of 5.8 years. If ^{228}Ra and its daughters are completely removed from a material, then the rate of ^{228}Ra decays will reach a factor ×1/2 that of ^{232}Th after six years. ^{228}Th follows two generations after ^{228}Ra, with a half-life of 1.9 years. In the scenario where all ^{232}Th daughters have been removed, ^{228}Th reaches a decay rate a factor ×1/2 that of ^{232}Th after nine years. The longest-lived daughter after ^{228}Th has a half-life on the order of minutes; the decay rates of all of the daughters thus closely shadow that of ^{228}Th.

Chain disequilibrium could also be introduced by the removal of only ^{228}Th and its daughters. In this case, chain equilibrium would be re-established within a factor ×1/2 after two years. This would also leave the isotope ^{228}Ac, which generates several high-energy γ rays easily detectable by γ radioassay. The most conservative assumption for ^{232}Th chain disequilibrium is therefore the removal of ^{228}Ra and its daughters, as this introduces the most appreciable lag in the re-establishment of chain equilibrium with a low chance of detection.

If a material were to be processed with a method that removed all ^{232}Th daughters and left the original ^{232}Th, then the timescale on which ^{232}Th / ^{228}Ra / ^{228}Th equilibrium is re-established would lead to a background source which increases significantly over the experiment lifetime. Consider a material which undergoes complete removal of all ^{232}Th daughters, and is then subject to radioassay 45 days afterward. After 45 days, the rate of ^{228}Ra decays (closely traced by detectable ^{228}Ac) would be only 1% the rate of ^{232}Th decays. The reported ^{232}Th rate from γ radioassay, which uses lines from ^{228}Ac and ^{228}Th daughters, would then be $\times 1/100$ the true ^{232}Th rate. The ^{228}Ra and ^{228}Th rates grow linearly with time, increasing over an order of magnitude over the experiment lifetime.

Fortunately, removal of all ^{232}Th daughters by chemical processing is unrealistic. ^{232}Th is chemically identical to ^{228}Th; any process which removes ^{228}Th would remove ^{232}Th in comparable quantities. If processing left ^{228}Th in the material, then ^{228}Th and its daughters would reach equilibrium within days. Gamma radioassay would then detect the ^{228}Th daughter signatures, and the inferred ^{232}Th quantity would be correct. Similar arguments apply to a scenario in which Th is introduced into a material during processing. It is notable that detection of a deficit of ^{228}Ac relative to ^{228}Th daughters would indicate that processing techniques had induced disequilibrium in the isotope chain before counting. This could serve as an indicator for potential disequilibrium conditions in the ^{238}U chain in the same material, as processes which removed Ra isotopes and left Th isotopes would be identified.

6.5 ^{238}U Alpha Emission Spectra and Neutron Yields

Experiments searching for low-energy NR signals are particularly sensitive to backgrounds from neutron scattering. With sufficient external shielding material, neutron generation from radionuclides in detector materials contributes the dominant NR rate in the target volume. Neutron generation from detector materials comes primarily from spontaneous fission (^{238}U having the most significant contribution through this channel), and from (α,n) interactions. Disequilibrium in primordial radionuclide chains can lead to an underestimation of α-generating isotopes, leading in turn to an underestimation of neutron yields from detector materials.

Neutron yields vary by orders of magnitude across the spectrum of α energies associated with ^{238}U chain isotopes, as described in a review of (α,n) yields by Heaton et al. [159]. The neutron rate from a given sub-chain convolves neutron yield as a function of α energy with the α energies of each sub-chain. For ^{238}U isotopes, α energy spectra are shown in Fig. 6.3.

The neutron spectrum as a function of initial α energy $E_{\alpha,0}$, for material comprised of an element with molar mass A, is calculated as

$$Y\left(E_{\alpha,0}, E_n\right) = \frac{N_A}{A} \int_0^{E_{\alpha,0}} \frac{\sigma\left(E_\alpha, E_n\right)}{S_\alpha\left(E_\alpha\right)} \mathrm{d}E_\alpha, \tag{6.1}$$

whereα particle with energy $E_{\alpha,0}$; $\sigma\left(E_\alpha, E_n\right)$ is the (α,n) cross section for incoming α energy E_α and outgoing neutron energy E_n; and $S_\alpha\left(E_\alpha\right)$ is the α stopping power for the material. The methodology follows that described in [142]. The (α,n) cross sections were calculated for several elements using the TALYS 1.4 simulation program [160]. $S_\alpha\left(E_\alpha\right)$ data were taken from the ASTAR database [161]. Integrated neutron production rates were compared to those listed in Heaton and found to match within a factor of two, with an average overproduction by a factor of 20%. The exception is C, for which the neutron yield is calculated to be an average ×5 higher than that reported in Heaton. The TALYS cross section results for C match measurements reported in [162], and are used for this work. Yield curves integrated over all neutron energies are shown in Fig. 6.4.

We define the ratio of ^{238}U early sub-chain to ^{226}Ra sub-chain X. We then define the (α,n) neutron yield multiplier from chain equilibrium $\Gamma\left(X, E_n\right)$, which is the fractional increase in yield for neutrons with energy E_n over the case of full-chain equilibrium, as a function of X. $X = 1$ corresponds to ^{238}U chain equilibrium. $\Gamma\left(X, E_n\right)$ is calculated as

$$\Gamma\left(X, E_n\right) = \frac{\left(X-1\right)\left(\sum_j Y\left(E_{\alpha,0,j}, E_n\right)\right)}{\sum_k Y\left(E_{\alpha,0,k}, E_n\right)} + 1, \tag{6.2}$$

where j and k are iterators spanning over the α particles generated from the ^{238}U early sub-chain and full ^{238}U decay chain in equilibrium, respectively. Fig. 6.5 shows the total neutron generation rate integrated over all neutron energies, $\int \Gamma\left(X, E_n\right) \mathrm{d}E_n$, as a function of X for several common elements in detector construction materials. The summed neutron yield per sub-chain decay for all ^{238}U sub-chains is given in Table 6.1.

Shown separately in Fig. 6.5 is the ^{238}U spontaneous fission rate, equal to 5.4×10^{-7} fissions per ^{238}U decay [78]. For materials with a low neutron yield below 5 MeV α energy, fission gives the dominant neutron yield in the case of ^{238}U early sub-chain excess. It should be noted that an extremely conservative model is used where each spontaneous fission event contributes a single neutron, with no other prompt emission. In reality, spontaneous fission promptly releases multiple neutrons and/or γ rays. The chance of veto of these events is extremely high due to multiple-scatter and high-energy event rejection in many dark matter detectors.

It is interesting to note the (α,n) yields for direct incidence of α particles on Ar and Xe target materials. The yield curves as a function of incident α energy are shown in Fig. 6.6. The Ar target is sensitive to all α energies found in the ^{238}U and ^{232}Th chains. A particular risk is that of neutron production from ^{222}Rn leakage into the Ar target material, which can occur from ^{226}Ra sources on the surface of detector materials. The presence of ^{222}Rn and its daughters results in a neutron generation rate of 470 n yr^{-1} (Bq ^{222}Rn)$^{-1}$. Xe targets are vulnerable only to the 7.8 MeV α from the ^{222}Rn decay chain, with a yield of 3.8×10^{-6} n yr^{-1} (Bq ^{222}Rn)$^{-1}$. Typical self-shielding cuts would have reduced effectiveness against this background due to the internal generation of the neutrons and the consequent reduction in path length required for the neutrons to escape.

Surface deposition of ^{222}Rn progeny on detector surfaces can also result in a significant ^{210}Pb concentration exposed directly to the target material. ^{210}Pb α particles yield 3.5 n yr^{-1} (Bq ^{210}Pb)$^{-1}$ on Ar, assuming 50% of α particles are emitted into detector surfaces and do not contribute to Ar (α,n). ^{210}Pb α interactions in Xe do not generate neutrons, as Xe (α,n) processes have an α energy threshold well above 5.3 MeV.

6.6 ^{238}U Disequilibrium Impact on Neutron Backgrounds for Dark Matter Experiments

The impact of neutrons on dark matter sensitivity was assessed by direct comparison of projected NR rates from neutrons and WIMPs. The example of fluoridated material (e.g.

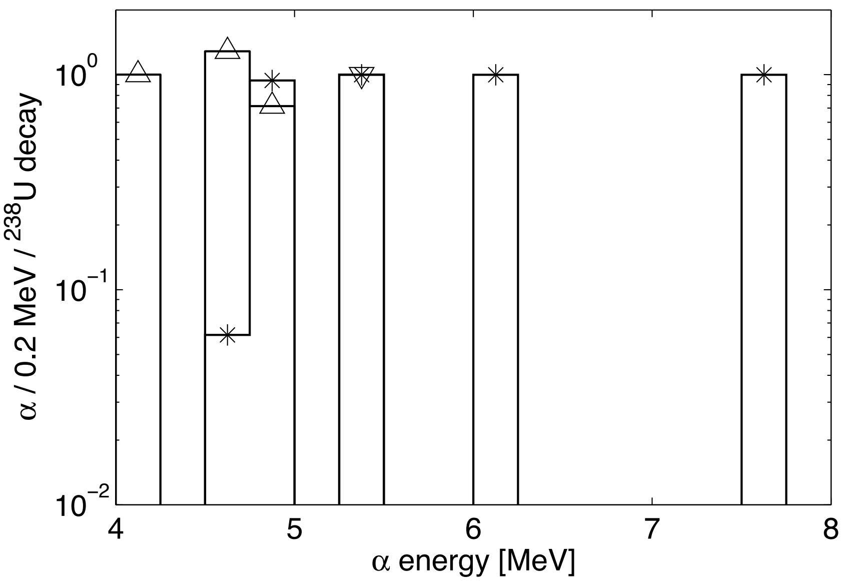

Figure 6.3: Alpha energies generated from ^{238}U decay chain isotopes, assuming full secular equilibrium. Alphas are shown corresponding to the ^{238}U early sub-chain (upward arrows), ^{226}Ra sub-chain (stars), and ^{210}Pb sub-chain (downward arrows). Data is taken from [135].

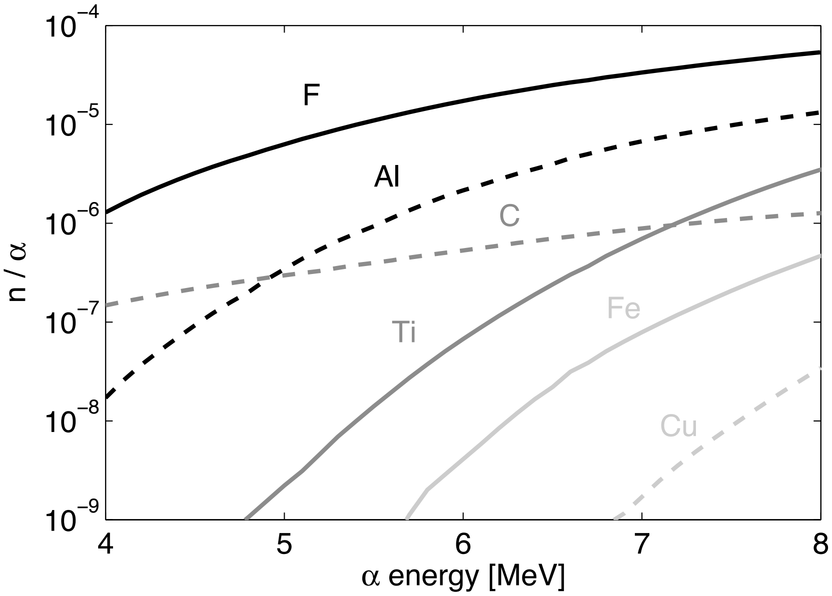

Figure 6.4: Neutrons produced per incident α particle for various common elements in detector construction materials, as a function of α kinetic energy. Lines are shown for F (dark solid), Al (dark dashed), Ti (medium solid), C (medium dashed), Fe (light solid), and Cu (light dashed).

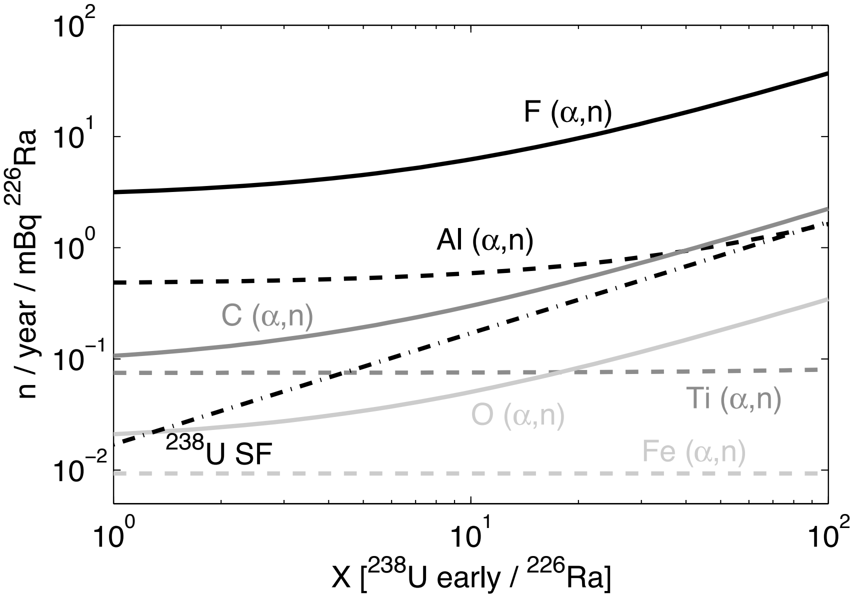

Figure 6.5: Neutron rate from (α,n) processes per ^{226}Ra sub-chain decay rate, as a function of ^{238}U early sub-chain / ^{226}Ra sub-chain ratio X, for various materials. Overlaid is the yield from ^{238}U spontaneous fission, assuming that fission yields single neutrons which cannot be vetoed by accompanying neutrons or γ rays. Lines are shown for F (dark solid), Al (dark dashed), Ti (medium solid), C (medium dashed), Fe (light solid), Cu (light dashed), and spontaneous fission (dark dash-dotted). Typical γ radioassay measurements limit the potential ^{238}U early fraction excess to ×20-60.

	^{238}U early	^{226}Ra	^{210}Pb
Al	37	1400	66
C	68	240	35
Cu	–	16	–
F	1100	8000	890
Fe	0.00030	30	0.0015
O	10	49	6.9
Ti	0.17	240	0.69

Table 6.1: ^{238}U sub-chain (α,n) neutron yields per parent decay, multiplied by 10^8, for common detector construction materials. Yields are calculated from α energies in Fig. 6.3 and (α,n) neutron yields in Fig. 6.4. Yields from the ^{238}U early sub-chain do not include contributions from ^{238}U spontaneous fission, the probability for which is 5.4×10^{-7}.

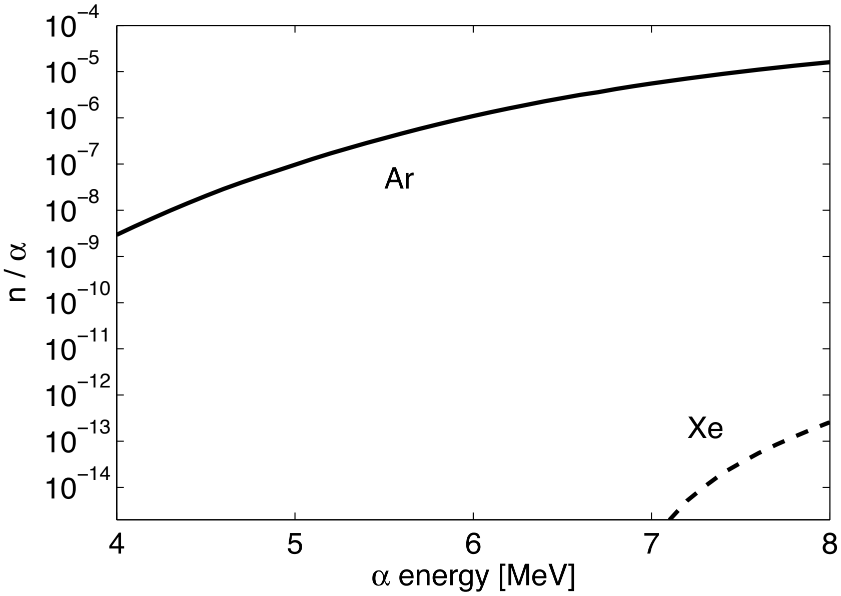

Figure 6.6: Neutrons produced per incident α particle for Ar (solid) and Xe (dashed), as a function of α kinetic energy.

PTFE, or Teflon®) was chosen for this study due to its relatively high neutron yield over other common detector construction materials. The neutron energy spectrum from (α,n) on F was calculated from Eq. 6.1 for the ^{238}U early sub-chain, ^{226}Ra sub-chain, and ^{210}Pb sub-chain. The ^{238}U spontaneous fission neutron spectrum was added to the ^{238}U early chain. The spectra are shown in Fig. 6.7.

The impact of ^{238}U chain disequilibrium is assessed by Monte Carlo for one tonne ideal liquid Ar and liquid Xe dark matter detectors. The simulations are based on the Geant4 toolkit. The detectors have a cylindrical geometry with 1:1 aspect ratio, and are surrounded by a cylindrical water shield of thickness 1 m. Neutrons are thrown from the border between the target material and the water shield, representing activity from detector internals. The neutron scatter rate is then found in a cylindrical 500 kg fiducial region with 1:1 aspect ratio. A single-scatter cut is applied, requiring events to have an energy-weighted standard deviation of <2 cm in radius and <0.5 cm in height, comparable to the typical spatial resolution for Xe TPC detectors [150, 106]. Single-scatter cut efficiency is insensitive to the exact length threshold used. Rates are plotted as a function of recoil energy in Fig. 6.8, normalized per neutron emitted.

The projected WIMP signal as a function of WIMP mass M_χ is shown in Fig. 6.9 for both Ar and Xe detectors. A WIMP-nucleon spin-independent interaction cross-section of 10^{-45} cm^2 is used. Overlaid are neutron scatter rates for each of the ^{238}U sub-chains, after application of analysis cuts. A parent rate of 1 Bq is assumed for each sub-chain. WIMP and neutron rates are calculated from Fig. 6.8 in the energy range 50-100 keV$_{\mathrm{nr}}$ for the Ar detector [163], and 5-30 keV$_{\mathrm{nr}}$ for the Xe detector [80, 150, 47], where keV$_{\mathrm{nr}}$ is defined as energy deposited in the detector by NR. WIMP rates are shown as bands which illustrate the projected change in sensitivity if the lower bound of the WIMP search window is lowered to 30 keV$_{\mathrm{nr}}$ for the Ar detector [153] and 2 keV$_{\mathrm{nr}}$ for the Xe detector [133]. Neutron rates increase by $<\times 2$ in these scenarios.

For both Ar and Xe detectors, the ^{238}U early sub-chain contributes $\times 1/10$ the neutron rate of the ^{226}Ra sub-chain. The increase closely tracks the raw neutron emission rate as a function of ^{238}U early chain imbalance in Fig. 6.5, indicating insensitivity to the exact shape of the neutron energy spectra in Fig. 6.7. The neutron rates in the two detectors are comparable in their respective WIMP search energy regions. The Xe detector takes advantage of its low energy threshold for a high WIMP detection rate. The WIMP signal rate in the Xe detector is a factor $\times 12$ above background and a factor $\times 40$ above the WIMP rate in the Ar detector, at $M_\chi = 100$ GeV. The Xe detector shows greater resilience against neutron backgrounds due to its higher WIMP signal rate, and is able to achieve comparable discovery potentials to the Ar detector with an order of magnitude higher background, or detect WIMPs with an order of magnitude lower interaction cross-section at comparable background levels.

6.7 ^{238}U Disequilibrium Impact on Gamma Backgrounds for Dark Matter Experiments

The γ energy emission spectra for the ^{238}U early sub-chain, ^{226}Ra sub-chain, and ^{210}Pb sub-chain are shown in Fig. 6.10. Gamma emission from the ^{238}U early sub-chain and ^{210}Pb sub-chain is subdominant in both intensity and energy to that from the ^{226}Ra sub-chain. This limits the impact of ^{238}U chain disequilibrium on ER backgrounds.

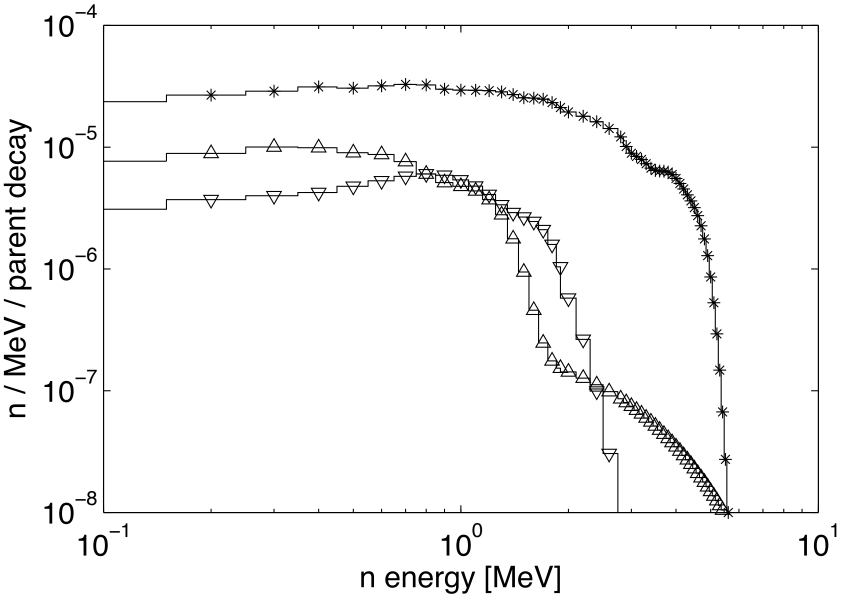

Figure 6.7: Neutron emission energy spectra corresponding to ^{238}U spontaneous fission and (α,n) emission on F from the ^{238}U early sub-chain (upward arrows), ^{226}Ra sub-chain (stars), and ^{210}Pb sub-chain (downward arrows). Spectra were calculated from Eq. 6.1.

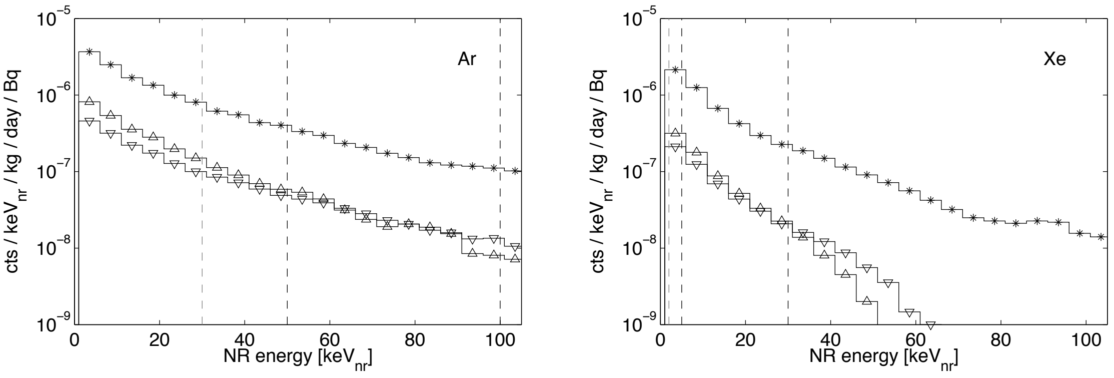

(a)

(b)

Figure 6.8: NR spectra in simulated one tonne (a) liquid Ar and (b) liquid Xe detectors, using geometry as described in Sec. 6.6. Recoil spectra correspond to neutrons generated from the ^{238}U early sub-chain (upward arrows), ^{226}Ra sub-chain (stars), and ^{210}Pb sub-chain (downward arrows), with incident neutron energy spectra given in Fig. 6.7. Black dashed vertical bars indicate typical WIMP search windows for both detectors, with gray bars indicating potential improvements in low-energy threshold. Rates are found in a 500 kg cylindrical fiducial volume. A cut removing multiple scatter events is applied.

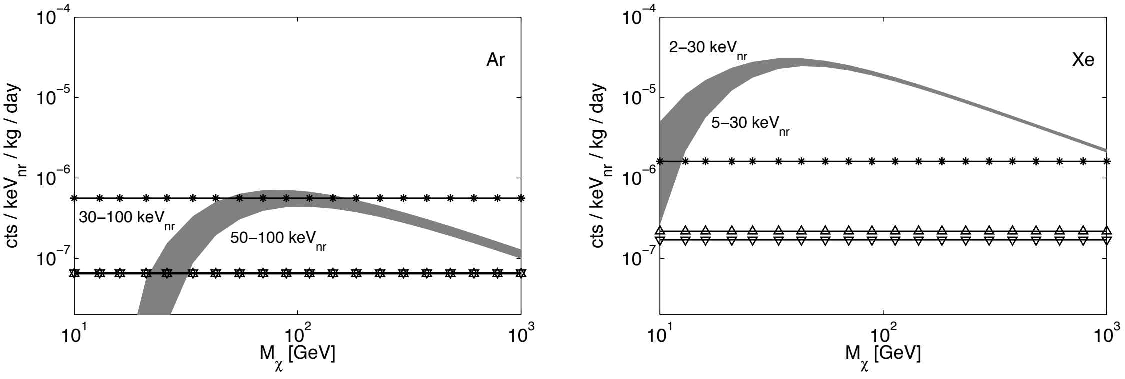

(a) (b)

Figure 6.9: WIMP signal and neutron rates as a function of WIMP mass M_χ in simulated one-tonne (a) liquid Ar and (b) liquid Xe detectors. A WIMP-nucleon spin-independent cross-section of 10^{-45} cm^2 is assumed. Neutron rates correspond to 1 Bq of ^{238}U early sub-chain (upward arrows), ^{226}Ra sub-chain (stars), and ^{210}Pb sub-chain (downward arrows). Note that ^{238}U early sub-chain and ^{210}Pb sub-chain NR rates overlap for the Ar detector, at 7×10^{-8}. Rates are calculated using NR energy windows of 50-100 keV$_{\rm nr}$ for Ar and 5-30 keV$_{\rm nr}$ for Xe. WIMP rates are shown as bands illustrating the effect of lowering the detection threshold to 30 keV$_{\rm nr}$ for Ar and 2 keV$_{\rm nr}$ for Xe, as shown in Fig. 6.8.

ER backgrounds from ^{238}U disequilibrium is assessed by Monte Carlo, using the detector and emission geometries for one tonne liquid Ar and liquid Xe detectors described in Sec. 6.6. Gamma energies following the probability distribution shown in Fig. 6.10, for each of the ^{238}U sub-chains, are thrown from the border between the target material and the water shield, representing activity from detector internals. Position cuts are used to remove multiple-scatter events, as well as events which deposit energy outside of the fiducial volume. Details of these cuts are discussed in Sec. 6.6.

ER event rates are found at low energies and normalized per keV$_{\rm ee}$, where keV$_{\rm ee}$ is defined as energy deposited in the detector by ER. The recoil energy spectrum in both Ar and Xe detectors is flat below the 46.5 keV$_{\rm ee}$ peak from ^{210}Pb decay. Rates are estimated in the range 1-45 keV$_{\rm ee}$.

Fiducial rate as a function of mass is shown in Fig. 6.11 for both detectors. Three scenarios are considered, in which the ^{238}U early / ^{226}Ra sub-chain fraction X is 1, 10 or 100. The number of γ rays passing the analysis cuts described above and depositing energy within the fiducial region is shown in units of counts keV$_{\rm ee}{}^{-1}$ kg^{-1} day^{-1} (Bq ^{226}Ra)$^{-1}$. Fiducial volume shape is optimized to yield the lowest activity, while keeping the fiducial boundary convex.

Both Ar and Xe detectors are insensitive to a disequilibrium condition of $X = 10$. At 500 kg fiducial mass, fiducial activity is increased by 10% for the Ar detector, and 9% for the Xe detector. Event rates are significantly increased for both detectors in the case of $X = 100$, with a factor ×2.2 increase for the Ar detector, and a factor ×2.0 increase for the Xe detector. Holding the event rate constant from the equilibrium case, a factor ×100 imbalance results in the loss of 73 kg fiducial mass for the Ar detector and 60 kg for the Xe detector, starting at a 500 kg fiducial in equilibrium. The case of $X = 100$ is used as a conservative example; standard γ counting techniques are typically sensitive to imbalances a factor ×1/2 this number or lower.

For completeness, the impact of an excess of ^{210}Pb sub-chain rate relative to ^{226}Ra sub-chain rate is shown in Fig. 6.12. The only significant γ emission in the ^{210}Pb sub-chain comes from the 46.5 keV γ from ^{210}Pb decay. The penetration length of this γ is 8 mm in Ar and 0.2 mm in Xe, and thus does not represent a significant background addition after modest fiducial cuts.

The spectrum of γ rays passing analysis cuts and contributing fiducial backgrounds is shown in Fig. 6.13. A 500 kg cylindrical fiducial mass with 1:1 aspect ratio was used, with single-scatter and energy cuts used as described above. The photoelectric cross-section is equal to or greater than the Compton cross-section for energies below 75 keV for Ar and 300 keV for Xe. Below these energies, γ mean free path drops sharply with energy.

The 500 kg fiducial ER rate in the Ar detector is a factor ×30 that of the Xe detector at 500 kg. However, Ar detectors can utilize powerful discrimination against ER events through characterization of the scintillation time constant, potentially reaching ER discrimination power of 10^9 [153, 163]. Xenon detectors rely on differences in ionization to scintillation ratio for ER discrimination, with typical values in the range 10^2-10^3, dependent on electric field strength [150, 126, 48]. In the case of Ar, ER backgrounds from detector components are subdominant to contributions from ^{39}Ar, a 565 keV endpoint β emitter with a rate of 1 Bq kg^{-1} in natural Ar. For a 500 kg fiducial, backgrounds from detector components only become relevant if ^{39}Ar is removed to a factor $\times 10^{-5}$ of its natural value, assuming a 1 Bq concentration of ^{238}U in equilibrium in detector internals. By using Ar found in natural

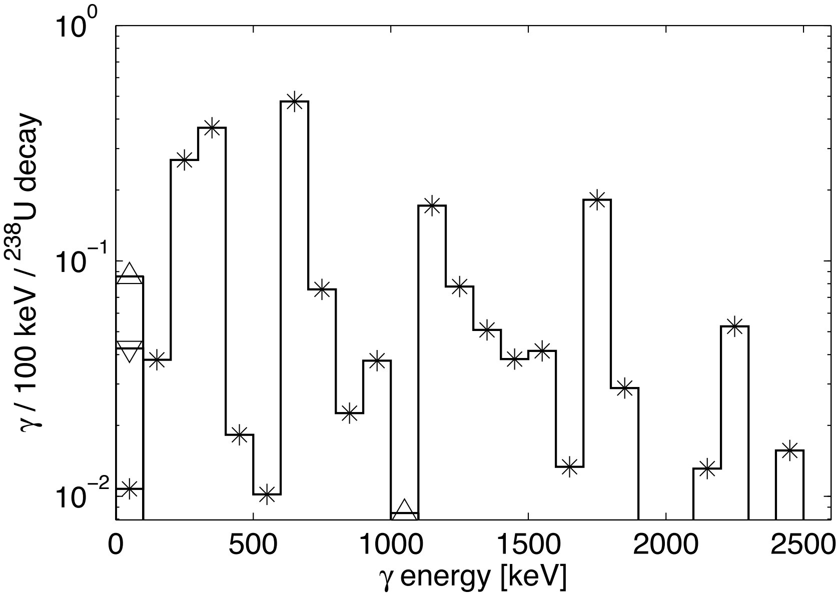

Figure 6.10: Gamma energy spectra generated from ^{238}U decay chain isotopes, assuming full-chain secular equilibrium. Gammas are shown corresponding to the ^{238}U early sub-chain (upward arrows), ^{226}Ra sub-chain (stars), and ^{210}Pb sub-chain (downward arrows). Data is taken from [135].

gas wells, the ^{39}Ar concentration has been shown to be reduced by a factor $\times 10^{-2}$ from its typical atmospheric concentration [79].

6.8 Conclusions

We find that the ^{238}U early sub-chain, ^{226}Ra sub-chain, and ^{210}Pb sub-chain from the ^{238}U decay chain have significantly different neutron yields per decay. For typical detector construction materials, the (α,n) neutron yield increases by one to three orders of magnitude as α energy increases in the range 4-8 MeV. The ^{238}U early sub-chain contributes three α particles per ^{238}U decay with energies of 4.2-4.8 MeV, at the lowest end of the range. The ^{226}Ra sub-chain contributes four α particles over a broader range, with energies spanning 4.8-7.8 MeV. If the ^{238}U early sub-chain has an order of magnitude greater concentration than the ^{226}Ra sub-chain, then the total neutron emission rate increases by only ×2-4, where the precise increase depends on the target material. A two order of magnitude increase results in a ×10 increase in total neutron emission rate. If a material has a low (α,n) yield, then neutron emission is dominated by spontaneous fission from ^{238}U. This leads

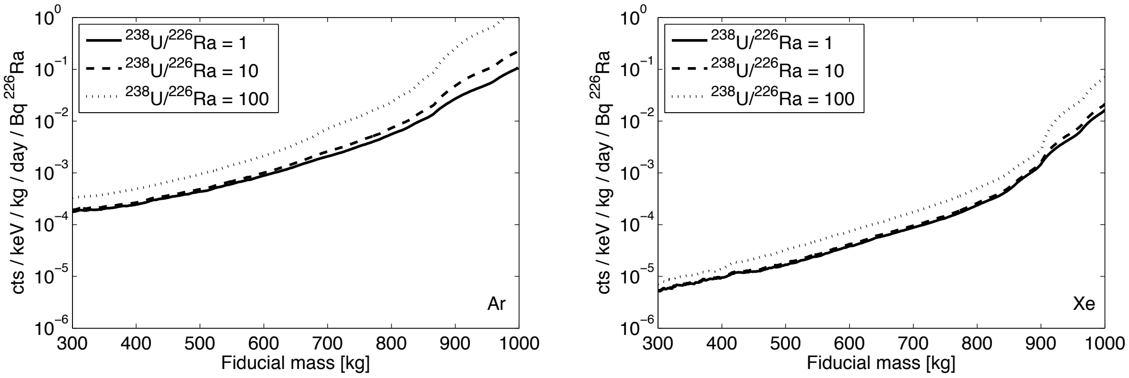

(a) (b)

Figure 6.11: Fiducial ER rate in simulated one tonne (a) liquid Ar and (b) liquid Xe detectors from ^{238}U sub-chain γ rays, as a function of fiducial mass. Three scenarios of ^{238}U early sub-chain / ^{226}Ra sub-chain ratio X are shown: $X = 1$ (solid), $X = 10$ (dashed), and $X = 100$ (dotted). The concentrations of ^{226}Ra sub-chain and ^{210}Pb sub-chain isotopes are held constant in all scenarios, while the concentration of ^{238}U early sub-chain isotopes is varied. Gammas depositing energy in the range 1-45 keV$_{\mathrm{ee}}$ are selected, and single-scatter cuts are applied which reject events with energy-weighted standard deviation above 2 cm in radius and 0.5 cm in height.

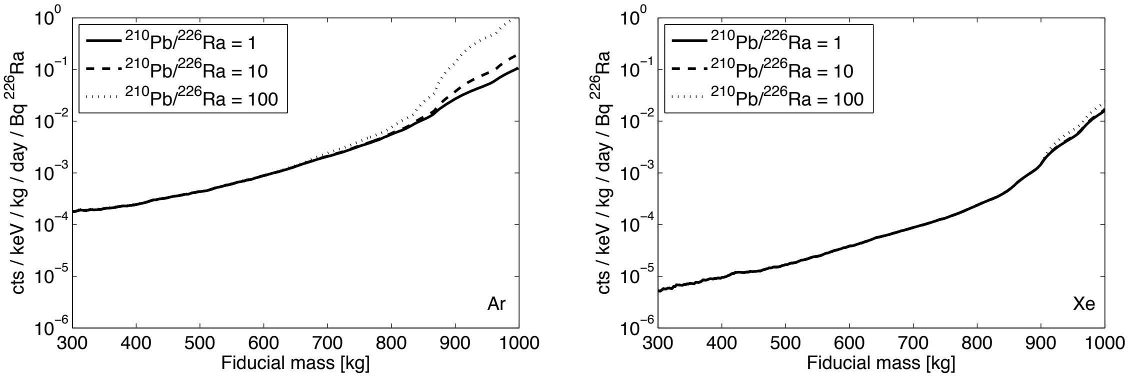

(a) (b)

Figure 6.12: Fiducial ER rate in simulated one tonne (a) liquid Ar and (b) liquid Xe detectors from ^{238}U sub-chain γ rays, as a function of fiducial mass. Three scenarios of ^{210}Pb sub-chain to ^{226}Ra sub-chain rate are shown: ×1 (solid, corresponding to ^{238}U chain equilibrium), ×10 (dashed), and ×100 (dotted). The concentrations of ^{238}U early sub-chain and ^{226}Ra sub-chain isotopes are held constant in all scenarios, while the concentration of ^{210}Pb sub-chain isotopes is varied. Cuts are used as described in Fig.6.11.

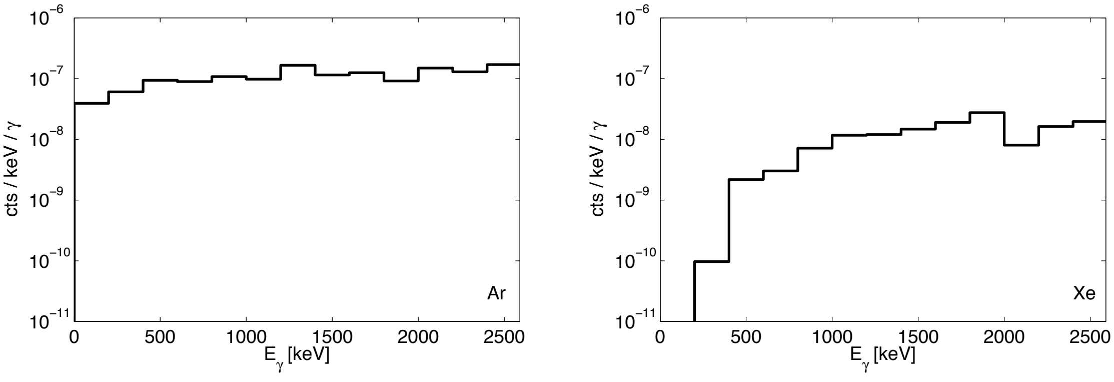

(a) (b)

Figure 6.13: Fraction of γ rays generating fiducial backgrounds in simulated one tonne (a) liquid Ar and (b) liquid Xe detectors, as a function of γ energy. Gamma rates are found in a 500 kg cylindrical fiducial mass with 1:1 aspect ratio is used. Single-scatter and energy cuts are applied as described in Fig. 6.11.

to a more linear relationship between neutron yield and the ratio of ^{238}U early sub-chain to ^{226}Ra sub-chain. In practice, spontaneous fission events are vetoed by their simultaneous generation of multiple neutrons and MeV γ rays, which would interact in the active region of the detector.

Typical γ screening with Ge detectors is ×20-60 more sensitive to ^{226}Ra sub-chain decay than to ^{238}U early sub-chain decay. This is due to the low emission probability per decay of high-energy gammas (×300 keV) from the ^{238}U early sub-chain compared to the ^{226}Ra sub-chain. If ^{238}U early sub-chain concentration is ×20(60) greater than ^{226}Ra sub-chain concentration, then neutron emission from high (α,n) yield materials such as F and Al is increased by a factor ×2(6). Mass spectrometry techniques can potentially detect ^{238}U directly. However, these techniques are insensitive to ^{238}U decay chain daughters due to their low concentrations, given their relatively small half-lives. Inhomogeneity in ^{238}U sub-chain concentrations within material samples can also significantly skew mass spectrometry results, which only sample small amounts of material. Gamma screening techniques sample large masses, and average well over inhomogeneous materials. For large dark matter detectors, bulk counting is crucial for sampling all detector construction materials, as there can be many tonnes of material used in close proximity to the detector active region.

Background neutron event rates from ^{238}U early sub-chain, ^{226}Ra sub-chain, and ^{210}Pb sub-chain decays in high (α,n) yield materials has been assessed by Monte Carlo for simplified one tonne liquid Ar and liquid Xe detectors. We find that the Xe detector has a signal-to-background ratio ×12 higher than the Ar detector, over neutron events from a similar level of ^{238}U chain isotope concentration, for identification of 100 GeV WIMPs. The ^{226}Ra sub-chain dominates neutron backgrounds per decay when compared to the ^{238}U early sub-chain and ^{210}Pb sub-chain by an order of magnitude. For a given sub-chain, the Ar and Xe detectors have similar neutron event rates when considering WIMP search energy windows of 50-100 keV$_{\mathrm{nr}}$ and 5-30 keV$_{\mathrm{nr}}$ respectively, which are typically quoted for these detectors.

Gamma backgrounds for Ar and Xe tonne-scale detectors are impacted negligibly by an excess of ^{238}U early sub-chain or ^{210}Pb sub-chain activity relative to ^{226}Ra sub-chain activity, for typically quoted γ screening limits. For the Xe detector, ER backgrounds from γ rays in the 500 kg fiducial are increased by only ×1.1 and ×2 when ^{238}U early sub-chain concentration is increased by a factor ×10 and ×100 from full-chain equilibrium, respectively. The ^{210}Pb sub-chain has negligible contribution, even at rates ×100 higher than in full-chain equilibrium. The Ar detector has comparable sensitivity to ^{238}U early sub-chain and ^{210}Pb sub-chain excesses as the Xe detector. Argon detector ER backgrounds are typically dominated by β backgrounds from ^{39}Ar, which contribute an ER rate in the 500 kg fiducial which is $\times 10^5$ higher than activity from 1 Bq of ^{238}U in construction materials.

For experiments in which background rates are dominated by NR events from neutrons, ^{238}U early sub-chain and ^{210}Pb sub-chain excesses can cause a significant increase in experiment backgrounds over expectations based on the assumption of full-chain equilibrium. A ^{238}U early sub-chain concentration which is ×60 higher than the ^{226}Ra sub-chain concentration leaves the possibility of a neutron emission rate which is ×6 higher than the emission rate from full-chain equilibrium, as discussed above. Experiments with NR-dominated backgrounds would then have a background rate ×6 higher than expectations. Experiments which have ER-dominated backgrounds are relatively insensitive to excesses of ^{238}U early sub-chain and ^{210}Pb sub-chain concentrations. ER backgrounds increase by less than a factor ×2 for ^{238}U early sub-chain excesses within γ screening limits, and increase negligibly for a ×100 ratio of ^{210}Pb sub-chain concentration to ^{226}Ra concentration.

Experiments which have NR-dominated backgrounds can potentially benefit from the use of mass spectrometry screening techniques to directly measure ^{238}U concentrations in construction materials. These techniques would compliment γ radioassay measurements in order to identify potential disequilibrium conditions. Experiments with ER-dominated backgrounds do not gain significant refinement in background expectation from the use of mass spectrometry counting, and are able to rely on screening from γ radioassay alone.

6.9 Acknowledgements

We thank Chamkaur Ghag for his insights into mass spectrometry techniques. This work is supported by the U.S. Department of Energy (DOE) under award numbers DE-FG02-91ER40688 and DE-FG02-13ER42023.

CHAPTER 7

THE LUX MATERIALS SCREENING PROGRAM

The LUX detector aims to measure dark matter interactions rates as low as a few in 30000 kg days. In order to clearly distinguish this extremely low event rate, a low background signal in the detector is crucial. The largest contributor to detector backgrounds is radiation from the decay of radioactive isotopes in detector materials.

Starting in 2007, a comprehensive program was put in place to ensure that the radioisotope concentrations in all LUX detector construction materials met the goal of contributing <1 background event after ER discrimination during the 30000 kg day detector run. The primary measurement technique used to ensure this low event rate was γ spectroscopy, performed at the Soudan Low-Background Counting Facility (SOLO). The measurements were closely interfaced with the simulation effort aimed at modeling LUX backgrounds, described in Ch. 5.

The SOLO facility and detector have been described in published work [129]. Sec. 7.2 includes excerpts from this work describing the detector, calibration procedure, and analysis methods. Additional information on detector sensitivity and data analysis is also provided. Sec. 7.3 includes excerpts from the same work on screening results for the LUX R8778 PMTs. A look ahead at PMT screening results for the next-generation LZ detector is given in Sec. 7.5.

7.1 Counting Goals

The goal of the LUX counting program was to ensure a background rate <1 mDRU$_{ee}$ contributed from γ backgrounds from detector construction materials. This goal was set in the original LUX proposal [71, 110]. The goal was established based on the following:

1. Early Hamamatsu screening results of R8778 PMTs, with upper limits on PMT radioisotope concentrations of <18 ^{238}U / <17 ^{232}Th / <30 ^{40}K /<8 ^{60}Co mBq/PMT;
2. A custom Geant4 Monte Carlo for a 50 cm × 60 cm liquid Xe volume with radioactive "end caps," which predicted a background rate of 0.83 mDRU$_{ee}$ from the PMTs in a 100 kg cylindrical fiducial volume;
3. Assumption that the PMTs would be the dominant radioactive load near the active region by a factor of ×5.

The goal of 1 mDRU$_{ee}$ was maintained through the counting program, despite measured PMT radioactive loads significantly lower than the upper limits reported initially by Hamamatsu (Sec 7.3.2). The goal of 1 mDRU$_{ee}$ was also a convenient marker for maintaining the very low background rate in LUX, as it corresponded to 1 WIMP-like background event in 300 livedays after ER rejection (assumptions: 100 kg, 300 days, energy range 1.3–8 keV$_{ee}$, 99.5% ER discrimination). The numbers informing the counting assumption evolved as LUX was constructed and calibrated, after the counting program was completed. It is important to note that the screening goal of 1 mDRU$_{ee}$ is not a complete background budget goal for the entire detector, as it does not account for backgrounds generated by cosmogenic activation or intrinsic contaminants. A breakdown of backgrounds from counting results, and a comparison with the established backgrounds from *in situ* measurements, is given in Sec. 7.4.

From LUX screening of the R8778 PMTs, and detailed background modeling using LUXSim (Sec. 5.2), it was determined that the actual PMT contribution to detector backgrounds in the optimized 100 kg fiducial is 0.5 mDRU$_{ee}$. The total LUX background counting goal was maintained at 1 mDRU$_{ee}$, allowing finite counting results for other detector components to fill the remaining 0.5 mDRU$_{ee}$ in the budget.

7.1.1 Goals for Major Internals

The PMTs were expected to be the dominant contributor to LUX low-energy ER backgrounds. This is due to the difficulty of low-background material selection for all PMT construction components, as well as their close proximity to the detector active region. Other detector construction materials are custom-made for the experiment, and are known to have relatively low radioisotope concentration relative to the PMTs. For this reason, the LUX counting program focuses on ensuring that backgrounds from detector construction materials are subdominant to those contributed by the PMTs.

The material screening program uses input from the background modeling program to set counting goals. Background modeling studies generate estimates of low-energy ER background rates in the fiducial volume, as a function of radioisotope concentration, for all detector components. This is referred to as "background efficiency." By setting a limit on the allowed background rate contribution from a given material, a corresponding limit is set on radioisotope concentration in that material, where the scaling factor is the background efficiency.

The combined counting goal for the large-mass internal construction components in close proximity to the active region (referred to as "major internals") was <0.5 mDRU$_{\mathrm{ee}}$, as described above. This is the most aggressive practical limit that could be set for the components. The large masses of the components used in the detector limited the effectiveness of small-sample screening in controlling the predicted background rate. The use of an upper limit on the 0.5 mDRU$_{\mathrm{ee}}$ combined contribution from all internals also has a very conservative meaning, as the limit is formed by the naive addition of 90% confidence upper limits from $\sim$10 different material samples. The confidence level set by the addition of several 90% limits is at the very least 90%, and likely much stricter.

7.1.2 Goals for Small Internals

An estimated 150 construction components are used in LUX which are either low-mass ($\lesssim$kg) or shielded from the active region by other construction components. These items are referred to as "small internals." For typical small components, the target background rate per component was set at <0.5 μ$\mathrm{DRU_{ee}}$ at 90% CL. This was chosen such that the addition of the 150 components would result in a <0.1 $\mathrm{mDRU_{ee}}$ contribution, which is subdominant to the total screening goal for the detector (and, as described in Sec. 7.1.1, the naive addition of the 90% limits results in a much stricter upper limit on the combined background rate). Although this background rate is extremely aggressive, the small amount of material used in the detector allows the goal to be met with a modest γ counting sample.

7.2 SOLO

7.2.1 The SOLO Facility and Diode-M Detector

The SOLO facility is located at the Soudan Underground Laboratory, at a depth of 2.0 km.w.e [164]. The SOLO chamber and detector are shown in Fig. 7.1. The counting chamber uses the "Diode-M" detector, a 0.6 kg high-purity Ge detector housed in a 0.15 cm thick Cu shield. The 20 cm × 25 cm × 30 cm chamber is enclosed with a minimum of 30 cm lead shielding on every side. The inner 5 cm lining of the chamber is comprised of ancient lead, with ^{210}Pb activity measured below 50 mBq kg^{-1}. A mylar shell and 2.5 slpm nitrogen gas purge are used to eliminate gaseous radon from the chamber. SOLO detector output is shaped with a 2 μs shaping time, using a Spectroscopy Amplifier, before digitization at a dedicated acquisition computer. Integrated sets of (energy bins, counts) data are written to files every 4 hours. Data files are hosted from a server at Soudan, and are transferred to Brown for analysis.

SOLO has been used since 2003 for screening and cataloging of low-background materials for use in liquid Xe detectors. SOLO was used in the screening program for XENON10 construction materials, and has been heavily engaged in the LUX material screening program since 2007 [71, 80, 112, 47]. SOLO detector sensitivity calibrations are accomplished using Geant4 Monte Carlo simulations. The geometry of the entire SOLO detector and chamber are reproduced, as well as the geometry and location of the counted sample. Emission spectra for each screened isotope, including the full decay chains of ^{238}U and ^{232}Th, are reproduced. These simulations account for effects including energy-dependent detection efficiency, sample location, sample size, and sample self-shielding. The simulations produce scaling factors between detector counts and source emission intensity for each γ line, referred to as the detection efficiency ε. The typical units of ε are DRU mBq^{-1}, where Bq $\equiv$ decays s^{-1}. ε can also be expressed in counts mBq^{-1}, when integrating over a given energy range and multiplying by detector mass and livetime. Analytic estimates of ε can be generated to cross-check simulation results. However, it is very difficult to include the effects of finite sample size and sample self-shielding in these estimates, whereas those effects are automatically included in the Monte Carlo analysis. A fit to a 1 mCi ^{60}Co source is shown in Fig. 7.2.

A typical background spectrum with the chamber empty is shown in Fig. 7.3 (black) for 21 live days. Features are seen at 662 keV and 1461 keV, corresponding to γ lines from ^{137}Cs and ^{40}K, respectively, and are used to verify energy bin calibration in conjunction with the 46.5 keV line from ^{210}Pb decay. Background baseline rise below 1 MeV is caused primarily by Bremsstrahlung radiation from ^{210}Pb β decay in the inner Pb shielding layers. Initial detector calibrations were performed using several samples with known contamination. Backgrounds are remeasured periodically to check for chamber contamination or Rn leakage, and are used to periodically verify calibrations. An example of Rn leakage in the chamber is shown in Fig. 7.4, where the 352 keV and 609 keV lines from ^{222}Rn daughter decays (^{214}Pb and ^{214}Bi, respectively) are clearly visible. The measured peak energy resolution as a function of energy is shown in Fig. 7.5. Peak sensitivity as a function of energy for a point calibration source at the bottom of the SOLO chamber, estimated from Monte Carlo, is shown in Fig. 7.6.

The projected sensitivity of the detector is calculated to predict the upper limit on activity for a given sample and counting livetime. The sensitivity, expressed in detected event rate (units of DRU, in SOLO) as a function of counting livetime, is shown for several common peaks in Fig. 7.7. The sensitivity is calculated from samples of a three week background dataset. The given rate must be multiplied by the expected efficiency factor ε to predict sensitivity to decay rates. For samples placed close to the detector, ε can reach $\sim$1 DRU mBq^{-1}. Samples placed far from the detector, or with significant self-shielding, can have an efficiency factor which is worse by an order of magnitude.

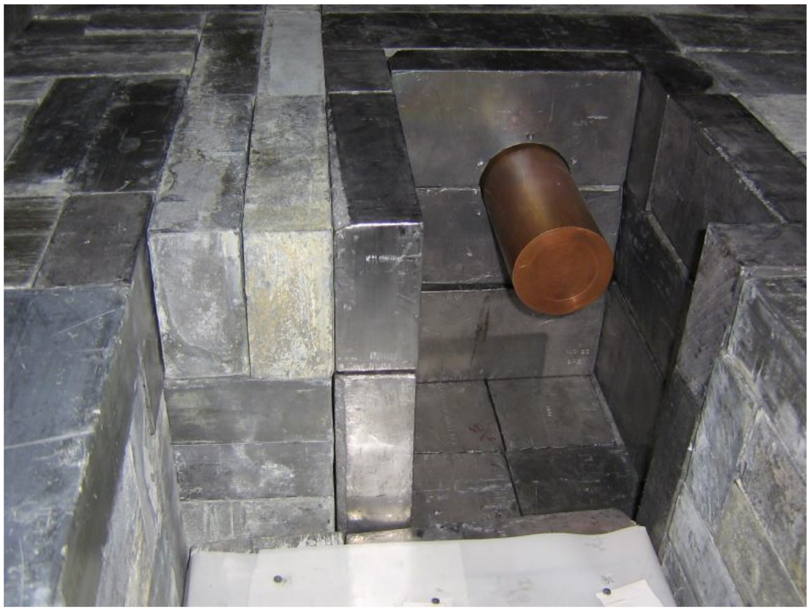

Figure 7.1: The open SOLO chamber, shown during construction of the shield in 2005. The 0.6 kg high-purity germanium detector is housed in a 1.5 mm thick Cu shield. The chamber is lined with >30 cm of lead shielding. The inner 5 cm lead layer was selected for its measured ^{210}Pb content (<50 mBq kg^{-1}) [164]. The inner chamber measures 25 cm × 20 cm × 30 cm.

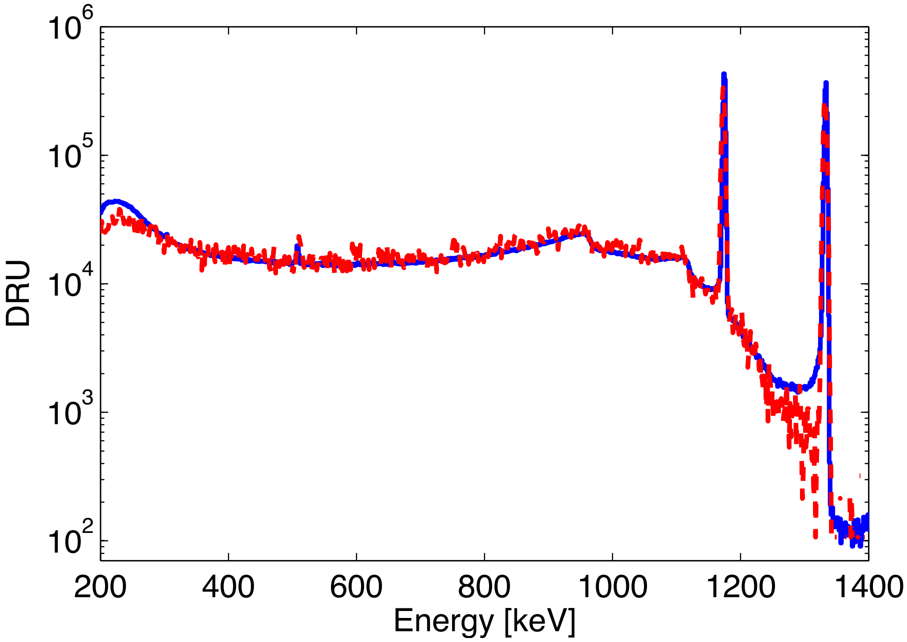

Figure 7.2: Comparison of calibration Monte Carlo output (solid blue) with SOLO data from a ^{60}Co source (dashed red). Calibration Monte Carlo includes the detailed SOLO chamber and detector geometries, as well as faithful reconstruction of the source geometry to account for finite sample size and self-shielding.

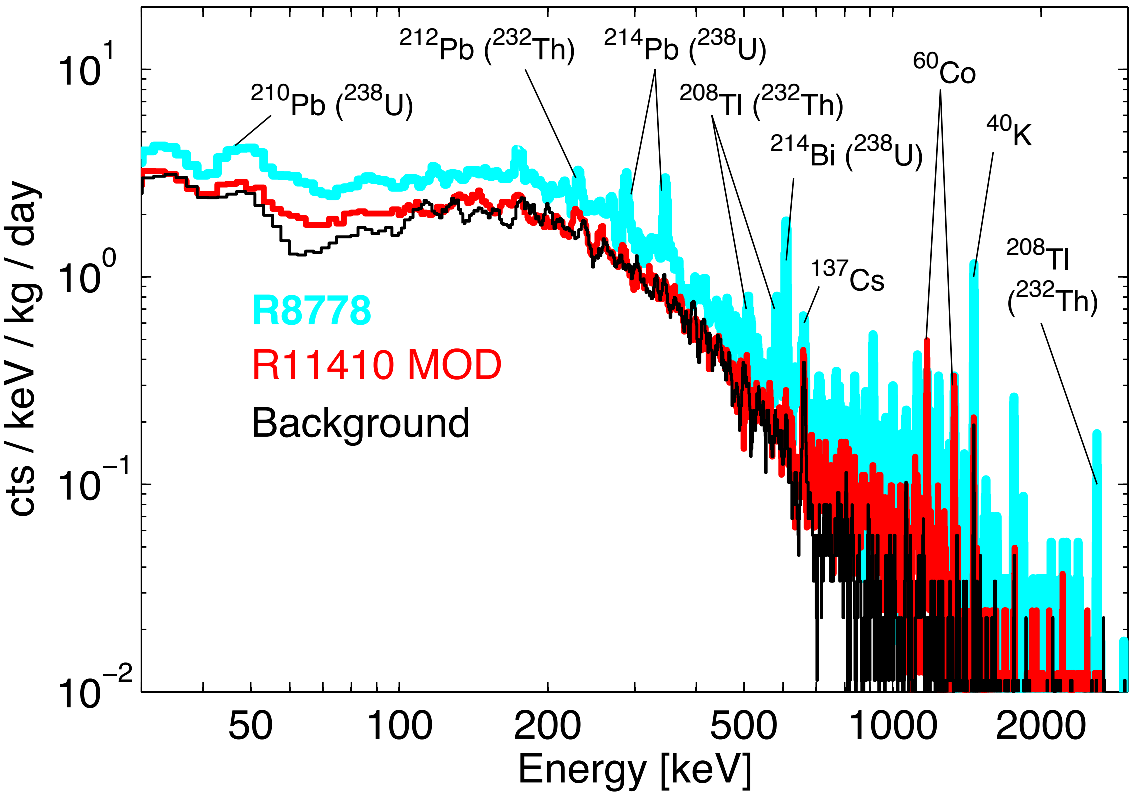

Figure 7.3: SOLO counting spectra for R8778 (14 live days, blue) and R11410 MOD (19 live days, red) PMTs, superimposed with a sample background run (21 live days, black). ^{238}U is primarily identified by lines from late-chain daughters at 295, 352, and 609 keV. ^{232}Th is identified by lines at 239, 511, 582, and 2614 keV. ^{40}K is identified by a single line at 1460 keV. ^{60}Co yields twin peaks at 1173 and 1333 keV. Strong lines in the R8778 spectrum indicate the presence of ^{238}U, ^{232}Th, ^{40}K and ^{60}Co radionuclides. The reduced activity of the R11410 MOD is readily apparent from the lack of distinct features in comparison with the R8778, with the only activity significantly above background from the presence of ^{60}Co. Lines at 46.5 keV (^{210}Pb), 662 keV (^{137}Cs) and 1460 keV are used to periodically verify detector calibration. SOLO datasets shown are lux_5_pmts_batch_2 (R8778), R11410_v2_post_clean (R11410-20), and bg_combined_2011 (background).

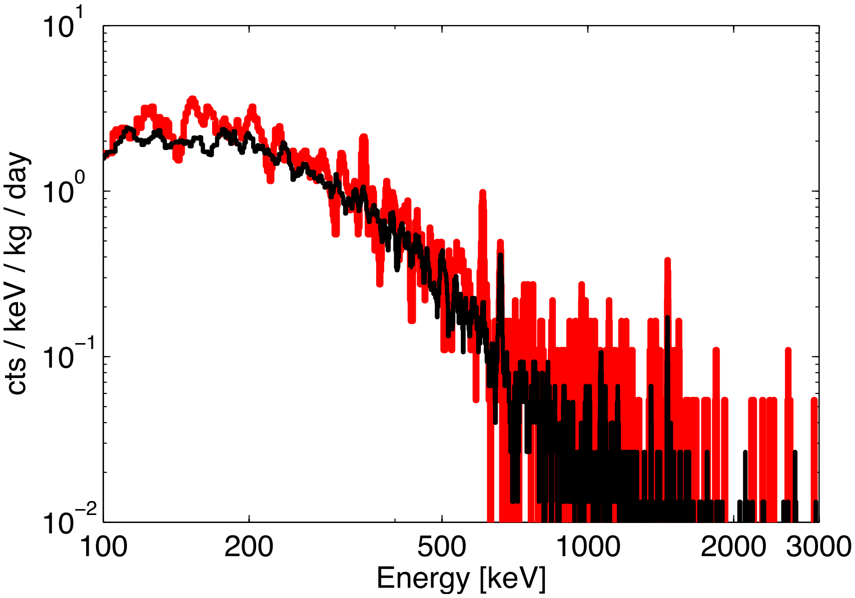

Figure 7.4: Example background plot from ^{222}Rn leakage into the SOLO chamber (red, 4 days), compared with standard background (black, 21 days). Chamber includes only radiopure polyethylene material, which was recounted after the radon leak was sealed to verify its low radioisotope content. Peaks from ^{222}Rn daughter decays (^{214}Pb and ^{214}Bi, respectively) at 352 keV and 609 keV are clearly visible. SOLO dataset 'inner_poly' is used for the contaminated dataset.

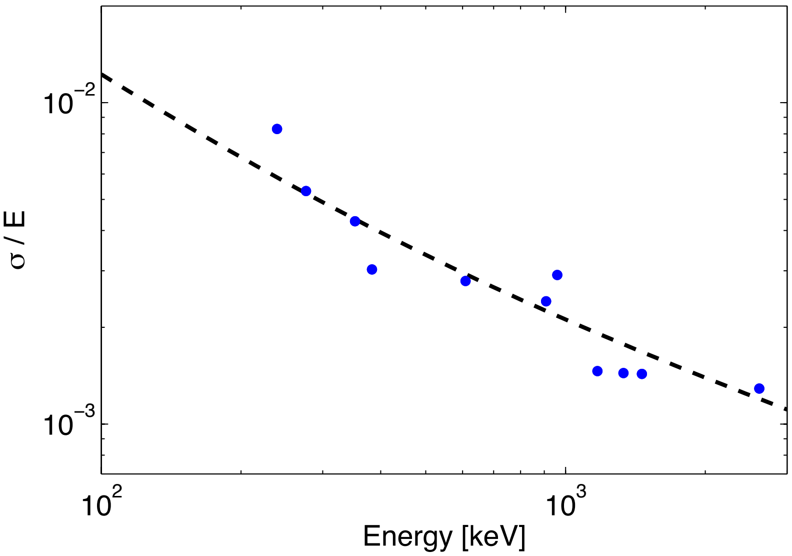

Figure 7.5: SOLO measured σ/μ energy resolution as a function of energy. The measured points are characterized by the curve $\sigma^2 = 0.0033E + 1.2$.

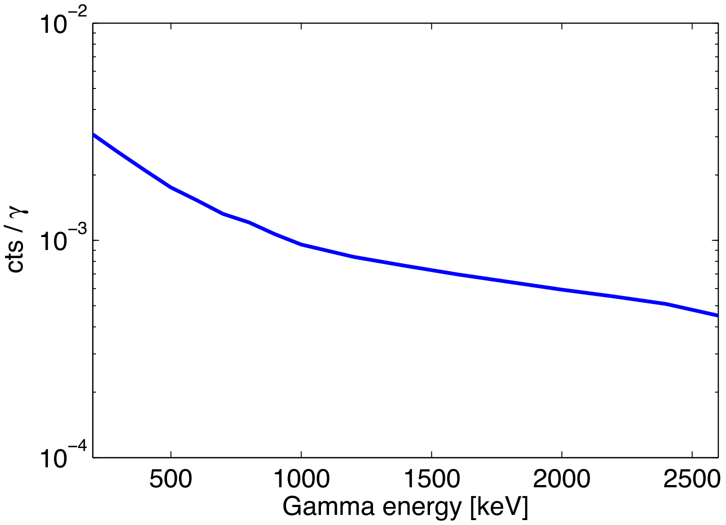

Figure 7.6: Simulated full-energy γ depositions in the SOLO detector per γ emitted, as a function of γ energy. A point source emission geometry is used, located at the bottom of the chamber, directly beneath the front face of the detector (17 cm from the bottom edge of the detector). Curve is obtained from calibration Monte Carlo.

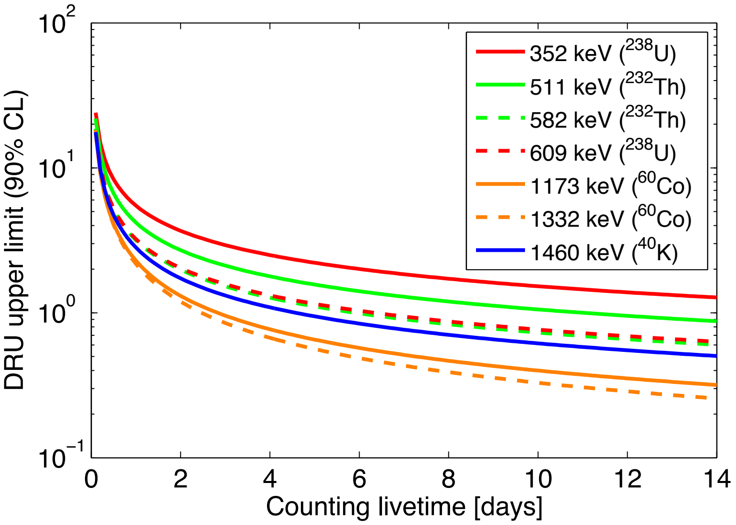

Figure 7.7: SOLO rate upper limits, as a function of counting livetime, for several common peaks. The DRU upper limit is calculated from measured background data.

7.2.2 Counting Methodology

Positive signatures of radioactive isotopes are identified through two high-branching ratio energy lines, when available. For measurement of the ^{238}U chain, lines at 352 keV and 609 keV are used, corresponding to the decay of ^{214}Pb and ^{214}Bi respectively. The ^{232}Th chain is identified by lines at 511 keV and 583 keV from ^{208}Tl decay. ^{60}Co is detected through peaks at 1173 keV and 1332 keV. ^{40}K offers only a single γ line, at 1461 keV.

It has been noted that ^{238}U decay chain secular equilibrium can be broken during certain manufacturing processes due to the solubility of ^{226}Ra in water (see Ch. 6). For this reason, a more direct estimate of ^{238}U concentration is made from measurement of the 1001 keV line from $^{234\mathrm{m}}$Pa, several steps above ^{226}Ra in the decay chain. The branching ratio for the 1001 keV line is a factor of $\times 1/62$ that of the branching ratio for the 352 keV line, and thus produces correspondingly weaker upper limits. It should be noted that there is no *a priori* reason to assume a break in equilibrium, unless a positive identification of the 1001 keV line is made. It should also be noted that the most relevant, high branching ratio γ rays are generated in the lower part of the ^{238}U chain, and this measurement is of the most relevance for the estimation of electromagnetic backgrounds. A full discussion of γ emission in ^{238}U chain disequilibrium is given in Ch. 6.

Upper limit estimates are always given at 90% confidence level, the standard used during LUX material counting. Quoted errors are statistical. Systematic errors are contributed primarily by uncertainty in sample placement within the chamber and in sample self-shielding, and are conservatively estimated to be at the level of ±20%.

Upper limits are calculated assuming a Poisson-distributed signal. The measured value N, in counts, accumulated over a livetime L, is defined as $N \equiv S + B$, where S is the number of γ signal counts, and B is the expected number of background counts for livetime L, measured from separate background-only datasets. As S depends on the efficiency of γ detection, it is defined as $S \equiv \varepsilon\alpha$, where α is the source radioactivity in units of mBq, and ε is the detection efficiency obtained from Monte Carlo calibration in units of counts mBq^{-1}. For a given confidence level CL (equal to 0.9 for all SOLO results), the following integral is numerically evaluated to determine the parameter α':

Gamma (Isotope/Chain)	ε^{-1} **[mBq DRU^{-1}]**
352 (^{214}Pb/^{238}U)	1.93
511 (^{208}Tl/^{232}Th)	9.23
582 (^{208}Tl/^{232}Th)	4.86
609 (^{214}Bi/^{238}U)	2.98
1173 (^{60}Co)	2.59
1332 (^{60}Co)	3.00
1460 (^{40}K)	25.9

Table 7.1: Detection efficiency ε for peaks used for identification of common radioisotopes, for a batch of five R11410-20 PMTs in the SOLO chamber. ε is calculated from Geant4 Monte Carlo, as described in Sec. 7.2.1, and folds in gamma branching ratio, sample geometry, material absorption, and finite detector size.

$$CL = \frac{\int_0^{\alpha'} p\left(N, \varepsilon\alpha + B\right) d\alpha}{\int_0^{\infty} p\left(N, \varepsilon\alpha + B\right) d\alpha} \tag{7.1}$$

where $p\left(N, \varepsilon\alpha + B\right)$ is the Poisson distribution function for measured value N and expectation λ. The value of α' then represents the upper limit source activity at confidence level CL. For radioisotopes with multiple characteristic peaks, the SOLO analysis conservatively measures upper limits for each peak independently, and reports the weaker upper limit constraint. The sensitivity can potentially be much greater if the joint likelihood for all characteristic peaks is used in the integrals in Eq. 7.1.

As an example, counting data from the R11410-20 screening for LZ PMTs (Sec. 7.5) is used here. (Dataset 'R11410_S12_PMT_batch_1', background dataset 'bg_combined_2011'.) The ε values for the dataset are listed in Table 7.1. The 352 keV peak is used for an example of setting the upper limit. From Monte Carlo, the detection efficiency for the peak is $\varepsilon^{-1} = 1.93$ mBq DRU^{-1}. The sample and background datasets are integrated in the range 340–355 keV, yielding $N = 83$ counts for 10.5 livedays and $B = 144$ counts for 17.9 livedays. Since N is found over fewer livedays, B is scaled by 10.5/17.9 to yield 84.8 expected background counts for the sample dataset. Using these inputs and numerically evaluating Eq. 7.1, the resulting 90% CL upper limit is <2.6 mBq, or <0.5 mBq PMT^{-1} (there are five R11410-20 PMTs in the chamber for this dataset).

7.3 Counting Results

7.3.1 Identified Radioisotopes and Predicted Cosmogenic Activation

Counting results for a given radioisotope in a given material are reported under two conditions: when the radioisotope is anticipated to be present in the material based on its composition, or when a peak is found at energies corresponding to that isotope. All materials are screened for ^{238}U and ^{232}Th, as these isotopes contribute the highest background per decay, and are common across many construction materials. Potassium-40 is also commonly found in many construction materials. Upper limits are not always measured for ^{40}K for all samples, since it contributes $\times 1/20$ the γ flux per decay of ^{238}U and ^{232}Th and is therefore of secondary importance.

Steel samples are commonly found to contain the isotopes ^{60}Co and ^{54}Mn. Cobalt-60 has a 5.3 year half-life, and is produced cosmogenically through muon capture on Ni. Cobalt-60 is also manmade, and is commonly introduced in high concentrations into small steel batches during manufacturing [165]. Subsequent recycling of the batches results in a ubiquitous presence of ^{60}Co in commercial steel. Manganese-54 is a 312 day half-life cosmogenic isotope, generated by neutron spallation reactions with ^{56}Fe. While several other isotopes (primarily cosmogenic in origin) are commonly measured in steel, ^{60}Co and ^{54}Mn are the most important to characterize, due to their relatively long half-lives and high-energy γ generation [158].

Cobalt-60 is also produced cosmogenically in Cu through neutron spallation reactions. A review of cosmogenic activation studies was used as a reference point for projected LUX Cu activity [166]. Calculations of ^{60}Co production in Cu at sea level show a factor $\times 4$ variation across all predictions [166, 167, 168, 169]. The mean and variance are taken from all predictions as 62 ± 29 kg^{-1} day^{-1}. The predicted production rate of ^{60}Co in LUX Cu during Run 2 at the LUX Surface Facility can be made naively, by scaling the sea level production rate by the change in total neutron flux at the altitude of the Surface Lab relative to sea level. This factor is found to be $\times 3.4$ from a study by Gordon et al. [170]. The ^{60}Co production rate in LUX Cu is then 210 ± 100 kg^{-1} day^{-1}. After an estimated 800 day exposure, the total estimated ^{60}Co concentration is calculated to be 1.0 ± 0.5 mBq kg^{-1}. It is assumed that any change in neutron energy spectrum shape between the Surface Lab and sea level has a subdominant effect on activation rates. The estimated amount of ^{60}Co produced in LUX Cu from Sec. 5.2.2 is 1.7 ± 1.0 mBq kg^{-1}, in agreement with these predictions.

Scandium-46 is a cosmogenic radioisotope with 84 day half-life, produced by ^{46}Ti(n,p)^{46}Sc, muon capture, and neutron spallation. A study of ^{46}Sc production in Ti was undertaken to estimate the decay rates contributed from these channels [171]. The ACTIVIA simulation program (v1.1) [172] was used to estimate the production rate of ^{46}Sc from neutrons at sea level. Assuming an unaltered neutron energy spectrum shape, scaling the spectrum by ×3.4 to account for altitude, multiplying by an additional factor ×2 to account for production by muon capture, and factoring in uncertainty for the relative contributions of the listed activation channels, projected ^{46}Sc rates were estimated to be in the range 2.7–4.8 mBq kg^{-1}. This estimate was found to be in agreement with directly measured activity of a Ti sample activated at the Surface Lab, detailed in Sec. 7.3.3.

7.3.2 PMTs

A total of 20 R8778 PMTs were screened at SOLO in order to yield high-statistics measurements of their radioactivity. Ten R8778 PMTs, purchased for initial testing at Brown University, were screened in two separate batches of five. After the purchase of the 122 PMTs for LUX, two additional batches of five LUX PMTs were counted. The screening spectrum from one of the batches of five R8778 PMTs is shown in Fig. 7.3. Counting results for ^{238}U/^{232}Th/^{60}Co varied between batches by less than 20%. ^{40}K was reduced between the advance PMT set and the LUX PMTs by 30% after iteration in material selection by Hamamatsu. Results indicate the presence of benchmark isotopes ^{238}U, ^{232}Th, ^{40}K and ^{60}Co in amounts of 9.5 ± 0.6, 2.7 ± 0.3, 66 ± 6, and 2.6 ± 0.2 mBq/PMT, respectively. The measured values represent an overall γ ray emission rate per PMT that is a factor of 3 below the conservative estimate originally used in the LUX proposal. The counting breakdown for all PMT batches is shown in Table 7.3, and again in summary in Table 7.5.

It is interesting to note that the measured value of ^{60}Co in the PMTs during the first

Isotope	**Material**	**Origin**	**Half-Life**	**Characteristic Gamma Lines [keV] (I%)**
^{238}U*	all	primordial	4.5×10^9 y	295 (19%) 352 (36%) 609 (47%)
^{232}Th*	all	primordial	1.4×10^{10} y	511 (23%) 583 (85%) 911 (26%) 960 (20%) 2614 (99%)
^{40}K	all	primordial	1.2×10^9 y	1460 (11%)
^{60}Co	steel, Cu	manmade, muon capture, neutron spallation	5.3 y	1173 (100%) 1332 (100%)
^{46}Sc	Ti	^{46}Ti(n,p)^{46}Sc, muon capture	84 d	889 (100%) 1121 (100%)
^{54}Mn	steel	neutron spallation	310 d	835 (100%)

Table 7.2: Commonly measured radioisotopes in detector materials, with their origins and characteristic attributes. Starred isotopes have associated decay chains which contribute to radiation emission. The relative γ contributions of the various decay chain isotopes are discussed further in Ch. 6.

LUX science run may be a factor ×1/2 that reported from screening. The 5.3 year ^{60}Co half-life will have reduced the ^{60}Co concentration in the PMTs to 1.3±0.1 mBq PMT^{-1}. ^{60}Co has been identified as being sourced from Kovar metal in further material screening campaigns in support of the development of the R11410 PMTs. These PMTs will be used in the LZ experiment, as discussed in Sec. 7.5.

7.3.3 Major Internals

All major internals (defined in Sec. 7.1.1) were screened before detector construction. The list of major internals, along with their materials, construction mass, and counting sample mass, is given in Table 7.4. Counting results are listed in Table 7.5.

The ^{238}U column in Table 7.5 lists measurements that are performed on γ lines from isotopes above ^{226}Ra in the ^{238}U decay chain. This segment of the ^{238}U chain is referred to as the "early" chain. Early chain γ lines provide the most direct measurement of ^{238}U content, but yield large errors and high upper limits due to the very low branching ratios

Sample	**Live Days Counted**	**Activity [mBq/PMT]**			
		^{238}U	**^{232}Th**	**^{40}K**	**^{60}Co**
Brown R8778 #1	11	8.8±1.0	2.8±0.5	92±9	2.6±0.4
Brown R8778 #2	4.5	13±2	1.6±0.7	82±14	5.6±1
LUX R8778 #1	13	9.1±1.7	1.5±0.6	64±10	2.4±0.5
LUX R8778 #2	15	10±1	2.9±0.5	66±7	<2
Average		**9.5±0.6**	**2.7±0.3**	**66±6**	**2.6±0.2**

Table 7.3: LUX PMT batch counting results. All measurements were performed at SOLO. Five PMTs were counted in each batch. Actual ^{40}K concentrations in LUX PMTs are taken to be equal to those measured for the LUX R8778 #1 and #2 samples, as Hamamatsu took steps to control the ^{40}K levels in the tubes after initial measurements were performed. The Brown batch ^{40}K results are not applicable to current LUX tubes.

of the characteristic γ rays. Measurements listed in the ^{226}Ra column are performed on γ lines from isotopes below ^{226}Ra in the chain. This segment is referred to as the "late" chain. Radium-226 measurements are typically used to infer ^{238}U concentration, because the corresponding γ rays have much larger branching ratios than γ rays from the early chain, and yield correspondingly lower activity limits. Both measurements are included for completeness (where available).

The early chain results are typically listed to show agreement between the early and late segments of the ^{238}U chain. If the ^{238}U chain is out of equilibrium, measurement of one chain segment alone can lead to a misrepresentation of the total ^{238}U background contribution in the detector. However, there is no *a priori* reason to assume a break in ^{238}U chain equilibrium unless conflicting measurements are explicitly listed, i.e. in the case of the cryostats. More details on chain equilibrium and backgrounds therefrom are given in Ch. 6.

The elevated ^{46}Sc measurement in the Ti cryostat material, highlighted in Table 7.5 in red, was likely the result of delivery of the sample to the Oroville counting facility by airplane. The predicted activation rate for LUX material is significantly lower than this measurement, as described in Sec. 7.3.1. In order to directly measure the ^{46}Sc activation rate for LUX Ti, a 6.7 kg Ti sample was counted at SOLO, and transported by ground to the Surface Lab. The sample was left at the Surface Lab for six months (2.2 half-lives), after which it was ground-transported back to SOLO. A clear measurement of the ^{46}Sc peaks was made, yielding an estimate of 4.4±0.3 mBq kg^{-1}, for a height of 1.4 km above sea level.

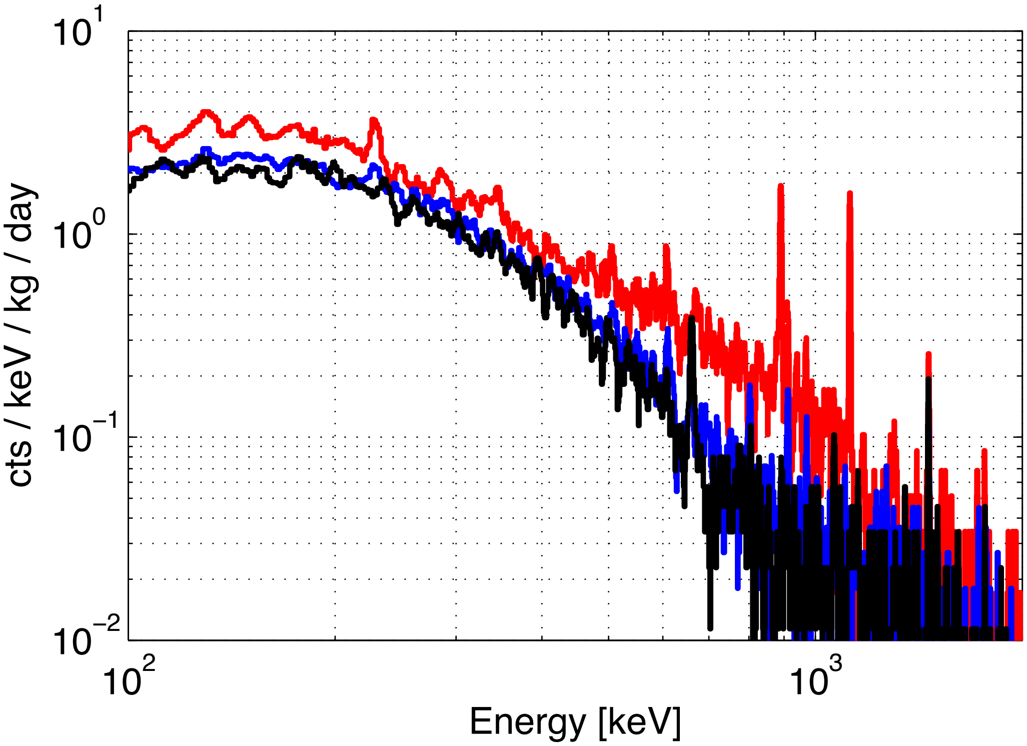

Figure 7.8: Counting spectra for a 6.7 kg Ti sample, before (blue) and after (red) a six-month activation period at the Sanford Surface Laboratory during the LUX surface run. Comparison is shown with background (black). The sample was shipped by ground to and from SOLO to avoid spurious cosmogenic activation. Peaks are clearly found at 889 and 1121 keV, corresponding to γ emission from ^{46}Sc decay.

The measurement falls within the 2.7–4.8 mBq kg^{-1} estimated range based on ACTIVIA simulations, assuming a naive linear scaling of production rates with total neutron flux and ignoring changes in spectral shape (Sec. 7.3.1). The counting spectrum is shown in Fig. 7.8.

7.3.4 Small Internals

Over 150 different construction components were catalogued during the construction phase of the experiment. A wide subset of these components, spanning all commonly-used construction materials, were screened at SOLO over a two-year period. The large number of small internal components made specific simulation modeling of individual components impractical. To inform counting goals, a generic simulation was created which estimated the background contributions from specific isotopes in 13 regions throughout the detector. Small components installed in a given region were assumed to yield WIMP search

Component	**Composition**	**Total Amount Used in LUX**	**Counting Facility**	**Counting Livedays**	**Counting Number**
PMTs		122 PMTs	SOLO	4 × ~8	4 ×5
PMT bases		122	SOLO	18	60
Field ring supports (inner panels)	HDPE	18.0 kg	SOLO	14	1.4
Field ring supports (outer panels)	HDPE	15.5 kg	SOLO	8.9	1.6
Reflector panels (main)	PTFE	15.5 kg	SOLO	9.5	2.4
Reflector panels (grid supports)	PTFE	9.3 kg	SOLO	6.7	2.0
Cryostats	Ti	231 kg	Oroville	13	8.0
Electric field grids	Stainless steel	4.5 kg	SOLO		37
Field shaping rings	Cu	28 kg	SOLO	9.0	15
PMT mounts	Cu	169 kg	SOLO	5.0	1.1
Weir	Cu	3.2 kg	SOLO	7.5	4.8
Filler chiller shield	Cu	293 kg	SOLO	–	–
Top shield	Cu	121 kg	SOLO	–	–
Superinsulation	Aluminized Mylar + polyester	2.2 kg	SOLO	13	0.6
Thermal insulation	HDPE	6.0 kg	SOLO	11	4.5

Table 7.4: Counting description for major internal material samples. The Total Amount Used in LUX column lists the total mass or number of the component used in LUX, e.g. all PMTs in both top and bottom arrays. Counting results are listed in Table 7.5.

Component	**Counting Unit**	**Counting Results [mBq/unit]**					
		^{238}U	**^{226}Ra**	**^{232}Th**	**^{40}K**	**^{60}Co**	**Other**
PMTs	PMT	<22	9.5±0.6	2.7±0.3	66±6	2.6±0.2	
PMT bases	base	1.0±0.4	1.4±0.2	0.13±0.01	1.2±0.4	<0.03	
Field ring supports (inner panels)	kg		<0.5	<0.35			
Field ring supports (outer panels)	kg		<6.3	<3.1			
Reflector panels (main)	kg		<3	<1			
Reflector panels (grid supports)	kg		<5	<1.3			
Cryostats	kg	4.9±1.2	<0.37	<0.8	<1.6		23±1 (^{46}Sc)
Cryostats	kg						4.4±0.3 (^{46}Sc)
Electric field grids	kg	<45	8.6±0.6	2.2±0.6		19±0.6	
Field shaping rings	kg		<0.5	<0.8		<0.3	
PMT mounts	kg		<2.2	<2.9		<1.7	
Weir	kg		<0.4	<0.2		<0.17	
Superinsulation	kg	<270	73±4	14±3	640±60		
Thermal insulation	kg		130±20	55±10	<100		

Table 7.5: Counting data for major internal material samples. See Sec. 7.3.3 for a discussion of the column definitions and relative sensitivities. The measurement of ^{46}Sc for the first listed cryostat sample, highlighted in red, has a significantly higher ^{46}Sc decay rate than that predicted for LUX material (see Sec. 7.3.1). The elevated rate is caused by sample exposure in an airplane. Scandium-46 counting results for LUX are given by the second Ti material measurement. Descriptions of all counting results are listed in Table 7.4.

backgrounds corresponding to the background efficiency factor for that region. Results for several selected materials are reported in Table 7.6.

7.3.5 Steel Pyramid

Several samples of steel were counted in an effort to identify material suitable for the construction of the external γ shield pyramid (Fig. 2.7). Counting results from this steel screening are listed in Table 7.7. Samples 1 and 2 were taken from separate steel batches, which were produced concurrently. Sample 3 was taken from a steel batch produced two years after those corresponding to samples 1 and 2. Sample 3 steel was used in the construction of the pyramid. Counting results for sample 3 showed elevated ^{232}Th rates, as well as a positive signature of ^{40}K. The measured activity rates were still acceptable for construction of the pyramid, despite their increase over previous measurements.

7.3.6 Concrete and Rock

A sample of the concrete used in construction of the underground laboratory was counted at SOLO for 3.0 livedays. The concrete was found to have activity levels which were quite high compared to typical Homestake cavern rock. The high activity was deemed acceptable due to the presence of the water shield, which reduces the γ and neutron flux from this material to negligible levels (Sec. 2.2.7). A separate sample was counted at the LBNL LBF. Results from both counting sessions are listed in Table 7.8. Variations in ^{238}U, ^{232}Th and ^{40}K isotopes are seen within a factor ×2 between the samples.

Counting results from LBNL for typical rock found in the Davis cavern are reported in Table 7.9 [173]. Results are for the average rock mass in the cavern ("bulk rock"), as well as results from small rhyolite intrusions, and from the shotcrete which was applied to the excavated cavern walls prior to laboratory construction. The steel pyramid, which has a radioactivity $\sim\times 1/500$ that of typical cavern rock, displaces a significant rock mass underneath the LUX water shield, and serves to further shield the detector from rock γ activity.

Component	Counting Unit	Counting Facility	Livetime [days]	Counting Results [mBq unit^{-1}]					
				^{238}U	^{226}Ra	^{232}Th	^{40}K	^{60}Co	Other
Field cage resistors	resistor	SOLO	4		0.104±0.009	0.010±0.004			
Stainless steel shoulder screws (PMT mounts)	screw	SOLO			0.14±0.08	0.16±0.04		0.66±0.03	
Be-Cu resistor sockets (field shaping rings)	socket	SOLO			<0.021	<0.0058		<0.001	
Wire (field shaping rings)	kg	SOLO	9		<8	<5.5	<1.2		
Threaded rods + nuts (cryostat flanges)	rod + 2 nuts	SOLO			<1.9	<1.6		4.9±0.6	
Helicoflex gaskets 4 5/8” (cryostat flanges)	gasket	SOLO			0.18±0.05	<0.05		0.18±0.07	
Helicoflex gaskets 8” (cryostat flanges)	gasket	SOLO			0.4±0.1	<0.1		0.4±0.15	
Cathode HV cable	m	SOLO			<1.7	<0.7	<5.7		
PMT HV cable	m	SOLO			<0.07	<0.05		<0.04	
Steel bellows (with nuts/bolts) (cryostats)	kg	SOLO						47±3	
Inner dome hangers (cryostats)	hanger	SOLO				8.5±2.0		9.3±1.6	13.7±2.5 (^{54}Mn)
Plastic tubing (active region)	m	SOLO			<0.3	<0.16			
PEEK (active region)	kg	SOLO			8.5±2.0	<2.4			
PTFE trifoils (active region)	trifoil	SOLO			<0.01	<0.005	<0.06		
Stainless steel connector components (active region)	kg	SOLO							
Stainless steel fittings (active region)	kg	Oroville	4.8		<5	<6	<16	13±1	
Stainless steel bolts (active region)	kg	Oroville	2.1	<37	<6	16±8	<22	15±2	
Stainless steel screws and washers (active region)	kg	Oroville	1.9	<49	<8.6	<8	<31	26±3	
Cu-clad Kapton (active region)	kg	Oroville	1.9		<19	<12	<93		
Stainless steel stock (active region)	kg	Oroville	1.9	<12	<5	<4	<15	11±2	
Cartridge heaters (gas system)	kg	Oroville	1.9	5.1±0.2	2.7±0.1	3.0±0.1	19000±600		

Table 7.6: Counting data for small internal material samples. Columns are the same as in Table 7.5.

Sample	**Livetime [days]**	**Counting Results [mBq/kg]**				
		^{238}U	^{232}Th	^{40}K	^{60}Co	^{54}Mn
1	9.9	<1.6	<1.3		<0.66	2.7±0.5
2	5.0	<3	<1.6		<1	2.9±0.6
3	4.3	<5.3	3.6±0.7	33±7	<0.75	3.2±0.6

Table 7.7: Counting results for several samples of steel for potential use in the construction of the external γ shield pyramid. All counting was performed at SOLO.

Sample	**Counting Facility**	**Livetime [days]**	**Counting Results [Bq/kg]**			
			^{238}U	^{226}Ra	^{232}Th	^{40}K
1	SOLO	3.0		25±0.1	5.4±0.1	640±3
2	LBNL LBF	2.0	18.8±0.3	15.2±0.1	9.6±0.1	272±2

Table 7.8: Counting results for Sanford underground concrete, counted at both SOLO and LBNL LBF.

Sample	**Counting Results [Bq/kg]**		
	^{238}U	^{232}Th	^{40}K
Bulk rock	0.73–1.1	0.98–1.2	56–600
Rhyolite	54.6–134	35.6–46.3	775–2400
Shotcrete	20.0–32.2	8.09–15.9	110–400

Table 7.9: Counting results for typical cavern materials in the LUX Underground Lab. Results are courtesy LBNL LBF [173].

7.4 Comparison of Counting Goals with Results

The effectiveness of the LUX screening program can be gauged in part by how closely the screening effort adhered to the counting goals set in Sec. 7.1. The goal for the combined naive addition background measurements and upper limits from all major internals was 0.5 $\mathrm{mDRU_{ee}}$. The estimated background contribution for all major internal materials from screening is listed in Table 7.10. The overall counting goal was met for all major internals, based on the naive addition of positive measurements and upper limits from screening results.

An informal goal, used as a baseline for individual sample measurements, was to ensure a background rate <0.05 $\mathrm{mDRU_{ee}}$ for each individual major internal material (with the exception of the PMTs). This informal goal was met for Ti (cryostats), HDPE panels, HDPE thermal insulation, and steel (grids). Goals were exceeded by PTFE (reflector panels) and Cu, by factors of ×1.2 and ×2.7 respectively. In some cases, gains could be made by ensuring that samples are placed optimally in the counting chamber, minimizing the distance between sample and detector. In the case of Cu counting, a detector with higher sensitivity than SOLO would be required to place a 90% CL upper limit of <0.05 $\mathrm{mDRU_{ee}}$ for ^{238}U / ^{232}Th. This was deemed low priority, as the OFHC Cu material used in LUX construction has been demonstrated to typically have very low ^{238}U / ^{232}Th concentrations [156, 167, 168].

Goal statistics have not been fully tabulated for small internals. However, measurements of small internal material radioactivities were typically translated into fractional background contribution relative to PMTs during evaluation of material suitability. For materials where this statistic has been calculated, background rate contributions from these materials were 1 PMTs' worth of activity, in line with the goal outined in Sec. 7.1.2. Final evaluation of LUX data has confirmed an event rate consistent with a PMT-dominated background, as discussed in Ch. 8.

The exercise of fitting the γ background measured *in situ* in LUX (Sec. 5.2.2) yielded refined radioisotope concentration estimates for materials located generally in the top, bottom, and sides of the active region. The best-fit results, along with the initial estimates based on screening results for the PMTs and thermal insulation (HDPE + superinsulation),

Material	**Estimated Background Rate [mDRU$_{ee}$]**
PMTs	0.5
Ti	<0.02
PTFE	<0.06
HDPE	<0.04 (panels) + 0.05 (thermal insulation)
Steel	0.02
Cu	<0.13
Total	**<0.82**

Table 7.10: Estimated low-energy ER background contribution in an optimized 100 kg cylindrical fiducial volume from each major material, based on screening results only, using LUXSim background simulations described in Ch. 5. The goal for all materials combined was 1 mDRU$_{ee}$. Titanium projections assume sufficient time underground for the ^{46}Sc background contribution to decay below upper limits from ^{238}U / ^{232}Th. Upper limits for individual materials are at 90% CL. The total upper limit is a naive addition of positive measurements and upper limits from screening, and has >90% CL.

are listed in Table 5.1. The best-fit estimates of the radioisotope concentrations are in line with the 1 mDRUee overall γ background goal for a 100 kg fiducial volume. The best-fit results also include backgrounds from cosmogenic activation of detector materials, which was not originally accounted for in the 1 mDRU$_{ee}$ screening goal. The PMTs contribute 73% of the observed γ backgrounds in the detector from non-cosmogenic sources in the LUX Run 3 fiducial volume (Table 5.2).

7.5 LZ PMTs

The LZ experiment is projected to have the lowest WIMP search fiducial background rate of any experiment. A major part of the incredibly low projected backgrounds for the experiment is the use of ultra-low background materials in the detector. A material screening and control program was put in place between Brown University and Hamamatsu in order to reduce the PMT background levels by over an order of magnitude per tube relative to the LUX R8778 models, matching recent developments in low-background materials used for other Hamamatsu PMTs [155, 174].

The development program has resulted in the creation of several large-area photocathode PMTs, notably the 7.6 cm diameter R11065 and its low-background variant, the R11410-20 [175, 176]. The R11065 was tested at Brown University and was found to yield an identical

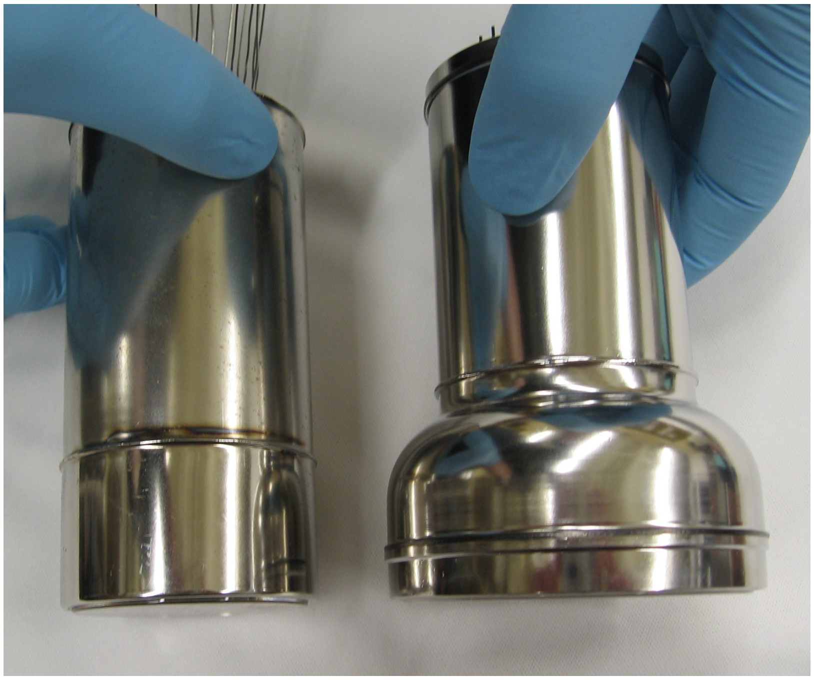

Figure 7.9: The Hamamatsu R8778 PMT, used in LUX (left), and the R11410-20 PMT, used in the upcoming LZ experiment (right). The R11410-20 features a 6.4 cm diameter photocathode, offering twice the surface area of the 4.5 cm diameter R8778 photocathode.

response to Xe scintillation light as the R8778, with gains measured up to 10^7 at 1500 V and a single photoelectron resolution of 32% while immersed in liquid Xe at 175 K. The R11410-20 has been selected for use in the LZ detector. The R11410-20 and R8778 PMTs are shown for comparison in Fig. 7.9.

7.5.1 Counting Results

An R11410-20 PMT mechanical sample was screened at SOLO for a period of 19 livedays. This PMT was produced after a thorough material screening program by the manufacturer, with strong reductions in benchmark isotopes expected. Placement of the R11410-20 was optimized within the chamber, and the counting time was extended a factor ×2 beyond the typical time for the R8778 batches, in order to maximize sensitivity for the single sample.

The R11410-20 showed a very significant reduction in ^{238}U, ^{232}Th and ^{40}K content compared to R8778 counting results, and the signal for these isotopes is consistent with background. The only positive signal was found at 1173 and 1332 keV, consistent with the presence of ^{60}Co in amounts comparable to those measured in the R8778 PMTs. R11410-20

PMT	**Activity [mBq/PMT]**				
	^{238}U (^{234m}Pa)	**^{238}U (^{226}Ra)**	**^{232}Th (^{228}Ra)**	**^{40}K**	**^{60}Co**
R8778	<22	9.5±0.6	2.7±0.3	66±6	2.6±0.2
R11410-20	<6	<0.4	<0.3	<8.3	2.0±0.2

Table 7.11: R8778 and R11410-20 radioactivity screening results, obtained at SOLO. R8778 PMT average counting results are taken from Table 7.3. The R11410-20 sample was counted for 19 live days. Separate columns are provided for completeness for “early” and “late” ^{238}U chain measurements, allowing for potential equilibrium breakage primarily due to ^{226}Ra solubility in water; however, as discussed in Sec. 7.3.3 and Ch. 6, that there is no *a priori* reason to assume an equilibrium breakage. Errors are statistical and quoted at $\pm 1\sigma$. Upper limits are given at 90% confidence level. Results are normalized per PMT.

counting results are summarized alongside R8778 results in Table 7.11, and the screening spectrum is overlaid with the R8778 spectrum and background in Fig. 7.3.

The number of PMTs used in an experiment is inversely proportional to the photocathode area per PMT. Thus a proper comparison of PMT activity must also normalize radioactivity by photocathode area. Screening results normalized per unit photocathode area are listed for R8778 and R11410-20 PMTs, as well as for 17 batches of R8520 PMTs counted at the University of Zurich and Laboratori Nazionali del Gran Sasso (LNGS) for the XENON collaboration [155], in Table 7.12. The R11410-20 offers by far the lowest activity per unit area, with upper limit activities a factor of ×0.3 / ×0.25 / ×0.1 that of the R8520 positive measurements in ^{238}U / ^{232}Th / ^{40}K, respectively. Activity per unit area for ^{60}Co is measured to be a factor ×0.3 below that of the R8520.

Counting of LZ R11410-20 PMTs began in January 2013, after publication of [129]. Counting efforts thus far have yielded results for five batches of five R11410-20 PMTs (25 total) to be used in LZ. Results are summarized in Table 7.13. The current R11410-20 PMTs show upper limits on ^{238}U (^{226}Ra), consistent with results from the R11410-20 prototype in [129]. Levels ^{60}Co are consistent with, or lower than by ×0.5, prototype results. LZ PMT ^{40}K positive measurements are higher than the prototype upper limit by a factor ×2. Two of five batches also show positive measurements for ^{232}Th at levels a factor ×4 higher than that reported for the prototype. These numbers are used for projections of LZ PMT backgrounds, discussed in Sec. 7.5.2.

PMT	**Photocathode-Normalized Activity [mBq/cm^2]**				
	^{238}**U (**^{234m}**Pa)**	^{238}**U (**^{226}**Ra)**	^{232}**Th (**^{228}**Ra)**	^{40}**K**	^{60}**Co**
R11410-20 (this work)	<0.19	<0.013	<0.009	<0.26	0.063 ± 0.0063
R8778 (this work)	<1.4	0.59 ± 0.038	0.17 ± 0.019	4.1 ± 0.13	0.16 ± 0.0063
R8520 (XENON10) [71]		0.03	0.03	2	0.4
R8520 (XENON100) [155]	<3.4	0.038 ± 0.002	0.035 ± 0.002	2.3 ± 0.07	0.18 ± 0.005
R11410-20 [155]	<3.0	<0.075	<0.12	0.40 ± 0.1	0.11 ± 0.02

Table 7.12: Counting results from Table 7.11, renormalized by PMT photocathode area. Based on this work, the R11410-20 offers the lowest radioactivity per PMT per unit photocathode area for all benchmark isotopes. In particular, ratios of R11410-20 upper limits to R8778 activities are ×1/45 ^{238}U / ×1/19 ^{232}Th / ×1/16 ^{40}K. The ratio for ^{60}Co, detected in both PMTs, is ×1/3. The very low normalized ratios make the R11410-20 the top candidate for use in the large-area tonne-scale LZ detectors. Included for comparison are counting results for the R8520 PMTs used in the XENON10 [71] and XENON100 [155] experiments, as well as counting results for a second R11410-20 PMT presented in [155] (referred to as "R11410 MOD" in that work).

Batch ID	**Activity [mBq/PMT]**			
	^{238}U (^{226}Ra)	**^{232}Th (^{228}Ra)**	**^{40}K**	**^{60}Co**
1	<0.46	<1.3	18 ± 3	1.4 ± 0.2
2	<0.6	1.0 ± 0.4	17 ± 3	1.1 ± 0.2
3	<1.8	<2	18 ± 3	2 ± 0.4
4	<1.3	1.5 ± 0.6	33 ± 4	2.7 ± 0.4
5	<2.6	<2.7	18 ± 3	1.4 ± 0.3

Table 7.13: Recent batch counting results for LZ R11410-20 PMTs. Each batch is comprised of five R11410-20 PMTs. All counting is performed at SOLO. Typical batch counting livetime is 12 days.

7.5.2 Impact on Dark Matter Backgrounds

It is interesting to note that no further reduction in PMT radioactivity beyond the R11410-20 is useful for the LZ experiment. In particular, LZ faces a background "floor" from neutrino scattering, causing ER events as well as NR events from coherent neutrino scattering [146]. The spectra for both ER and NR backgrounds are shown in Fig. 7.10. Further discussion of neutrino backgrounds is given in Sec. 5.7.

ER backgrounds are predicted to be dominated by scattering of solar neutrinos from the p-p chain, even with the use of PMTs equivalent to the LUX R8778 PMTs. With the use of R11410-20 PMTs in the tonne-scale experiment, the PMT NR background contribution can be reduced below the level of coherent neutrino scattering from atmospheric and diffuse supernova background neutrinos above 5 keV$_{\text{nr}}$. This will facilitate a direct measurement of these scattering spectra.

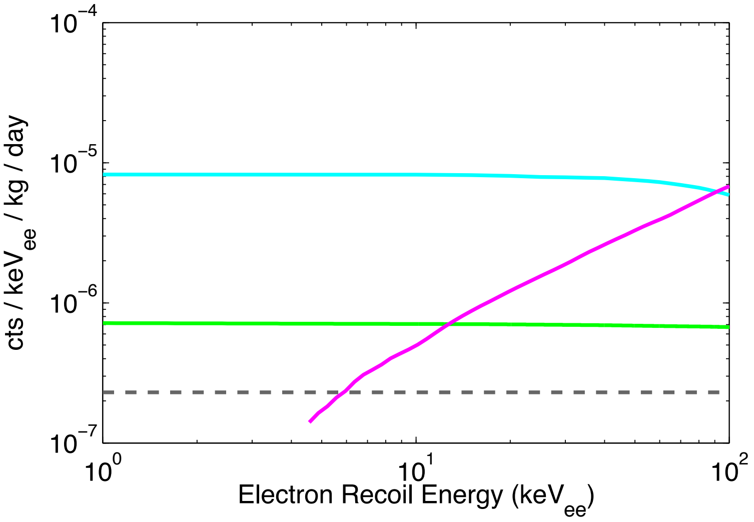

(a)

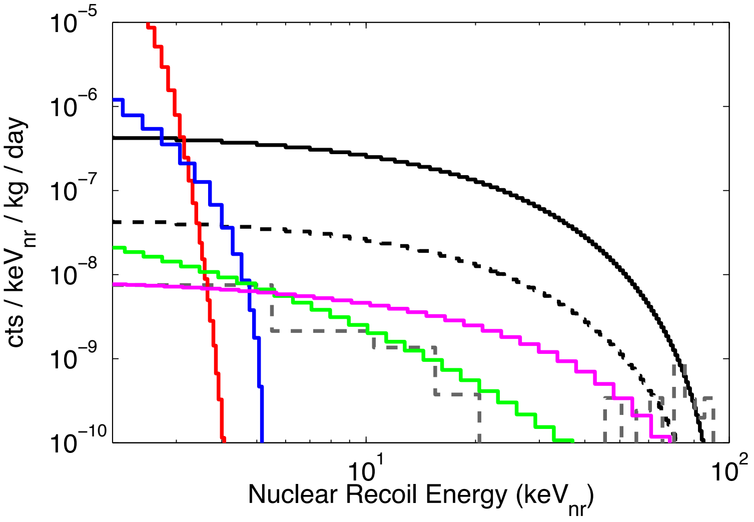

(b)

Figure 7.10: (a) LZ ER background spectra. Background spectra are shown from the PMTs (gray), p-p solar neutrino scattering (cyan) [76], ^{7}Be solar neutrino scattering (green) [77], and ^{136}Xe two-neutrino double β decay (magenta) [73]. The ^{136}Xe spectrum uses a 2.1×10^{21} yr lifetime. The average (flat spectrum) projected PMT ER background is overlaid from current LZ studies, assuming a conservative 3 ^{238}U / 3 ^{232}Th / 30 ^{40}K / 2.5 ^{60}Co mBq PMT^{-1} for the R11410-20 PMTs. No discrimination factor is applied. (b) LZ NR WIMP and background spectra. WIMP spectra are shown in black for $m_\chi =$ 100 GeV, assuming a spin-independent WIMP-nucleon cross-section of 10^{-47} (solid) and 10^{-48} (dashed) cm^2. Neutrino coherent scattering backgrounds are adapted from [146]. Overlaid are neutron background spectra for both (α,n) and fission contributions from the PMTs (gray). Neutrino coherent scattering backgrounds are shown from ^{8}B decays (red), proton-^{3}He collisions (blue), cosmic ray interactions in the atmosphere (magenta), and the diffuse supernova background (green). Further discussion of neutrino backgrounds is given in Sec. 5.7. 100% NR acceptance is shown.

CHAPTER 8

LUX RUN 3 RESULTS

The third data run of the LUX detector has yielded the most stringent constraint on WIMP dark matter parameters to date. The detector yielded an extremely systematic-free dataset, allowing an analysis of the dark matter data to be published within six months of the beginning of the run. The data yielded not only WIMP search information, but also extensive information pertaining to generators of WIMP search backgrounds.

The LUX detector underwent three data runs from 2011–2013. The first two runs were technical runs designed to test detector response, electronics and data processing systems. The technical runs were performed at the LUX Surface Facility, as detailed in Sec. 2.3.2. The first technical run, Run 1, was a gaseous Ar run which served primarily as a functionality test for the electronics. Run 2 was a liquid Xe run, which provided valuable calibration data for use in underground running. Run 2 technical results are published in [106].

Run 3 was the first underground science run of the experiment, conducted from February–August 2013. The run used an 85 liveday data acquisition to perform an unblinded WIMP search run, proving the low-background detection capabilities of the detector. Results from Run 3 have been submitted to PRL [46]. The ultimate LUX results will come from a blinded one year run (expected to be called “Run 4”), as set forward in the original LUX proposal [110].

Results in this chapter focus on analysis of Run 3 data pertinent to the establishment and confirmation of the LUX background model. The background model was used in the profile likelihood ratio analysis leading to the LUX Run 3 WIMP search result. The data also solidifies projections of background rates for the ultimate one year LUX WIMP run.

8.1 S1-Only Data

The first underground liquid Xe data from LUX was taken during minimal tests of the data acquisition system on Feb. 12. The electric field grids were grounded, creating a zero-field environment in the liquid Xe. Without field, only S1 signals were generated. This data was useful for initial characterizations of γ background rate, and allowed for identification of intrinsic contamination. The spectrum of S1 signals is shown in Fig. 8.1.

The S1 rate above 100 phe is 6.3 Hz. The rate is dominated by γ interactions in the detector, and by activated Xe isotope decays. The Xe isotopes were identified both by their signal sizes and by their homogeneous distribution in the detector. The distribution of the signals in S1 top vs S1 bottom space was used as a measure of the Z coordinate of the event, in lieu of more precise characterization from S2 signals. The distribution in S1 top vs bottom space is shown with comments in Fig. 8.2. A discussion of activated Xe isotopes is given in Sec. 5.3.1.

The observed peaks in total S1 from activated Xe isotopes were fitted by a five-parameter model. The model used the energy deposition spectra from ^{127}Xe, ^{129m}Xe, ^{131m}Xe, and ^{133}Xe, taken from LUXSim energy deposition studies. The model also featured an exponential baseline. The best-fit results are shown in Fig. 8.3. The measured isotope decay rates in the detector, taken from the best-fit model, are 2.7 ± 0.5 mBq kg^{-1} (^{127}Xe), 3.6 ± 0.7 mBq kg^{-1} (^{129m}Xe), 4.4 ± 0.9 mBq kg^{-1} (^{131m}Xe), and 3.6 ± 0.7 mBq kg^{-1} (^{133}Xe) on Feb. 12. Errors are estimated at 20%. The total decay rate of activated Xe isotopes was 3.9 ± 0.4 Hz. Assuming that γ backgrounds comprise the dominant background rate in the detector other than early activated Xe isotopes, the inferred γ rate is 2.4 ± 0.4 Hz. This value matches expectations based on a PMT-dominated γ emission model, as established by screening results.

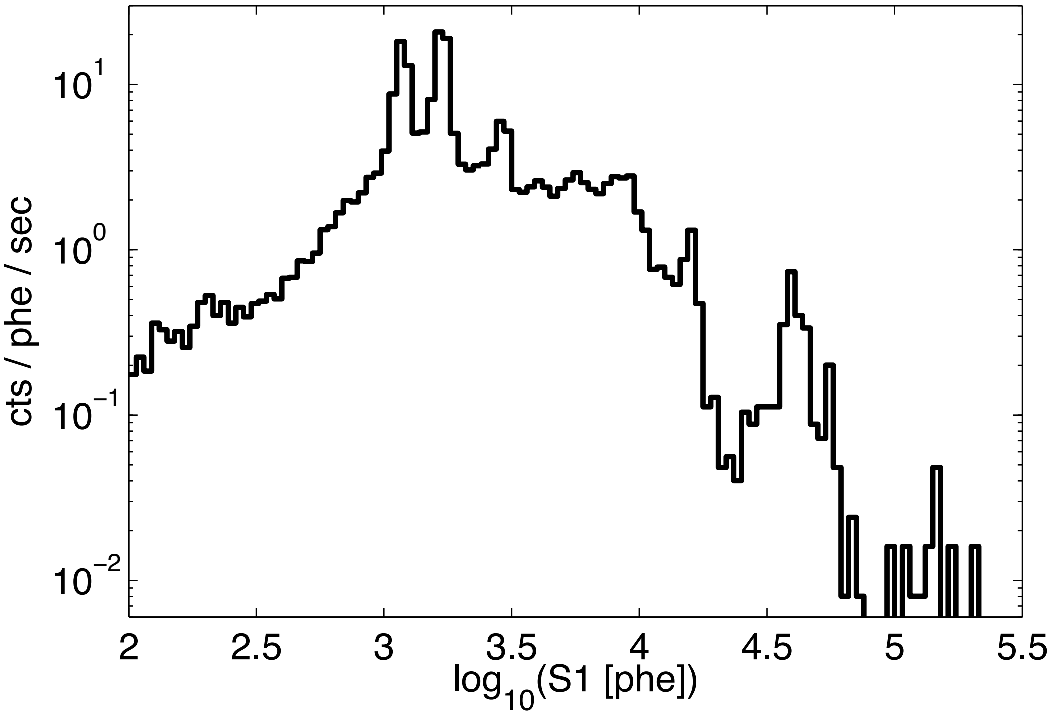

Figure 8.1: Initial S1-only histogram from LUX underground running. Data was taken over a period of 1.2 hours on Feb. 12. A correction factor is applied to the data, normalizing total pulse area to detector midpoint. Clear peak features are visible, later matched to known features from γ spectra of radioisotopes and decay energies of activated Xe radioisotopes.

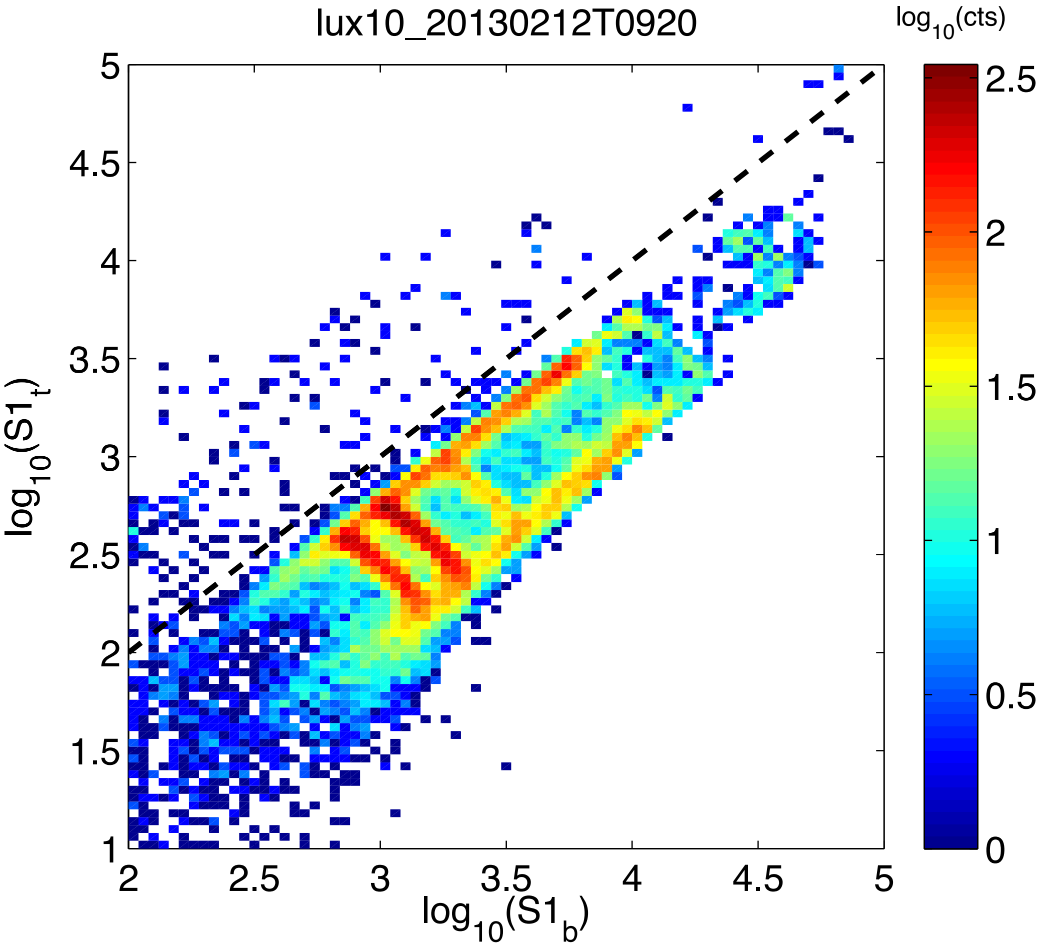

Figure 8.2: Data from Fig. 8.1, plotted in top PMT array vs bottom PMT array view. The top/bottom ratio acts as a proxy for event height in the detector. The addition of top and bottom signals acts as a proxy for energy. Gamma scattering continua are seen as the southwest–northeast hotspots, clustered at the top and bottom of the active region, forming the frame of the "ladder" feature. Activated Xe features are clearly visible as the ladder "rungs," as they are monoenergetic signals distributed uniformly in height throughout the active region. S1 signals equally distributed in the top and bottom PMT arrays fall on the dashed black line.

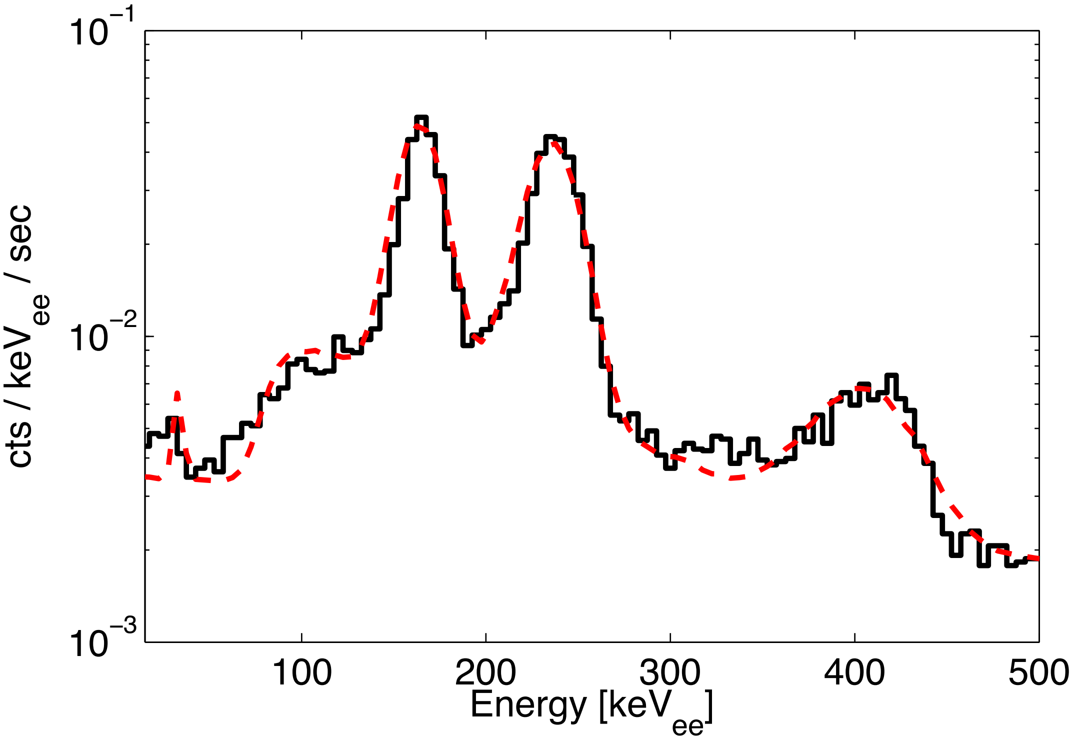

Figure 8.3: Fit to the activated Xe peaks from Fig. 8.1 (Feb. 12), using simulated spectra from Fig. 5.6. A resolution factor of 5% is applied to simulated spectra in order to match measured data. A fixed exponential baseline is used, which connects the bins at 30 keV$_{ee}$ and 450 keV$_{ee}$. Best-fit isotope decay rates are 2.7 ± 0.5 mBq kg^{-1} (^{127}Xe), 3.6 ± 0.7 mBq kg^{-1} (^{129m}Xe), 4.4 ± 0.9 mBq kg^{-1} (^{131m}Xe), and 3.6 ± 0.7 mBq kg^{-1} (^{133}Xe).

8.2 Light Collection

LUX light collection was measured using several monoenergetic ER sources. In early detector data, the activated Xe peak at 164 $\mathrm{keV_{ee}}$ from $^{131\mathrm{m}}$Xe was used to establish the detector photon collection efficiency. The measurement was confirmed and measured periodically during calibrations, using $^{83\mathrm{m}}$Kr 31 $\mathrm{keV_{ee}}$ and 9.4 $\mathrm{keV_{ee}}$ signals.

Light collection was measured in S1+S2 data through use of Eq. 2.1, relating the energy deposition to the number of photons and electrons generated at the event site. Eq. 2.1 can be rewritten as

$$E = W \cdot \left(\frac{S1}{\alpha} + \frac{S2}{\beta} \right), \tag{8.1}$$

where α and β are the photon and electron efficiency factors for the detector, in units of phe per photon or phe per electron respectively. W is 13.7 eV from Sec. 2.1.2. LUX S1 light collection can be inferred from a measurement of α, which is a multiplication of the S1 photon geometric collection efficiency with PMT DE (see Sec. 3.2.2 for definitions).

α and β were estimated from direct measurements of the 164 $\mathrm{keV_{ee}}$ monoenergetic signal in (S1,S2) space, as shown in Fig. 8.4. Eq. 8.1 can be rewritten as

$$E = A \cdot \left(S1 \cdot \sin(\theta) + S2 \cdot \cos(\theta) \right), \tag{8.2}$$

where A is an arbitrary scaling factor and θ is an angle that can be directly measured from data. From the 164 $\mathrm{keV_{ee}}$ peak, $\theta = 88.9° \pm 0.1°$. From Eq. 8.1 and 8.2, $\alpha = 0.1392 \pm 0.0003$ phe per photon. A very small error in α is possible due to the insensitivity of $\sin(\theta)$ to error in θ, when θ is close to 90°. A measurement of β is not practical from this data, as $\cos(\theta)$ is extremely sensitive to error in θ near 90°. β was measured from single electron measurements to be 25 ± 7 phe per electron. The value of α was tracked with $^{83\mathrm{m}}$Kr over the course of Run 3, with <1% improvement observed.

The measurement of α can be related back to projections of LUX light collection and LUX PTFE reflectivity from early Monte Carlo studies, detailed in Sec. 3.3. Assuming the 33% average QE and 90% CE for the LUX R8778 PMTs [94], the photon geometric collection efficiency at the detector center is 47%. From Fig. 3.12, this corresponds to a minimum of 95% LUX PTFE reflectivity, assuming electric field grids with 80% reflectivity (well above the expected value). In the limit that the field grids are poorly reflective, LUX PTFE reflectivity is close to 100%.

This result, while surprising in the sense that PTFE is not expected to reflect UV photons with such high efficiency [113], follows the trend from XENON10 and other liquid Xe experiments which report light collection consistent with extremely high PTFE reflectivity. The extensive use of PTFE in the LUX detector results in very high photon collection efficiency. In comparison to XENON10, LUX photon collection is actually limited by PMT QE and not by absorption on detector materials. Because of this excellent light collection, LUX is able to push its low-energy sensitivity lower than previous Xe dark matter experiments, with strong implications for low-mass WIMP detection claims from other detectors (Sec. 8.9).

8.3 Gamma Backgrounds

Gamma backgrounds in the detector were measured in detail using a combined S1+S2 estimate of energy deposition. The measurement of the high-energy portion of the γ spectrum was used to constrain the radioisotope decay rates in the top, bottom and sides of the detector. Both single scatters (SS) and multiple scatters (MS) were reconstructed from data, maximizing the observed peak sizes and minimizing potential systematics from comparison with Monte Carlo. Details of the Monte Carlo modeling work are given in Sec. 5.2. The details of the analysis technique are recorded below.

8.3.1 Data Quality Cuts

8.3.1.1 Gamma Selection Cuts

Cuts are placed on the S1 top/bottom distribution in order to remove gas events from consideration. A high-S1 cut also eliminates α events. This cut is drawn by eye around the main γ population in the detector, and is shown in Fig. 8.5.

Very little deviation in S2/S1 is seen for the γ population. The S2/S1 distribution is

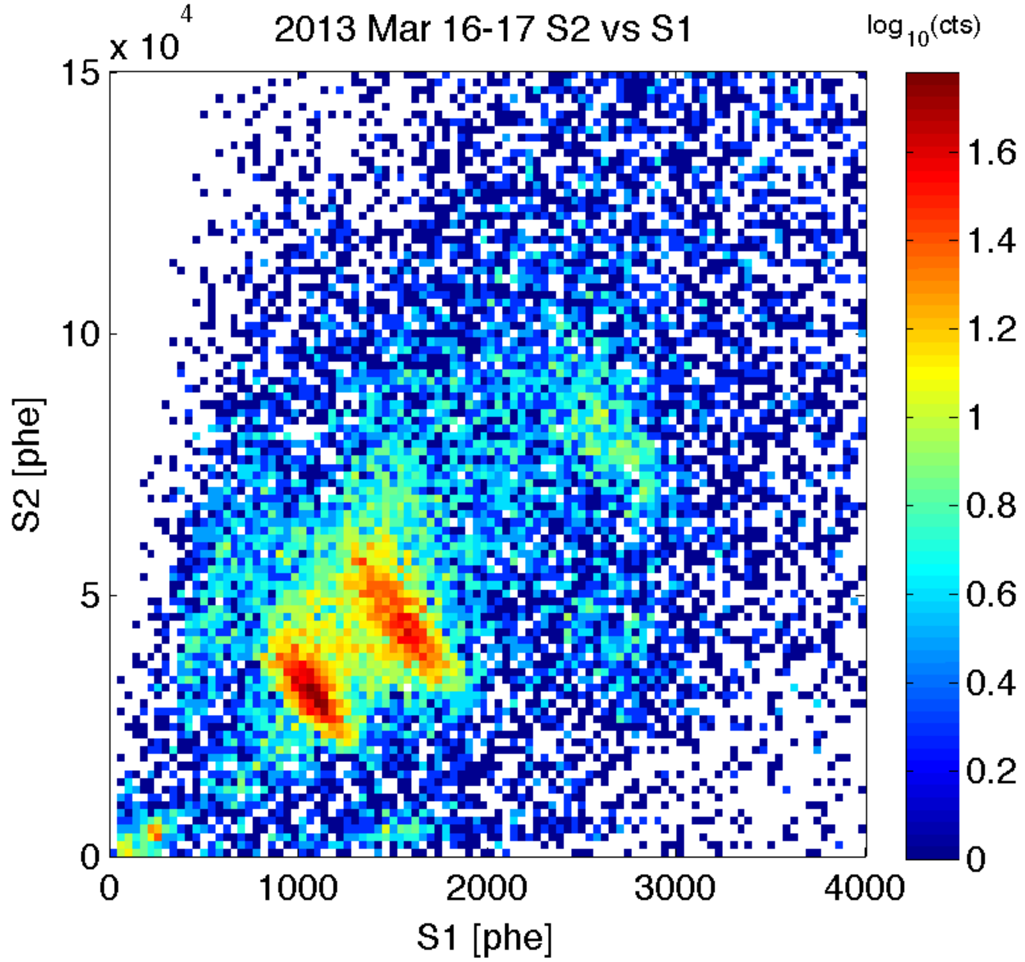

Figure 8.4: (S1,S2) space for early LUX data, showing the monoenergetic 164, 236, and 375 keV_{ee} signals from the ^{131m}Xe, ^{129m}Xe and ^{127}Xe respectively. S1 and S2 are corrected in Z relative to signals at the detector midpoint. The angle in S2 vs S1 space yields a measurement of the detection efficiencies for photons and electrons in the detector.

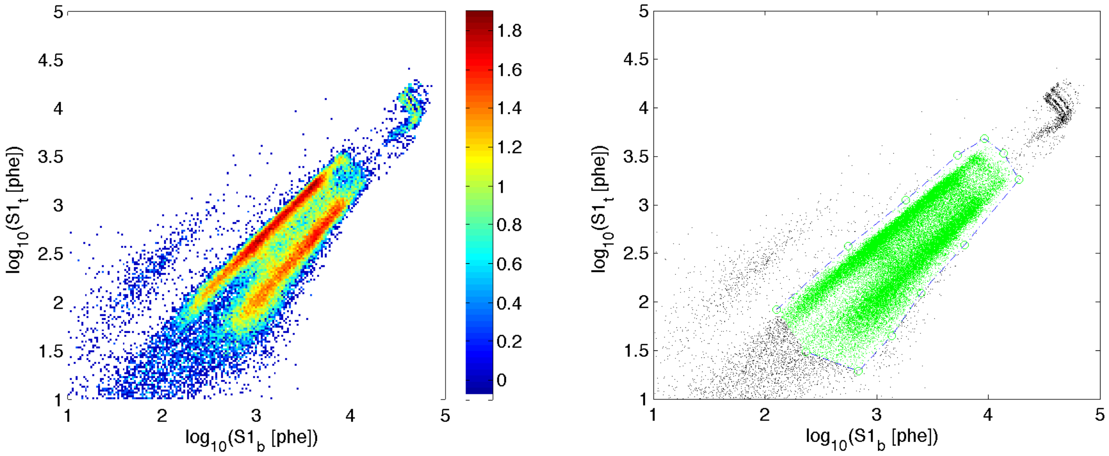

(a) (b)

Figure 8.5: (a) S1 top vs bottom for all background data considered in this study. The large island is the main γ population, with energies extending to 3 MeV. The small island in the upper right corresponds to α events, excluded from this study. The island in the upper left corresponds to gas event S1s, also excluded from this study. (b) S1 top vs bottom, showing the S1 selection cut used for events in this study. The cut has negligible impact on energies >500 keV$_{\mathrm{ee}}$, which is the region of primary interest for γ background fitting.

plotted as a function of energy in Fig. 8.6. A small anomalous population is seen in S2/S1 with very low S2 ratio, concentrated at energies below those used for background fitting. The population comprises 1–10% of the event rate per energy bin at low energies, and does not significantly influence background fitting.

8.3.1.2 Single Scatter Cuts

The data processing pulse finding algorithms used in this analysis were tuned to low-energy events. For very large pulses, systematics such as high S2 tails can prevent the breakdown of multiple S2s into individual pulses. An example is shown in Fig. 8.7, where the pulse is reconstructed with total energy 2.6 MeV.

To tag events such as those shown in Fig. 8.7 as MS events, an S2 width cut is imposed. S2 width is shown as a function of drift time in Fig. 8.8. The width cut requires that the S2 width for a SS event is <1 μs larger than the mean width at that event's depth. Given the variation in single-scatter cut representation between simulation and real data, and given the success of the energy reconstruction for MS events, a SS cut is not ultimately used

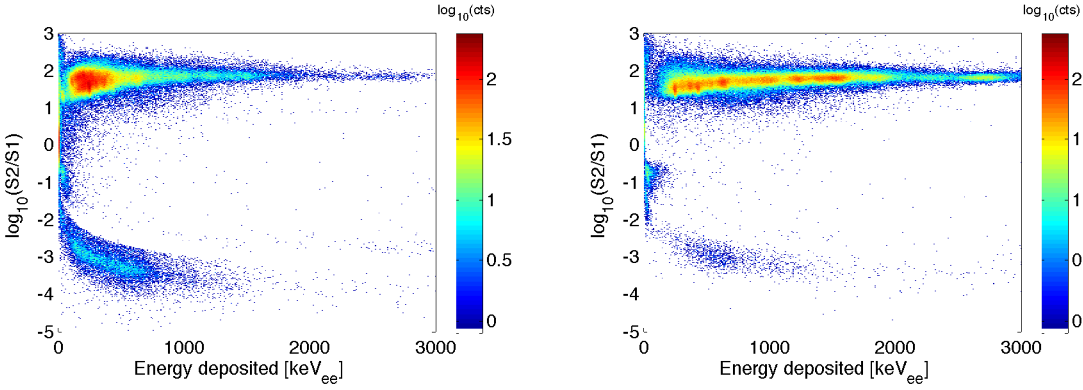

(a)

(b)

Figure 8.6: S2/S1 ratio vs energy for γ events in the active region. Event selection criteria using the S1 cut shown in Fig. 8.5 is used. Data is shown for (a) SS and (b) MS events, where MS cut criteria are described in Sec. 8.3.1.2.

during simulation comparisons.

8.3.2 Energy Reconstruction

8.3.2.1 Single-Scatter Calibration

Energy calibration is performed for all SS events, where S1 and S2 correction factors can be applied. Calibration is performed by combining S1 top+bottom and S2 bottom signals. The signals are added following Eq. 8.1, where α is the S1 photon collection efficiency normalized to the middle of the drift region (160 µs), in units of phe photon^{-1}, and β is the S2 collection efficiency, assuming an electron lifetime correction normalized to zero drift time, in units of phe electron^{-1}. β is a combination of the measured single electron signal size in the bottom PMT array (11 phe (extracted electron)$^{-1}$, measured from background data used in this work), and the estimated extraction efficiency for liquid electrons (70% at LUX extraction fields).

No pulse saturation cut is used. Events where peak shapes and sizes are distorted by PMT anode saturation or capacitor depletion are accepted into the background dataset. Fortunately, peaks above this limit are still easily resolvable.

MS events with vertices within cm in Z of one another can potentially leak into the single-scatter population. This is because large S2s close in time are difficult to separate

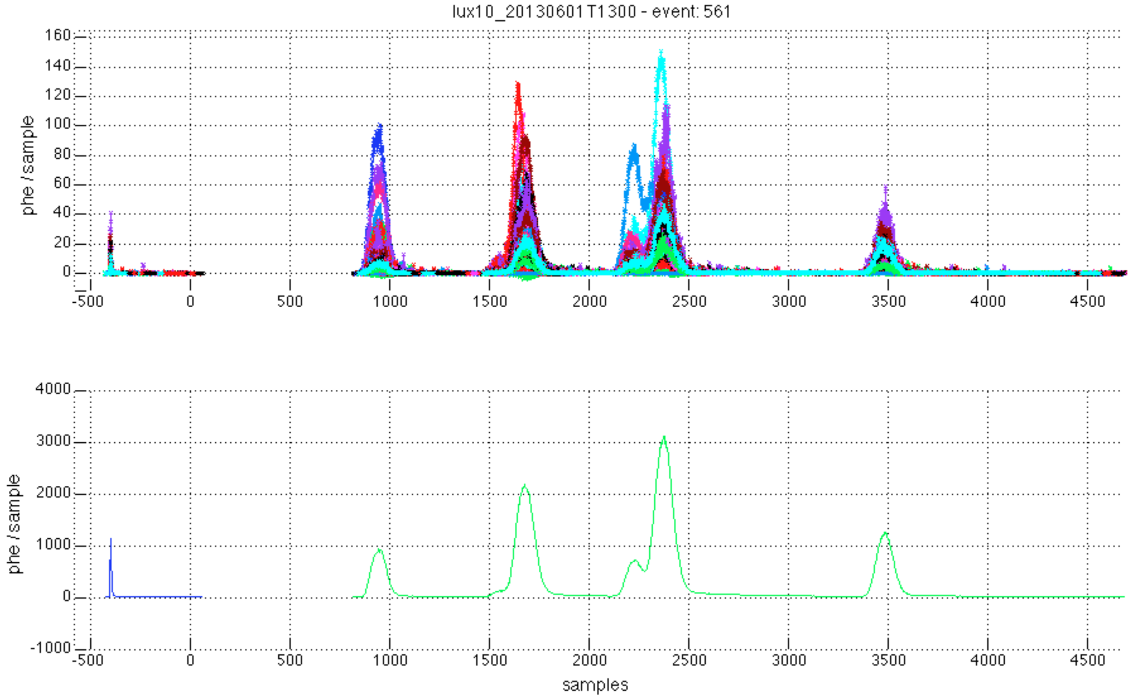

Figure 8.7: Example of a MS event with unseparated S2s. X axis is time, in units of 10 ns samples (LUX PMT data is digitized at 100 MHz). Y axis is normalized to phe sample^{-1}. The event is reconstructed with energy 2.6 MeV, with Z positions ranging from 2 cm to 6 cm below the liquid surface.

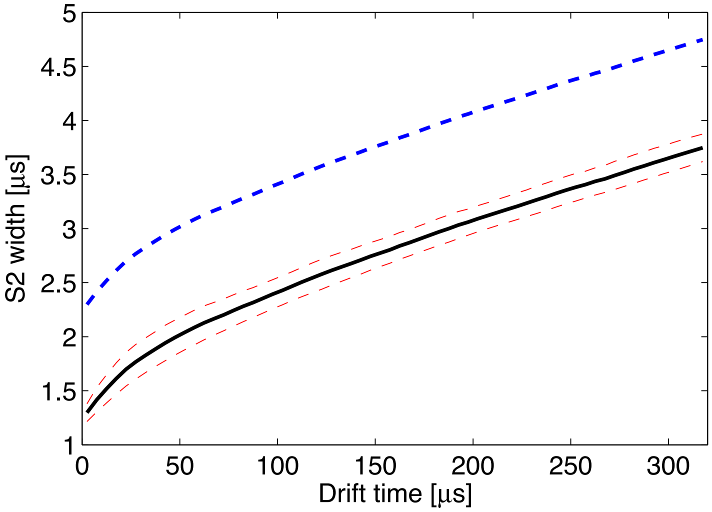

Figure 8.8: S2 width vs drift time, measured from fits to background data. Black points indicate peak centers (error bars shown, tiny). Red dashed lines indicate measured $\pm 1\sigma$ on width distribution (NOT measurement error). An S2 width cut using this trend is used to distinguish MS events. The cut is shown as the blue dashed line. Events with width above the line are tagged as MS.

in data processing. The pulse width cut described in Sec. 8.3.1 eliminates many of these events. However, SS-style energy reconstruction is still performed for events which do not pass this width cut. This is done in order to provide some energy estimate for these events. The MS energy calibration outlined in Sec. 8.3.2.2 cannot be used in these events, as timing and relative S2 size information is not available from RQs. It is assumed that the closeness of the S2 pulses in Z leads to only a small skew in position-reconstructed S1 and S2 sizes.

8.3.2.2 Multiple-Scatter Calibration

MS energy calibration cannot be determined in a straightforward manner as is done with SS events. The time overlap of the S1 signals from multiple event sites impedes S1 position correction. A guess must be made as to the fraction of the total S1 signal generated from each event site. The guess uses NEST to estimate the energy deposited at each vertex, based on the S2 size. The relative S1 contributions from each vertex are then estimated from the energy. S1 from the top tubes only and S2 from the bottom tubes only are used for this calibration, reducing errors from PMT anode saturation or capacitor depletion. These systematics are described in detail in [94].

The total measured S1 signal for scattering vertex i is:

$$S1_i = E_i\left(S2_i\right) \times Y\left(E_i\left(S2_i\right)\right) \times \alpha\left(\vec{x}_i\right), \tag{8.3}$$

where $S1_i$ is the measured S1 contribution from vertex i; E_i is the total ER energy deposited at vertex i; $Y\left(E\right)$ is the energy-dependent photon yield per ER energy deposition; and $\alpha\left(\vec{x}_i\right)$ is the photon detection efficiency at position $\vec{x}_i$. $Y\left(E\right)$ is taken from [90]. The value of E_i at each vertex is found from the S2 size at each vertex, based on NEST curves.

The $S1_i$ values are individually position-corrected and summed into a corrected S1 signal. Energy reconstruction then proceeds for each vertex individually with the summed, position-corrected S1 and S2 signals using Eq. 8.1. The total event energy is then calculated as the sum of the vertex energies. XYZ positions for each event are calculated as the energy-weighted mean positions of each hit vertex. This is the same definition as used by the simulation for MS event positions.

8.3.2.3 Energy Nonlinearity

Energy nonlinearity was measured in the reconstructed position of the ^{40}K 1461 keV$_{\mathrm{ee}}$ peak as a function of Z in the detector. The position of the peak after application of the energy reconstruction formulae in Eq. 8.1 and 8.3 was measured for several Z slices in the detector. The peak position was fit with a linear curve defined by $E_c = E_0 \left(1.72 \times 10^{-4} \cdot dt + 0.98\right)^{-1}$, where E_c is the reconstructed energy, E_0 is the initial reconstructed energy, and dt is the event drift time in µs.

The energy nonlinearity is likely due to S2 signal nonlinearity in the bottom PMT array. The reconstructed energy falls with higher Z, due to finite electron drift length. The reconstructed energy is also nonlinear with energy, since a larger fraction of the S2 signal is lost for larger S2s. The nonlinearity in the peak position is obvious for high Z slices, as shown in Fig. 8.14, where the 2.6 MeV peak drifts by 100 keV between the bottom and top of the active region. This drift does not significantly impact the final results of the fitting, and explains the skewed position of the 2.6 MeV peak in the data/simulation comparison.

8.3.3 Comparison with Calibration

Calibration at high energies is confirmed from ^{228}Th calibration data. Thorium-228 is a parent of ^{208}Tl. Thallium-208 generates a 2.6 MeV γ which is easily visible in data. This is the same γ used to tag ^{232}Th, which is a parent of ^{208}Tl (and ^{228}Th). The comparison between data and background is shown in Fig. 8.9. Note that this comparison uses data from a ^{228}Th calibration set where a high-energy veto is not used. Later calibrations employed a high-energy veto, cutting off the 2.6 MeV peak. The 2.6 MeV peak, averaged over all Z slices in the detector, is reconstructed at 2510 ± 30 MeV, showing the nonlinearity mentioned in Sec. 8.3.2.3.

8.3.4 Peak Identification

The energy spectrum for the full drift region is shown in Fig. 8.10. Modest radius and drift time cuts are applied to remove β and gamma-X events near the grids and PTFE. Background data are measured from June 1–15, with a cumulative 11 livedays.

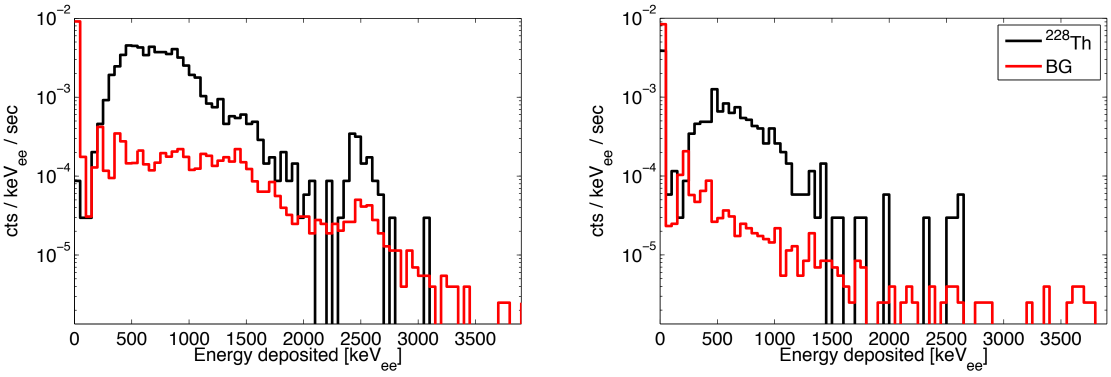

(a)

(b)

Figure 8.9: Calibration taken with a ^{228}Th source (black), compared with standard background data (red). Spectra are shown for (a) all events and (b) SS events. Energy reconstruction is performed as described in Sec. 8.3.2. The 2614 keV$_{ee}$ peak from ^{208}Tl is recreated at 2510±30 keV$_{ee}$. A position cut is used, requiring R < 19 cm and 50 μs < dt < 250 μs.

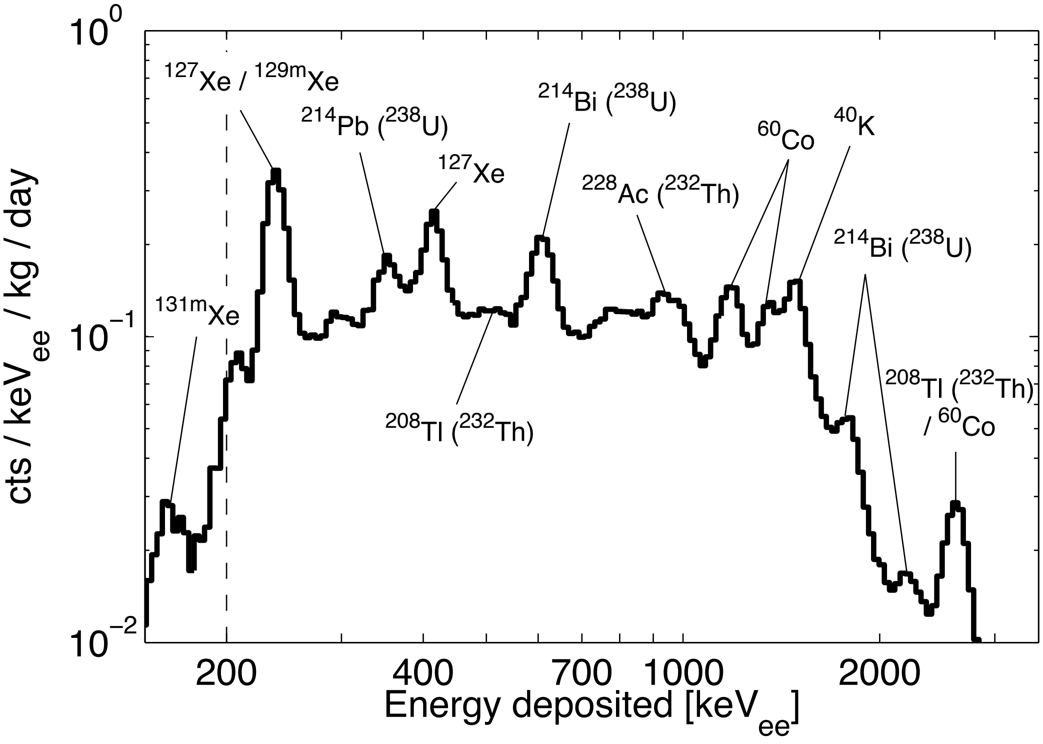

Figure 8.10: LUX γ energy spectrum, with drift time cut applied requiring 20 < dt < 300 (3 cm removed from top and bottom of the drift region) and R < 21 cm (3 cm removed from outer radius). The total Xe mass is 170 kg. The dashed line indicates the approximate low-energy threshold from the γ S1 cut (Sec. 8.3.1.1). Energy is reconstructed from S1+S2 for both SS and MS events as described in Sec. 8.3.2.

8.3.5 Simulation Comparison

8.3.5.1 Simulation Datasets

The background search in this work does not have the sensitivity required to perform a background match on small scales, e.g. to find variations in PMT radioactivity, or differences between PMT and Cu ^{60}Co content. In order to simplify the search and minimize free parameters, simulations are included from three regions only: the top PMT array, the bottom PMT array, and the lateral sides of the active region. These simulation sets cover the major areas where radioactivity can produce significantly differing energy spectra as a function of position within the detector. The simulations are discussed further in Sec. 5.2.

The simulation datasets use radioisotope decays for a realistic generation of γ energy spectra and coincidences. In the case of ^{238}U and ^{232}Th decays, the entire decay chain is simulated, assuming secular equilibrium. The simulation ends with γ energy deposition in the active region. Photon and ionization electron generation is not incorporated into these simulations. Event energy depositions are simply tallied from the total energy deposited at each event vertex. Positions are calculated as the energy-weighted mean position of the event vertices, matching the treatment of data in Sec. 8.3.2.2.

Four major isotopes were identified during counting of LUX internals: ^{238}U, ^{232}Th, ^{40}K, and ^{60}Co. All four isotopes were identified during PMT screening, and are known to be present in both top and bottom arrays. ^{238}U, ^{232}Th and ^{40}K were found in significant concentrations in the plastic insulation and/or superinsulation around the inner cryostat, and are therefore known to be present in the lateral radioactive load. ^{60}Co is not identified from screening data in lateral construction materials. However, a simulation of this isotopes is included in the lateral component, since it could be introduced from Cu cosmogenic activation or from steel plumbing components near the active region.

An energy spectrum corresponding to ^{222}Rn decays in the active region is also included, with a fixed activity measured by α counting (Sec. 8.5). The ^{85}Kr energy spectrum is also included, assuming a 3.5 ppt $^{\mathrm{nat}}$Kr/Xe concentration. These spectra minimally influence the predicted energy spectrum shape, as the ER rate from gammas is much higher than the ER rate from internal sources in all energy bins above 500 keV$_{\mathrm{ee}}$. Note that the energy spectrum

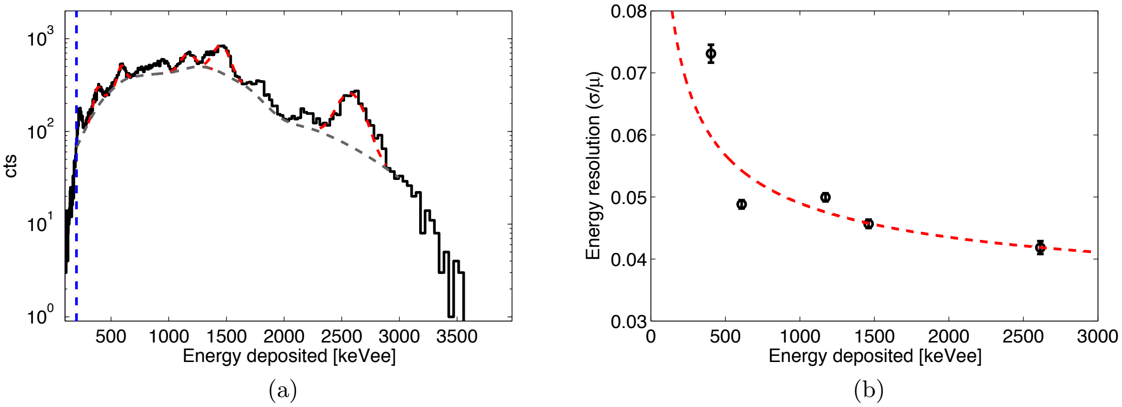

(a) (b)

Figure 8.11: (a) Peak fits for γ lines at 403 keV, 609 keV, 1172 keV, 1461 keV, 1764 keV, and 2614 keV. The gray dashed line shows the Compton baseline, estimated by continuum activity around all visible peaks. The blue dashed line denotes the approximate energy cutoff due to the cutoff in S1 acceptance. Data is taken for SS+MS events, with 145 μs < dt < 175 μs, and R < 21 cm (b) Measured resolution vs energy, from peak fits shown in Fig. (a). Resolution is fit with the curve $0.59 \cdot (E)^{-1/2} + 0.03$.

from ^{127}Xe cuts off at 410 keV$_{\mathrm{ee}}$, and therefore has no influence on energy spectrum shape above 500 keV$_{\mathrm{ee}}$.

8.3.5.2 Energy Resolution

Energy resolution is measured from peaks found in Fig. 8.10. The Compton baseline is estimated from the activity around each peak. Results are shown in Fig. 8.11. Systematics in the energy resolution measurement are estimated to be ±0.005 from uncertainties in the baseline shape.

8.3.5.3 Single-Scatter Cut Efficiencies

SS cut efficiencies are compared between data and Monte Carlo as a function of energy in Fig. 8.12. The comparison is made in the region 50 μs < dt < 250 μs, R < 20 cm. This region is chosen to avoid β events near the grid wires and PTFE surfaces. Simulation and data show agreement within 10% for energies above 100 keV$_{\mathrm{ee}}$. A SS cut was not ultimately used during fitting of simulation spectra to data, due to the success of the MS energy calibration and the added complexity of matching SS cut parameters between simulation and data.

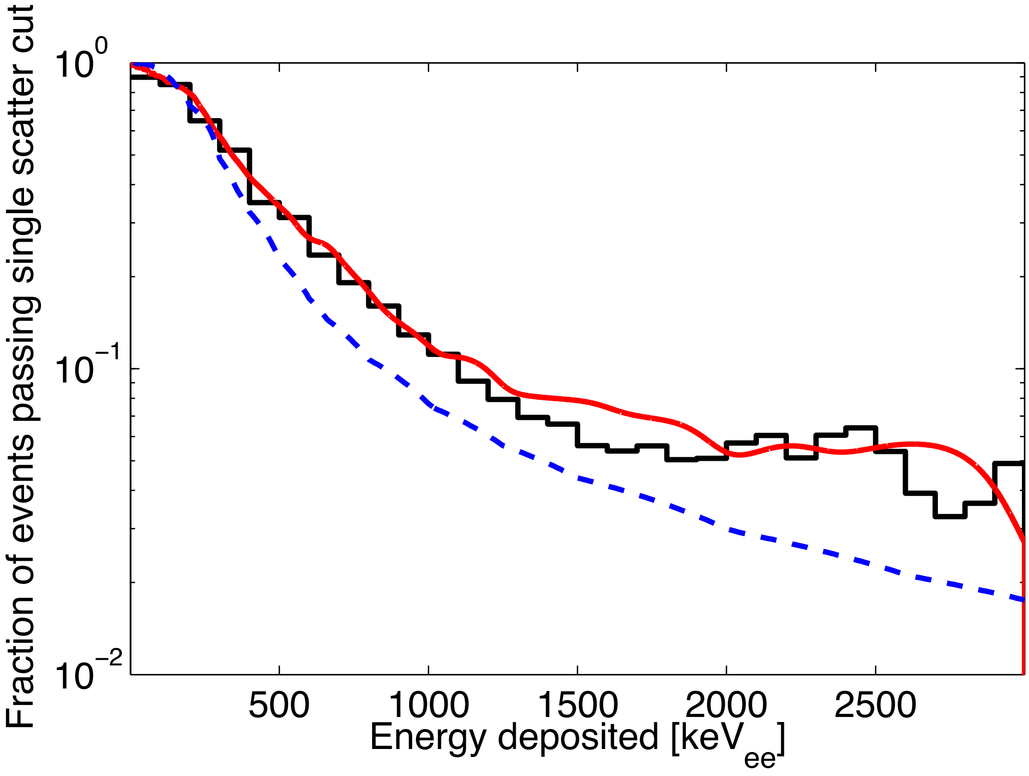

Figure 8.12: SS cut efficiency as a function of energy, shown for data (black) and simulation (red). Shown for comparison is the ratio of photoelectric cross-section to photoelectric + Compton + pair production cross-section (blue dashed), which represents the SS cut expected in a detector with perfect position resolution for MS events. A fiducial cut with R < 20 cm and 50 μs < dt < 250 μs is used.

8.3.5.4 Comparison of Drift Region Spectra and Best-Fit Results

Comparisons of measured energy spectra in the drift region are shown with LUXSim Monte Carlo projected energy spectra, the details of which are covered in Sec. 5.2. The energy spectrum for the full drift region is compared to Monte Carlo in Fig. 8.13, with the simulation scaling factors based on positive measurements from SOLO shown in gray. This includes measurements of activity from the top and bottom PMT arrays, superinsulation, and plastic thermal insulation. There is no radial cut on this data, and a modest 2 cm Z cut is used to remove events close to the cathode and gate grids. Close agreement with the simulation predictions are seen for peaks corresponding to ^{238}U, ^{232}Th and ^{40}K. A factor ×2.5 deficit is seen in the 2.4–2.6 MeV range. This is due to a deficit of ^{60}Co from unaccounted-for cosmogenic activation of Cu. The peak also has a contribution from ^{232}Th, which could be sourced from uncounted steel plumbing components in the active region. The data / simulation comparison is broken down by Z slices in Fig. 8.14, using no radial cut as was done for Fig. 8.13. The deficit in the 2.4–2.6 MeV range is largest at the detector center, suggesting that the additional activity comes primarily from lateral components.

The radioactive loads were allowed to float to find a best-fit combination of simulation spectra. Fitting used combined SS and MS data, matching the energy spectrum above 500 keV$_{\mathrm{ee}}$. The 500 keV$_{\mathrm{ee}}$ limit was chosen to avoid influence from activated Xe isotopes, which have a maximum peak energy of 410 keV$_{\mathrm{ee}}$. Initial fitting attempts using χ^2 minimization failed, due to imperfect energy reconstruction at higher energies. Fitting was successfully performed using least-squares minimization on the log of the energy spectra. This maximizes sensitivity to both the high- and low-energy spectral features, greatly improving fits over those found by χ^2 minimization. The error on the best-fit values is estimated to be 25%, based on the variation observed from changing parameters. These parameters include the exact dimensions of the drift region in the simulation, and the energy scale correction factor for the data.

Best-fit results are shown for the entire drift region average in Fig. 8.13, and per Z slice in Fig. 8.14, as the red dashed curve. The 2.4–2.6 MeV peak is well fit by an increase in the lateral ^{232}Th and ^{60}Co components, as expected from uncounted steel components and

Cu cosmogenic activation. An excess of ×1.5–2 in the Compton tail below 1000 keV is seen for Z slices in the upper half of the detector, which potentially indicates an overestimate of ^{232}Th by this factor in the lateral components. The best-fit parameters are compared to the parameters based on screening results in Table 5.1.

Differences between best-fit and screening expectation concentrations are found for the top and bottom regions in the range from -1.6σ–$+1.7\sigma$. Of note is a measurement of ^{238}U in the lateral components which is 5σ below expectation, and a measurement of lateral ^{232}Th which is 3σ higher than expectations. It should also be noted that ^{232}Th and ^{60}Co are partially degenerate due to their contributions to the peak in the 2.4–2.6 MeV range, which is poorly resolved due to saturation effects. The final best-fit simulation spectra are shown in comparison with ^{222}Rn and ^{85}Kr spectra in Fig. 5.4.

The total predicted detector event rate from the best-fit quantities above 500 keV$_{\rm ee}$ (including S1-only events, below the cathode grid) is 1.3 Hz. The total predicted rate above 500 keV$_{\rm ee}$ based on screening results is 1.1 Hz. The observed S1 rate in LUX above 2500 phe (corresponding to ~500 keV$_{\rm ee}$) during the June 1–15 period is 1.3 ± 0.1 Hz, with uncertainty stemming from the S1 cutoff corresponding to 500 keV$_{\rm ee}$. The best-fit overall event rate is in good agreement with the observed total S1 rate in the detector.

8.4 Activated Xenon Measurements

Activated Xe radioisotope signatures were clearly visible through the duration of Run 3. A discussion of these isotopes, and their contributions to WIMP search backgrounds, is given in Sec. 5.3.1. Inital rate estimates for Xe radioisotopes were made based on peak measurements shown in Fig. 8.3. A much stronger constraint on the activated Xe decay rates was placed by tracking the evolution of each characteristic peak rate over time, as shown in Fig. 8.15. The $^{131{\rm m}}$Xe decay rate is 46 ± 9 mBq kg^{-1} as of April 22. The ^{127}Xe decay rate on the same date is 0.46 ± 0.09 mBq kg^{-1}.

No clear estimate of the $^{129{\rm m}}$Xe decay rate was made after initial measurements. The $^{129{\rm m}}$Xe peak overlaps the 238 keV$_{\rm ee}$ peak from ^{127}Xe (comprised of the 203 keV$_{\rm ee}$ γ plus a 35 keV$_{\rm ee}$ x-ray). The $^{129{\rm m}}$Xe decay rate was quickly suppressed relative to that of ^{127}Xe,

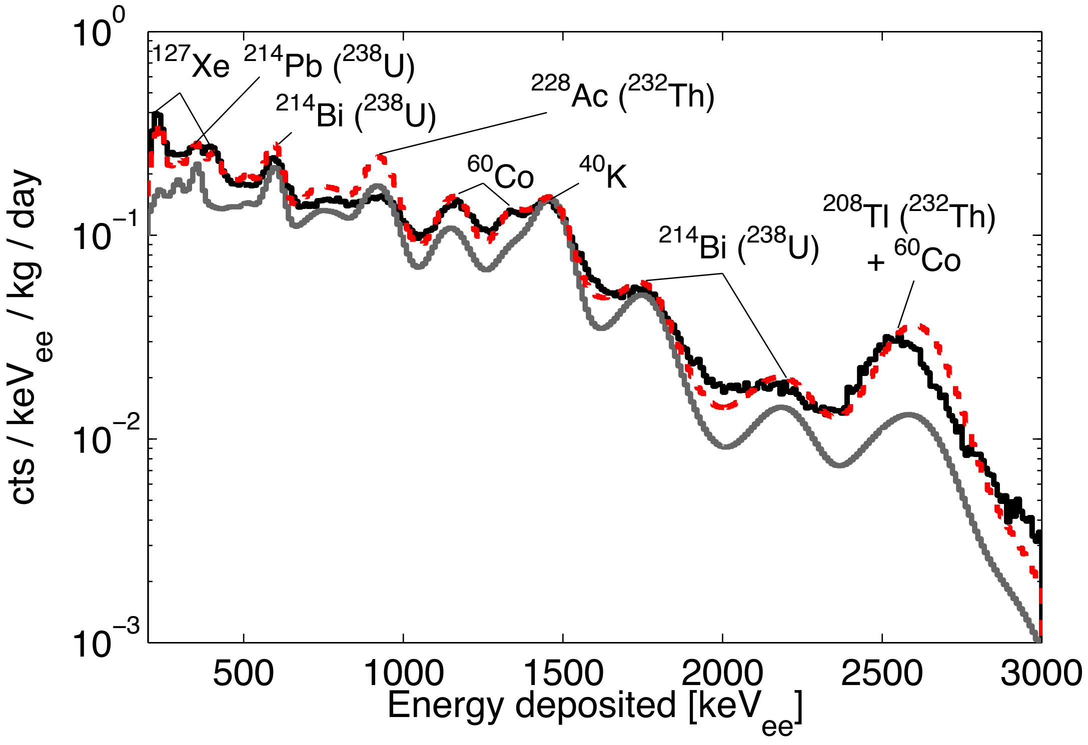

Figure 8.13: Drift region measured energy spectrum, compared with simulation best-fit scaling factors (red) and simulation projections based on positive screening results only (gray), giving the expected lower limit for γ activity. Scaling factors correspond to the "Best Fit" and "Screening" columns in Table 5.1, respectively. The lower bound used for fitting was 500 $\mathrm{keV_{ee}}$. The low-energy cutoff for the dataset is estimated at 200 $\mathrm{keV_{ee}}$ due to S1 selection cuts. Data includes both SS and MS events, with energy and position reconstruction explained in Sec. 8.3.2. A Z cut is used to remove 2 cm from the top and bottom of the drift region. No radial cut is used. The ^{127}Xe spectrum is added in to show the continued agreement between model and data at energies below 500 $\mathrm{keV_{ee}}$.

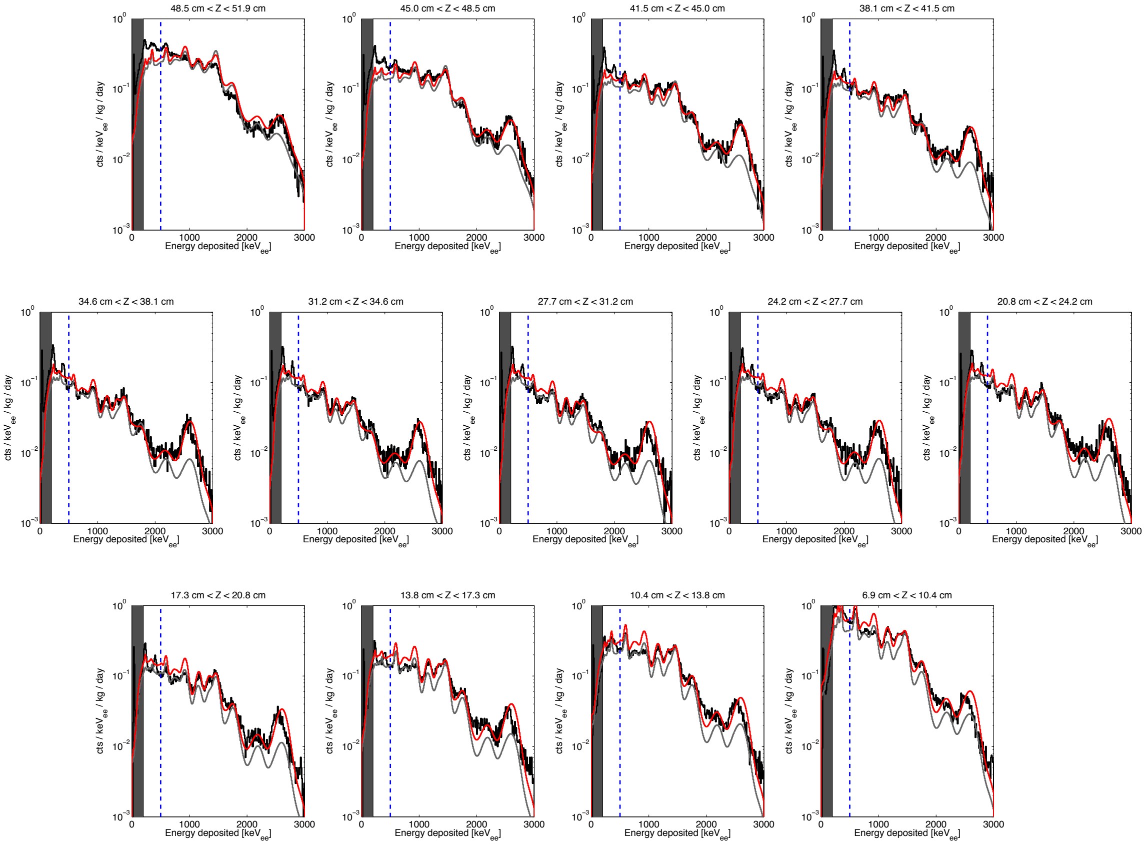

Figure 8.14: Drift region best-fit simulation energy spectra for 3.4 cm slices in Z, compared with data. All curves are shown as detailed in Fig. 8.13. The ^{127}Xe spectrum is not included in the Z slice histograms.

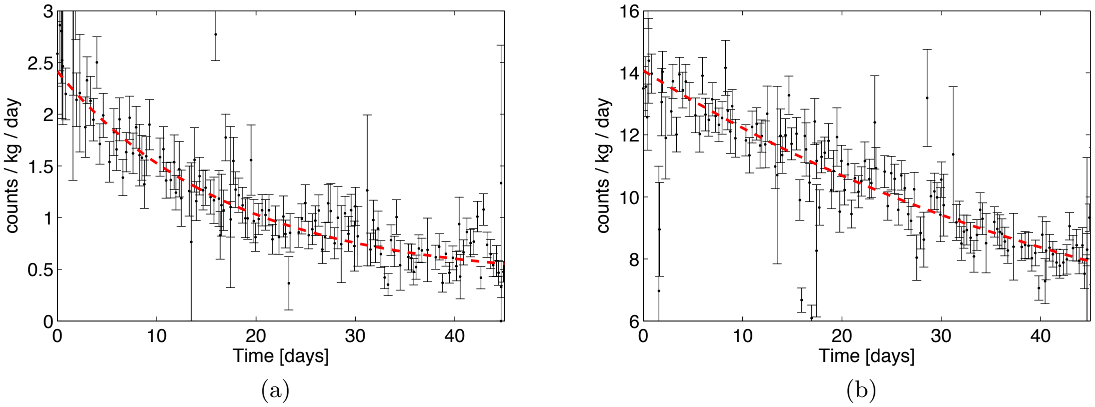

(a) (b)

Figure 8.15: Measurement of peak rates at (a) 164 $\mathrm{keV_{ee}}$ from $^{131\mathrm{m}}$Xe and (b) 410 $\mathrm{keV_{ee}}$ from ^{127}Xe, over the duration of the Run 3 WIMP search. Peak rates were measured in the energy range 150–175 $\mathrm{keV_{ee}}$ for the 164 $\mathrm{keV_{ee}}$ peak, and 350–450 $\mathrm{keV_{ee}}$ for the 410 $\mathrm{keV_{ee}}$ peak. The peak rates are fit with exponential functions with decay constants $\tau_{131m} = 17.1$ days and $\tau_{127} = 52.5$ days for $^{131\mathrm{m}}$Xe and ^{127}Xe, respectively. t_0 corresponds to May 1.

due to the difference in half-lives (8.9 days and 36 days respectively). The ^{127}Xe decay rate dominated the 236 $\mathrm{keV_{ee}}$ region for the duration of the WIMP search run. The ^{133}Xe decay signature was quickly suppressed relative to the Compton continuum before WIMP search running began, due to its 5.2 day half-life.

8.5 Radon

As discussed in Sec. 5.3.2, ^{222}Rn chain decays in the detector must be well-modeled to understand low-energy event contributions. The isotope of primary concern is ^{214}Pb, which undergoes naked β decay with 11% probability. Several bounds were placed on the ^{214}Pb decay rate in LUX, as outlined in the following subsections.

8.5.1 ^{214}Pb Activity Bounds from ^{222}Rn Daughters

The most direct bound on ^{214}Pb activity comes from measurement of ^{222}Rn chain α decays within the active region. The ^{222}Rn chain is shown in Fig. 5.10. If the ^{222}Rn chain is assumed to be in a state of dynamic equilibrium, where daughter isotopes are removed with some characteristic time constant, then it can be assumed that the ^{214}Pb decay rate is bounded between the decay rate of its immediate parent (^{218}Po) and its immediate daughter (^{214}Bi).

Isotope	Measured Decay Rate in Drift Region [mBq]	Geometric Series Estimate in Drift Region [mBq]
^{222}Rn	$17.9 \pm 0.2_{\text{stat}} \pm 1.3_{\text{sys}}$ (α)	17.9
^{218}Po	$14.4 \pm 0.2_{\text{stat}} \pm 1.1_{\text{sys}}$ (α)	17.0
^{214}Pb	3.5–14.4 (α); <8.3 (γ, 90% CL)	7.4
^{214}Bi	3.5 (inferred from ^{214}Po)	3.5
^{214}Po	$3.5 \pm 0.1_{\text{stat}} \pm 0.3_{\text{sys}}$ (α)	3.5
^{210}Po	14.3 (PTFE); 7.2 (cathode)	–

Table 8.1: Alpha decay rate measurements for all ^{222}Rn chain radioisotopes, as well as the measured α rate from 210Po (from the 210Pb chain). Data is taken from [138]. Measured decay rates are compared with rate predictions based on a geometric series, using ^{222}Rn and 214Po measurements to fix the endpoints of the series.

Direct detection of the ^{218}Po decay rate is accomplished through direct measurement of the α peak at 6.1 MeV. Decays from ^{214}Bi cannot be directly measured with confidence, as ^{214}Bi undergoes β decay and thus yields no obvious peak signature. However, the immediate daughter of ^{214}Bi, ^{214}Po, decays with 160 μs half-life, making the ^{214}Po decay rate identical to that of ^{214}Bi under any isotope removal model. This decay rate can be efficiently tagged from its characteristic 7.8 MeV α. A full analysis of LUX α rates is given in [138].

The measured α decay rates for all ^{222}Rn species are given in Table 8.1. The quoted values for ^{218}Po and ^{214}Po decay rates are $14.4 \pm 0.2_{\text{stat}} \pm 1.1_{\text{sys}}$ and $3.5 \pm 0.1_{\text{stat}} \pm 0.3_{\text{sys}}$, respectively. Taking the 90% upper (lower) limit for the ^{218}Po (^{214}Po) measurements, the ^{214}Pb rate is bounded in the range 3.2–15 mBq. This is a factor ×5 uncertainty in the ^{214}Pb low-energy background contribution. The uncertainty must be narrowed to gain a meaningful insight into the ^{214}Pb low-energy event contribution.

8.5.2 Upper Bound from High-Energy Data

A constraint has been placed on the amount of ^{214}Pb in the active region by examining the energy spectrum in the range between the ^{127}Xe peaks at 238 keV and 410 keV, with a 30 kg fiducial cut ($R < 13$ cm, $100\ \mu\text{s} < dt < 220\ \mu\text{s}$). It is conservatively assumed that the dominant contribution to the spectrum in the range around the ^{127}Xe peaks comes from ^{214}Pb, as the γ contribution is significantly reduced by the fiducial cut. A SS cut is used (one S1, one S2 only) to further reduce γ background contributions. Data and best-fit ^{214}Pb spectra are shown in Fig. 8.16.

The shape of the ^{214}Pb energy spectrum is taken from Monte Carlo, shown in Fig. 5.11. The ^{127}Xe peaks are very well fit by Monte Carlo predictions for both SS and MS events, giving confidence that the estimate of SS cut efficiency for the Monte Carlo ^{127}Xe is close to that in measured data. Resolution is determined empirically from the best fit, and the same resolution is applied to the ^{214}Pb spectrum. The efficiency of the SS cut for ^{127}Xe agrees with simple estimates based on the ratio of de-excitation by internal conversion electron to de-excitation by γ. As ^{214}Pb exhibits a similar decay scheme to ^{127}Xe, generating comparable γ energies to ^{127}Xe, it can reasonably be assumed that the ^{214}Pb SS cut efficiency is also well-modeled by simulation, and thus is well matched to data. The ^{214}Pb decay rate in the 30 kg fiducial is expected to have a 50% reduction from the SS cut, based on the internal conversion to γ ratio and the γ mean free path. The observed number passing the SS cut is 40%; this is within range of expectations due to the naive model of the SS topology.

A 90% CL upper limit taken between the tails of the ^{127}Xe peaks in the range 310–340 keV$_{ee}$ is measured at 32 mBq kg^{-1}, or 8.3 mBq for the entire drift region. This limit is a factor ×1.8 lower than the limit set from α counting alone. The estimated background rate from 32 mBq kg^{-1} ^{214}Pb is 0.23 mDRU$_{ee}$.

8.5.3 Geometric Series Activity Estimate

The most likely ^{214}Pb activity rate in the detector can be predicted by a simple model where the ^{222}Rn chain isotope decay rates progress through a geometric series, where the steps in the series are set by the isotope half-lives. The measured ^{222}Rn and ^{214}Po rates are used to fix the series endpoints. The interpolated ^{218}Po, ^{214}Pb and ^{214}Bi rates are shown in Table 8.1. The calculated ^{214}Pb decay rate is 7.4 mBq for the entire active region, consistent with <8.3 mBq (90% CL) calculated in Sec. 8.5.2.

8.6 Xenon Flow Imaging with ^{222}Rn Decays

Xenon circulation in the active region was imaged using fast decays between ^{222}Rn and its immediate daughter, ^{218}Po. The goal of this observation was to determine if there was

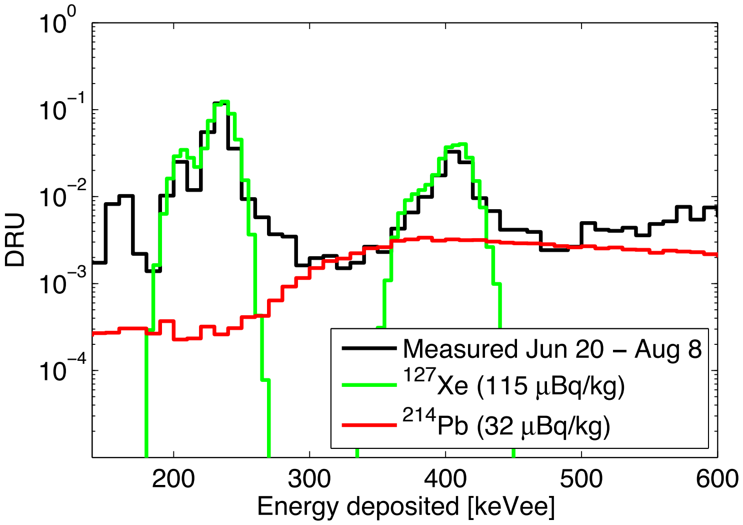

Figure 8.16: Best-fit ^{214}Pb spectrum (red) for a 30 kg fiducial (R $<$ 13 cm, 100 μs $<$ dt $<$ 220 μs), constrained in the range 310–340 keV$_{ee}$. Measured data is shown in black. A simple SS cut is used, requiring one S1 and one S2. No γ continuum contribution is assumed. Xenon-127 peak models are overlaid with measured data (green). Data and ^{127}Xe normalization is shown from June 20–August 8.

a clear bias in the drift direction of ^{222}Rn decay daughters due to electrostatic attraction to the grids. Attraction is assumed due to the emission of the α particle by ^{222}Rn decay, leaving the ^{218}Po daughter with a charge of -2, assuming no disruption of the electron cloud during the decay. The attraction of the ^{222}Rn decay daughters toward the grids would have implications for the assumed distribution of ^{214}Pb in the active region, and influence the choice of fiducial volume used.

^{222}Rn and ^{218}Po decays were selected by their S1 signals. The analysis made use of ^{218}Po decays which occurred within 10 sec of a ^{222}Rn decay, assuming that the decaying ^{218}Po was the daughter of the observed ^{222}Rn decay. The analysis used 30 livedays of WIMP search data. Only the Xe in the range 20 μs $>$ dt $>$ 160 μs was investigated, as the α peaks used for ^{222}Rn and ^{218}Po identification suffered significant degradation due to PMT saturation below this range.

The Xe flow pattern in the upper half of the active region is shown in Fig. 8.17. The flow pattern shows a clear bias from $-X$ to $+X$ across the center of the detector. A counterflow can be seen at the active region edges. The Xe is in a clear upward flow pattern on the $-X$ side of the detector, falling downward towards the $+X$ side.

The observed flow speeds are on the order of cm s^{-1}. The predicted speed of the ^{218}Po ion from electrostatic attraction is much lower than this, on the order of 0.1 cm s^{-1} [156]. It is believed that convection cells play the dominant role in ion transport throughout the active region. Given the long half-life of ^{214}Pb compared to the time required to circulate across the active region, the ^{214}Pb concentration is assumed to be homogeneous across the detector.

8.7 Neutron Multiple Scatter Analysis

Neutron events in the LUX detector are very rare, and pose a challenge in terms of setting background limits. Neutron emission and interaction rates in the LUX detector are well below the emission and interaction rates of EM backgrounds. EM background rates in particular are dominated by radioactivity in detector internals, yielding a ∼3 Hz detector event rate. By contrast, the rate of neutron events in the detector is predicted to be 5 μHz. The rate of neutron SS events, a direct WIMP background against which there is no discrimination, is projected to be another three orders of magnitude lower than this. Fortunately and unfortunately, no direct measurement of the neutron SS rate can be made, given the WIMP search data in hand.

Neutron events can be distinguished from EM background by their relative abundance of low-energy (<120 phe) MS events. A low-energy MS EM event is a rare occurrence relative to the rate of low-energy EM SS events. By contrast, an MeV-scale neutron deposits its maximum scattering energy with an S1 yield on the order of 100 phe. The relatively low yield of scintillation photons and ionization electrons from NR energy depositions enables one to perform a neutron search by looking for MS events $\lesssim$100 phe.

In this work, a prediction of neutron SS rates is made through identification of NR MS events. The expected ratio of MS to SS events is taken from LUXSim Monte Carlo neutron energy deposition studies, performed as part of the background modeling program (Sec. 5.10). NEST Monte Carlo (v0.99β, for this study) is analytically folded in to the existing energy deposition studies in order to gain an understanding of the expected S1 and S2 distributions from ER and NR MS events.

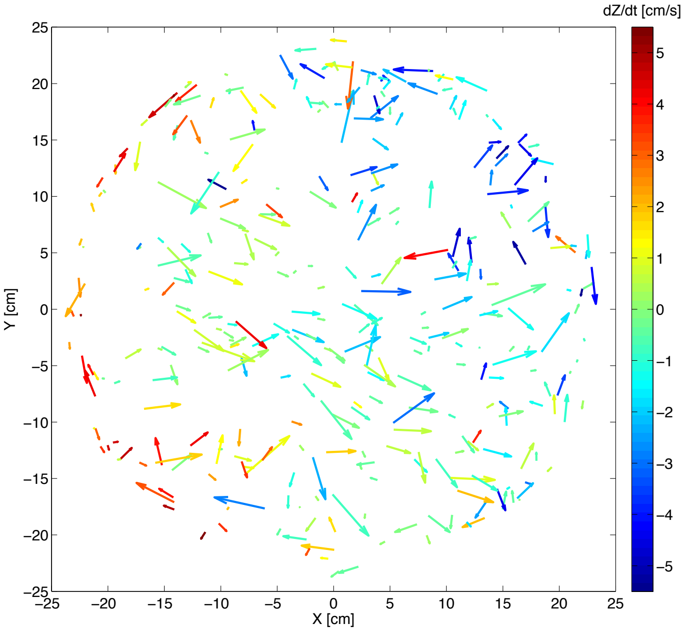

(a)

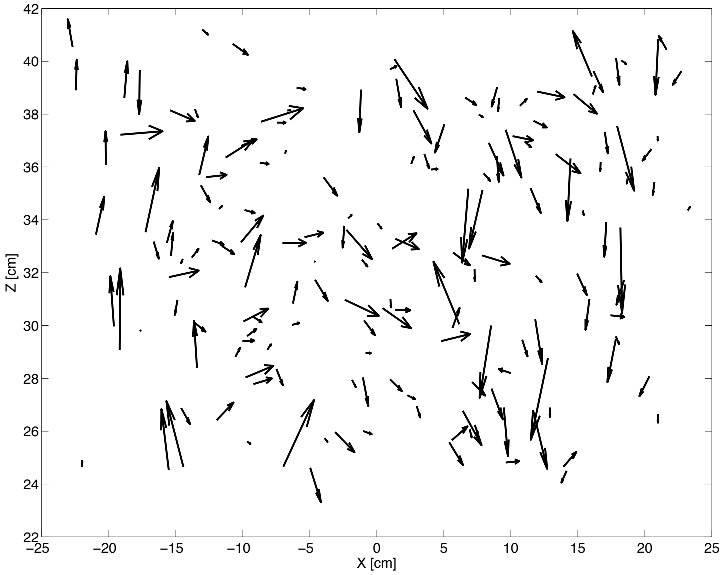

(b)

Figure 8.17: Xenon flow patterns in the upper half of the active region (20 µs > dt > 160 µs). Flows are imaged by coincident ^{222}Rn-^{218}Po decays, occurring within 10 s of one another. Drift speeds are ascertained by the spatial and timing separation of the paired decay events. (a) XY velocity distribution, with Z velocity shown in color. Arrow length corresponds to XY speed, with the longest arrows corresponding to 3 cm s^{-1}. (b) XZ velocity distribution. Arrow length corresponds to XZ speed. The Y velocity component is not represented.

8.7.1 Simulation Studies

8.7.1.1 Neutron Studies

LUX neutron background studies are detailed in Sec. 5.5. The studies focused on neutrons generated from (α,n) and ^{238}U fission processes in the PMT arrays. The relative rates of these sources, both in terms of absolute emission and the relative interaction rates of neutrons from each source, are summarized in Table 8.2. The table also reports the calculated ratio of MS events (within a 180 kg search fiducial) to SS events (within the standard 100 kg or 118 kg fiducial volumes). Different fiducial volumes are used to maximize the expected number of MS events, giving the greatest leverage over the SS rate. The 180 kg fiducial is defined as $R < 21$ cm, 7 cm $< Z <$ 52 cm. The rate estimates fold in an EM veto cut, which rejects NR events which contain an accompanying EM component >30 keV$_{ee}$. (Note that there is no difference between a 30 keV$_{ee}$ threshold and a 0 keV$_{ee}$ threshold, as all of the EM veto power comes from detection of gammas from inelastic scatter events with minimum energy 40 keV$_{ee}$.)

Also reported in Table 8.2 is the maximum expected S1 yield for each neutron dataset, along with the rate-weighted mean. The rate is reported at the 95% upper S1 value of the spectrum. A MS search using this S1 cutoff then has >95% detection efficiency with respect to S1.

8.7.1.2 NEST S1/S2 Studies

It is crucial to the identification of NR MS events to understand their distribution in S2/S1 vs S1 space, in order to distinguish them from ER MS events. The location and width of the ER and NR bands for MS events is not expected to be the same as for SS events. MS events combine two (or more) events linearly in corrected S1, and the corresponding S2 is the sum of the corrected S2s. The resulting event is, on average, higher in S2/S1 than a SS with the same S1 signal, since the linear combination of the S2 signals is dominated by the S2 signal above the band mean (recall that the band is constructed in log-space). It is also important to fold in the expected underlying energy distribution of the ER and NR events comprising the S2/S1 distribution, as this can significantly influence the position and shape

Dataset	**Rate [n/PMT/yr]**	**Relative Rate in Detector**	**MS (180 kg) / SS (118 kg)**	**MS (180 kg) / SS (100 kg)**	**Max MS S1 (95%, 180 kg) [phe]**
Bottom Th (α,n)	0.21	0.12	12	20	101
Bottom U (α,n)	0.60	0.35	11	22	116
Bottom U fission	0.33	0.19	10	18	91
Top Th (α,n)	0.21	0.064	17	25	101
Top U (α,n)	0.60	0.18	16	25	115
Top U fission	0.33	0.10	18	36	91
Rate-weighted mean			13	23	106

Table 8.2: Results from LUXSim neutron background studies (Sec. 5.5). Datasets correspond to neutron emission from bottom and top PMT arrays. Neutron emission rates are calculated in Sec. 5.5. Relative rates are calculated from the total fraction of neutrons interacting in the detector, multiplied by the neutron emission rate from each source. MS / SS ratios are calculated for MS events within a 180 kg ($R < 21$ cm, 7 cm $< Z < 52$ cm) volume, and SS events with the standard 118 kg ($R < 18$ cm, $7 < Z < 47$ cm) or 100 kg ($R < 17$ cm, $9 < Z < 47$ cm) fiducial volumes. S1 estimates are taken from folding in NEST NR scintillation and ionization yields in post-processing, combined with analytic functions to fold in detector efficiencies.

of the bands.

Results from NEST MC studies were folded in atop LUXSim energy deposition studies to estimate the expected S1 and S2 distributions for MS NR events. The S1 and S2 distributions were calculated as a function of NR energy following the description in Sec. 5.10, and the resulting distributions were linearly summed for NR MS events. The predicted S2/S1 vs S1 distribution for the LUXSim neutron MS events are shown in Fig. 8.18a. The mean of the S2/S1 vs S1 band for NR SS events is shown for comparison. Note that the band mean for MS events is higher than that for SS events, as predicted.

NEST was also used to predict the band corresponding to MS ER events, which, though rare, form a background for the NR search. The S1 and S2 distributions for MS ER events were created through the random addition of two single ER events, assuming a flat single ER energy distribution. This best represents the distribution from a MS γ event, which should be dominated by two-scatter topologies. Gammas are the dominant contributor of MS ER events <150 phe; intrinsic events which yield multiple S2s generate energies that fall above this S1 threshold. The resulting S2/S1 vs S1 distribution is shown in Fig. 8.18b. The ER SS band mean is shown for comparison.

The bands also highlight the expected distribution of the events in S1. The ER MS band shows a profile which increases with S1 as a power law with slope 0.65. In contrast, the NR MS band is well characterized by a falling exponential function with two distinct time constants. The S1 distributions for both ER MS and NR MS are shown in Fig. 8.19.

8.7.2 Event Reconstruction

8.7.2.1 S1 and S2 Reconstruction

MS events are corrected in S1 as discussed in Sec. 8.3.2. It should be noted that the NEST ansatz uses the ER photon and electron yield model. It is well understood that the relative photon and electron yields differ for ER and NR events (Fig. 2.2a). A future iteration of this analysis should use both ER and NR models, to create two “alternate realities” in which the MS events were actually ER or NR in nature. This can be accompanied by some score which gauges the ER-ness and NR-ness from each reconstruction, allowing some measure

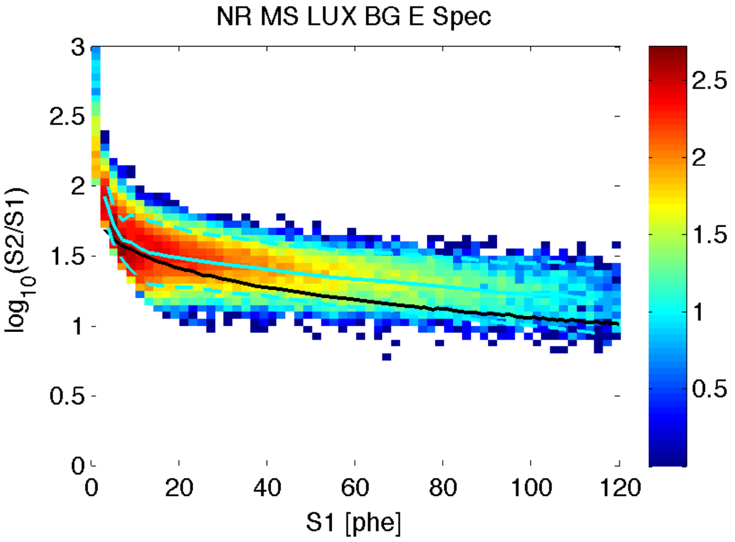

(a)

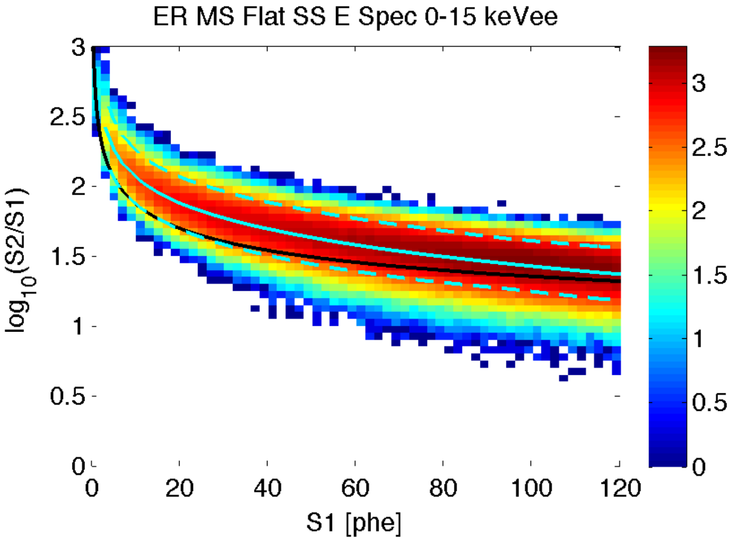

(b)

Figure 8.18: S2/S1 vs S1 distributions for MS events, coupled in post-processing with NEST scintillation and ionization yields. The measured band mean and 90% contours (5%–95%, corresponding to 1.64σ) are drawn in cyan solid and dashed, respectively. Shown for reference is the mean of the S2/S1 vs S1 band for SS events in black. (a) NR distribution using the MS energy distribution from LUXSim neutron background studies. (b) ER MS distribution, using the random addition of two ER events which have an initial flat energy distribution.

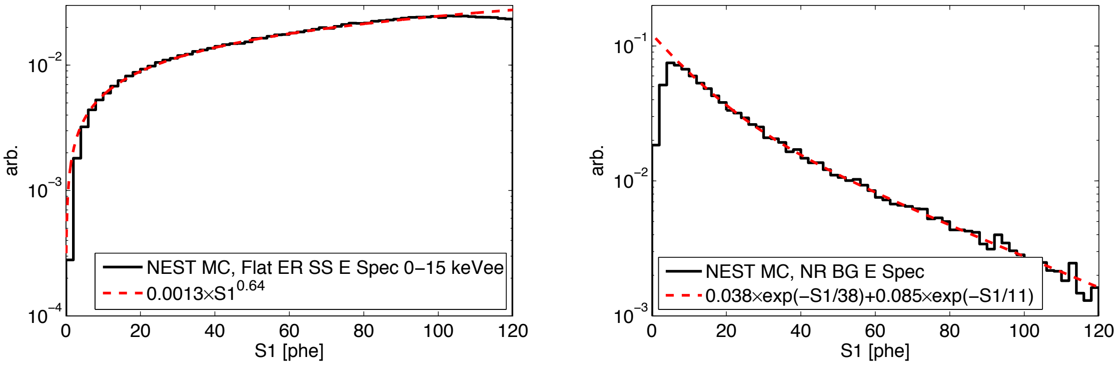

(a) (b)

Figure 8.19: S1 distributions using LUXSim / NEST data from Fig. 8.18. (a) ER distribution. S1 is characterized by a power law. (b) NR distribution. S1 is characterized by a double falling exponential.

of ER rejection.

8.7.2.2 Position

The event position for a MS event is calculated as the energy-weighted mean position of all vertices. The energy at each vertex is calculated by the summed S1 and S2 signals. This definition matches that used in the LUXSim energy deposition Monte Carlo work, where true energy depositions were recorded for each vertex and used to calculate MS positions. This position definition is used to select events inside the search fiducial.

8.7.3 Cuts

8.7.3.1 MS Selection

MS selection is performed simply by selecting events where the pulse finder/classifier data processing module (PFC) has designated >1 pulse in an event as an S2. An additional criterion is imposed, requiring the S2 to be >200 phe. This is done to remove large shadow event populations, and is identical to the cut used on Run 3 WIMP search data [98].

The primary concern for MS identification is the possibility of missing one or more S2s in the event, removing the event from the MS pool. An S2 could be missed in two ways. An S2 could be missed by misclassification by the pulse classifier. An S2 could also be missed by the order of operations used in LUX pulse identification. In the latter case, the first S2 would be identified, and nine other pulses would be found earlier than that S2, filling up the allotted pulse register (10 max).

The efficiency of tagging low-energy MS events should be very high, and should not significantly change the overall efficiency of the MS search. Any event in which the second S2 was missed will have a large amount of trash in the event. These events tend to be parts of electron trains, and are excluded from the analysis with no significant impact to livetime, as shown in the WIMP search analysis. This analysis therefore relies on the PFC pulse classification to identify >1 S2 within an event, in order to characterize the event as a MS.

8.7.3.2 S1 Range

An S1 range of 0–120 phe is used for the MS search. An upper bound of 120 phe is conservatively chosen based on Table 8.2, allowing >95% efficiency in catching all NR MS from the predicted neutron energy spectra. The efficiency of this cut is then taken as 95%. There is no significant efficiency loss from S1 detection threshold, as the MS spectrum has >98% of all events with 3+ phe S1 signals where detection efficiency is 100% [46].

8.7.3.3 Fiducial

The fiducial volume is chosen based on the maximum radius in which position reconstruction is thought to be reliable. The volume is defined as $R < 21$ cm, 7 cm $< Z <$ 52 cm. The Z cut excludes 2 cm of Xe around the cathode and gate grids. It is necessary to remove the Xe layers near surfaces in order to ensure that the MS population is not contaminated by coincident β-γ events.

8.7.3.4 S2/S1 Discrimination

The ER and NR predicted bands for MS events in LUX are shown in Fig. 8.18. The accuracy of the NEST band centroids, in terms of reconstruction of the observed SS ER and NR distributions in the detector, gives good confidence that the same NEST model can accurately predict the shape of the MS bands, assuming the underlying energy distributions are understood. However, it is known that the ER band width is not precisely reproduced with the current NEST model, as demonstrated by ^{3}H data. NR MS events are therefore selected by including only events that fall below the predicted NR MS band centroid. This gives a 50% selection efficiency. The selection does not rely on correctly predicting the width of the bands, and provides a strong measure of ER rejection. Note that this is conservative; if the ER width is actually much wider than expected (likely not the case, extrapolating from SS ^{3}H results), then some fraction of ER background will leak into the NR search region, raising the upper limit set on true NR background events.

8.7.3.5 Bad Area

The MS S2/S1 vs S1 distribution contains shadow events, stemming from the same sources as those seen in SS WIMP search data [98]. It is therefore reasonable to apply a similar cut to remove these events. The bad area cut from the WIMP search analysis is used, with a slight modification to better fit the observed bad vs good area spectrum. The corner at which a 10% slope is implemented is moved from 1000 phe good area (SS) to 1700 phe good area (MS). This more aggressively removes shadow events from higher populations in MS data, while still retaining >99% efficiency for detection of true MS events. This was confirmed by sampling event traces by eye from both sides of the bad area cut. The cut and data are shown in Fig. 8.20.

8.7.4 Results

8.7.4.1 Multiple Scatters in LUX Data

The reconstructed MS S2/S1 vs S1 distribution is shown in Fig. 8.21. The predicted ER and NR bands for MS events are overlaid. After application of the bad area cut, 35 events remain with S1 $<$ 120 phe in the 180 kg fiducial, which are not consistent with the raincloud above the ER band. The events are also spaced relatively uniformly across the entire 120 phe range, which is inconsistent with expectations for NR MS (see Fig. 8.19). The overall distribution is therefore consistent with ER MS. None of the events fall below the NR band centroid.

There is a significant "raincloud" of events above $\log_{10}(\mathrm{S2/S1}) = 2.5$. The raincloud

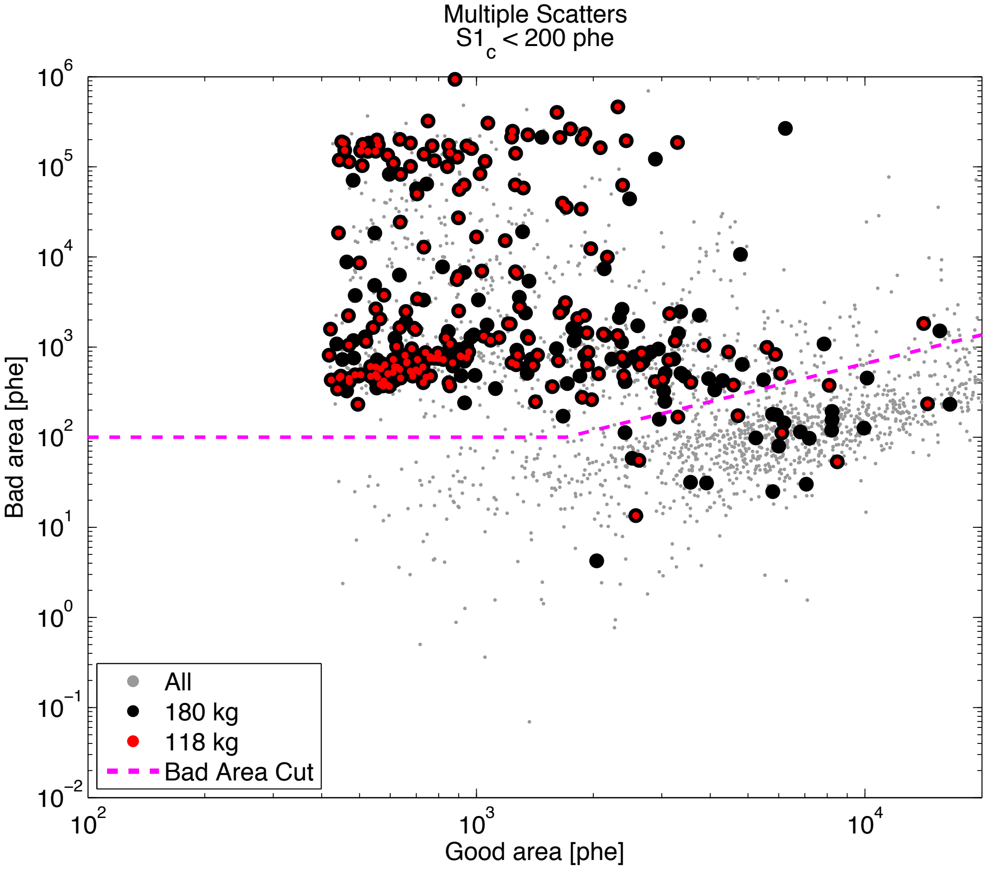

Figure 8.20: Bad vs good area for MS events with corrected S1 < 120 phe. Points are shown corresponding to all events (gray), events within the 180 kg search region (black), and events within the 118 kg WIMP search fiducial used for Run 3 (red). The bad area cut boundary used in this analysis is shown as the magenta line. The bad area cut requires events to fall below the line. The cut is defined as flat in the range 0–1700 phe good area, with a 10% slope for good area above 1700 phe.

Fiducial Volume	**Observed Events**	**UL (90% CL)**	**Search Efficiency**	**Ratio MS (180 kg) / SS (WIMP)**	**Livetime Ratio**	**NR SS UL (90% CL)**
118 kg	0	<2.3	48%	13	1 (85 d)	<0.37
100 kg	0	<2.3	48%	23	3.4 (300 d)	<0.71

Table 8.3: NR SS upper limits from observed LUX data. The 118 kg fiducial is the standard WIMP search fiducial used in Run 3 ($R < 18$ cm, 7 cm $< Z < 47$ cm). The 100 kg fiducial is defined as $R < 17$ cm, 9 cm $< Z < 47$ cm, and is used for NR background projections for Run 4. Search efficiency is combined from all cuts listed in Sec. 8.7.3. MS / SS ratio is taken from LUXSim background studies, listed in Table 8.2. Upper limits are listed at 90% CL.

events seen in Fig. 8.21 appear to be the tail of a much larger distribution with ratio in the range 3.5–7. These events are a mixture of noisy events, SS events with long S2 tails, and other anomalies inconsistent with neutron MS events in the 180 kg fiducial volume.

8.7.4.2 Single Scatter UL for Run 3 and Run 4

No scatters are observed in the search region 0–120 phe below the calculated NR band centroid. This corresponds to an upper limit of 2.3 MS events at 90% CL. The cumulative search efficiency from Sec. 8.7.3 is 48% (50% S2/S1, 95% S1 range). The resulting 90% upper limits on NR SS, using results from LUXSim background studies, is <0.37 for Run 3 and <0.71 for Run 4. The Run 4 figure is adjusted for a smaller fiducial, and 300 livedays exposure. The figures are summarized in Table 8.3. The predicted rate of NR events in 118 kg (100 kg) is nominally 0.1 (0.06) WIMP-like events per year, assuming a dominant contribution from the PMTs at 1.2 n PMT^{-1} yr^{-1}. Even with the enlarged 180 kg fiducial, statistics are insufficient for a positive measurement of neutron MS events.

8.8 Low-Energy ER Backgrounds

8.8.1 Observed Event Rates

The low-energy ER background contributions from all measured sources in the range 2–30 phe (0.9–5.3 $\mathrm{keV_{ee}}$) are listed in Table 8.4. The values for background predictions are taken from Table 5.6. The measured data use all WIMP search analysis cuts, discussed briefly in [46]

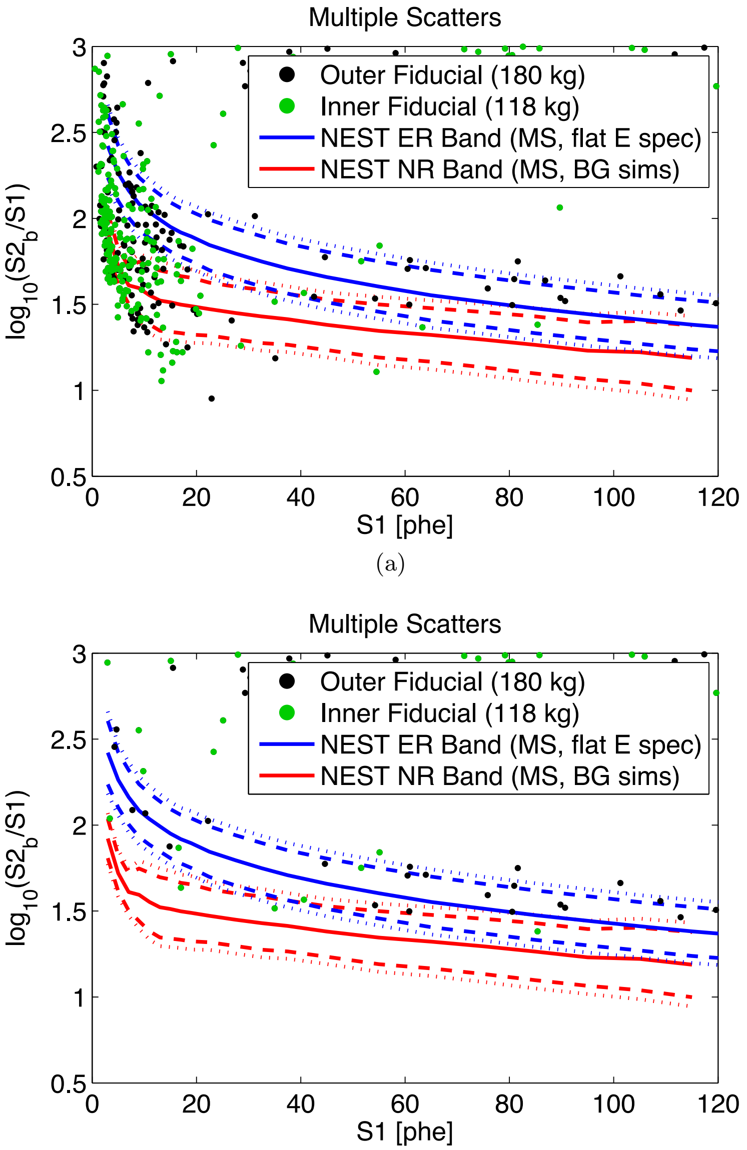

(a)

(b)

Figure 8.21: $\log_{10}$(S2/S1) vs S1 for MS events. S1 and S2 correction and position definition are given in Sec. 8.7.2. Events are shown (a) before and (b) after application of the bad area cut defined in Sec. 8.7.3.5. Overlaid are the ER (blue) and NR (red) MS bands determined from LUXSim and NEST Monte Carlo studies. The band centroids are shown as the solid lines, and band widths are shown at 1.28σ (1.65σ) with dashed (dotted) lines. The NR band centroid sets the upper bound of the neutron MS search window.

Source	**Background Rate 0.9–5.3 keV$_{ee}$ [mDRU$_{ee}$]** **118 kg**	 **100 kg**	 **50 kg**
γ	$1.8 \pm 0.2_{\text{stat}} \pm 0.3_{\text{sys}}$	$0.9 \pm 0.1_{\text{stat}} \pm 0.1_{\text{sys}}$	0.47 ± 0.1
^{127}Xe	$0.5 \pm 0.02_{\text{stat}} \pm 0.1_{\text{sys}}$	$0.32 \pm 0.02_{\text{stat}} \pm 0.07_{\text{sys}}$	0.2 ± 0.1
^{222}Rn	0.11–0.22 (0.2 expected)	0.2	0.2
^{85}Kr	$0.17 \pm 0.10_{\text{sys}}$	$0.17 \pm 0.10_{\text{sys}}$	$0.17 \pm 0.10_{\text{sys}}$
Total Predicted	$2.6 \pm 0.2_{\text{stat}} \pm 0.4_{\text{sys}}$	$1.6 \pm 0.1_{\text{stat}} \pm 0.2_{\text{sys}}$	1.0 ± 0.2
Total Obs. (Mean)	3.6 ± 0.3	2.4 ± 0.2	2.2 ± 0.3
Total Obs. (Early)	4.7 ± 0.3	3.0 ± 0.3	2.9 ± 0.5
Total Obs. (Late)	2.8 ± 0.4	1.7 ± 0.3	1.4 ± 0.3

Table 8.4: Low-energy ER background rate contributions from all sources measured in Run 3 data. Measurements and projections are averaged over the energy range 0.9–5.3 keV$_{ee}$. Rates are calculated for three fiducial volumes: 118 kg (as used in the Run 3 WIMP search result); 100 kg (projected to be used for the Run 4 one year WIMP search run); and a 50 kg inner fiducial. Data is measured from April 22–August 8 in the "mean" row. The total observed early and late rows correspond to measurements in the date range April 22–June 13 and June 14–August 8, respectively.

and detailed in [98]. Rates are given for three fiducial volumes: the 118 kg fiducial defined for Run 3; the 100 kg fiducial volume projected for use during the one year WIMP search run; and a reference inner 50 kg fiducial volume. Observed rates are reported for the first half ("early") and second half ("late") of the WIMP search run. Time variation of the backgrounds is discussed further in Sec. 8.8.3.

8.8.2 Background Distributions

The distribution of low-energy backgrounds observed in the Run 3 118 kg fiducial volume is shown in Fig. 8.22, along with predictions from the four-component background model in Table 8.4. Measured and projected backgrounds are compared in radius, height, and S1 in Fig. 8.23. The S1 distribution is calculated using NEST photon and electron distributions as a function of energy, combined with binomial and Gaussian fluctuations using measured LUX detection efficiencies. Calculation of the S1 spectrum is discussed in Sec. 5.10. The detection efficiencies used are given in Table 5.7.

The height and S1 distributions are in strong agreement with measured data. The p values calculated by KS test are 26% and 94% respectively. The projected radial distribution slope is greater than that observed in data, resulting in a p value of 0.004% for that dis-

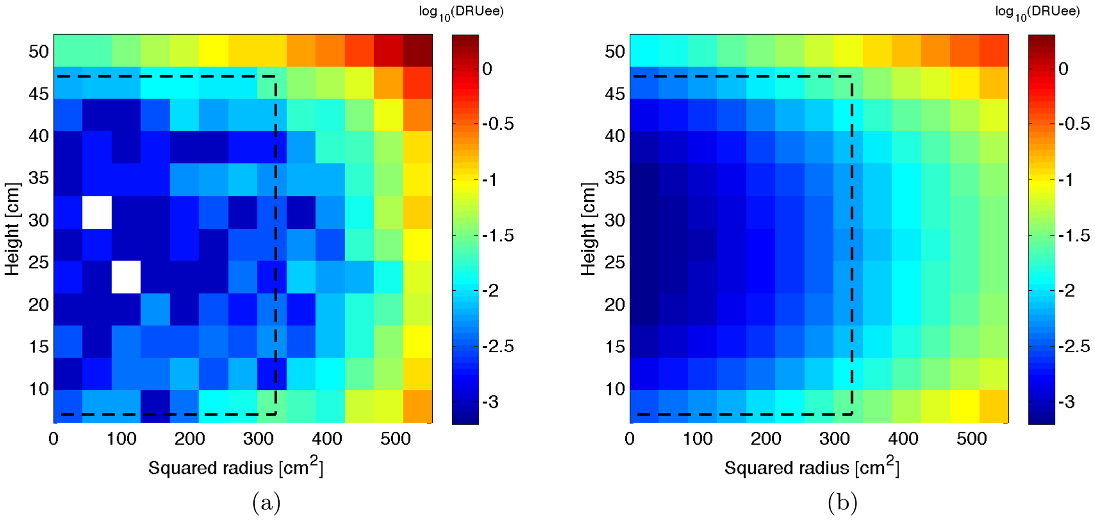

(a)

(b)

Figure 8.22: Low-energy background distributions in RZ, from (a) measured data and (b) model predictions. Rates are taken in the range 0.9–5.3 keV$_{\mathrm{ee}}$ (2–30 S1 phe). Rates are shown in units of $\log_{10}$ (DRU$_{\mathrm{ee}}$). The 118 kg fiducial volume used in the 85 day WIMP search run is shown in dashed black. The model includes low-energy background contributions from γ Compton, ^{127}Xe, ^{214}Pb, and ^{85}Kr sources. The measured data at large radii includes a significant contribution from low-energy ^{210}Pb decays at the detector walls. These decays are not included in the background model in Fig. (b).

tribution. The difference between the measured and projected radial distributions can be compensated in radial bins below 15 cm by an additional flat background component. However, the disagreement in radial distribution above 15 cm is not addressed by this addition. The observed radial distribution is brought into strong agreement with simulation if a radially varying position reconstruction systematic is assumed, where events are reconstructed towards the center with a bias varying from 0–1 cm between 0 cm $<$ R $<$ 15 cm. This scenario is unlikely in reality, as the position reconstruction systematic is well constrained from measurements of homogeneous calibration sources in the active region [98].

8.8.3 Time Variation of Low-Energy Backgrounds

The total measured background rates in the WIMP search region drop by 40% between the first and second halves of Run 3. This drop is a factor ×2.7 larger than that predicted due to ^{127}Xe alone. Given the independent constraints on the amount of ^{127}Xe in the detector, it is likely that another transient background was the source of the enhanced event rate at the beginning of the WIMP search run. The observed background rates during the latter

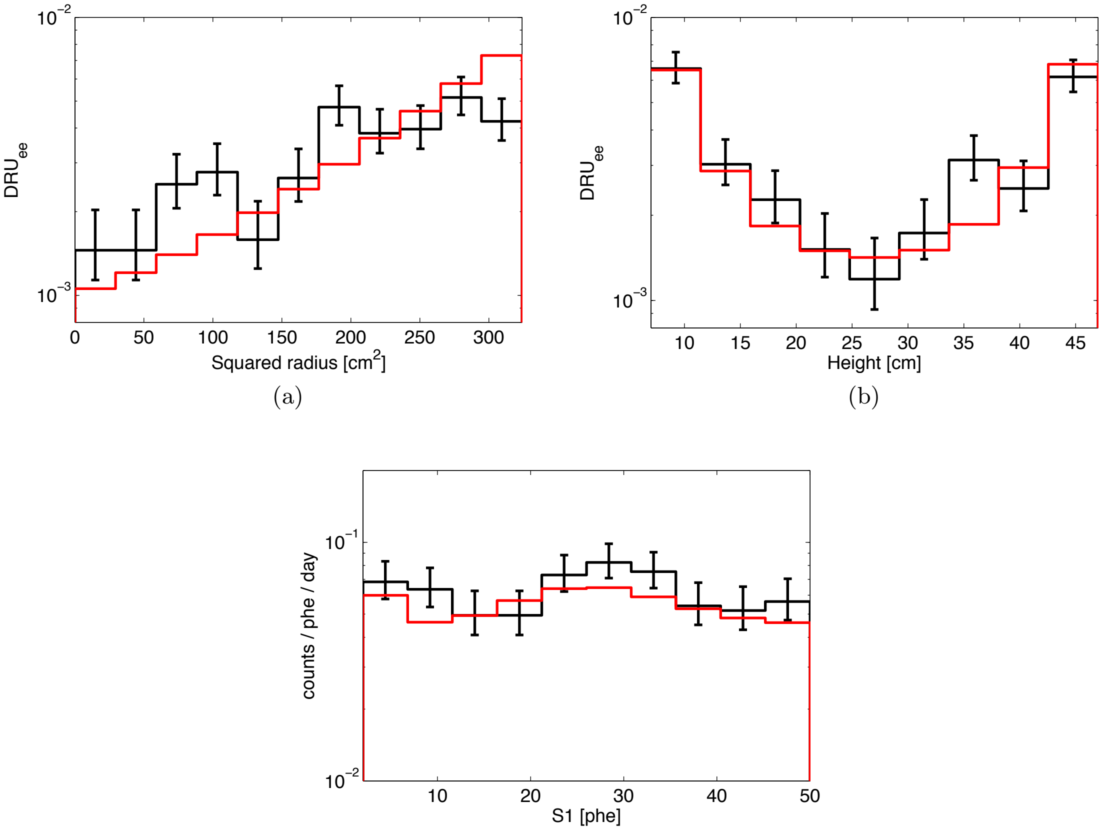

(a)

(b)

(c)

Figure 8.23: Low-energy background distributions in (a) radius, (b) height, and (c) S1, within the LUX 118 kg fiducial volume, measured over the full 85 liveday WIMP search run. Measured data are indicated by the black histogram with error bars. Simulation data are shown in red. Simulated distributions are reconstructed from high-energy background studies, and are not a fit to measured low energy data. The simulated S1 distribution folds in NEST (v0.99β) estimates of total photon yields and measured LUX light collection efficiency, detailed in Sec. 5.10.

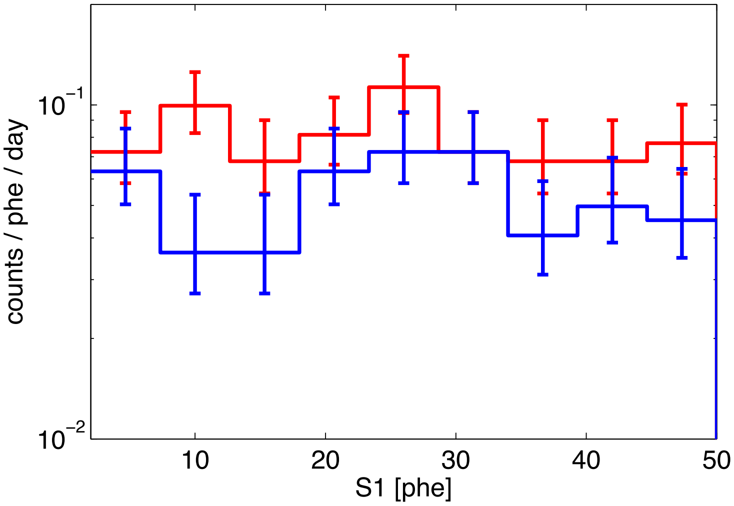

Figure 8.24: S1 distribution observed in the first half (red) and second half (blue) of the WIMP search run. Data is shown in the 118 kg fiducial volume, with WIMP search cuts applied. The first half of the run spans from April 22–June 13, and the second half spans from June 14–August 8.

half of the run are in statistical agreement with predictions based the background model presented in Ch. 5. The measured background rates during the first and second halves of the run are listed in Table 8.4. The measured early and late S1 spectra are compared in Fig. 8.24.

8.8.4 Parameterization of Low-Energy Background Model

Simulation predictions for the low-energy spatial and energy distributions were parameterized for use in the Run 3 WIMP search profile likelihood ratio (PLR) analysis. The simulation results are reported in terms of energy deposition ($\mathrm{DRU_{ee}}$). No model of S1 and S2 generation was folded in for the background models for the PLR. The PLR uses a separate treatment of S1 and S2 generation.

The functional forms of the background parameterized models are motivated by the physics of each background signal. The physical models of backgrounds from all sources are described in detail in Ch. 5. The analytic functions for the background sources are given in Table 8.5, with best-fit parameters in Table 8.6. The differences between simulation and analytic model RZ distributions are shown graphically in Fig. 8.25. The rates are in statistical agreement with the predictions from simulation results. It should be noted

Background Source	**Function**
γ + ^{214}Pb + ^{85}Kr	$A_1 \cdot \exp\left(\left(\frac{R}{\lambda_R}\right)^2 + \left(\frac{Z-Z_0}{\lambda_Z}\right)^2\right) + A_2$
^{127}Xe	$\exp\left(-t/\tau_{^{127}\mathrm{Xe}}\right) \cdot \left(A_1 \cdot \exp\left(\frac{R}{\lambda_R}\right) + A_2 \cdot \exp\left(\frac{\lvert Z-Z_0\rvert}{\lambda_Z}\right)\right)$

Table 8.5: Analytic model functions for all major low-energy ER background sources. Best-fit parameters are listed in Table 8.6. The functions are used in the WIMP search PLR analysis.

Background Source	$\mathbf{A_1}$ **[DRU$_{\mathbf{ee}}$]**	$\mathbf{A_2}$ **[DRU$_{\mathbf{ee}}$]**	$\boldsymbol{\lambda}_{\mathbf{R}}$ **[cm]**	$\boldsymbol{\lambda}_{\mathbf{Z}}$ **[cm]**	$\mathbf{Z_0}$ **[cm]**
γ + ^{214}Pb + ^{85}Kr	1.11×10^{-4}	4×10^{-4}	11.3	11.7	26.9
^{127}Xe	2×10^{-6}	3×10^{-7}	2.56	2.56	26.9

Table 8.6: Best-fit analytic model function parameters. Parameters correspond to models listed in Table 8.5. For the ^{127}Xe model, $\tau_{^{127}\mathrm{Xe}} = 52.5$ days and $t = 0$ on May 1.

that the fit to time-independent backgrounds was optimized jointly on the intrinsic and γ sources; as such, the constant offset term in the analytic model does not strictly represent the predicted contribution from ^{214}Pb and ^{85}Kr.

8.9 WIMP Search Results

The WIMP search run was conducted with 85.3 livedays of data, using a non-blind analysis. The non-blind analysis allowed for the development of a minimal set of data quality cuts, as well as a full understanding of the detector background model. LUX observed a low-energy signal consistent with the projected ER background outlined in this chapter and in Ch. 5. No discovery is claimed, and a 90% exclusion curve is produced in $(m_\chi,\ \sigma_\chi)$ space as discussed in Sec. 1.4.3. The final WIMP search data is shown in (S1,S2/S1) space in Fig. 8.26.

The exclusion limit is calculated using a PLR test statistic. The test statistic uses the analytic model of the distribution of backgrounds in radius and height in Sec. 8.8.4, as well as measured and projected distributions in S1 and S2/S1 space for ER and NR signatures. The normalizations on the γ Compton, ^{127}Xe, and flat-energy background models input to the PLR are allowed to float with 30% error, to optimize the match between the background

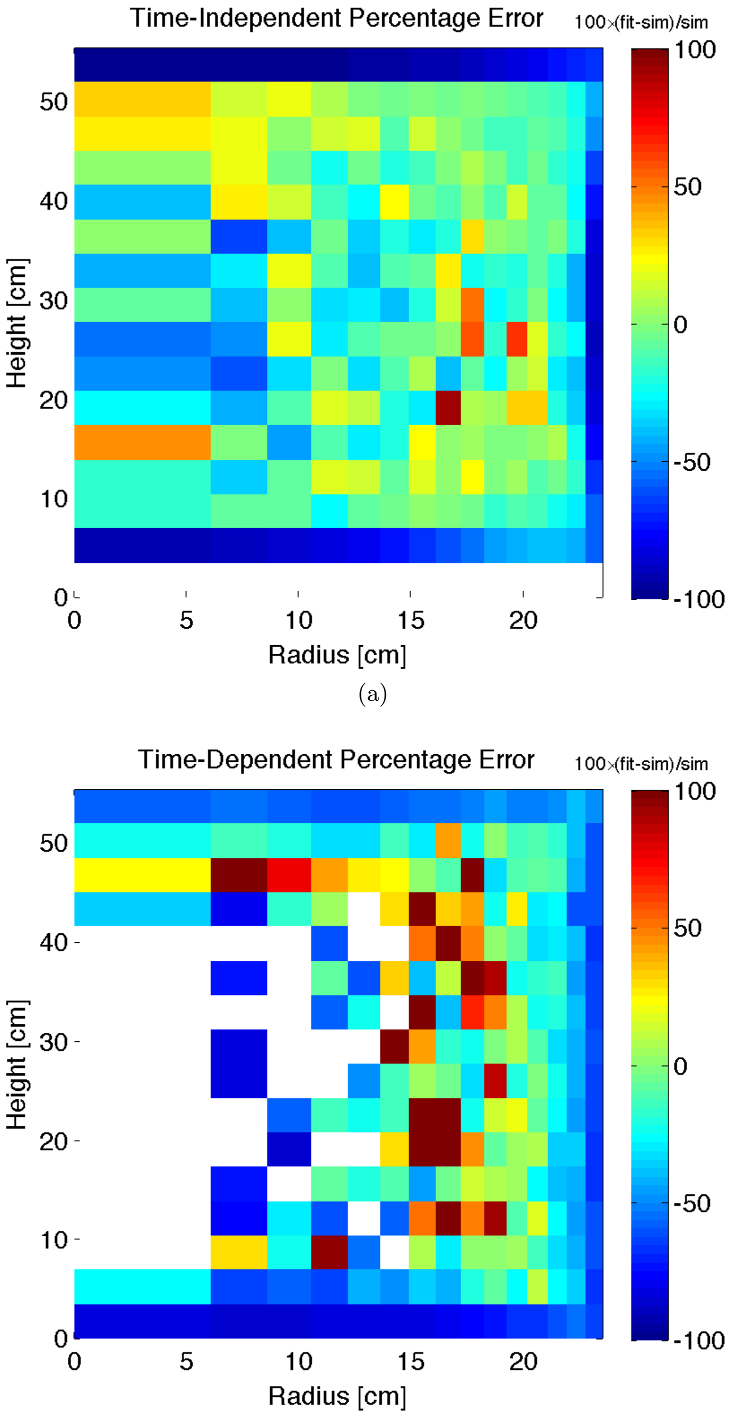

(a)

(b)

Figure 8.25: Percent variation per bin between simulated low-energy ER background event rates and analytic best-fit models for (a) time-independent (γ Compton + ^{214}Pb + ^{85}Kr) and (b) time-dependent (^{127}Xe) models. White bins have 0 simulation counts. Analytic functions are listed in Table 8.5.

model and the observed low-energy data. The resulting WIMP search limit is shown in Fig. 8.27. Greater detail on the PLR analysis and WIMP search data treatment will be covered in upcoming LUX publications, as well as [98].

LUX provides a very strong constraint on the low-mass end of the WIMP parameter space, in clear tension with potential signals reported by some dark matter experiments. LUX is not the first experiment to rule out these signal claims with 90% confidence; however, LUX is able to make such claims using very conservative signal models. In particular, it is assumed that the light yield from any dark matter signals below the 3.4 keV_{nr} threshold is zero, ensuring that LUX does not take advantage of assumptions of up-fluctuations from the low-energy portion of the WIMP scatter spectrum. For this reason, in addition to the overall cleanliness of the data, simplicity of the data quality cuts used, and the extremely low background, LUX has delivered an exclusion curve for WIMP interaction which is extremely robust. The LUX exclusion curve is expected to provide the most stringent constraint of any experiment on WIMP dark matter properties, until the curve is superceded by the results of the one year LUX WIMP search run in 2015.

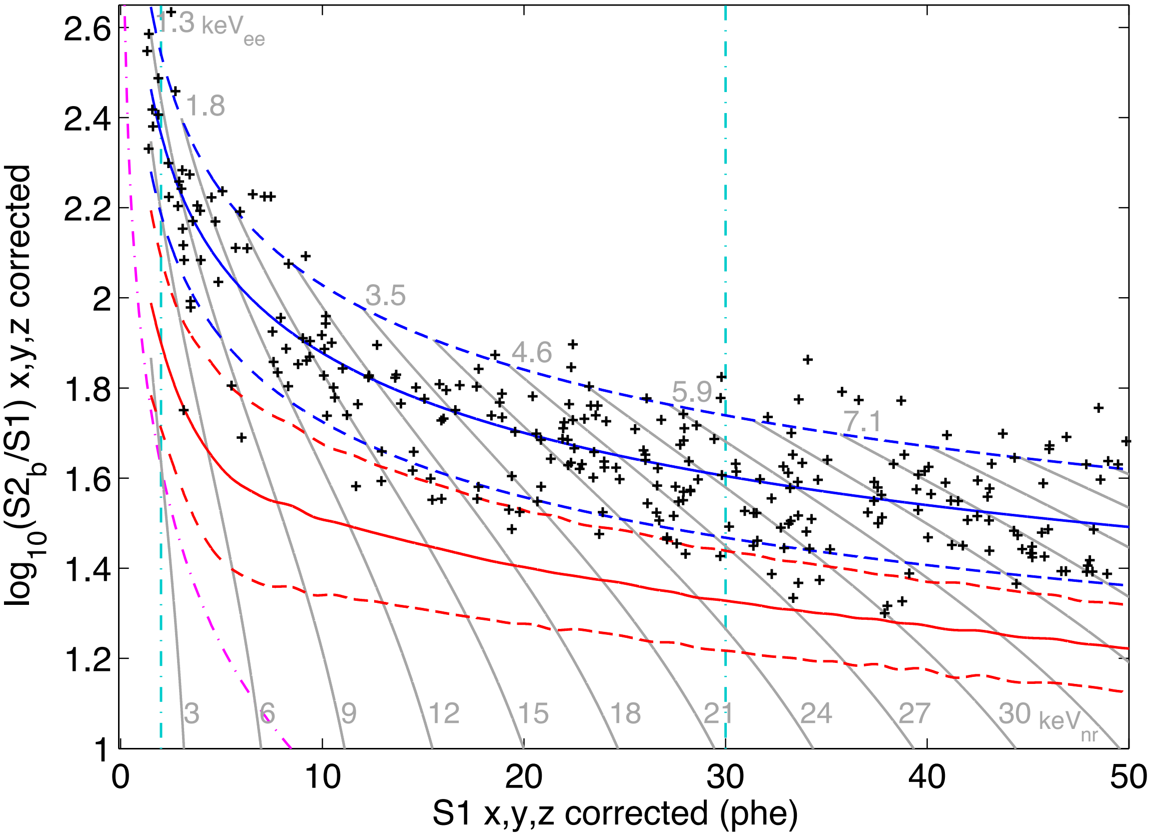

Figure 8.26: WIMP search data from the LUX Run 3 85 liveday run. 160 events are found after data quality, SS and fiducial cuts in the range 2–30 phe. Overlaid are the measured ER band from ^{3}H calibration (blue), and the projected NR band from LUXSim / NEST (red), confirmed using external AmBe / ^{252}Cf calibration. Constant-energy contours are overlaid in gray, giving keV$_{ee}$ energies above the ER band and keV$_{nr}$ energies below the NR band. Plot taken from [46].

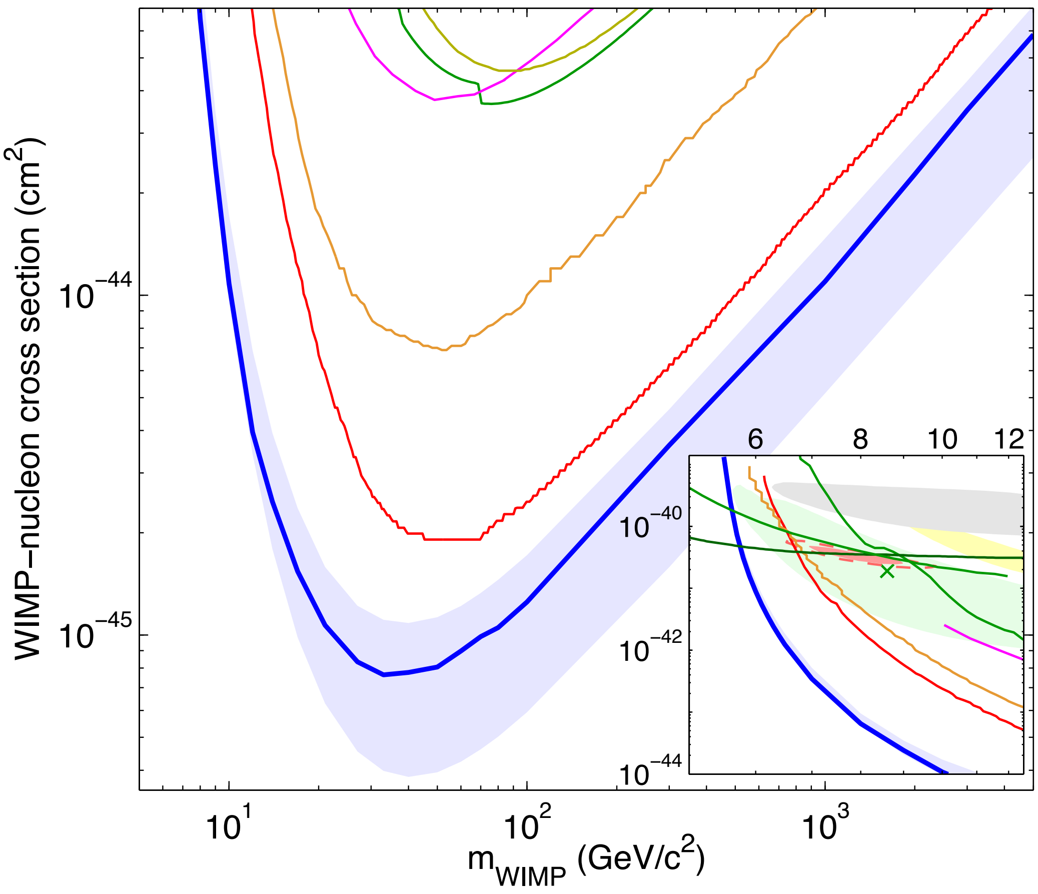

Figure 8.27: WIMP search 90% exclusion limit set by the LUX Run 3 85 liveday run, in comparison with previous experimental exclusion limits and allowed regions [46]. The LUX limit is shown as the dark blue curve. The $\pm 1\sigma$ light blue band denotes the expected region for the actual curve, based on repeated trials of the PLR analysis using the parameterized background and signal models. 90% exclusion curves are also shown for XENON100 100 day [54] (orange) and 225 day [49] (red) results, ZEPLIN-III [55] (magenta), CDMS II [56] (green), and Edelweiss II [57] (yellow). The inset shows allowed contours from DAMA/LIBRA [58, 59] (gray), CRESST II [60] (yellow), CDMS II Si detectors [61] (green, centroid denoted by the x), and CoGeNT annual modulation signals [62] (red). Plot taken from [46].

Bibliography

[1] B. Ryden, *Introduction to Cosmology.* Benjamin Cummings, October, 2002. [link].

[2] P. A. R. Ade, *et al.*, "Planck 2013 results. I. Overview of products and scientific results,"*ArXiv e-prints* (Mar., 2013) . arXiv:1303.5062 [astro-ph.CO].

[3] C. Frenk and S. White, "Dark matter and cosmic structure," *Annalen der Physik* **524** (2012) no. 9-10, 507–534. [link].

[4] P. A. R. Ade, *et al.*, "Planck 2013 results. XVI. Cosmological parameters,"*ArXiv e-prints* (Mar., 2013) . arXiv:1303.5076 [astro-ph.CO].

[5] D. Samtleben, S. Staggs, and B. Winstein, "The Cosmic Microwave Background for Pedestrians: A Review for Particle and Nuclear Physicists," *Annual Review of Nuclear and Particle Science* **57** (2007) no. 1, 245–283. http://www.annualreviews.org/doi/pdf/10.1146/annurev.nucl.54.070103.181232.

[6] K. Nakamura and Particle Data Group, "Review of Particle Physics," *Journal of Physics G: Nuclear and Particle Physics* **37** (2010) no. 7A, 075021. [link].

[7] R. Massey, T. Kitching, and J. Richard, "The dark matter of gravitational lensing," *Reports on Progress in Physics* **73** (2010) no. 8, 086901. [link].

[8] A. G. Riess, *et al.*, "New Hubble Space Telescope Discoveries of Type Ia Supernovae at $z \geq 1$: Narrowing Constraints on the Early Behavior of Dark Energy," *The Astrophysical Journal* **659** (2007) no. 1, 98. [link].

[9] D. J. Eisenstein, *et al.*, "Detection of the Baryon Acoustic Peak in the Large-Scale Correlation Function of SDSS Luminous Red Galaxies," *The Astrophysical Journal* **633** (2005) no. 2, 560–574. [link].

[10] F. Zwicky, "Die Rotreshiebung von extragalaktishen Nebeln," *Helv. Phys. Acta* **6** (1933) 110–127.

[11] F. Zwicky, "On the Masses of Nebulae and of Clusters of Nebulae,"*ApJ* **86** (Oct., 1937) 217. [link].

[12] S. van den Bergh, "The Early History of Dark Matter,"*Publications of the Astronomical Society of the Pacific* **111** (June, 1999) 657–660. astro-ph/9904251.

[13] V. C. Rubin and W. K. J. Ford, "Rotation of the Andromeda Nebula from a Spectroscopic Survey of Emission Regions,"*ApJ* **159** (Feb., 1970) 379. [link].

[14] K. G. Begeman, A. H. Broeils, and R. H. Sanders, "Extended rotation curves of spiral galaxies - Dark haloes and modified dynamics,"*Monthly Notices of the Royal Astronomical Society* **249** (Apr., 1991) 523–537.

[15] E. Pointecouteau and J. Silk, "New constraints on modified Newtonian dynamics from galaxy clusters,"*Monthly Notices of the Royal Astronomical Society* **364** (Dec., 2005) 654–658. astro-ph/0505017.

[16] R. Schodel, *et al.*, "A star in a 15.2-year orbit around the supermassive black hole at the centre of the Milky Way,"*Nature* **419** (Oct., 2002) 694–696. [link].

[17] E. I. Gates, G. Gyuk, and M. S. Turner, "The Local Halo Density,"*ApJL* **449** (Aug., 1995) L123+. astro-ph/9505039.

[18] G. Bertone, D. Hooper, and J. Silk, "Particle dark matter: evidence, candidates and constraints," *Physics Reports* **405** (2005) no. 5-6, 279 – 390. [link].

[19] M. Kamionkowski and S. M. Koushiappas, "Galactic substructure and direct detection of dark matter,"*Physical Review D (Particles and Fields)* **77** (May, 2008) 103509. arXiv:0801.3269.

[20] R. Catena and P. Ullio, “A novel determination of the local dark matter density,”*Journal of Cosmology and Astroparticle Physics* **8** (Aug., 2010) 4. `arXiv:0907.0018 [astro-ph.CO]`.

[21] S. Garbari, *et al.*, “A new determination of the local dark matter density from the kinematics of K dwarfs,”*Monthly Notices of the Royal Astronomical Society* **425** (Sept., 2012) 1445–1458. `arXiv:1206.0015 [astro-ph.GA]`.

[22] M. Brhlik and L. Roszkowski, “{WIMP} velocity impact on direct dark matter searches,” *Physics Letters B* **464** (1999) no. 3-4, 303 – 310. `[link]`.

[23] K. G. Begeman, “H I rotation curves of spiral galaxies. I - NGC 3198,”*Astronomy and Astrophysics* **223** (Oct., 1989) 47–60.

[24] D. Clowe, *et al.*, “A Direct Empirical Proof of the Existence of Dark Matter,”*Astrophys. J.* **648** (Sept., 2006) L109–L113. `astro-ph/0608407`.

[25] J. R. Brownstein and J. W. Moffat, “The Bullet Cluster 1E0657-558 evidence shows modified gravity in the absence of dark matter,” *Monthly Notices of the Royal Astronomical Society* **382** (2007) no. 1, 29–47. `http://mnras.oxfordjournals.org/content/382/1/29.full.pdf+html`.

[26] J. L. Feng, “Dark Matter Candidates from Particle Physics and Methods of Detection,”*Annual Review of Astronomy and Astrophysics* **48** (Sept., 2010) 495–545. `arXiv:1003.0904 [astro-ph.CO]`.

[27] R. J. Gaitskell, “Direct Detection of Dark Matter,” *Ann. Rev. Nucl. Part. Sci.* **54** (2004) 315–359. `[link]`.

[28] **The Fermi-LAT Collaboration** Collaboration, M. Ackermann, *et al.*, “Constraining Dark Matter Models from a Combined Analysis of Milky Way Satellites with the Fermi Large Area Telescope,”*Phys. Rev. Lett.* **107** (Dec, 2011) 241302. `[link]`.

[29] A. Geringer-Sameth and S. M. Koushiappas, “Exclusion of Canonical Weakly Interacting Massive Particles by Joint Analysis of Milky Way Dwarf Galaxies with

Data from the Fermi Gamma-Ray Space Telescope,"*Phys. Rev. Lett.* **107** (Dec, 2011) 241303. [link].

[30] M. Ackermann, *et al.*, "Constraints on the Galactic Halo Dark Matter from Fermi-LAT Diffuse Measurements," *The Astrophysical Journal* **761** (2012) no. 2, 91. [link].

[31] M. Ackermann, *et al.*, "Dark Matter Constraints from Observations of 25 Milky Way Satellite Galaxies with the Fermi Large Area Telescope,"*ArXiv e-prints* (Oct., 2013) . arXiv:1310.0828 [astro-ph.HE].

[32] M. Aguilar, *et al.*, "First Result from the Alpha Magnetic Spectrometer on the International Space Station: Precision Measurement of the Positron Fraction in Primary Cosmic Rays of 0.5–350 GeV,"*Phys. Rev. Lett.* **110** (Apr, 2013) 141102. [link].

[33] K. Blum, B. Katz, and E. Waxman, "AMS-02 Results Support the Secondary Origin of Cosmic Ray Positrons,"*Phys. Rev. Lett.* **111** (Nov, 2013) 211101. [link].

[34] D. Grasso, *et al.*, "On possible interpretations of the high energy electron-positron spectrum measured by the Fermi Large Area Telescope," *Astroparticle Physics* **32** (2009) no. 2, 140 – 151. [link].

[35] D. Hooper and T. Linden, "Origin of the gamma rays from the Galactic Center,"*Phys. Rev. D* **84** (Dec., 2011) 123005. arXiv:1110.0006 [astro-ph.HE].

[36] D. Hooper and L. Goodenough, "Dark matter annihilation in the Galactic Center as seen by the Fermi Gamma Ray Space Telescope,"*Phys. Lett. B* **697** (Mar., 2011) 412–428. arXiv:1010.2752 [hep-ph].

[37] D. Hooper and T. Linden, "Are lines from unassociated gamma-ray sources evidence for dark matter annihilation?,"*Phys. Rev. D* **86** (Oct., 2012) 083532. arXiv:1208.0828 [astro-ph.HE].

[38] M. Su and D. P. Finkbeiner, "Strong Evidence for Gamma-ray Line Emission from the Inner Galaxy,"*ArXiv e-prints* (June, 2012) . arXiv:1206.1616 [astro-ph.HE].

[39] C. Weniger, “Tentative observation of a gamma-ray line at the Fermi LAT,” in *American Institute of Physics Conference Series*, F. A. Aharonian, W. Hofmann, and F. M. Rieger, eds., vol. 1505 of *American Institute of Physics Conference Series*, pp. 470–473. Dec., 2012. `arXiv:1210.3013 [astro-ph.HE]`.

[40] K. N. Abazajian and M. Kaplinghat, “Detection of a gamma-ray source in the Galactic Center consistent with extended emission from dark matter annihilation and concentrated astrophysical emission,”*Phys. Rev. D* **86** (Oct., 2012) 083511. `arXiv:1207.6047 [astro-ph.HE]`.

[41] Y. Bai, P. J. Fox, and R. Harnik, “The Tevatron at the frontier of dark matter direct detection,”*Journal of High Energy Physics* **12** (Dec., 2010) 48. `arXiv:1005.3797 [hep-ph]`.

[42] S. Chatrchyan, *et al.*, “Search for Dark Matter and Large Extra Dimensions in *pp* Collisions Yielding a Photon and Missing Transverse Energy,”*Phys. Rev. Lett.* **108** (Jun, 2012) 261803. `[link]`.

[43] J. D. Lewin and P. F. Smith, “Review of mathematics, numerical factors, and corrections for dark matter experiments based on elastic nuclear recoil,” *Astroparticle Physics* **6** (1996) no. 1, 87 – 112. `[link]`.

[44] J. Engel, “Nuclear form factors for the scattering of weakly interacting massive particles,” *Physics Letters B* **264** (1991) no. 1-2, 114 – 119. `[link]`.

[45] G. Duda, A. Kemper, and P. Gondolo, “Model-independent form factors for spin-independent neutralino-nucleon scattering from elastic electron scattering data,” *Journal of Cosmology and Astroparticle Physics* **2007** (2007) no. 04, 012. `[link]`.

[46] D. S. Akerib, *et al.*, “First results from the LUX dark matter experiment at the Sanford Underground Research Facility,”*ArXiv e-prints* (Oct., 2013) . `arXiv:1310.8214 [astro-ph.CO]`.

[47] **XENON** Collaboration, J. Angle *et al.*, “First Results from the XENON10 Dark Matter Experiment at the Gran Sasso National Laboratory,” *Phys. Rev. Lett.* **100** (2008) 021303. `arXiv:0706.0039 [astro-ph]`.

[48] H. Araújo, “Performance results from the first science run of ZEPLIN-III,” *Nuclear Instruments and Methods in Physics Research Section A: Accelerators, Spectrometers, Detectors and Associated Equipment* **604** (2009) no. 1-2, 41 – 44, PSD8 - Proceedings of the 8th International Conference on Position Sensitive Detectors. `[link]`.

[49] E. Aprile, *et al.*, “Dark Matter Results from 225 Live Days of XENON100 Data,”*Physical Review Letters* **109** (Nov., 2012) 181301. `arXiv:1207.5988 [astro-ph.CO]`.

[50] R. Bernabei, *et al.*, “Dark Matter Investigation by DAMA at Gran Sasso,” *International Journal of Modern Physics A* **28** (2013) no. 16, 1330022. `http://www.worldscientific.com/doi/pdf/10.1142/S0217751X13300226`.

[51] C. E. Aalseth, *et al.*, “Search for an Annual Modulation in a p-Type Point Contact Germanium Dark Matter Detector,”*Phys. Rev. Lett.* **107** (Sep, 2011) 141301. `[link]`.

[52] **The BayesFITS Group** Collaboration, A. Fowlie, *et al.*, “Constrained MSSM favoring new territories: The impact of new LHC limits and a 125 GeV Higgs boson,”*Phys. Rev. D* **86** (Oct, 2012) 075010. `[link]`.

[53] J. Cao, *et al.*, “A light SUSY dark matter after CDMS-II, LUX and LHC Higgs data,”*ArXiv e-prints* (Nov., 2013) . `arXiv:1311.0678 [hep-ph]`.

[54] E. Aprile, *et al.*, “Dark Matter Results from 100 Live Days of XENON100 Data,”*Physical Review Letters* **107** (Sept., 2011) 131302. `arXiv:1104.2549 [astro-ph.CO]`.

[55] D. Akimov, *et al.*, “WIMP-nucleon cross-section results from the second science run of ZEPLIN-III,” *Physics Letters B* **709** (2012) no. 1-2, 14 – 20. `[link]`.

[56] Z. Ahmed, *et al.*, “Dark Matter Search Results from the CDMS II Experiment,”*Science* **327** (Mar., 2010) 1619–. `arXiv:0912.3592 [astro-ph.CO]`.

[57] E. Armengaud, *et al.*, “Final results of the EDELWEISS-II {WIMP} search using a 4-kg array of cryogenic germanium detectors with interleaved electrodes,” *Physics Letters B* **702** (2011) no. 5, 329 – 335. `[link]`.

[58] R. Bernabei, *et al.*, “First results from DAMA/LIBRA and the combined results with DAMA/NaI,” *European Physical Journal C* **56** (2008) 333. `arXiv:0804.2741`.

[59] C. Savage, *et al.*, “Compatibility of DAMA/LIBRA dark matter detection with other searches,” *Journal of Cosmology and Astroparticle Physics* **2009** (2009) no. 04, 010. `[link]`.

[60] G. Angloher, *et al.*, “Results from 730 kg days of the CRESST-II Dark Matter search,”*European Physical Journal C* **72** (Apr., 2012) 1971. `arXiv:1109.0702 [astro-ph.CO]`.

[61] R. Agnese, *et al.*, “Silicon Detector Dark Matter Results from the Final Exposure of CDMS II,”*ArXiv e-prints* (Apr., 2013) . `arXiv:1304.4279 [hep-ex]`.

[62] C. E. Aalseth, *et al.*, “CoGeNT: A search for low-mass dark matter using p-type point contact germanium detectors,”*Phys. Rev. D* **88** (Jul, 2013) 012002. `[link]`.

[63] R. Gaitskell, V. Mandic, and J. Filippini, “DMTools Dark Matter Results Plotter.” http://dmtools.brown.edu. `[link]`.

[64] The SNO Collaboration, “The Sudbury Neutrino Observatory,” *NIM* **A449** (2000) 172–207.

[65] K. Abe, *et al.*, “Solar neutrino results in Super-Kamiokande-III,”*Phys. Rev. D* **83** (Mar, 2011) 052010. `[link]`.

[66] CMS Collaboration, “Energy calibration and resolution of the CMS electromagnetic calorimeter in pp collisions at $\sqrt{s} = 7$ TeV,” *Journal of Instrumentation* **8** (2013) no. 09, P09009. `[link]`.

[67] The Borexino Collaboration, “First real time detection of Be7 solar neutrinos by Borexino,” *Physics Letters B* **658** (2008) 101. `[link]`.

[68] Borexino Collaboration, *et al.*, “Final results of Borexino Phase-I on low energy solar neutrino spectroscopy,”*ArXiv e-prints* (Aug., 2013) . `arXiv:1308.0443 [hep-ex]`.

[69] V. Lepeltier, “Review on TPC’s,” *Journal of Physics: Conference Series* **65** (2007) no. 1, 012001. `[link]`.

[70] Z. Ahmed, *et al.*, “Results from a Low-Energy Analysis of the CDMS II Germanium Data,”*Physical Review Letters* **106** (Apr., 2011) 131302. `arXiv:1011.2482 [astro-ph.CO]`.

[71] L. de Viveiros, *Optimization of Signal versus Background in Liquid Xe Detectors used for Dark Matter Direct Detection Experiments*. PhD thesis, Brown University, May, 2010.

[72] E. Aprile, *et al.*, “Study of the electromagnetic background in the XENON100 experiment,”*Physical Review D: Particles and Fields* **83** (Apr., 2011) 082001. `arXiv:1101.3866 [astro-ph.IM]`.

[73] N. Ackerman, *et al.*, “Observation of Two-Neutrino Double-Beta Decay in ^{136}Xe with the EXO-200 Detector,”*Phys. Rev. Lett.* **107** (Nov, 2011) 212501. `[link]`.

[74] The GERDA collaboration, *et al.*, “The background in the neutrinoless double beta decay experiment GERDA,”*ArXiv e-prints* (June, 2013) . `arXiv:1306.5084 [physics.ins-det]`.

[75] **SNO Collaboration** Collaboration, B. Aharmim, *et al.*, “Low-energy-threshold analysis of the Phase I and Phase II data sets of the Sudbury Neutrino Observatory,”*Phys. Rev. C* **81** (May, 2010) 055504. `[link]`.

[76] V. Gehman, “LZ Internal Note,” tech. rep., Lawrence Berkeley Laboratory, 2013.

[77] K. Arisaka, *et al.*, "XAX: A multi-ton, multi-target detection system for dark matter, double beta decay and pp solar neutrinos," *Astroparticle Physics* **31** (2009) no. 2, 63 – 74. [link].

[78] L. Ekstrom and R. Firestone, "WWW Table of Radioactive Isotopes (version 2/28/99)," January, 2013. [link].

[79] H. Back, *et al.*, "Depleted Argon from Underground Sources," *Physics Procedia* **37** (2012) no. 0, 1105 – 1112, Proceedings of the 2nd International Conference on Technology and Instrumentation in Particle Physics (TIPP 2011). [link].

[80] D. Akerib, *et al.*, "The Large Underground Xenon (LUX) experiment," *Nuclear Instruments and Methods in Physics Research Section A: Accelerators, Spectrometers, Detectors and Associated Equipment* **704** (2013) no. 0, 111 – 126. [link].

[81] E. Aprile, *et al.*, *Noble Gas Detectors*, vol. 362. Wiley-VCH, December, 2006. ISBN-10: 3527405976 ISBN-13: 978-3527405978.

[82] A. Baldini, *et al.*, "Absorption of scintillation light in a 100 l liquid xenon gamma-ray detector and expected detector performance," *Nuclear Instruments and Methods in Physics Research Section A: Accelerators, Spectrometers, Detectors and Associated Equipment* **545** (2005) no. 3, 753 – 764. [link].

[83] G. M. Seidel, R. E. Lanou, and W. Yao, "Rayleigh scattering in rare-gas liquids," *Nuclear Instruments and Methods in Physics Research Section A: Accelerators, Spectrometers, Detectors and Associated Equipment* **489** (2002) no. 1-3, 189 – 194. [link].

[84] N. Ishida, *et al.*, "Attenuation length measurements of scintillation light in liquid rare gases and their mixtures using an improved reflection suppresser," *Nuclear Instruments and Methods in Physics Research Section A: Accelerators, Spectrometers, Detectors and Associated Equipment* **384** (1997) no. 2-3, 380 – 386. [link].

[85] B. Jordan and E. Wright, “Xenon as an Anesthetic Agent,”*American Association of Nurse Anesthetists* **78** (October, 2010) 387–392.

[86] NASA Glenn Research Center, “Innovative Engines,” March, 1999. `[link]`.

[87] M. Berger, *et al.*, “XCOM: Photon Cross Sections Database,” December, 2011. `[link]`.

[88] P. Sorensen and C. E. Dahl, “Nuclear recoil energy scale in liquid xenon with application to the direct detection of dark matter,” *Phys.Rev.* **D83** (2011) 063501. `arXiv:1101.6080 [astro-ph.IM]`.

[89] C. E. Dahl, *The physics of background discrimination in liquid xenon, and first results from Xenon10 in the hunt for WIMP dark matter.* PhD thesis, Princeton University, September, 2009.

[90] M. Szydagis, *et al.*, “NEST: a comprehensive model for scintillation yield in liquid xenon,” *Journal of Instrumentation* **6** (2011) no. 10, P10002. `[link]`.

[91] M. Szydagis, *et al.*, “Enhancement of NEST Capabilities for Simulating Low-Energy Recoils in Liquid Xenon,”*ArXiv e-prints* (July, 2013) . `arXiv:1307.6601 [physics.ins-det]`.

[92] P. Sorensen *et al.*, “The scintillation and ionization yield of liquid xenon for nuclear recoils,” *Nucl. Instrum. Meth.* **A601** (2009) 339–346. `arXiv:0807.0459 [astro-ph]`.

[93] M. Horn, *et al.*, “Nuclear recoil scintillation and ionisation yields in liquid xenon from ZEPLIN-III data,” *Physics Letters B* **705** (2011) no. 5, 471 – 476. `[link]`.

[94] C. Faham, *Prototype, Surface Commissioning and Photomultiplier Tube Characterization of the Large Underground Xenon (LUX) Direct Dark Matter Search Experiment.* PhD thesis, Brown University, August, 2013.

[95] C. M. B. Monteiro, *et al.*, “Secondary scintillation yield in pure xenon,” *Journal of Instrumentation* **2** (2007) no. 05, P05001. `[link]`.

[96] M. Szydagis, "Private communication.".

[97] A. I. Bolozdynya, "Two-phase emission detectors and their applications," *Nuclear Instruments and Methods in Physics Research Section A: Accelerators, Spectrometers, Detectors and Associated Equipment* **422** (1999) no. 1-3, 314 – 320. [link].

[98] J. Chapman. PhD thesis, Brown University, 2014.

[99] L. W. Kastens, *et al.*, "A 83mKr source for Use in Low-Background Liquid Xenon Time Projection Chambers," *Journal of Instrumentation* **5** (2010) no. 05, P05006. [link].

[100] A. Dobi, *et al.*, "Study of a zirconium getter for purification of xenon gas," *Nuclear Instruments and Methods in Physics Research Section A: Accelerators, Spectrometers, Detectors and Associated Equipment* **620** (2010) no. 2-3, 594 – 598. [link].

[101] "Nitrogen Gas Purifier Overview," September, 2013. [link].

[102] D. Akerib, *et al.*, "Data acquisition and readout system for the {LUX} dark matter experiment," *Nuclear Instruments and Methods in Physics Research Section A: Accelerators, Spectrometers, Detectors and Associated Equipment* **668** (2012) no. 0, 1 – 8. [link].

[103] Brown University, "Center for Computation & Visualization," 2013. [link].

[104] V. Solovov, *et al.*, "Position Reconstruction in a Dual Phase Xenon Scintillation Detector," *IEEE Trans.Nucl.Sci.* **59** (2012) 3286–3293. arXiv:1112.1481 [physics.ins-det].

[105] D. Akerib, *et al.*, "The {LUX} prototype detector: Heat exchanger development," *Nuclear Instruments and Methods in Physics Research Section A: Accelerators, Spectrometers, Detectors and Associated Equipment* **709** (2013) no. 0, 29 – 36. [link].

[106] D. Akerib, *et al.*, “Technical results from the surface run of the LUX dark matter experiment,” *Astroparticle Physics* **45** (2013) no. 0, 34 – 43. `[link]`.

[107] B. T. Cleveland, *et al.*, “Measurement of the Solar Electron Neutrino Flux with the Homestake Chlorine Detector,”*Astrophysical Journal* **496** (Mar., 1998) 505. `[link]`.

[108] S. Mitchell, *Nuggets to Neutrinos: The Homestake Story.* Xlibris Corporation, 2010. `[link]`.

[109] D.-M. Mei and A. Hime, “Muon-induced background study for underground laboratories,” *Physical Review D (Particles and Fields)* **73** (2006) no. 5, 053004. `[link]`.

[110] LUX Collaboration, “Construction of the LUX Dark Matter Experiment at the Sanford Underground Science and Engineering Laboratory,” July, 2007.

[111] A. Baldini, *et al.*, “Liquid xenon scintillation calorimetry and Xe optical properties,” *Dielectrics and Electrical Insulation, IEEE Transactions on* **13** (2006) no. 3, 547–555. `[link]`.

[112] E. Aprile, *et al.*, “Design and performance of the XENON10 dark matter experiment,” *Astroparticle Physics* **34** (2011) no. 9, 679 – 698. `[link]`.

[113] C. Silva, *Study of the Reflectance Distributions of Fluoropolymers and Other Rough Surfaces with Interest to Scintillation Detectors.* PhD thesis, Universidade de Coimbra, 2009.

[114] C. Silva, *et al.*, “A model of the reflection distribution in the vacuum ultra violet region,” *Nuclear Instruments and Methods in Physics Research Section A: Accelerators, Spectrometers, Detectors and Associated Equipment* **619** (2010) no. 1-3, 59–62. `[link]`.

[115] S. Agostinelli, *et al.*, “Geant4-a simulation toolkit,” *Nuclear Instruments and Methods in Physics Research Section A: Accelerators, Spectrometers, Detectors and Associated Equipment* **506** (2003) no. 3, 250 – 303. `[link]`.

[116] S. Bricola, *et al.*, "Noble-gas liquid detectors: measurement of light diffusion and reflectivity on commonly adopted inner surface materials," *Nuclear Physics B - Proceedings Supplements* **172** (2007) no. 0, 260 – 262. [link].

[117] R. Gomez, "Characterization of the Xenon-10 Dark Matter Detector with Regard to Electric Field and Light Response," Master's thesis, Rice University, 2007.

[118] V. N. Solovov, *et al.*, "Measurement of the refractive index and attenuation length of liquid xenon for its scintillation light," *Nuclear Instruments and Methods in Physics Research Section A: Accelerators, Spectrometers, Detectors and Associated Equipment* **516** (2004) no. 2-3, 462 – 474. [link].

[119] A. Siegman, *Lasers*. University Science Books, 1986.

[120] I. Roberts and E. G. Wilson, "The intrinsic photoconductivity of liquid zenon," *Journal of Physics C: Solid State Physics* **6** (1973) no. 13, 2169. [link].

[121] Hamamatsu Photonics Co., "PMT Handbook.".

[122] "Quartz Glass for Optics: Data and Properties," December, 2009. [link].

[123] P. Sorensen, *A Position-Sensitive Liquid Xenon Time-Projection Chamber for Direct Detection of Dark Matter: The XENON10 Experiment*. PhD thesis, Brown University, July, 2008.

[124] Hamamatsu Photonics K.K., "R550 Datasheet," tech. rep., 2004.

[125] A. I. Bolozdynya *et al.*, "Using a wavelength shifter to enhance the sensitivity of liquid xenon dark matter detectors," *IEEE Trans. Nucl. Sci.* **55** (2008) 1453–1457. [link].

[126] E. Aprile *et al.*, "Simultaneous Measurement of Ionization and Scintillation from Nuclear Recoils in Liquid Xenon as Target for a Dark Matter Experiment," *Phys. Rev. Lett.* **97** (2006) 081302. arXiv:astro-ph/0601552.

[127] M. Yamashita, *et al.*, "Scintillation response of liquid Xe surrounded by PTFE reflector for gamma rays," *Nuclear Instruments and Methods in Physics Research*

Section A: Accelerators, Spectrometers, Detectors and Associated Equipment **535** (2004) no. 3, 692 – 698. `arXiv:astro-ph/0503621`.

[128] D. Akerib, *et al.*, "LUXSim: A component-centric approach to low-background simulations," *Nuclear Instruments and Methods in Physics Research Section A: Accelerators, Spectrometers, Detectors and Associated Equipment* **675** (2012) no. 0, 63 – 77. `[link]`.

[129] D. Akerib, *et al.*, "An Ultra-Low Background PMT for Liquid Xenon Detectors," *Nuclear Instruments & Methods in Physics Research, Section A: Accelerators, Spectrometers, Detectors, and Associated Equipment* **703** (2013) 1–6. `[link]`.

[130] J. Verbus. PhD thesis, Brown University, 2015.

[131] Adelphi Technologies Incorporated, "DD108 Neutron Generator," 2013. `[link]`.

[132] R. J. Howerton *et al.*, "Evaluated Nuclear Data Library (ENDL): Evaluation Techniques, Reaction Index, and Description of Individual Evaluations," Sept., 1975.

[133] J. Angle, *et al.*, "Search for Light Dark Matter in XENON10 Data,"*Phys. Rev. Lett.* **107** (Jul, 2011) 051301. `[link]`.

[134] J. Allison, *et al.*, "Geant4 developments and applications," *Nuclear Science, IEEE Transactions on* **53** (2006) no. 1, 270–278. `[link]`.

[135] "National Nuclear Data Center Chart of Nuclides," January, 2013. `[link]`.

[136] S. Chu, L. Ekström, and R. Firestone, "Table of Radioactive Isotopes," 1, 2004. http://ie.lbl.gov/toi/. `[link]`.

[137] "A Citizen's Guide To Radon: The Guide To Protecting Yourself And Your Family From Radon," May, 2012. `[link]`.

[138] A. Bradley. PhD thesis, Case Western Reserve University, 2014.

[139] T. Doke, *et al.*, "Absolute Scintillation Yields in Liquid Argon and Xenon for Various Particles," *Japanese Journal of Applied Physics* **41** (2002) no. Part 1, No. 3A, 1538–1545. `[link]`.

[140] J. K. Shultis and R. E. Faw, *Fundamentals of nuclear science and engineering.* CRC Press, 2002. [link]. pp. 137.

[141] D. Mei and C. Zhang, "Neutron Yield in Materials," 2008. http://neutronyield.usd.edu/. [link].

[142] D. M. Mei, C. Zhang, and A. Hime, "Evaluation of (alpha,n) Induced Neutrons as a Background for Dark Matter Experiments," *Nucl. Instrum. Meth.* **A606** (2009) 651–660. arXiv:0812.4307 [nucl-ex].

[143] R. Heaton, *et al.*, "Alpha-induced neutron activity in material," *Nucl. Geophys.* (1990) .

[144] D. S. Akerib, *et al.*, "Radio-assay of Titanium samples for the LUX Experiment,"*ArXiv e-prints* (Dec., 2011) . arXiv:1112.1376 [physics.ins-det].

[145] R. Gaitskell, *et al.*, "The statistics of background rejection in direct detection experiments for dark matter," *Nuclear Physics B - Proceedings Supplements* **51** (1996) no. 2, 279 – 283, <ce:title>Proceedings of the International Symposium on Sources and Detection of Dark Matter in the Universe</ce:title>. [link].

[146] L. E. Strigari, "Neutrino coherent scattering rates at direct dark matter detectors," *New Journal of Physics* **11** (2009) no. 10, 105011. [link].

[147] C. E. Dahl, "Private communication," 2008.

[148] R. Gaitskell, "LUX internal note," tech. rep., Brown University, 2013.

[149] D. C. Malling, *et al.*, "Dark Matter Search Backgrounds from Primordial Radionuclide Chain Disequilibrium," *Submitted for publication* (2013) . [link].

[150] E. Aprile, *et al.*, "The XENON100 dark matter experiment," *Astroparticle Physics* **35** (2012) no. 9, 573 – 590. [link].

[151] D. C. Malling, *et al.*, "After LUX: The LZ Program,"*Proceedings of the 2011 Meeting of the Division of Particles and Fields of the American Physical Society* (October, 2011) . arXiv:1110.0103 [astro-ph.IM].

[152] XENON1T Collaboration, “The XENON1T Dark Matter Search Experiment,” *Proceedings of DM2012 at UCLA, Marina del Rey* (2012) .

[153] A. Marchionni, *et al.*, “ArDM: a ton-scale LAr detector for direct Dark Matter searches,” *Journal of Physics: Conference Series* **308** (2011) no. 1, 012006. `[link]`.

[154] D. Akimov, *et al.*, “Light Yield in DarkSide-10: a Prototype Two-phase Liquid Argon TPC for Dark Matter Searches,”*ArXiv e-prints* (April, 2012) . `arXiv:1204.6218 [astro-ph.IM]`.

[155] E. Aprile, *et al.*, “Material screening and selection for {XENON100},” *Astroparticle Physics* **35** (2011) no. 2, 43 – 49. `[link]`.

[156] V. Álvarez, *et al.*, “Radiopurity control in the NEXT-100 double beta decay experiment: procedures and initial measurements,” *Journal of Instrumentation* **8** (2013) no. 01, T01002. `[link]`.

[157] P. Finnerty, *et al.*, “Low-background gamma counting at the Kimballton Underground Research Facility,” *Nuclear Instruments and Methods in Physics Research Section A: Accelerators, Spectrometers, Detectors and Associated Equipment* **642** (2011) no. 1, 65 – 69. `[link]`.

[158] W. Maneschg *et al.*, “Measurements of extremely low radioactivity levels in stainless steel for GERDA,” *Nucl. Instrum. Meth.* **A593** (2008) 448–453. `[link]`.

[159] R. Heaton, *et al.*, “Neutron production from thick-target ([alpha], n) reactions,” *Nuclear Instruments and Methods in Physics Research Section A: Accelerators, Spectrometers, Detectors and Associated Equipment* **276** (1989) no. 3, 529 – 538. `[link]`.

[160] A. Koning, S. Hilaire, and M. Duijvestijn, “TALYS-1.4: A nuclear reaction program,” December, 2011. `[link]`.

[161] M. Berger, *et al.*, “ESTAR, PSTAR, and ASTAR: Computer Programs for Calculating Stopping-Power and Range Tables for Electrons, Protons, and Helium Ions (version 1.2.3),” January, 2013. `[link]`.

[162] S. Harissopulos, *et al.*, "Cross section of the ^{13}C(α,n)^{16}O reaction: A background for the measurement of geo-neutrinos,"*Phys. Rev. C* **72** (Dec, 2005) 062801. `[link]`.

[163] A. Hime, "The MiniCLEAN Dark Matter Experiment,"*Proceedings of the 2011 Meeting of the Division of Particles and Fields of the American Physical Society* (October, 2011) . `arXiv:1110.1005 [physics.ins-det]`.

[164] M. Attisha, *et al.*, "Soudan Low Background Counting Facility (SOLO)," vol. 785, pp. 75–78. AIP, 2005. `[link]`.

[165] S. Chen, *et al.*, "NCRP Report No. 141: Managing Potentially Radioactive Scrap Metal," tech. rep., National Council on Radiation Protection and Measurements, Bethesda, MD, 2002.

[166] N. Ackerman, *et al.*, "Cosmogenic activation in germanium and copper for rare event searches," *Astroparticle Physics* **33** (2010) 316–329. `[link]`.

[167] J. A. Formaggio and C. Martoff, "Backgrounds to sensitive experiments underground," *Annual Review of Nuclear and Particle Science* **54** (2004) no. 1, 361–412. `[link]`.

[168] M. Laubenstein and G. Heusser, "Cosmogenic radionuclides in metals as indicator for sea level exposure history," *Applied Radiation and Isotopes* **67** (2009) 750–754. `[link]`.

[169] D.-M. Mei, Z.-B. Yin, and S. Elliott, "Cosmogenic production as a background in searching for rare physics processes," *Astroparticle Physics* **31** (2009) no. 6, 417 – 420. `[link]`.

[170] M. Gordon, *et al.*, "Measurement of the flux and energy spectrum of cosmic-ray induced neutrons on the ground,"*Nuclear Science, IEEE Transactions on* **51** (Dec., 2004) 3427–3434. `[link]`.

[171] S. Fiorucci, "LUX Internal Note," 2010.

[172] J. J. Back and Y. A. Ramachers, "ACTIVIA: Calculation of Isotope Production Cross-sections and Yields," *Nuclear Instruments & Methods in Physics Research, Section A: Accelerators, Spectrometers, Detectors, and Associated Equipment* **586** (2008) 286. `arXiv:0709.3472`.

[173] K. T. Lesko, *et al.*, "Deep Underground Science and Engineering Laboratory - Preliminary Design Report,"*ArXiv e-prints* (Aug., 2011) . `arXiv:1108.0959 [hep-ex]`.

[174] J. Liu and the XMASS collaboration, "The XMASS 800kg detector," *Journal of Physics: Conference Series* **375** (2012) no. 1, 012022. `[link]`.

[175] *R11065 Data Sheet*, March, 2009.

[176] Hamamatsu Photonics K.K., *R11410 MOD Data Sheet*, October, 2009.